Doctoral Dissertation
Doctoral Program in Material Science and Technology (34th Cycle)

Multifunctional cyclodextrin derivatives for digital light processing 3D-printing

Andrea Cosola

Supervisors:

- Prof. Marco Sangermano, Supervisor, Politecnico di Torino, Department of Applied Science and Technology (Torino, Italy)
- Dr. Annalisa Chiappone, Co-Supervisor, Università degli Studi di Cagliari, Department of Chemical and Geological Sciences (Cagliari, Italy)

Doctoral Examination Committee:

- Prof. Angels Serra Albet, Universitat Roviri i Virgili (Tarragona, Spain) (Referee)
- Prof. Francesco Secci, Università degli Studi di Cagliari, Department of Chemical and Geological Sciences (Cagliari, Italy) (Referee)
- Dr. Sandra Schlögl, Polymer Competence Center Leoben (Leoben, Austria)
- Dr. Giancarlo Rizza, Laboratoire des Solides Irradiés (LSI), Institut Polytechnique de Paris, CEA/DRF/IRAMIS, CNRS, Ecole Polytechnique, (Palaiseau, France)

Politecnico di Torino
2022

Declaration

I hereby declare that the contents and organization of this dissertation constitute my own original work and does not compromise in any way the rights of third parties, including those relating to the security of personal data.

Andrea Cosola

Turin, 2022

* This dissertation is presented in partial fulfillment of the requirements for **Ph.D. degree** in the Graduate School of Politecnico di Torino (ScuDo).

In loving memory of my father

Acknowledgments

First and foremost, I would like to express my gratitude and sincere appreciation to my supervisors Prof. M. Sangermano and Dr. A. Chiappone for giving me the opportunity to carry out my PhD in their groups and for their long-lasting support, guidance, trust and patience over these years.

I also would like to express my deepest thanks to Prof. H. Grützmacher who hosted me in his labs at ETH Zürich, introducing me to the intriguing world of phosphorous chemistry. I truly believe this experience has been fundamental for the further development of my research activities.

A particular thank to Dr. I. Roppolo for his valuable suggestions on 3D-printing.

I would like to thank Prof. M. Messori for his precious collaboration in the shape memory investigations.

My special thanks to Dr. R. Conti for his support during my stay at ETH, whether it was about chemistry or anything else. Thank you for considering me as a friend and not just as a colleague.

I take the opportunity to thank all the former and current members of Photopolymer-group and "3D-group", and all the lifelong colleagues of PoliTo for the daily discussions and nice moments we spent together (not only in the lab!): Matteo C., Lorenzo V., Luisa, Simone, Gustavo, Angelo, Jacopo, Lorenzo P., Michael, Diana, Alberto, Daniele, Alejandra, Beatrice, Matteo T., Andrea, Carlo and Cristian.

I would also like to thank the "Grützis" who make me feel as a real member of the Grützmacher group and not just a guest.

A special thanks to Camilla for being constantly by my side and for always believing in me, smiling even in the difficult moments. Thanks for being Camilla!

Last but not least, I would like to thank my family for encouraging and always supporting me, and for being so close in every moment of my life.

Abstract

By virtue of an almost unlimited freedom of design and customization, a near-zero material waste and the possibility to fabricate in one-single stage complex parts, additive manufacturing (alias 3D-printing) has opened in the last twenty years new horizons in many different fields, from automotive to medicine. In particular, photopolymerization based 3D-printing technologies (i.e. vat polymerization) are attracting growing interest due to the high versatility given by photochemistry, that is the possibility to exploit light to tune the structure-property relationships of polymers via fast and spatiotemporal controlled reactions. However, the need of polymers having suitable photopolymerizable functionalities limits the choice of printable materials and thus also the large-scale adoption of these techniques. To deal with this issue and the new stringent request of a more sustainable manufacturing, the research community is endeavoring to enlarge the photopolymers palette with "greener" alternatives prepared from natural molecules or their derivatives. In this framework, the experimental investigations presented throughout this dissertation focus on the synthesis of multifunctional cyclodextrin derivatives suitable for vat polymerization. Indeed, cyclodextrins are very versatile molecules and can be used as building blocks for the development of molecularly well-defined derivatives because their hydroxyl groups can be rather easily converted into the desired functionalities.

After a brief overview of additive manufacturing (chapter 1) and an in-depth investigation of vat polymerization (from the photochemical reactions involved to the photoresins typically used, chapter 2), the first experimental contribution (chapter 3) is focused on the synthesis of a multi-acrylated cyclodextrin and its use as photocurable macromer in bio-based formulations for digital light processing 3D-printing. Specifically, combining this multifunctional cyclodextrin derivative with a monofunctional monomer is presented as the most promising strategy, since this allows to get thermosetting polymers whose mechanical properties can be tuned by balancing the high crosslinking efficiency of the former and the plasticizing effect of the latter.

However, the use of photocurable formulations containing multiunsaturated monomers as the multi-acrylated cyclodextrin presented in this study inherently

entails anomalous behaviors, above all the incomplete conversion of the photopolymerizable functionalities during the printing step. In this sense, different strategies of post-printing functionalization are presented in the second experimental contribution (chapter 4) as a powerful tool to turn the unreacted acrylate functions into a potential advantage, since these can provide active sites for surface modifications. To support this, Michael-addition reactions are exploited to tune the surface-wettability of 3D-printed structures via the grafting of hydrophobic/hydrophilic polymeric brushes. Moreover, the modification of the surface with a thiolated active interface is used for a subsequent surface-anchoring of photoreduced silver nanoparticles.

In the third experimental contribution (chapter 5), cyclodextrins are used as building blocks to prepare a molecularly well-defined multifunctional photoinitiator via the grafting of multiple bis(acyl)phosphane oxide photoactive units. The high photoinitiating efficiency of this multi-photoactive cyclodextrin derivative is demonstrated, even when using it at low molar concentrations. But mostly, this multifunctional photoinitiator stands out by its ability to serve simultaneously as photo-crosslinking agent to convert monofunctional monomers into mechanically stable thermosets without the need of additional crosslinkers.

This unique feature is finally exploited in the last experimental contribution (chapter 6) to enable the printability of crosslinkers-free formulations. Indeed, a novel photopolymerizable system based only on monofunctional methacrylates bearing hydrogen-bonding groups is used to fabricate thermoresponsive shape memory polymers by means of digital light processing 3D-printing. In this context, the multi-photoactive cyclodextrin derivative is used as a *two-in-one* photoinitiator and crosslinking agent ensuring the printability of the monomethacrylates-based system. Moreover, it provides covalently crosslinked net-points which serve to impart dimensional stability and prevent chain slippage when heating the printed structures to above their glass transition temperature in the deforming and recovery stages of the shape memory cycle. The properties of the fabricated shape memory polymers are investigated in details and their potential integration in the fabrication of a smart thermoresponsive device is proved by the succesful development of a prototype.

“3D-printing is already shaking
our age-old notions of what can and can’t be made.”

Hod Lipson

Table of contents

1. Brief overview of additive manufacturing

Principles, applications and processes

1.1 Technological innovation and impact on the society

Additive manufacturing (AM), generally referred to as three-dimensional (3D) printing, was introduced in 1986 when C. W. Hull filed a patent on the fabrication of 3D-objects via the selective UV-irradiation of a liquid resin,[1] and refers to a wide range of technologies that enable the fabrication of complex 3D-geometries using Computer Aided Design (CAD) software.[2–6]

Being able to reduce the gap between ideas-conceptualization and product-development and to stimulate a substantial transformation and digitalization of the entire manufacturing sector, AM has been recognized as a technological breakthrough of the latest industrial revolution.[7,8] Indeed, as opposed to conventional subtractive manufacturing methodologies that make products by removing materials, AM allows to build up parts in an additive fashion without the need for expensive molds, dies, tools or additional equipment, thus limiting material wastes, costs and the number of iterative stages. Moreover, AM inherently entails an approximately unlimited freedom of design which let to meet individual demands via the production of customized parts otherwise difficult to obtain, ranging from prototypes to small series for specific applications. This design-flexibility is remarkably relevant, since it allows to rapidly turn the tide using computers and automated processes throughout, which means that eventual amendments could be easily shifted to the earlier stages of the production cycle avoiding any increase in processing time and expensive corrections.[2,9]

Despite these unique features, AM was originally limited to rapid prototyping (RP) and mostly used by designers and engineers to create models for validation purposes and to fasten the development of items to be put into industrial production. However, in the last years it has rapidly evolved beyond RP giving a significant

boost to both academic research, as evidenced from the growing number of yearly scientific publications on the topic (**Figure 1.1**), and industrial fields, where it proved to be effective in the re-shaping of many manufacturing processes (**Figure 1.2**).[10–12]

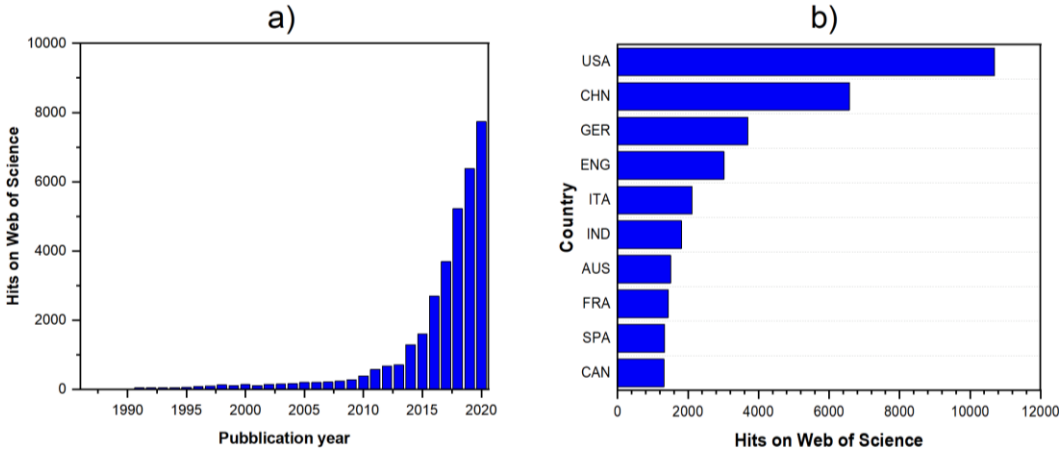

Figure 1.1. a) Number of the yearly scientific publications and b) ten most prolific countries in research-topics related to AM between 1986 and 2020 (the data were obtained from the citation indexing service of Web of Science, last access on September 27, 2021).

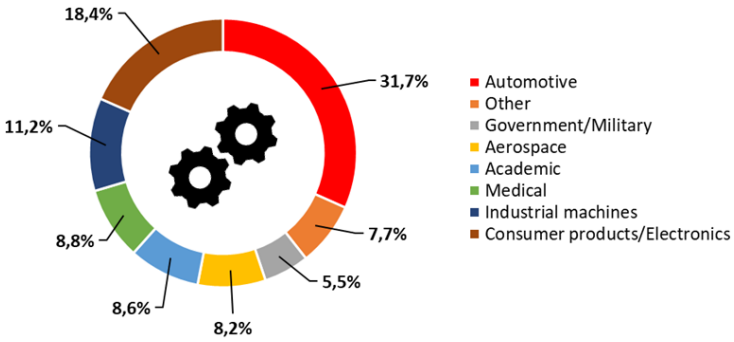

Figure 1.2. Industrial applications of AM according to the worldwide market revenues of 2020 (data from Wohlers Report 2020).

The significant impact of AM reflected into a growing financial market led by major industrial players, such as Stratasys Ltd., 3D Systems Corporation, ExOne Co., General Electric Company (GE Additive) and Proto Labs Inc. In this sense, the global AM revenues were valued at USD 19 billion in 2020, with the largest

revenues belonging to polymeric materials (mostly photopolymers) and are expected to reach 64 billion by the end of 2026 at a compound annual growth rate (CAGR) of 29.48%, with Asia-Pacific as the fastest-growing region (**Figure 1.3**).[13]

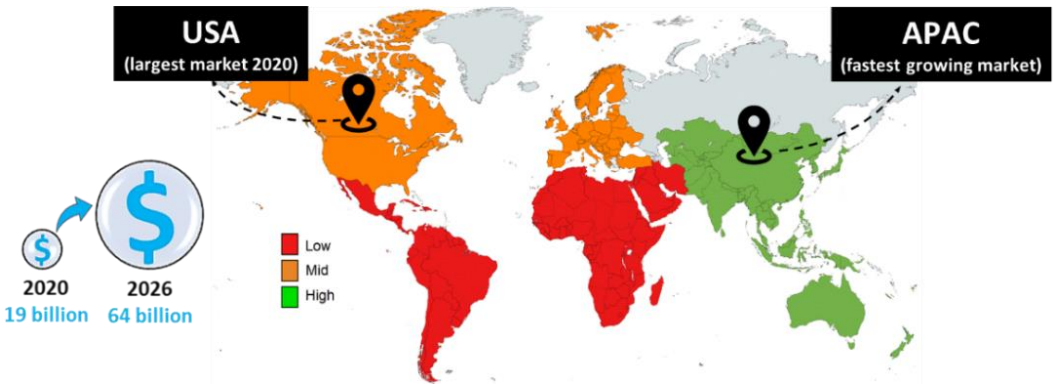

Figure 1.3. Expected growth rate (2020-2026) of the AM market monitored by countries/region (data from Mordor Intelligence - Industry Trends, Growth, Size).

Over the last two decades, AM have been proposed in the automotive and aerospace fields, helping to fabricate lighter parts with similar strength to those produced by conventional manufacturing processes (e.g. bumpers, cooling vents, valves and pumps for automotive and rib-web components, turbine engine cases and engine blades for the aerospace industries), while also reducing the part count to a single component.[10,12,14,15] Notably, AM is showing a great potential in the medical field, ranging from the preparation of models for surgical planning to the design and fabrication of implants for tissue engineering. Indeed, the combination of computer tomography and/or magnetic resonance imaging with CAD modelling and AM technologies allows to meet the individual needs of the patients for customized bioimplants or prothesis.[16–19] Likewise, AM provided a new platform for the on-demand production of personalized drug delivery systems for individual treatments,[20–23] and still, it is being explored for optical applications, to fabricate parts with submicrometric resolution such as optical waveguides,[24,25] or to produce components capable to harvest and store energy.[26,27] Moreover, AM is being used in the construction industry to increase customization while reducing material wastage, processing time and manpower. In this context, researchers across the world are even making progress in the fabrication of entire houses.[28–31] Also, AM found application in textile, where the freedom of design gives many opportunities in apparel making, as well as in the

jewelry field and in functional-art.[32–34] More recently, AM also joined the food-processing field aimed to 1) provide products for individual needs; 2) control the nutrition content while using a very limited feedstock of materials; 3) give new options for molecular gastronomists; 4) enable a customized food design and 5) offload from time expenditure and the expertise required by conventional cooking procedures.[35–38]

Remarkably, the interdisciplinary advancement will surely allow AM to meet a wider range of practical applications in the near future. Indeed, within the framework of a continuous innovation, engineers are pushing boundaries of AM in the development of new technologies, while chemists are working on new printable systems with a growing interest for bio-based materials and to materials with specific functionalities.[39] In this context, the design of functional materials, the manufacturing of components having specific topological structures or the development of versatile postprocessing methods for surface modification are already further extending AM capabilities. In particular, the modification of polymeric surfaces opened-up new horizons allowing to impart to the printed structures superior features (e.g. biocompatibility, antifouling, drag-reduction, tunable wettability and antibacterial properties).[40] Moreover, also the so-called four-dimensional (4D) printing, initially defined as “3D-printing plus time” has recently emerged as a powerful innovation for advanced AM systems. The 4D concept was pioneered by Skylar Tibbits, as referred to 3D-printed objects capable to shift either their shape, property or functionality with time when exposed to a predetermined stimulus such as heat, water, pH, light etc.[41,42] In this sense, the development of stimuli-responsive polymers, such as shape-memory polymers, may give a significant boost to the fabrication of smart 3D-objects with programmable shape and/or properties, with potential applications in soft robotics, regenerative medicine, bioprinting, smart packaging, drug delivery and others.[17,43–48] Furthermore, the recent advances in multimaterial printing have shown the potential to further extend the possibilities given by AM, enabling the fabrication of customized multifunctional parts by varying either the composition or the type of materials within the layers.[49]

1.2 AM technologies

According to the American Society for Testing and Materials (ASTM), more than 50 AM technologies have been developed since stereolithography was introduced by Hull in the late 1980s. These mainly differ in terms of materials feedstock (i.e.

polymers, metals, ceramics and even composites) and operating principles. As a result, a wide numbers of machines appeared on the market (**Figure 1.4**).[50]

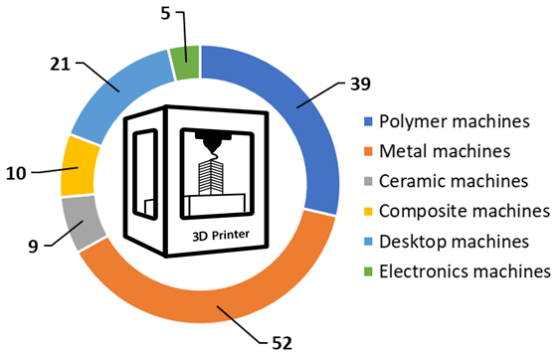

Figure 1.4. Types of 3D-printers currently available on the market (data from AMFG, *Additive Manufacturing Landscape 2020*).

However, the AM process-workflow is common to most of the technologies and involves a design phase followed by pre-processing, building and post-processing stages.

First digital 3D-models are prepared by using professional CAD software or processed from the direct inspection of physical objects using reverse engineering equipment (e.g. 3D-scanners). The CAD model so obtained is then converted in a standard triangulation language (STL) format and uploaded to the printer where it is sliced in an array of horizontal 2D cross-sections. Subsequently, once some preliminary operations have been completed (e.g. orientation and position of the model on a building platform, addition of supports and set-up of the printing parameters) the process moves to the computer-controlled building stage, which proceeds layer-by-layer till the part is completed or the material source is finished. Ideally, the printed object should be ready to be used. More realistically, some manipulations are required such as the removal of the additional supports eventually used to prevent the build from collapsing or warping, and/or a cleaning step to remove surrounding excess of materials. Post-processing may be needed to improve the surface finish or specific properties of the part for the final application purposes.[2]

The main step involved in an AM process are schematically summarized in **Figure 1.5,** which shows an example of AM process-workflow, from CAD to part, relative to the fabrication of a polymeric spinning wheel via a light-based AM technique.

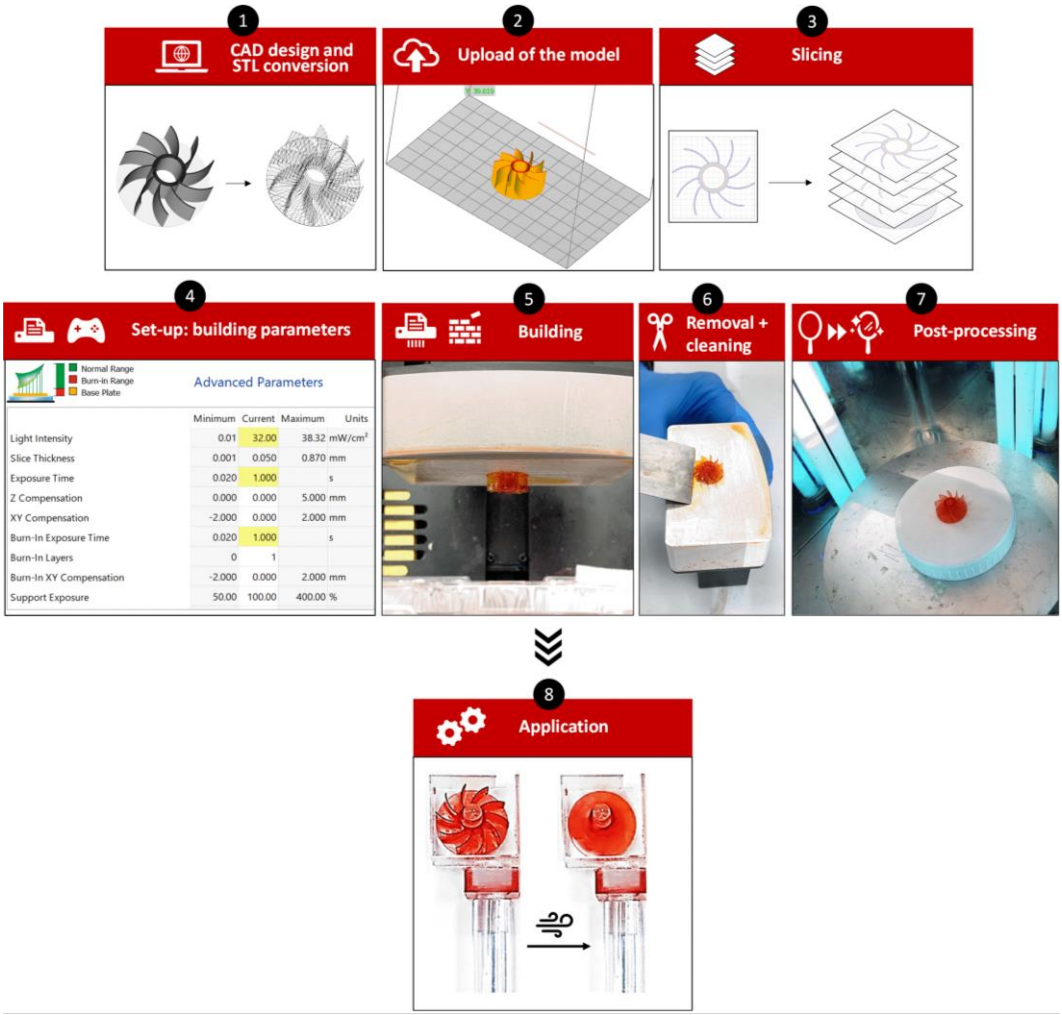

Figure 1.5. Generic process-workflow of AM: 1) preparation of the digital model using a professional CAD software and conversion of the CAD file in a STL format; 2) upload and manipulation of the STL file using the software of the AM machine; 3) slicing; 4) setting of the printing parameters; 5) computer-controlled building stage performed layer-by-layer; 6) removal of the printed part from the building platform and cleaning; 7) post-processing (e.g. post-curing, typical for parts printed from photopolymers) and 8) application after final assembly.

Despite some exceptions, all the commercially available AM machines follow the abovementioned layer-by-layer building approach, but they mainly differ in terms of material processing and/or layer deposition. Some technologies extrude materials in the form of filaments, others exploit the light irradiated from lasers or projectors to cure a photosensitive liquid resin. Also, lasers or even electron beams are exploited to melt or sinter powders together, while still other techniques use

inkjet-type printing heads to accurately spray binder or solvent onto powders.[2,3,51] Specifically, ASTM grouped AM processes into 7 main categories (ISO/ASTM 52900:2015):

1) Material extrusion processes, such as fused deposition modeling (FDM) and 3D bio-plotting, based on the selective extrusion of a material through a nozzle.
2) Material jetting processes, such as inkjet-printing systems, based on the selective deposition of liquid droplets of material.
3) Binder jetting processes based on the selective deposition of a liquid bonding agent on powder materials.
4) Sheet lamination processes based on the bonding of sheets of material.
5) Powder bed fusion processes, such as selective laser sintering (SLS) and electron beam melting (EBM), based on the selective fusion of material powders with the thermal energy provided by either a laser or an electron beam.
6) Direct energy deposition processes based on the use of thermal energy (e.g. laser or plasma arc) to locally melt metals as they are being deposited.
7) Vat polymerization (VP) processes, such as stereolithography (SLA), digital light processing (DLP), continuous liquid interface production (CLIP), two photon polymerization (2PP) and other volumetric techniques, based on the selective photopolymerization of a liquid resin.

Looking at polymeric AM, the analysis of the financial market revealed that polymers are currently mainly manufactured via material extrusion or VP processes, even if the use of powder bed fusion processes is expected to increase by 2027 (**Figure 1.6**).[52]

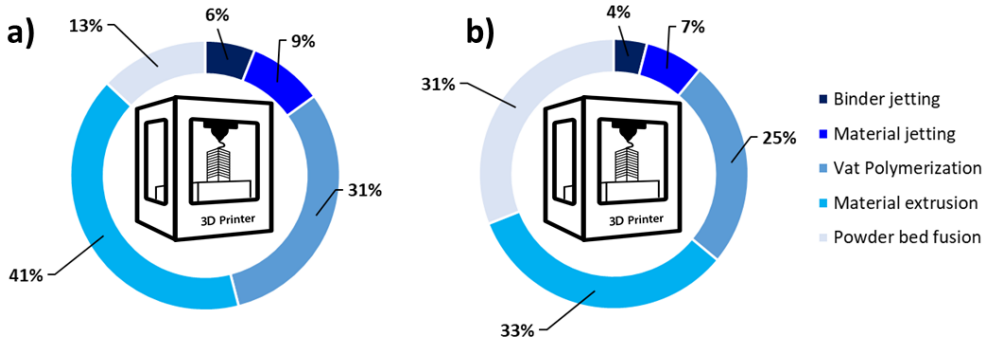

Figure 1.6. Polymer 3D-printing processes used in professional environments in a) 2018 and b) expected evolution by the end of 2027 according to the analysis of the global market revenues (data from SmarTech Publishing, *Additive Manufacturing with Polymers and Plastics 2018*).

The main features of these technologies (building speed, costs and resolution, suitable materials, final properties of the fabricated parts) and the major global manufacturers, are shown in **Figure 1.7**.[3–6,53]

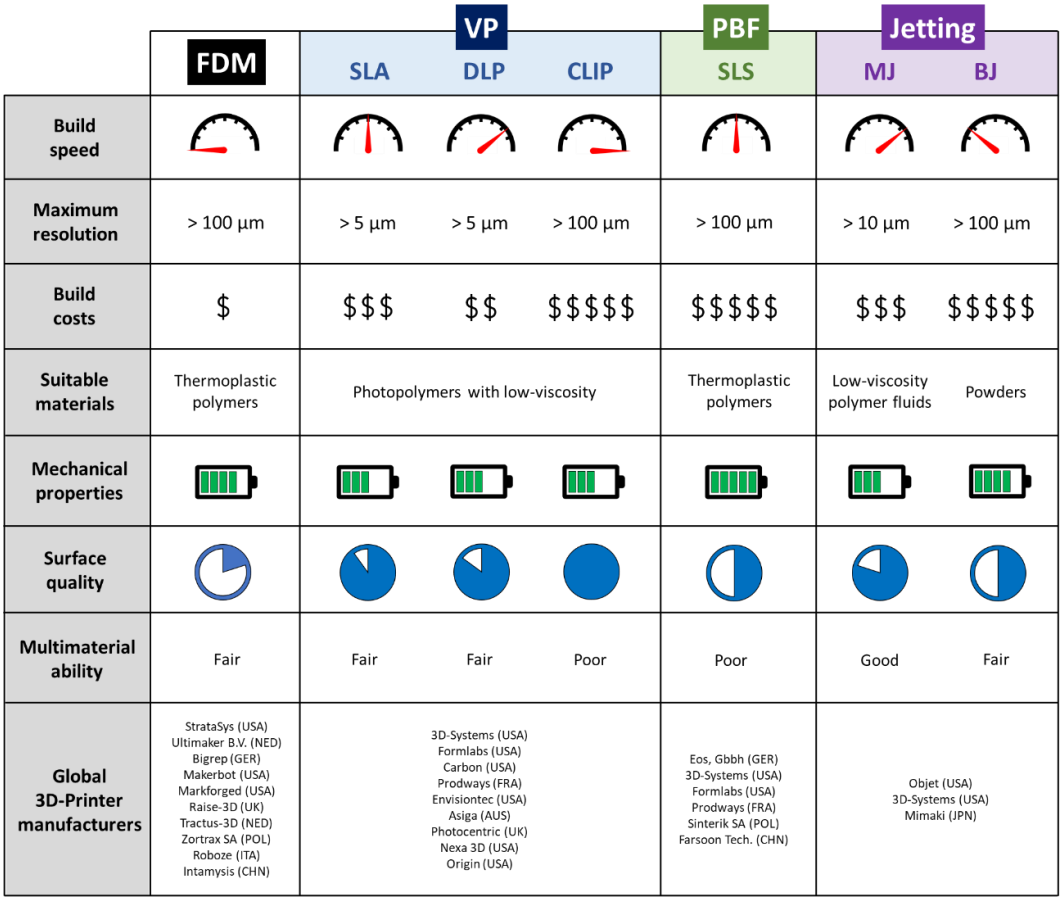

Figure 1.7. Main features, usable materials, final properties of the fabricated parts and major global manufacturers of AM technologies for polymeric materials.

Considering the experimental studies presented throughout this dissertation, the next chapter will be entirely dedicated to an in-depth investigation of VP. In particular, the emphasis will be given to 1) the basic principles of photochemistry behind the photopolymerization reactions involved in the printing process, 2) the available VP technologies, 3) the photoresins typically employed according to the current state of the art and 4) the recent advances and future directions of VP.

2. AM meets photochemistry

Fundamentals, technologies and materials

2.1 The power of light in polymer science

The use of light to finely tune the structure–property relationships in polymeric materials is undoubtedly one of the most powerful paradigms in polymer chemistry. The ability to activate photochemical reactions to create, modify or cleave chemical bonds at room temperature and with a spatiotemporal control enabled over the years the use of photochemistry in the processing of UV-curable coatings, inks and adhesives; as well as for energy, optics, photonics, microelectronics, biomedicine and stereolithography applications. Indeed, photochemical processes are energetically favored at ambient temperature and occur on reasonable timescales when activated, suffice it to say the energy in a mole of photons at 365 nm is more than 130 times higher than the thermal energy available to activate a reaction at 25 °C. Moreover, the spatial and temporal control can be easily achieved by turning on and off the light source and using shutter or masks, respectively.[54]

The basic principle of photochemistry, universally valid for all the photochemical processes based on one-photon absorption (OPA), is that a photon needs to be absorbed to activate any subsequent reactions in a molecule. The absorption of a photon upon light excitation is charged either directly by a molecule having the targeted reactive functional group, by a molecule that generates reactive intermediates, or by a photosensitizer which reacts with other molecules to activate one of the former reactions. In particular, the absorbed photon promotes an electron of the chromophore from its ground state (S_0) to its excited singlet state (S_1), as illustrated in a typical Jablonski diagram (**Figure 2.1**).[54,55] The short-lived S_1 may then deactivate to S_0 by fluorescence emission or by internal conversion via non radiative transitions. Alternatively, it may relax via intersystem crossing (ISC) to a lower energetic triplet state (T_1), which in turn may be deactivated to S_0 via different photophysical processes (e.g. phosphorescence emission) or may lead to the occurrence of primary photochemical reactions.

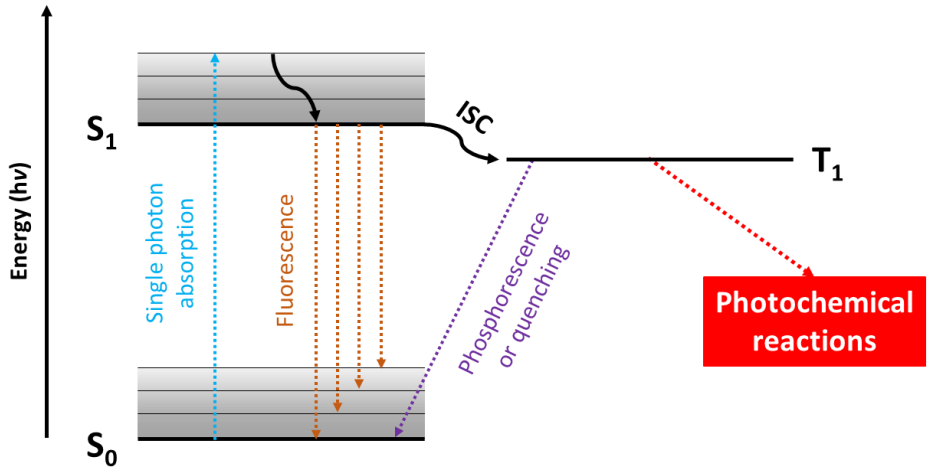

Figure 2.1. Jablosnki diagram illustrating electronic states and transitions activated upon single-photon absorption: the excited singlet state (S_1) undergoes intersystem crossing (ISC) to a triplet state (T_1), which leads to different photochemical reactions.

For each photochemical OPA process, the initiation rate of the desired primary photochemical reaction (R_i) is determined as follows (Eq. 2.1):

$$R_i = \varphi I_A \qquad \text{Eq. 2.1}$$

where φ is the quantum yield, i.e. the fraction of the photons absorbed that lead to the target molecular transformation, and I_A is the intensity of the absorbed light calculated with the Beer–Lambert law. As both the light intensity, the molar absorptivity, and the quantum yield depend on the wavelength, I_A and R_i are calculated by integrating over the absorption spectra of the absorbing molecule and the emission spectra of the light source. In the case of photoinduced radical reactions, where the initiation rate for polymerization is the product of initiating efficiency of the primary radicals, quantum yield, and absorbed photon flux, the efficiency classically represents the fraction of photogenerated radicals that successfully react with a monomer unit to start the polymerization.[54]

Primary photochemical transformations in polymers science involve a library of isomerizations,[56–61] bond-forming [62–65] and bond-breaking reactions.[66–69], some examples of which are provided in **Figure 2.2**. Among these, a particular attention is given hereafter to the analysis of those bond-breaking reactions typically used to generate radicals and acid/cationic reactive intermediates which serve to activate photopolymerization processes.

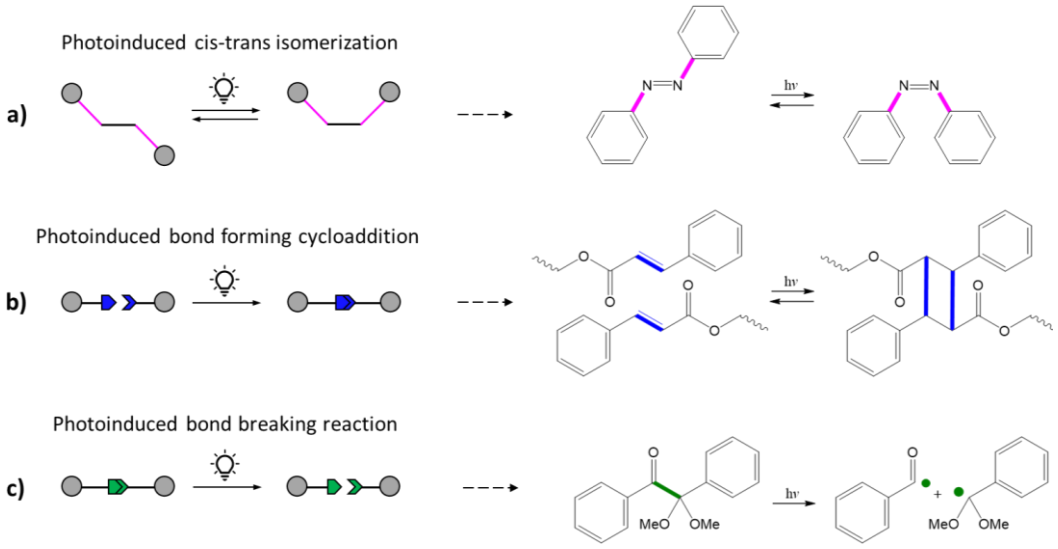

Figure 2.2. Examples of typical primary photochemical reactions: a) photoinduced cis-trans isomerization of azobenzene; b) cycloaddition reaction of cinnamate containing polymers with formation of a new C-C bond and c) photoinduced generation of radical reactive intermediates via direct cleavage of a C-C bond of dimethoxyphenyl acetophenone.

The photoinduced generation of radicals is one of the most famous implementations of photochemistry in polymer science. As previously mentioned, a photon needs to be absorbed by a specific molecule to enable any subsequent photochemical reaction to occur from the non-deactivated T_1 (see Figure 2.1). Generally, radicals can be generated via two different reactions mechanisms depending on the type of the molecular system being involved in the photochemical process.

Norrish type I reactions (NT1) involve an unimolecular photochemical cleavage (or homolysis) to generate two reactive radical intermediates.[70–73] Note that the homolytic cleavage may occur directly from S_1, but since the excited T_1 reached by ISC is similar in energy to S_1 but longer lived, the photogeneration of radicals from the triplet predominates. The photolysis of bis(2,4,6-trimethylbenzoyl)phenylphosphine oxide is given in **Figure 2.3** as an example of a NT1 mechanism. As can be observed in the figure, the photocleavage from the activated T_1, commonly known as α-cleavage since the homolytic scission involves the carbon-carbon (C-C) bond adjacent (i.e. α position) to the carbonyl (C=O) chromophore group, leads to the generation of a phosphinoyl radical (a) and a benzoyl radical (b). In the absence of trapping agents these primary radicals can

recombine or form different products (c-f) via either cage or escape reactions.[74] But, in the presence of reactive monomers such as (meth)acrylates, they serve to initiate free-radical polymerizations. Remarkably, it was reported that the phosphinoyl radical is two to six times more reactive than the benzoyl one.[75]

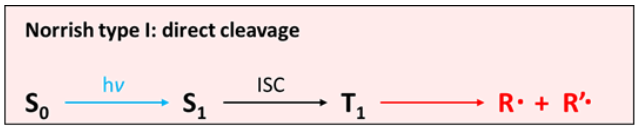

Generation of reactive radicals from *phenylbis(2,4,6-trimethylbenzoyl)phosphine oxide*

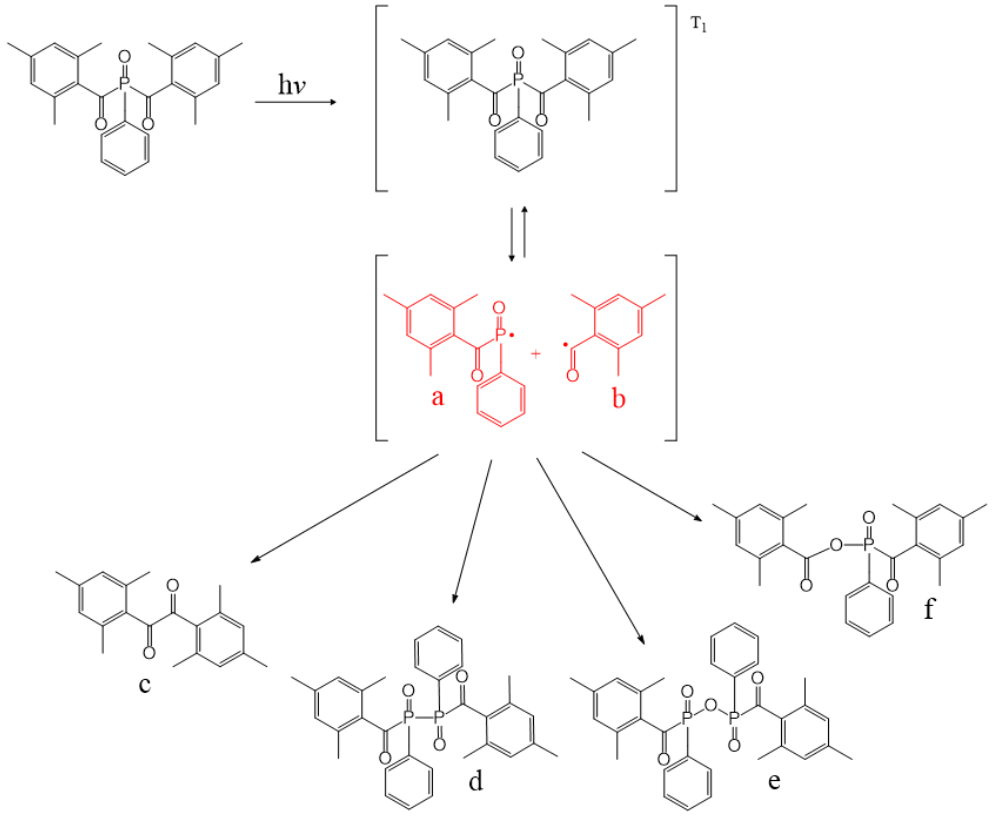

Figure 2.3. a-b) Radical products formed during the photolysis of bis(2,4,6-trimethylbenzoyl)phenylphosphine oxide via a NT1 mechanism and c-f) products which may form from the recombination of the phosphinoyl radical (a) and (b) benzoyl radical by means of escape or cage reactions.

On the contrary, Norrish type II reactions (NT2) involve a bimolecular photochemical mechanism in which a chromophore interacts with a hydrogen-

donor molecule (DH, typically amines) to generate radicals by means of hydrogen abstraction.[70,73,76,77] **Figure 2.4** shows the generation of radical intermediates via the NT2 mechanism involving camphorquinone (CQ). As schematically illustrated, CQ is promoted to an excited T_1 when exposed to light of a specific wavelength. While in its T1, CQ reacts with a tertiary amine used as reducing agent to form an excited complex state commonly known as "exciplex." Then, two ion species are generated by electron transfer from the electron-donor amine to the activated carbonyl of CQ, which behaves as the electron acceptor. Finally, two radicals are generated via intramolecular H-abstraction: a CQ-ketyl radical (a) relatively unreactive and mainly involved in radical recombination reactions and an aminoalkyl radical (b) which can serve to initiate the radical polymerization of monomers/oligomers such as (meth)acrylates.[78]

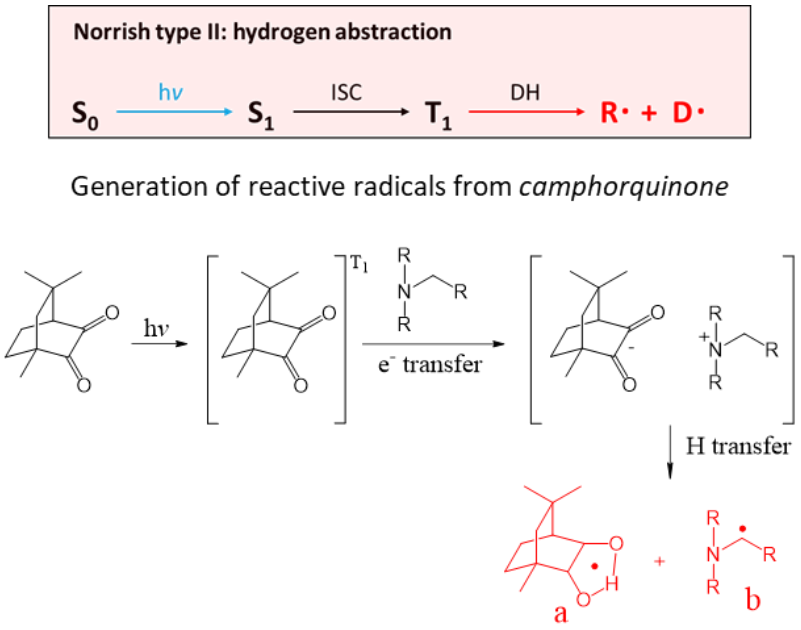

Figure 2.4. a-b) Radical products formed after the NT2 rection involving camphorquinone and a tertiary amine.

Another typical bond-breaking reaction induced by light-exposure is the generation of acid/cation reactive intermediates. In such a type of photochemical process, the photoinduced decomposition of a photoacid generator (PAG) in the presence of a non-nucleophilic counterion yields a mixture of cations, radical cations and other intermediates which are responsible to activate further acid-catalyzed reactions. PAGs find widespread use in photoinduced cationic

polymerization since the subsequent reaction of the radical cations with specific monomers leads to the generation of a Bronsted acid, which initiates the polymerization.

Onium salts are amongst the most famous PAGs and consist of an organic cation coupled with an inorganic anion. The former is the light-absorbing component and seat of the photochemistry of these ionic compounds, while the latter determines the strength of the acid generated after the photolysis and the reactivity of the propagating ion pair.[66,79] The photodecomposition mechanism of a diaryliodonium salt ($Ar_2I^+MtX_n^-$) having a complex metal halide anion (MtX_n^-, such as BF_4^-, PF_6^-, AsF_6^- and SbF_6^-) is a typical example of light-induced bond-breaking reaction which leads to the generation of acid/cation reactive intermediates (**Figure 2.5**). The mechanism is quite complex since radicals can be photogenerated from both S_1 and T_1. Indeed, the UV irradiation induces both homolytic and heterolytic cleavages of Ar–I giving reactive cations, radical-cations, and other radicals. The further reaction of these reactive intermediates with hydrogen-donor species present in the reaction mixture, leads to the generation of Bronsted acids ($HMtX_n$) that are typically used as the primary initiating species for cationic polymerization.[66,80] These acids generated upon photolysis are generally referred to as "superacids" since their acidity values in the Hammet scale range from -14 to -30, where the acidity increases with the increase of dimension of the counterion ($BF_4^- < PF_6^- < AsF_6^- < SbF_6^-$), due to a lower nucleophilic character of the latter.

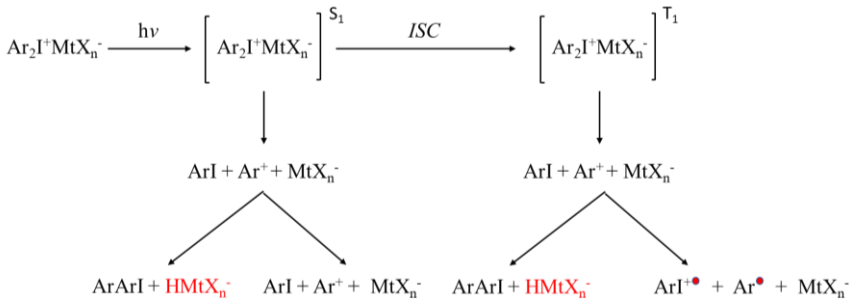

Figure 2.5. Generation of acid/cationic reactive intermediates upon photoinduced decomposition of diaryliodonium salts.

2.2 Principles of photopolymerization

Among all the implementations of photochemistry involving polymers, the photopolymerization of photosensitive liquid resins is undoubtedly one of the most

famous and widely used. Such a type of photochemical process requires a photoinitiator (PI), namely that molecule able to absorb photons and to convert photolytic energy into the generation of intermediate reactive species (radicals or cations, see previous subsection) which are responsible to drive the polymerization of suitable monomers or oligomers. Depending on whether monounsaturated or multiunsaturated monomers are used (i.e. according to the number of photopolymerizable functional groups), linear, branched or crosslinked polymers (thermosets) can be generated.[81,82] Broadly, the photopolymerization can be activated at different wavelengths, ranging from X-rays[83,84] to NIR.[85,86] However, most of the reactions are carried out within the UV-Vis range.[87,88]

Focusing on the photopolymerization of systems containing multifunctional specie, which are of particular interest for light-based AM processes, the liquid phase typically consists of a mixture of low molecular weight monomers/oligomers. As soon as the system is exposed to light irradiation, the PI absorbs photons and generates reactive radicals or ions (according to the mechanisms discussed in the previous subsection) which are responsible to activate the polymerization. The reaction proceeds via the sequential addition of unreacted specie so that both the degree of branching and crosslinking increase and a polymer of infinite size begins to form. This brings to the so-called gelation, which means that the growing polymer starts to generate an insoluble and no more liquid-like gel phase characterized by an ever-higher number of intermolecular connections. The further advancement of the reaction leads to a gradually increase of the crosslinking density, resulting into the formation of a thermosetting 3D-network (**Figure 2.6**).[89]

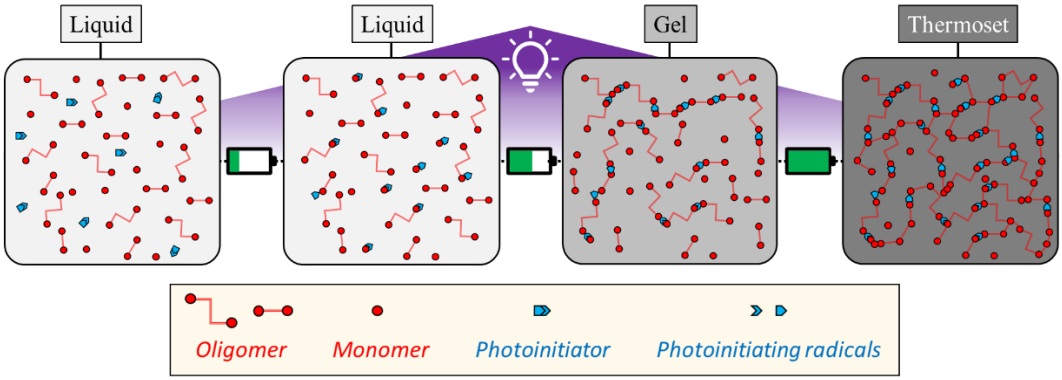

Figure 2.6. Schematic representation of the main stages of the photoinduced polymerization of a liquid system containing multifunctional specie: generation of reactive specie, activation of the polymerization of the monomers/oligomers, formation of an

insoluble gel-like phase (gelation) via an ever-growing number of intermolecular connections and final generation of a thermosetting polymer.

Generally, the photopolymerization proceeds via a chain-growth mechanism, as typical for those reactions involving either radical or cationic systems. However, also a step-growth mechanism is possible, as in the case of radical-mediated thiol-ene reactions. A brief overview on the basic principles of these reactions is presented hereafter, given that radical, cationic and thiol-ene systems are the typical ingredient of the photoresins being used in VP.

Photoinduced radical polymerization

Photoinduced radical polymerization is one of the most used photochemical reactions and typically involves the photopolymerization of (meth)acrylates in the presence of a radical PI. This type of polymerization follows the conventional chain-growth mechanism, which consists of three different stages: initiation, propagation, and termination (**Figure 2.7**).

The initiation step is a two-step reaction. First, initiating reactive radicals (R*) are generated upon light-exposure due to the photolysis of the PI, either a NT1 (typically benzyl ketals, hydroxyalkyl ketones, acylphosphine oxides, acylgermanes and corresponding derivatives) or NT2 molecule (benzophenone, camphorquinone, thioxantone and derivatives mainly in the presence of amines as H-donors), according to the photochemical processes described in the previous subsection. The rate of generation of R* is a function of 1) light intensity, 2) PI concentration and 3) PI quantum yield. Remarkably, since the photogeneration of R* is slower than both the addition and termination stages, this step results the rate-determining one.

Then, these initiating radicals rapidly react with the unsaturated carbon-carbon (C=C) double bonds of the (meth)acrylate monomers/oligomers (M) to form a chain charrier (RM*). The reaction proceeds via the subsequent addition of unreacted monomer/oligomer chains to the growing macroradicals (propagation step).

Ideally, the polymerization could propagate until all the C=C double bonds of the monomers/oligomers have been consumed. However, due to their high reactivity, free radicals tend to rapidly interact to form inactive covalent bonds. In this context, termination mechanisms may occur mainly via bimolecular interaction of two chain ends following two different routes: recombination (coupling of two chain ends to generate a longer chain) or disproportionation (hydrogen abstraction from one chain end to give a new unsaturated group and two “dead” chains).[90,91]

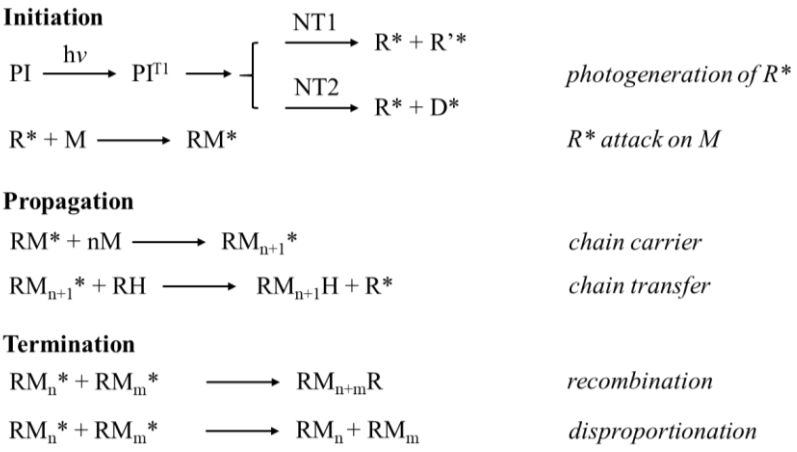

Figure 2.7. Schematic representation of the main stages of a photoinduced free radical polymerization: initiation via the photogeneration of radicals followed by radical attack on a monomer/oligomer unit; propagation of the chain carriers with eventual chain transfer reactions and termination via recombination or disproportionation of radicals/macroradicals.

Although acrylate-based systems are the most used in photopolymerization, they inherently entail some shortcomings, namely the short life of the propagating radicals, which results in an incomplete C=C conversion, the generation of shrinkage stress upon curing and mostly a strong oxygen inhibition. Indeed, oxygen inhibits radical polymerization by either quenching the excited triplet state of the PI or forming a peroxide reacting with a free radical of a chain carrier.[92]

However, not all the radical polymerizations proceed with a chain-growth mechanism. Indeed, thiol-ene click-reactions follow a step-growth process. The click-concept was introduced by Sharpless et al. referring to a small set of chemical reactions characterized by high yield, stereospecificity and most of all orthogonality.[93,94] In this sense, the radical-mediated coupling of thiols and reactive C=C double bonds (hence the name thiol-ene reaction) displays the typical features of click-chemistry,[95] namely 1) quantitative yields/conversions, 2) small quantities of catalyst required, 3) high rates, 4) spatiotemporal and orthogonal propagation and 5) regioselective products. As already mentioned, these reactions follow a radical step-growth or Michael-addition mechanism, which allows to avoid many of the typical issues related to the chain-growth photopolymerization. Indeed, thiol-ene systems exhibit reduced network relaxation or stress accumulation after crosslinking than the acrylate ones, mainly due to the delay of gelation towards higher conversions. Moreover they are insensitive to oxygen inhibition and still, more homogeneous networks are obtained upon irradiation.[4,5,96] These unique

features enabled the use of such type of reactions for a broad range of applications, from surface modifications,[97,98] to VP 3D-printing.[99]

The typical mechanism of a thiol-ene reaction is schematically illustrated in **Figure 2.8**. The light exposure of a thiol-containing molecule in the presence of a conventional radical PI leads to the generation of thiyl radicals by means of hydrogen abstraction from the thiol moieties. Then, these intermediate thiyl radicals may form thioether bonds with alkenes via the radical attack of C=C bonds. The resulting carbon-centered radicals may then react with a second thiol molecule by chain transfer, giving a thiol-ene addition product and generating simultaneously a new thiyl radical.[94] Broadly, the reaction rate is mainly affected by the electron density nearby the C=C double bond, that is it increases with increased electron density.[100]

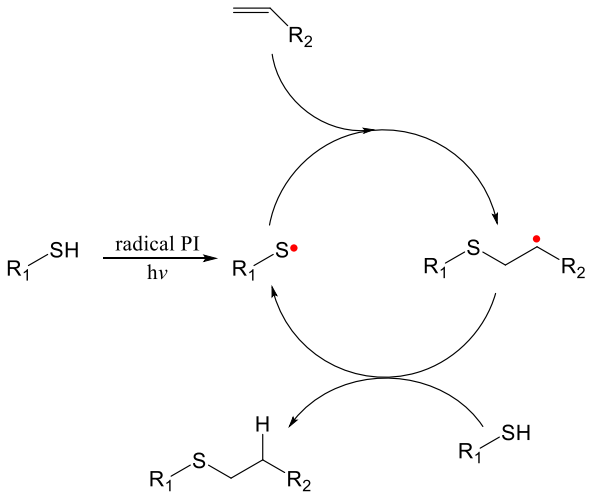

Figure 2.8. Schematic representation of a thiol-ene click reaction.

Photoinduced cationic polymerization

Cationic photopolymerization was developed in the 1970s mainly with the aim to solve some shortcomings of radical systems. One of the main advantages of cationic systems is the absence of oxygen inhibition, which eliminates the need for a protective atmosphere during photocuring.[4,5] Also, while in radical systems free radicals are short-lived and rapidly deactivate thus leading to low values of conversion, the longer life of the propagating cation center of cationic systems results in further monomer conversion. Moreover, the photopolymerization of cationic systems (mainly epoxides) leads to lower volumetric shrinkage and better

mechanical properties and thermal resistance than their corresponding radical system counterparts. Remarkably, cationic polymerization is non-terminating, which means it can proceed via a chain-growth mechanism for a considerable time after the light irradiation has been switched off. This feature, generally defined as ‘‘dark polymerization’’, clearly distinguished cationic from radical photopolymerization, which quickly ceases when the light source is removed.[79]

Cationic systems typically involve the use PAGs (see previous subsection) as PIs. Indeed, as previously mentioned, the photolysis of PAGs yields a mixture of cations, radical cations, and radical intermediates by means of bond-breaking reactions. The further reaction of such reactive intermediates with epoxides, cyclic ethers, lactones, and cyclic acetals or vinyl ethers and oxetane, leads to the formation of super acids $HMtX_n$ (see Figure 2.5),[79,81] which serve as the main initiators for the cationic polymerization.[101] Since Crivello described the use of those PAGs to activate the polymerization of nearly every known type of cationic monomers,[66,80] a variety of new onium salts have been developed, focusing in particular on the substitution of the diaryl iodonium group with alkyloxy moieties to reduce toxicity issues.[91]

2.3 Light in AM: vat polymerization

Based on the great advantage to transform liquid resins into crosslinked thermosets at high rates, with a spatiotemporal or even orthogonal control and nearly no release of volatile organic compounds, photopolymerization has been pushed to the forefront of AM processes.

The first reports of the fabrication of solid structures by selectively exposing photocurable polymers to light irradiation with movable masks, optical fibers, or laser beams date back to the early 1980s.[102] Not too long after, C. Hull coined the term stereolithography (SLA) as referred to the layer-by-layer lithographic fabrication of solid objects, and his patent dated 1986 laid the groundwork for the development and commercialization of SLA and SLA-derived VP techniques.[1]

The strategy behind these light-based AM technologies is the projection of light with a specific wavelength to trigger the solidification of a liquid resin placed in a vat via a photopolymerization reaction (hence the name vat polymerization, VP). The temporal control of the photochemical reaction allows to obtain complex 3D-structures via the sequential polymerization of 2D-slices with controlled thickness one on top of the other. The layer-by-layer fabrication is afforded by exploiting the motion of a movable building platform in the z-axis direction (**Figure 2.9**).[4,5,103–105]

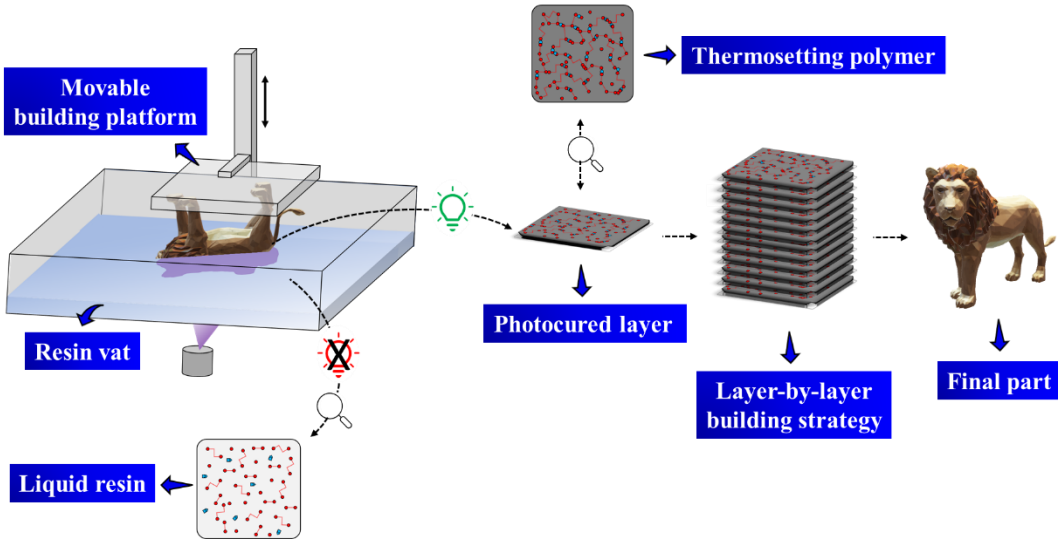

Figure 2.9. Setup of a generic VP printer and illustration of the layer-by-layer building process.

As VP proceeds in a layer-by-layer fashion, the "green", that is the photopolymerized part in progress, must be dimensionally and mechanically stable during the building process. This means the energy exposure must be sufficient to let the polymer to overcome its gel point and generate a stable thermoset. Indeed, once reached the gelation, the polymer forms an insoluble phase which is no more liquid-like and any further advancement of the reaction leads to the generation of an ever-more crosslinked thermoset. This is crucial because, beside requiring a sufficient mechanical stability, the photocured polymer must not solubilize while coming repetitively in contact with the liquid resin in the vat.

In this sense, the critical exposure (E_c) to induce gelation of photoresins (with no inorganic fillers) in VP processes can be defined as:

$$E_C = E_0 e^{\left(-\frac{C_d}{D_p}\right)} \qquad \text{Eq. 2.2}$$

where E_0, C_d are the energy dose at the surface and the curing depth, respectively, while D_p is the penetration depth defined as follows:

$$D_p = \frac{1}{2.3\varepsilon_{PI}[PI]} \qquad \text{Eq. 2.3}$$

This means that the light absorption depends only on the PI concentration [PI] and molar extinction coefficient (ε_{PI}) at the specific wavelength of the light source used in the process. However, the strength of the polymer at the gel point is

generally too low to reach the required stability during the building.[4] Therefore, to compensate, an excess of energy (E_x) is necessary:

$$E_X = E_C \left(\frac{D_p}{C_d}\right) \left[e^{\left(\frac{C_d}{D_p}-1\right)} - 1\right] \quad \text{Eq. 2.4}$$

Accordingly, E_x is directly proportional to E_c and inversely proportional to C_d, which means that the green strength can be improved either by increasing E_0 or by lowering D_p. It follows that the development of photocurable resins that required smaller energy doses to reach the gelation, allowed to speed up the manufacturing process.

Looking at the technological aspects, VP offers the opportunity to fabricate parts having complex geometry without the need of any complex machine configuration or supporting tools.[4,5,103–105] Moreover, higher level of accuracy and better surface finish can be achieved as compared to the other AM technologies (see Figure 1.7, subsection 1.2). Remarkably, the high versatility offered by photochemistry allows to tailor the properties of the printed objects (mechanical, chemical, optical or even functional) by simply tuning the composition of the photocurable resins.

2.3.1 VP technologies

Since the first SLA printers were commercialized in the U.S. in the late 1980s by Hull's 3D Systems and shortly after in Japan by CMET, many others VP apparatuses have been developed, mainly differing in terms of irradiation sources, building speed and maximum resolution achievable.[4,5,103–107] An overview of the main features of such VP technologies is given in the following subsections.

2.3.1.1 Stereolithography (SLA)

SLA works through in-plane raster scans of a laser beam across a resin vat to induce local curing. Generally, SLA printers have a top-down configuration, which means the laser beam is scanned from above the vat and, as soon as the photopolymerization of one layer is completed, the movable building platform descends a distance equal to the thickness of a layer and the cycle is repeated in an additive fashion (**Figure 2.10**). It follows that the curing time needed depends on the movement speed of the laser beam and on the extension of the area to be scanned and lightened. However, the most recent machines also display an inverted configuration (bottom-up), that is the irradiation from the bottom of the vat and the upward z-movement of the platform. This allows to reduce the consumption of the photoresin while limiting the oxygen inhibition. The slice information is given as a

set of spatial coordinates which define the tilt angle of a pair of galvano-mirrors that in turns focus the position of the laser beam along the xy plane.

The use of a focused laser as the photon source provides a high spatial resolution, which can be adjusted by simply varying the spot size of the beam. Indeed, high-quality parts with a resolution of 10 μm can be obtained. The vertical resolution depends on the curing depth, which can be adjusted either by adding dyes as light absorbers or regulating the exposure dose (intensity or time). Moreover, the sequential irradiation of each layer allows to selectively modify the energy dose controlling the intensity of the laser, thus enabling the processing of grayscale patterns. Shortcomings for SLA includes a narrow materials choice and relatively slow manufacturing speed (several mm/h) due to the point-wise exposure.[108] Recently micro-stereolithography (μSLA) and projection micro-stereolithography (PμSL) apparatuses have been introduced to increase both printer resolution (5 μm) and printing speed.[109]

Post-printing processes are typically performed on the printed parts, including the washing of exceeding resins with alcohol-based solutions and post-curing treatment to increase the conversion.

2.3.1.2 Digital light processing (DLP)

DLP has been developed to significantly reduce the printing times of SLA, while maintaining its high fabrication accuracy and resolution. Indeed, as opposed to the point-wise exposure of SLA, DLP works through the all-at-once illumination of each layer in the form of black and white patterns which are dynamically generated by a digital micromirror device (DMD). This allows a 2D-projection of light in the resin vat and hence a significant reduction of the building time (printing speed often reported in cm/h).

In a DLP system, the light source, which evolves over the years from conventional lamps to the more modern light emitting diodes (LED), illuminates the resin vat from below through a transparent window while the building platform is dipped into the photo-resin from above (bottom-up configuration, Figure 2.10b). This enables the consumption of low volumes of resins. Moreover, the layer being polymerized is less affected by oxygen inhibition since it is on the bottom of the vat and not in direct contact with air, as already discussed for the inverted configuration of SLA. The xy resolution depends on the number of pixels provided by the DMD and the optics used to project the patterns, but it typically ranges from 5 to 50 μm. Whereas, the vertical resolution depends on the light penetration depth and can be

adjusted by using additives or changing the exposure dose, as already reported for SLA.

Post-printing processes (washing, post-curing etc.) are typically performed on the printed parts, as already discussed for SLA.

2.3.1.3 Continuous liquid interface production (CLIP)

Pioneered in 2015 by DeSimone et al. as a variation of the traditional DLP machine, CLIP enables the continuous manufacturing of objects by going beyond the conventional layer-by-layer approach.[110,111] The key innovation was the introduction of an oxygen permeable window (typically made of fluoropolymers, such as Teflon AF 2400, due to the high O2 permeability, UV transparency and chemical inertness) at the bottom of the vat (Figure 2.10).[4,5] This allows to generate an oxygen-containing interfacial layer (generally 20−30 μm thick), which inhibits the photopolymerization at the surface of the vat (hence the name "dead zone" for that locally inhibited region) and avoids the need of sequentially recoating. Indeed, oxygen inhibit radical polymerizations by quenching the radicals chain carriers, as discussed in subsection 2.2. Therefore, a thin liquid layer remains uncured in the dead zone facilitating fast printing speeds (30 cm/h) and a continuous layerless fabrication. The resolution is reported to be below 100 μm.[110,111]

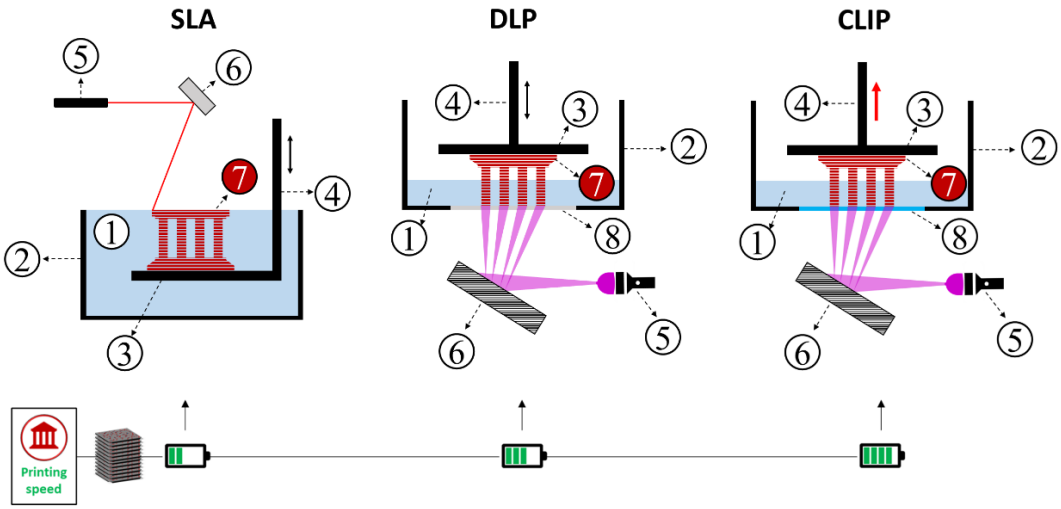

Figure 2.10. Graphical representation of SLA/DLP/CLIP VP techniques and relative printing speed. Main elements of the VP apparatuses: 1) liquid resin, 2) vat, 3) building platform, 4) movable elevator 5) light source (laser for SLA, led/projectors for DLP/CLIP); 6) galvano-mirrors for SLA and DMD for DLP/CLIP; 7) growing build; 8) transparent window for DLP and oxygen permeable window for CLIP.

2.3.1.4 Volumetric techniques: 2PP, CAL and xolography

Two-photon polymerization (2PP) is another type of VP technique but, similarly to CLIP, it does not follow the conventional layer-by-layer building approach since the laser can be moved in any direction within the resin by using either piezo-actuators or galvanoscanners. This makes 2PP a volumetric 3D-printing technology. Moreover, differently from SLA, a femtosecond near-infrared laser is used instead of a continuous beam to locally activate the polymerization via a simultaneous two-photon absorption (TPA).[112]

This photochemical process does not follow the conventional Jablonski diagram presented in subsection 2.1 (see Figure 2.1). Indeed, for a TPA to occur, a light source with high photon densities is needed to drive a transition via a very short-lived (fs) intermediate virtual state to the excited state (S_2) having energy roughly equals to twice that of the excitation wavelength (see new adapted diagram reported in **Figure 2.11a**). This means that the required energy transition to activate the photogeneration of radicals can be reached by 1) the simultaneous absorption of two photons, each one having half of the energy difference S_2-S_0 or 2) absorption of two photons having different energy, following a non-degenerate process.[113,114]

The TPA was already investigated in the 1960s, but it was just in the late 1980s that suitable femtosecond (fs) near-infrared lasers were developed (typically Ti:sapphire, emission wavelength near 790 nm, laser powers between 10 and 700 mW and pulse duration between 50 and 150 fs) to provide sufficient intensity to enable a TPA and the consequent exploration of 2PP.[4] Notably, since the photoresins are transparent in the near-infrared spectrum, the photopolymerization occurs just in the focal volume of the laser.[115,116]

The main advantages of this technique are: 1) nanoscale resolution (< 100 nm, the highest resolution among all the VP techniques), 2) mild processing conditions, 3) lack of oxygen inhibition and 4) lack of recoating steps (i.e. layerless manufacturing). However, 2PP inherently entails some drawbacks, namely low printing speeds, small overall dimensions (around 1 cm^3) and difficult handling of the printed parts (both in terms of removal from the apparatus and post-processing).

Another step-forward of volumetric manufacturing systems was the recent development of computer axial lithography (CAL) and xolography. CAL exploits computer tomography techniques to generate a hologram within the resin (Figure 2.11b). This is achieved by rotating the vat while multiple 2D-images are simultaneously projected to induce the curing of a volume of resin. It follows that

the main challenges of this technologies rely on the rotation speed of the vat and on the viscosity of the resin. The resolution of CAL has been reported as 300 µm, limited by energy dose fluctuations caused by light beams that pass through polymerized regions during the printing process. However, Loterie et al. recently proved the possibility of a higher-resolution (80 µm) volumetric production.[117]

Xolography though, exploits photo-switchable PIs to induce the photopolymerization of a volume of resin confined at the intersection of two light beams with different wavelength (Figure 2.11c). This technology, developed by Hecht et al., allows to reach values of resolution that are about ten times higher than CAL and a volumetric manufacturing speed four to five orders of magnitude higher than 2PP.[107]

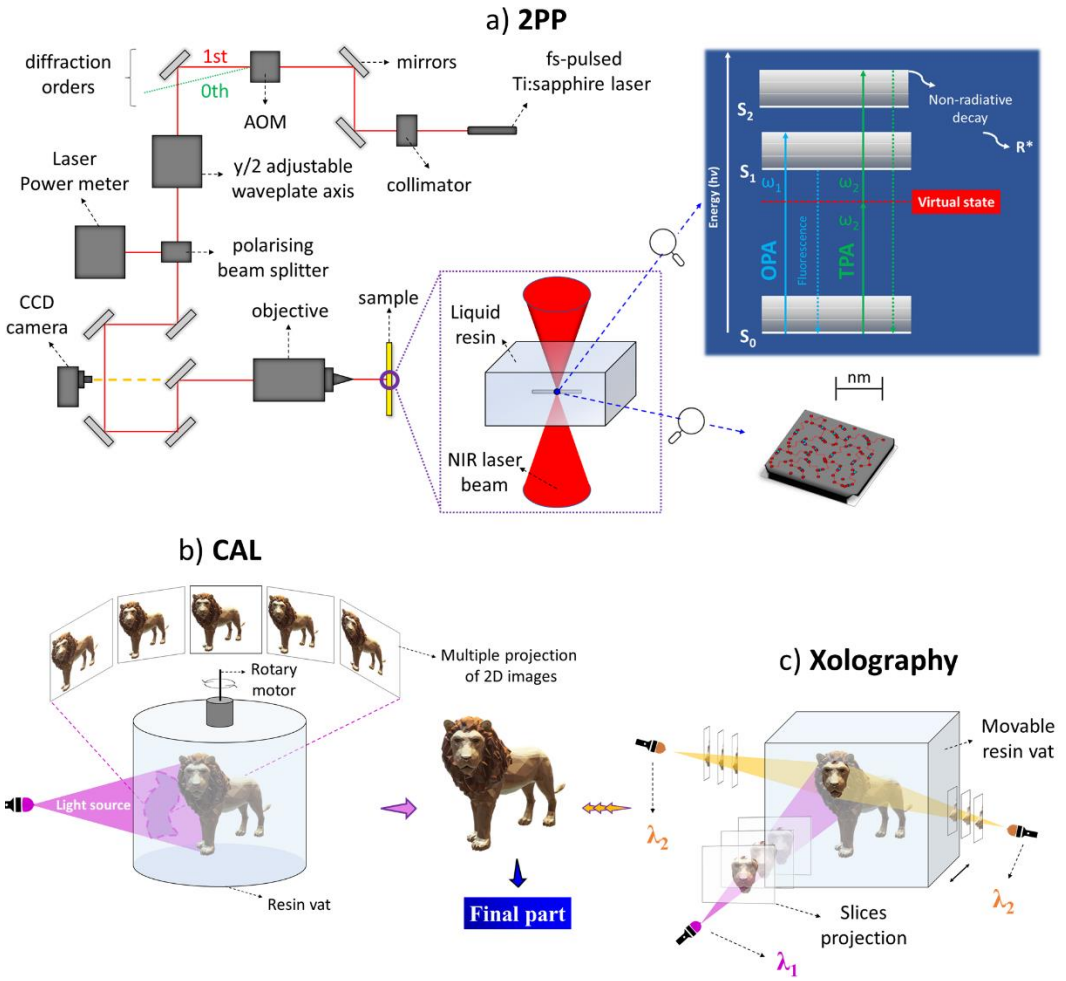

Figure 2.11. Schematic representation of the typical setup of a) 2PP; b) CAL and c) xolography.

2.3.2 Photoresins for VP

Photocurable formulations for VP processes mainly consist of three different ingredients: 1) reactive monomers/oligomers; 2) a suitable PI to activate the photopolymerization and 3) additives, such as radical inhibitors (to prevent premature gelation); dyes (to improve the final resolution of the printed parts without affecting the polymerization process); photosensitizers (to shift the absorption of the PI towards higher wavelengths) or fillers (to impart specific functional properties to the cured polymers).

The photochemical process behind photopolymerization have been already explored, as well as the different reaction mechanisms. Therefore, the following subsections are dedicated to give an overview of the ingredients of the photoresins typically used for VP, focusing on radical systems.

2.3.2.1 Photoinitiators

As previously discussed, depending on the type of the photopolymerizable monomers/oligomers being used, PIs can be either radical or cationic. As regards the former, even if the first reported photocurable system contained benzophenone as NT2 PI,[1] most of the commercially available radical PIs are NT1. Benzyl ketals are NT1 PIs typically used for SLA, since their low energy n → π* transitions (i.e. excitation around 350 nm) are compatible with the UV emission of the laser sources (He−Cd laser with wavelength of 325 nm or frequency tripled Nd:YAG sources emitting at 355 nm). Common benzyl ketals, such as 2-hydroxy-2-methyl-1-phenyl-propan-1-one (Darocure 1173), 2,2-dimethoxy-2-phenylacetophenone (DMPA; Irgacure 651), 1-hydroxycyclohexyl phenyl ketone (Irgacure 184) and 2-benzyl-2-(dimethylamino)-1-[4-(morpholinyl)phenyl]-1-butanone (Irgacure 369), have been used for several 3D-printing applications, including the fabrication of hybrid nanocomposites,[118] and biocompatible hydrogel scaffolds.[119]

Likewise, 2-hydroxy-4'-(2-hydroxyethoxy)-2-methylpropiophenone (Irgacure 2959), which displays even lower energy for the n → π* transitions (excitation around 275 nm) is typically used with SLA system for biomedical applications due to its biocompatibility and water solubility.[120,121] Also, 2,2'-azobis[2-methyl-n-(2-hydroxyethyl)propionamide] (VA-086) has been successfully exploited as efficient PI in biocompatible SLA-printable systems due to its low cytotoxicity.[122–124]

Acylphosphine oxides are another class of frequently used NT1 PIs, by virtue of their exceptional properties: i) photolysis yielding an acyl and a phopshinoyl

initiating radicals by homolytic α-cleavage of the phosphoryl-carbonyl bonds upon even low-intensity irradiation; ii) extended absorption in the UV-vis region; iii) long-wavelength photobleaching and iv) high thermal (>100°C) and storage stability.[70,87,125,126] Although these PIs were initially intended to be used with UV irradiation, their blue-shifted n → π* transitions (λ = 360 - 420 nm) is particularly appealing for DLP processes, whose light sources have typically longer wavelength emission than SLA (e.g. LEDs with wavelengths of 365, 385, and 405 nm).[5] Moreover, their excellent photobleaching prevents yellowing and makes it possible for incident light to penetrate deeper because of a decreasing optical density. This enables the DLP-printing of highly filled photoresins.

The most widely used acylphosphane oxides for DLP-printing are phenylbis(2,4,6-trimethylbenzoyl)phosphine oxide (Omnirad 819 or Irgacure 819),[127–134] diphenyl(2,4,6-trimethylbenzoyl)phosphine oxide (Darocure TPO; Lucirin TPO),[135,136] ethyl(2,4,6-trimethylbenzoyl)phenylphosphinate (Lucirin TPO-L) and lithium phenyl(2,4,6-trimethylbenzoyl)phenylphosphinate (LAP).[137,138]

Remarkably, the synthesis of functionalized bis(acyl)phosphane oxides (BAPOs) via the variation of the substituent on the phosphorus atom enabled the use of these PIs in an increasing number of applications. In this context, the Grützmacher group of ETH Zürich has recently developed a simple procedure to convert elemental phosphorus into sodium bis(mesitoyl)phosphide $NaP(COMes)_2$, which can be used as platform for the synthesis of a wide range of P-functionalized BAPOs.[139–141] Indeed, carbon-substituted BAPOs can be prepared via the nucleophilic substitution of $NaP(COMes)_2$ with alkyl halides FG-(CH_2)n-X followed by oxidation with hydrogen peroxide. Alternatively, $NaP(COMes)_2$ can be protonated with acetic acid to give bis(mesitoyl)hydrogen phosphane $HP(COMes)_2$, which in turn can be used as building block for the synthesis of substituted BAPOs following the path of a phospha-Michael addition onto activated olefins. Further, the oxidation of $HP(COMes)_2$ gives bis(mesitoyl)phosphinic acid (BAPO-OH),[142] which can also serve as starting materials for other functionalized BAPOs. Among all the derivatives being recently prepared by following one of the abovementioned synthetic strategies, water-soluble BAPO salts, as well as a poly(ethylene glycol)substituted BAPO and BAPOs grafted on cellulose nanocrystals were synthetized and used for the DLP-printing of hydrogels.[143,144]

Based on the previous considerations on the better suitability of acylphosphine oxides than benzyl ketals with higher wavelengths irradiations due to their blue-

shifted n → π* transitions, it follows that the performance of the PI is strictly dependent on the light source. In this context, the photopolymerization under visible-light irradiation has attracted a growing interest in the past few years for many different reasons, namely 1) lower risk of exposure, 2) no release of ozone, 4) low thermal effect and 5) higher compatibility with living cells. But, the use visible-light sources requires blue-shifted PIs.[5]

Among these PIs, CQ is used due to its long-wavelength absorption (468 nm). Being a NT2 PI, it is typically coupled with tertiary amines such as ethyl 4-dimethylaminobenzoate (DMAB) to initiate the photopolymerization.[145] However, such a photoinitiating system has some limitations, due to toxic side effects and discoloration properties of the amines, and a low reactivity.

The new generation of germanium based NT1 PIs, among which bis(4-methoxybenzoyl)diethylgermanium (Ivocerin), stand out as promising alternatives to CQ for DLP-processes, given their long wavelength absorption (> 400 nm) and excellent photobleaching properties (similar to acylphosphine oxides).[71] Recently, also naphthalimide derivatives, such as (5-amino-2-benzyl-1-benzo[de]isoquinoline-1,3(2H)-dione (NDP2), were successfully used as visible-light PIs using a DLP-printer with a LED projector emitting at 405 nm.[146] Moreover, organometallic compounds typically employed as photoredox catalyst, such as tris(2,2-bipyridyl) dichlororuthenium(II) hexahydrate (Ru), have been successfully used as blue-shifted PIs for 3D-printing.[147,148] Furthermore, dimethyl-10-ribitylisoalloxazine (Riboflavin),[149] 3-hydroxyflavone (3HF),[150] Eosin Y[151] and Rose Bengal[152] have also been used for visible-light 3D-printing due to their strong visible light absorption. The chemical structures of the abovementioned PIs are given in **Figure 2.12**.

Turning now to cationic systems, the first PIs were aryl iodonium salts with non-nucleophilic counterions (BF_4^-, PF_6^-, AsF_6^- and SbF_6^-), as previously discussed. Not long after the discovery of those PAGs by Crivello,[66] several derivatives were developed by substituting the diaryl iodonium group with alkyloxy moieties. Among them sulfonium and iodonium salts like diphenyl(4-methoxyphenyl) sulfonium and bis(4-tert-butylphenyl)-iodonium hexafluorophosphate (Iod) are used for 3D-printing applications.[4] Also, azahelicenes (AZs)[153] and metallocene compounds such as Irgacure 261[154] can be employed as cationic PIs for 3D-printing. Moreover, NT1 radical PIs can also be used with iodonium or sulfonium salts to generate cationic initiating systems, since the radical intermediates from the former can react with those of PAGs to give active radical

cations (e.g. naphthalimide derivatives or zinctetraphenylporphyrin (ZnTPP) in combination with Iod).[146,153]

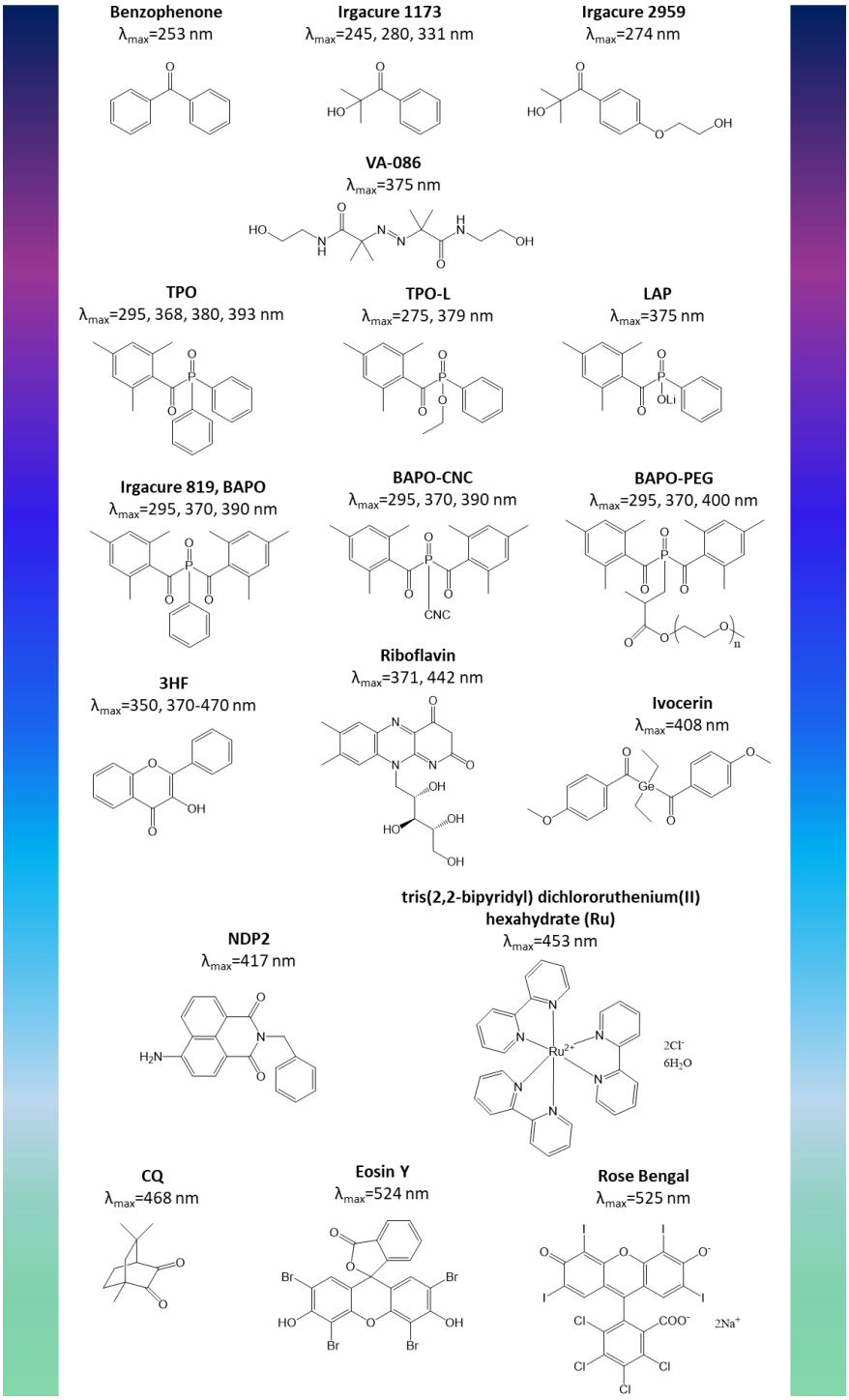

Figure 2.12. Examples of radical PIs used for DLP/SLA 3D-printing.

2.3.2.2 Monomers/oligomers

We have come a long way from the first SLA-printable materials used by Hull, which consisted of a resin originally intended for the preparation of adhesives.[1] Over the years, the research focused on the development of photopolymerizable resins aiming to increase the penetration depth, fasten the curing rate and tailor the properties of the printed parts for specific applications, trying to extend the concept of a "design for manufacturing" also to the materials choice.

To date, (meth)acrylates are the most frequently used monomers for VP due to both their high reactivity and their compatibility with many different 3D-printers. The selection of the acrylate-based system depends on many factors, including photopolymerization kinetic, viscosity, mechanical properties to impart to the printed object, but also volatility, toxicity, shelf life, odor and costs.[155] Broadly, a mixture of both acrylate and methacrylate monomers/oligomers is typically required, being the curing kinetic of the latter too slow when used on their own while pure acrylate system brings to dimensional distortions and stress developments in the printed parts.[4]

Multiunsaturated oligomers/monomers are typically used to form the backbone of the polymer network and to enable fast reaction rates, due to an autoacceleration phenomenon occurring in the early stages of the chain growth. However, this can lead to early gelation and/or vitrification, which in turn hinders a complete double bond conversion and brings to the formation of heterogeneous and brittle networks.[156–159] On the contrary, monounsaturated specie serves as reactive diluent to adjust the viscosity of the system and to modulate the effect of the multifunctional specie.

The most used (meth)acrylate monomers/oligomers for VP are polyethyleneglycol diacrylate (PEGDA), triethyleneglycol dimethacrylate (TEGDMA), urethane dimethacrylate (UDMA), bisphenol A-glycidyl methacrylate (Bis-GMA), trimethylolpropane triacrylate (TTA) or pentaerythritol tetraacrylate (PETA), bisphenol A ethoxylate diacrylate (BEDA), bisphenol A ethoxylate dimethacrylate (BEMA), hexandyol diacrylate (HDDA), butyl acrylate (BA) and others (**Figure 2.13**).[4,5,155,160]

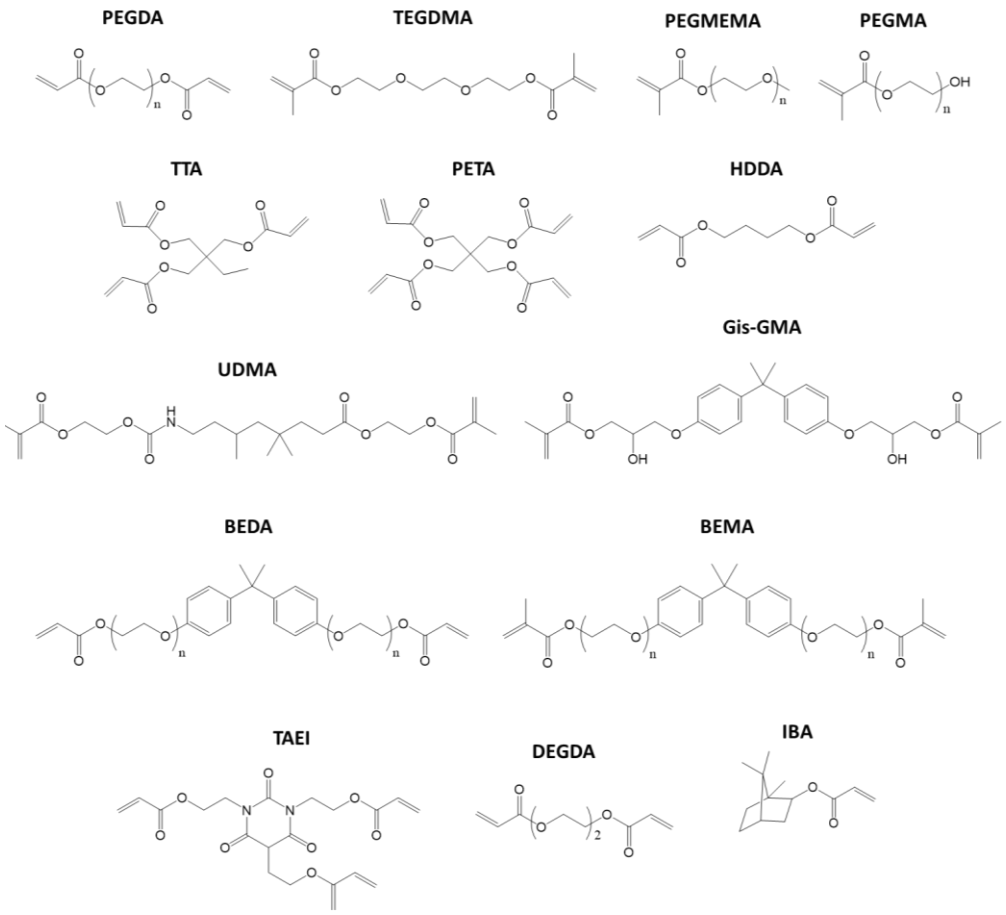

Figure 2.13. Common (meth)acrylate monomers/oligomers used for VP.

However, as already mentioned in subsection 2.2, acrylate systems have some limitations, i.e. oxygen inhibition, shrinkage, stress development and low conversion. As far as oxygen is concerned, the partial inhibition is not such a significant issue in VP, since the amount molecular oxygen dissolved in the resin is low, especially in DLP-systems where the on-curing surface is not in constant contact with air.[4,5] Therefore, the propagation of carbon radicals results less inhibited. Remarkably, the oxygen inhibition is taken into advantage in two different ways: 1) the unreacted double bonds at the interface (i.e. on the cured layer) can react during the light-irradiation of the subsequent layer leading to a stronger interface adhesion,[161] and 2) the local inhibition allows to avoid the attachment of the polymerized part to the bottom of the vat during the printing process. The latest DLP-printers (CDLP/CLIP) are even based on the generation of

a thin oxygen layer (dead-zone) to guarantee a continuous manufacturing process, as already discussed (see subsection 2.3.1.3).

Whereas the development of shrinkage-stress during the polymerization mainly depends on the type of monomer being used. Indeed, the photopolymerization of monomers having a high number of reactive functionalities leads to the occurrence of gelation at low double bond conversions.[162,163] This in turns brings to a limited flow of the remaining uncured resin and any further polymerization implies higher shrinkage-stress during the layer-by-layer fabrication. However, this phenomenon depends also on the composition of the curable system. Indeed, the use of either aromatic, high molecular weight or monofunctional methacrylates results in a shrinkage reduction.[164]

Other approaches to modulate the molecular architecture of the cured polymer and lower the amount of shrinkage could be the use of chain transfer agents or to change the polymerization mechanism from a chain-growth to a step-growth by exploiting thiol-ene click chemistry. Indeed, as already introduced in subsection 2.2, thiol-ene systems show much lower shrinkage and stress development than the acrylate-based counterparts, mainly due to the delay of gelation towards higher conversions.[165] Therefore, thiols such as trimethylolpropane tris (3-mercaptopropionate) (TMPMP), pentaerythritol tetra(3-mercaptopropionate) (PETMP), tris[2-(3-mercaptopropionyloxy) ethyl] isocyanurate (TMI), and pentaerythritol tetrakis (3-mercaptopropionate) (PE-1) can be added to acrylate formulations as effective tools to modulate the final properties of the cured resin (**Figure 2.14**).[5,99,160,166,167]

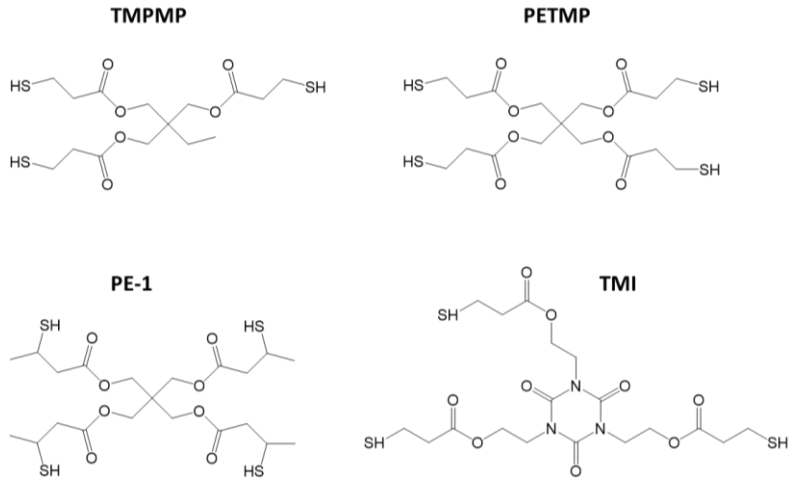

Figure 2.14. Examples of thiols typically used for the preparation of thiol-ene systems for VP.

However, also thiol-ene systems entail some issues that limit their further development for 3D-printing applications, namely the poor shelf life of thiols because of oxidative disulfide bond (S-S) formation; bad odor and too flexible thiol-bridges which significantly soften the polymer network and reduce the useful temperature range of the cured material. Nevertheless, the softening can be reduced by using norbornene end-capped oligourethanes in combination with TMPMP.[168]

Furthermore, cationic systems (mainly epoxides) are also commonly used for VP. Epoxides typically used for 3D-applications are 3,4-epoxycyclohexylmethyl 3',4'-epoxycyclohexanecarboxylate (ECC or EPOX) and bisphenol A diglycidyl ether (DGEBA).[150,153] Notably, epoxides undergo less shrinkage but show slower curing rates than acrylates. For this reason, rather than being used on their own, they are commonly combined with the more reactive vinyl ethers and/or oxetanes monomers which allow to fasten the polymerization and further minimize the shrinkage during post-curing.[4] Vinyl ether and oxetane monomers commonly used for VP are 1,4-cyclohexanedimethanol divinyl ether (CDVE) and disubstituted oxetane (DSO). The chemical structures of the abovementioned cationic monomers are shown in **Figure 2.15**.

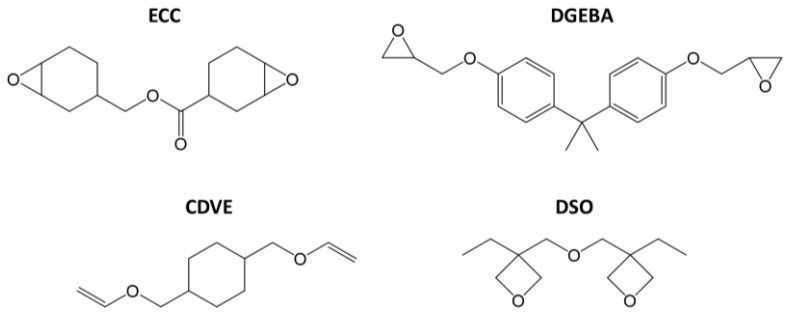

Figure 2.15. Examples of epoxide, vinyl ether and oxetane monomers typically used for the preparation of cationic or dual-cure formulations for VP processes.

Moreover, dual-cure formulations (i.e. the combination of a cationic and a radical monomer) can be used to tailor both the photopolymerization rate and the mechanical properties of the final 3D-printed parts. Indeed, in such a type of hybrid system, acrylates and epoxides undergo different polymerization mechanisms and essentially do not react with each other, resulting in the generation of an interpenetrating network.[169]

2.3.2.3 Additives

Photocurable formulations for VP may also contain additives other than monomers/oligomers and PIs.

Radical inhibitors such as butylated hydroxy toluene (BHT) and monomethyl ether hydroquinone (MEHQ) are normally used at low concentration (50-200 ppm) to extend the shelf life of the monomers/oligomers by preventing premature polymerization. However, due to their aerobic character, they require a minimum concentration of oxygen dissolved in the resin to serve effectively as inhibitors.[170]

Light adsorber, generally referred to as dyes, are typically used in VP to reduce the penetration depth of light across the photocurable resin and hence to enhance the resolution of the printed structures avoiding light diffusion in the vat during the building stage.[171] The influence of the use of dyes on D_p can be explained by slightly modifying the previous Eq. 2.3 with the following expression (Eq. 2.5)[4]:

$$D_p = \frac{1}{2.3(\varepsilon_{PI}[PI]+\varepsilon_A[A])} \qquad \text{Eq. 2.5}$$

Accordingly, D_p depends on the extinction coefficient (ε) and concentration of both the PI and the light absorber. It follows that the lower the D_p the better the z-resolution. Moreover, dyes are also able to confine the irradiation in width, while avoiding overcuring phenomena.[171]

The selection of the dye mainly depends on the light source of the VP printer, while its concentration in the formulation should be balanced with the one of the PI. Indeed, high concentrations may negatively affect the efficiency of the PI due to competitive photon absorption processes, while too low concentrations may lead to a poor printing resolution. Sudan I,[172,173] Reactive Orange 16 (RO 16),[133] Methyl Red (MR)[127,128] has been widely used to limit D_p and increase the z-resolution while printing (meth)acrylates-based resins. Anthracenes and stilbene derivatives, such as 2-ethyl-9,10-dimethoxy anthracene (EDMA) and 1,4-bis(2-dimethylstyryl)benzene (BMSB), respectively, have been reported as effective light adsorbers for epoxy/vinyl ether-based resins.[4] The chemical structures of the abovementioned dyes are illustrated in **Figure 2.16**.

Remarkably, in the last years the synthesis of organic or organometallic molecule with specific functional groups has widened the use of dyes to implement functional properties to the polymeric material, allowing to obtain light-emitting devices, electroluminescent and mechano-chromic materials, smart temperature sensors and liquid crystals dispersed in polymers.[128,171,174–176]

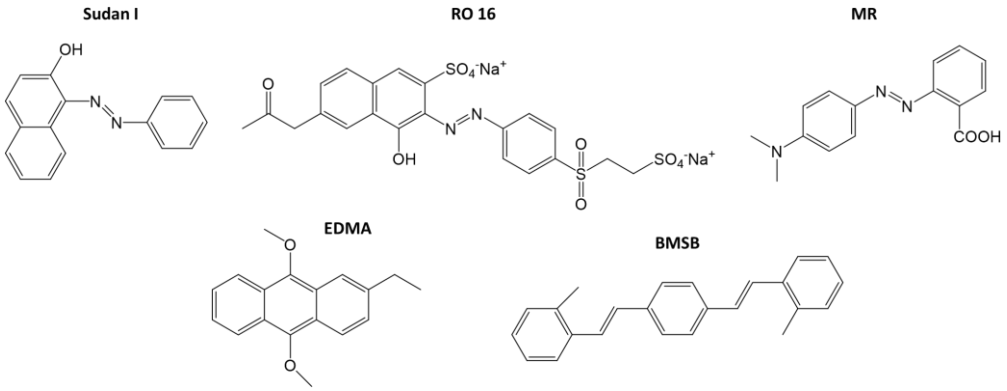

Figure 2.16. Light absorbers (dyes) commonly used for VP.

Furthermore, photosensitizers can be added to the photocurable formulations to extend the absorption of the PI (enabling the use of long-wavelength light source) or to lower the E_c needed to induce the gelation at a specific wavelength. As a way of examples, dyes such as anthracene, coumarins and thioxantones can extend the use of cationic PIs up to 400 nm.[4]

Finally, different types of nanofillers can be added to enable the fabrication of polymeric nanocomposites having specific thermomechanical, electrical, or even functional properties. Typical examples of nanofiller employed for 3D-printing applications are carbon nanotubes, graphene, silver salts, magnetic nanoparticles and tetraethyl orthosilicate.[118,129–134,177–179]

2.3.3 Recent advances and future directions of VP

As deeply explored in this chapter, VP has attracted a growing interest in the scientific community due to the versatility given by photochemistry. Indeed, VP enables the fabrication of complex multifunctional objects having controllable properties and high resolution with extremely low feature sizes. This opened new perspective in many fields, such as soft-robotics, microfluidics, tissue engineering, dentistry and others.[4,5]

However, even though the use of VP is rapidly growing in both academic and industrial environments, lots of challenges remain to be addressed to further expand its scope and unlock its full potential. In this context, challenging research areas could be 1) the design of novel 3D-printable systems to both widen the current set of photocurable materials and tune the thermomechanical, functional, or even

physiochemical properties of the printed parts and 2) the 4D-printing of smart materials for the development of functional devices.

2.3.3.1 "Print it greener": bio-derived monomers

The development of new and environmentally friendly photopolymers is one of the major challenges to unlock the widespread adoption of VP. So far, as deeply explored in the previous subsection, the materials choice is limited to the commercially available acrylates or epoxides derived from petroleum-based resources that have a significantly high carbon footprint. However, the development of more sustainable and bio-based photoresins is gaining a growing interest.[180–182]

Over the last few years, several natural products have been suitably modified to become printable by means of VP processes. The typical strategies used to impart photocurable functionality to natural molecules include 1) the conversion of hydroxyl-, acid- and epoxy groups into methacrylate or acrylate functions and 2) the epoxidation of unsaturated moieties.[182]

Vegetable oils are amongst the most used natural resources to prepare bio-based photocurable resins. Epoxidized soybean oil acrylate (ESOA) and methacrylate (ESOMA, **Figure 2.17a**) with different numbers of functionalities were synthetized by Guit et al. via a "green" and solvent-free route and then used to prepare DLP-printable inks with a bio-based content of 74-83%.[183] Also epoxidized soyate oil was methacrylated and combined with commercial monomers (biobased content of 42%) to develop new resins for VP.[184] Likewise, Branciforti et al. reports the use of epoxidized linseed oil for SLA.[185]

Lignin (Figure 2.17b),[186] vanillin,[187] and eugenol[188] methacrylate derivatives have also been reported as interesting bio-sources for SLA-inks with a biobased content ranging between 15 and 35%. Besides, even carboxylic acids have been used to prepare bio-based photocurable inks. Miao et al. reported the methacrylation of both succinic and itaconic acid and the successful DLP-printing of well-defined structure with interesting mechanical properties and good layer adhesion.[189] Unsaturated polyesters, obtained by reacting bioacids with glycols, were also used for SLA applications.

Also, gelatin,[190], starch,[138] cellulose (Figure 2.17c),[191] and chitosan (Figure 2.17d),[192] were suitably methacrylated and successfully used for the DLP-printing of hydrogels. Kim et al. used silk fibroin functionalized with methacrylate functions for the DLP-printing of biocompatible scaffolds which

mimick organ shapes.[193] Also terpenes photocurable derivatives were used to print porous structures by DLP/SLA, exploiting thiol-ene chemistry.[194]

As becomes evident, the ever-growing interest for bio-based systems has opened a new research field which could be further explored in the future.

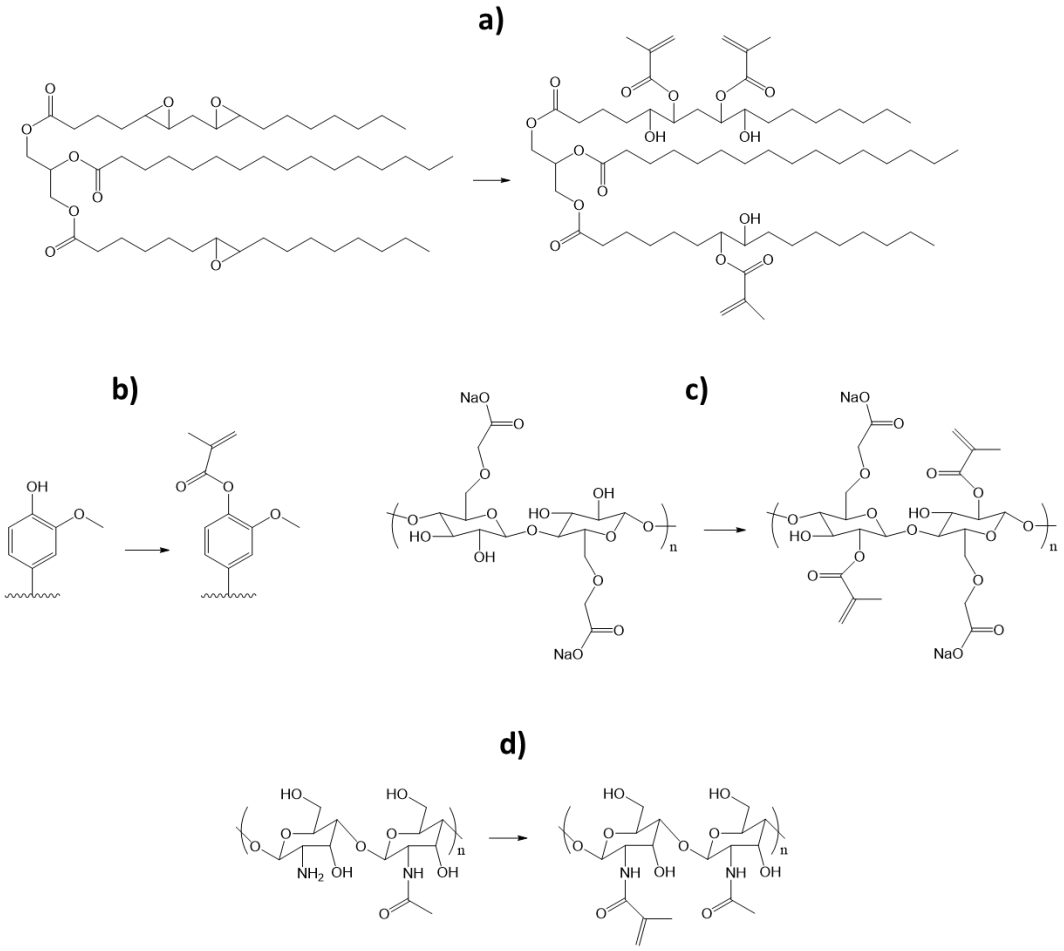

Figure 2.17. Methacrylation of a) epoxidized soybean oil, b) lignin, c) cellulose and d) chitosan by means of epoxy/hydroxyl/amine groups substitution, respectively.

2.3.3.2 4D-printing

As briefly introduced in subsection 1.1, the possibility to fabricate customized parts whose shape or properties can evolve over time in response to an external trigger has turned 4D-printing a hot topic of advanced manufacturing. However, AM

technologies for 4D applications mainly involve polyjet or extrusion printing, even if both entail some limitations, such as high equipment cost, stringent resin property requirement, slow printing speed and relatively low resolution. Instead, the use of VP is still in its infancy, mainly due to the scarcity of suitable photoresins. Nevertheless, in the last years some interesting works have been reported on the use of DLP and SLA for 4D-applications.

Zhao et al. develop hydrophilic/hydrophobic composite 3D-structures which are patterned using DLP and display a solvent-responsive behavior. More specifically, they photopolymerized a layered hydrophilic/hydrophobic composite alternating PEGDA and poly(propylene glycol) dimethacrylate, which has a controlled shape shifting during swelling.[195] Zarek et al. printed shape memory parts made of a thermoresponsive methacrylated polycaprolactone using a customized DLP-printer.[196,197] Dutta et al. fabricated with SLA macroscopic valves which can respond both to temperature fluctuations and to pH-variations. This was achieved by copolymerizing the thermoresponsive poly(ethylene oxide)-poly(propylene oxide)-poly(ethylene oxide) with the pH-sensitive acrylic acid.[198] Ge et al. fabricated with SLA thermoresponsive structures combining benzyl methacrylate with difunctional acrylate oligomers, envisaging their potential use for biomedical applications.[199] Liu et al. prepared reversible origami structures exploiting grayscale patterns with a DLP-printer.[200] Likewise, Wu et al. have taken advantage of grayscale patterns to prepare via DLP-printing smart flowers that can change their shape upon swelling in acetone due to a mismatch in the crosslinking density of the layers.[201] Invernizzi et al. fabricated with a DLP-printer thermoresponsive actuators combining methacrylated polycaprolactone with ureido-pyrimidone units,[202] while Li et al. developed polyimides-based system to prepare thermoresponsive grippers.[203]

More recently, DLP has been explored for the fabrication of electroactive smart nanocomposites. Cortés et al. reported the DLP-printing of carbon nanotubes doped polymers whose shape memory properties can be triggered either electrically by joule's heating or by infrared irradiation.[131,179] Whereas Lantean et al. developed magnetoresponsive smart structures by embedding Fe_3O_4 nanoparticles in a soft polymeric matrix.[129,130]

However, there is still a long way to go to further develop VP 4D-printing. Interdisciplinary research and technological advances will surely allow to develop novel photocurable materials in view of the fabrication of smart devices.

3. Photopolymerizable cyclodextrins for DLP-printing

3.1 Motivation and outline

As introduced in subsection 2.3.3.1, even if the global market of 3D-printing is continuously growing and half of it is mainly claimed by the sale of photopolymers, one of the main limitations to a widespread use of VP processes is the enlargement of the printable materials palette towards greener alternatives. Indeed, many different photocurable formulations have been proposed for a wide range of applications,[5] but the availability of environmentally-friendly photopolymers is still limited. In this sense, the growing interest for a more sustainable engineering may have a crucial role in the attempt to reduce the environmental impact of VP. As evidence of this, the synthesis and application of 3D-printable monomers derived from natural products has become an ever-more stringent request, especially in the last few years which have seen a significant rise in the number of scientific publications on the topic.[182]

Within this framework, cyclodextrins (CyDs) are proposed in this chapter as building blocks to prepare a novel DLP-printable multifunctional macromer. Indeed CyDs, which are starch-derived toroidal-shaped macrocyclic oligosaccharides consisting of glucopyranose subunits (**Figure 3.1**),[204–207] are very versatile molecules since they display several hydroxyl sites (-OH) which can be rather easily chemically modified.[208] Hence, they are particularly appealing to prepare photocurable bio-based alternatives since, as already reported, one of the typical strategies used to impart photopolymerizable functionality into natural molecules is the conversion of -OH groups into methacrylate or acrylate functions.[182]

In particular, γ-CyDs were chosen as the building block for the synthesis of the multifunctional macromer amongst all the natural CyDs commercially available, given their higher number of functionalizable -OH sites (i.e. 24 for γ-CyD, 21 for β-CyD and 18 for α-CyD). Accordingly, a multi-acrylated γ-CyD derivative was

synthetized by means of -OH groups substitution and used to prepare novel bio-based formulations for DLP-printing. The reactivity of the novel photocurable systems upon UV-light irradiation was investigated by means of real-time photoreology and the printability was assessed. Then, the properties of the cured thermosets were studied, focusing on the influence of the novel macromer on their thermo-mechanical behavior.

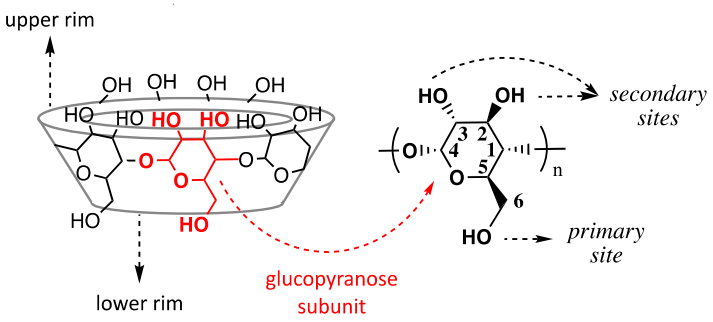

Figure 3.1. Schematic representation of the toroidal structure of natural cyclodextrins and detailed view of the glucopyranose subunits (n correspond to six, seven, or eight subunits depending on the CyD molecule, namely α-CyD, β-CyD, and γ-CyD) and hydroxyl groups located at primary and secondary sites.

Part of the work reported in this chapter has been already published and it is available at the reference[209]:

Cosola, A.; Conti, R.; Grützmacher, H.; Sangermano, M.; Roppolo, I.; Pirri, C. F.; Chiappone, A. Multiacrylated Cyclodextrin: A Bio-Derived Photocurable Macromer for VAT 3D printing. *Macromol. Mater. Eng.* **2020**, 305, 2000350, doi: 10.1002/mame.202000350.

3.2 Experimental

3.2.1 Materials and chemicals

γ-Cyclodextrin (γ-CyD) was purchased from ABCR. Acryloyl chloride, anhydrous n-methyl pyrrolidone (NMP), poly(ethylene glycol) methyl ether methacrylate (PEGMEMA, M_n = 500 g/mol), propylene carbonate (> 99%), phenylbis(2,4,6-trimethylbenzoyl)phosphine oxide (Omnirad 819), methyl red (MR), deuterated dimethyl sufoxide (DMSO-d6, 99%) and ethanol (EtOH) were obtained from Sigma Aldrich and used as received.

3.2.2 Procedures

Synthesis of the multi-acrylated γ-cyclodextrin derivative (Ac-γ-CyD)

The multi-acrylated γ-cyclodextrin derivative was prepared following a synthetic route already reported by Gil et al.[210] Once being dried at 90 °C under vacuum for 24 h, γ-CyD (20 g, 15.42 mmol) was charged in a 500 mL Schlenk flask containing 160 mL of anhydrous NMP and the reaction mixture was left to stir under Argon atmosphere until the solution became homogeneous. Then, acryloyl chloride (36.07 mL, 0.44 mol) was added dropwise at 0 °C and the reaction mixture was stirred at room temperature (RT, 25 °C) for 72 h. Dropping slowly the mixture into 2 L of deionized water (DI-H_2O) gives Ac-γ-CyD as a white precipitate. After decanting the mixture for 30 min at RT, the product was filtered, washed four times using DI-H_2O and finally dried for two days under high vacuum.

Preparation of the photocurable formulations

The multi-acrylated macromer Ac-γ-CyD was used to prepare two sets of photocurable formulations. Different amounts of Ac-γ-CyD, i.e. 5, 10, 20 and 30 wt%, were dissolved either in propylene carbonate (strategy 1) or in PEGMEMA, a monofunctional methacrylate oligomer used as reactive diluent (strategy 2). Then 0.5 phr (per hundred resin) of Omnirad 819 as photoinitiator and 0.05 phr of MR as dye were added in each formulation and the mixtures were stirred until becoming homogeneous. The two sets of formulations were named Ac-γ-CD-X and PEG-AcγCD-X, respectively, where X corresponds to the wt% of Ac-γ-CyD being used.

DLP-printing

Different formulations (both Ac-γ-CD-X and PEG-AcγCD-X) were 3D-printed using an ASIGA MAX X27 DLP printer (building volume of 119 mm x 67 mm x 75 mm, nominal XY pixel resolution of 27 μm, and a light-emitting diode source, 385 nm, 32 mW/cm^2). The printed objects were washed in EtOH to remove the excess of resin and finally post-cured under UV-light (4 min, 12 mW/cm^2) using a medium-pressure mercury lamp provided by Robot Factory.

3.2.3 Characterization methods

Solution nuclear magnetic resonance (NMR) spectroscopy

NMR spectroscopy was used to confirm the successful functionalization of γ-CyD with photopolymerizable acrylate functions. DMSO-d6 was used as solvent to prepare the samples for the analyses. ^{1}H- and ^{13}C-NMR spectra were recorded at RT on a Bruker 300 spectrometer. The chemical shifts (δ) were measured according

to IUPAC and are given in parts per million (ppm) relative to the standard tetramethylsilane (TMS) for ^{1}H and ^{13}C. The recorded spectra were evaluated using MestReNova software.

Infrared (IR) spectroscopy

IR spectroscopy was used to further confirm the successful acrylation of the γ-CyD. The spectra were recorded by using a Perkin Elmer Spectrum 2000 FTIR spectrometer (Perkin Elmer, Norwalk, CT, USA) equipped with a single reflection attenuated total reflectance (ATR) accessory. 32 scans were recorded for each sample from 4000 to 500 cm^{-1} with a resolution of 4 cm^{-1}. The recorded spectra were evaluated using Omnic software.

Mass spectrometry (MS)

Maldi MS was used to estimate the degree of functionalization of Ac-γ-CyD. The measurements were carried out by the MS Service of the Laboratory of Organic Chemistry at ETH Zürich.

Real time photorheology

The reactivity of the photocurable formulations was investigated by means of photorheology using an Anton PAAR Modular Compact Rheometer (Physica MCR 302, Graz, Austria) in parallel-plate mode (25 mm diameter). The photocuring kinetics of the formulations was evaluated via real-time measurements carried out at RT, using a UV-curing set-up inclusive of a quartz bottom plate and a UV-light source (Hamamatsu LC8 lamp equipped with an 8 mm light guide, 30 mW/cm^2) positioned underneath. During the measurements, the gap between the two plates was set to 0.2 mm and the sample was kept under a constant shear frequency (62 rad/s). The light was switched on after 60 s to assure the stability of the system before the onset of photopolymerization. According to preliminary amplitude sweep measurements, all the tests were carried out in the linear viscoelastic region setting a strain amplitude of 0.8 %. The onset of photopolymerization (i.e. the delay time required to induce crosslinking) and the curing rate were also investigated.

Gel content (GC) measurements

Gel content (GC) measurements were performed to evaluate the insoluble fraction (covalently crosslinked polymer) of the photocured PEG-AcγCD-X thermosets. Flat samples (20 mm x 10 mm x 0.5 mm) were prepared by casting into silicon molds the photocurable formulations and irradiating for 1 min under nitrogen atmosphere, using a Dymax ECE 5000-UV lamp (320-390 nm). Then, the samples were held in an ultra-fine metal net, weighed, and immersed in chloroform to

remove the soluble fraction (un-crosslinked polymer). After 24 h, the samples were removed from the chloroform bath and dried in a vacuum furnace (500 mbar, 80 °C, 6 h). The gel content (GC) was measured gravimetrically using the following equation:

$$\mathrm{GC}\ (\%) = \frac{W_d}{W_0} \times 100 \qquad \text{Eq. 3.1}$$

where W_d is the weight of the dried sample after solvent extraction and W_0 is the initial weight of the sample.[143]

Dynamic mechanical thermal analyses (DMTA)

DMTA were carried out to evaluate the thermomechanical properties of the PEG-AcγCD-X thermosets. The measurements were performed with a Tritec 2000 DMA (Triton 6 Technology Ltd, London UK). All the experiments were carried out between -90°C and 25 °C, setting a temperature ramp of 3°C/min and applying a force to the sample under a frequency of 1 Hz with a displacement of 20 μm. The variation of both the storage modulus (E') and the damping factor (tanδ) was monitored as a function of the temperature. The glass transition temperature (T_g) was measured as the temperature corresponding to the maximum of the tanδ curve, as reported by standard conventions. The crosslinking density (ν_e) of the cured samples was calculated as number of moles of crosslinking point per unit of volume, according to the statistical theory of rubber elasticity using the equation:

$$\mathrm{E}' = \nu_e RT \qquad \text{Eq. 3.2}$$

where E' is elastic modulus above T_g, T is the temperature and R is the universal gas constant.

Amplitude and frequency sweep measurements

The viscoelastic properties of the PEG-AcγCD-X thermosets were further investigated by means of amplitude and frequency sweep measurements performed on fresh-photocured samples (thickness = 0.2 mm) with the rheometer apparatus already used for the photorheology investigation. The amplitude sweep measurements were carried out at RT over the strain amplitude range 0.01 - 1000% setting a constant shear frequency (62 rad/s). Likewise, frequency sweep tests were performed setting a frequency range 0.1 - 100 rad/s while keeping the strain amplitude constant at 0.8 %.

Thermogravimetrical analysis (TGA)

The thermal stability of the PEG-AcγCD-X thermosets was investigated by means

of TGA, using a Mettler Toledo TGA1. The measurements were carried out with a heating ramp of 10 °C/min up to 700 °C under N_2 atmosphere (40 ml/min).

Printing resolution

The printing resolution (i.e. the fidelity of the printed structures to the original CAD models) was investigated by means of optical microscopy and 3D Scanning. Optical images of the samples were collected with a Leica DM2500 microscope. Then, the dimensions of the smallest 2D features were measured and compared with those of the corresponding digital model. 3D-Scanning was performed using a 3D optical scanner (E4, 3 Shape).

3.3 Results and discussion

3.3.1 Synthetic strategy and chemical characterization of Ac-γ-CyD

The photopolymerizable γ-cyclodextrin derivative Ac-γ-CyD was prepared according to a synthetic route reported by Gil et al. that consists of the substitution of -OH sites with multiple acrylate functions, using acryloyl chloride as functionalizing agent (**Figure 3.2**).[210]

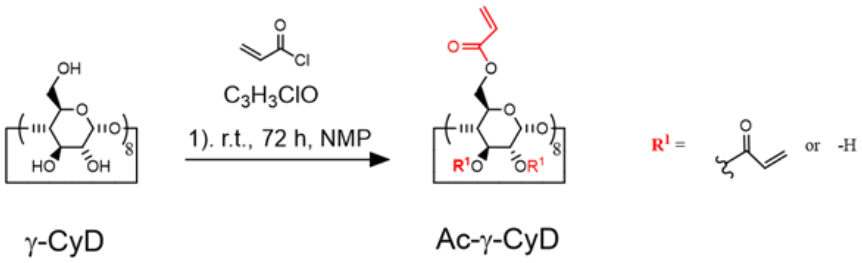

Figure 3.2. Schematic representation of the synthetic route followed to prepare the bio-based photocurable multi-acrylated γ-cyclodextrin derivative (Ac-γ-CyD).

The successful acrylation of γ-CyD was first proved by ^{1}H-NMR and $^{13}C\{^{1}H\}$-NMR. Indeed, the characteristic ^{1}H signals corresponding to the vinyl protons (δ = 5.95, 6.18, and 6.32 ppm) as well as the ^{13}C shifts for both the vinyl carbons (δ = 128.39 and 132.06 ppm) and carbonyl carbons (δ = 165.57 ppm) can be clearly identified in the spectra of Ac-γ-CyD (**Figure 3.3a** and Figure 3.3b, respectively).

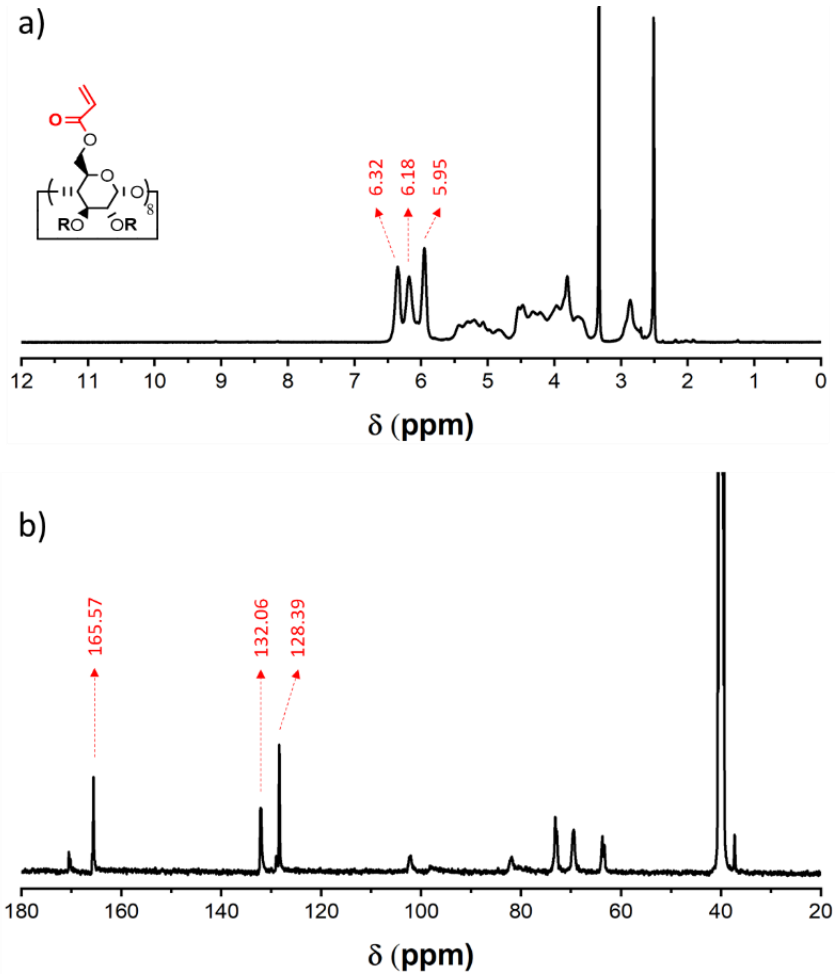

Figure 3.3. a) ^{1}H-NMR and b) ^{13}C{^{1}H}-NMR spectra of Ac-γ-CyD.

The acrylation was further evidenced by ATR-FTIR spectroscopy (**Figure 3.4**), since the typical stretching vibration of the vinyl groups can be observed in the spectrum of Ac-γ-CyD at 1633, 1410, and 809 cm^{-1} as well as those of carbonyl groups at 1727 cm^{-1}. Moreover, the pronounced reduction in the intensity of the peak at around 3300 cm^{-1} (-OH vibration) suggests a high substitution of the hydroxyl groups. This was confirmed by mass spectrometry. Indeed, despite a variable degree of functionalization was observed (in good agreement with variable substitutions reported elsewhere [210–212]) the results ($M_{w,\ Ac\text{-}\gamma\text{-}CyD}$ = 2450 g/mol) indicated that 21 hydroxyl groups per molecule were successfully replaced by acrylate functions, on average. Considering that the original -OH sites of γ-CyD are so distributed, 8 primaries and 16 secondaries at the lower or upper rim, the obtained

degree of substitution indicates that the functionalization involved both primary and secondary sites (**Figure 3.5**).

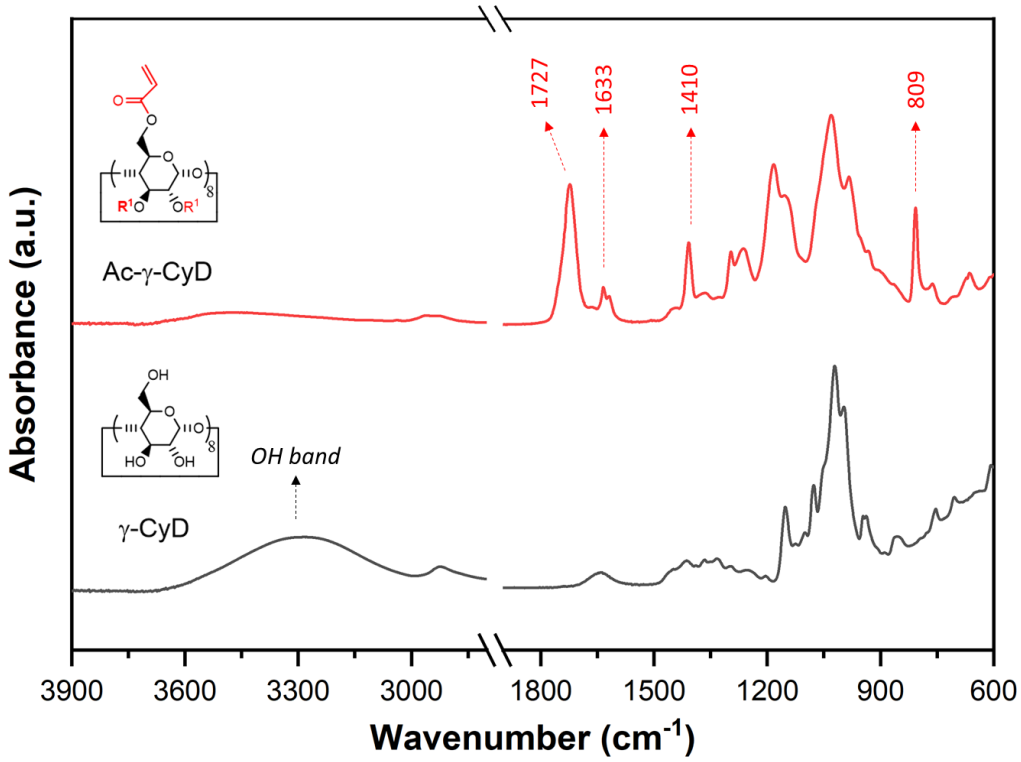

Figure 3.4. ATR-FTIR spectra of pristine γ-CyD and Ac-γ-CyD.

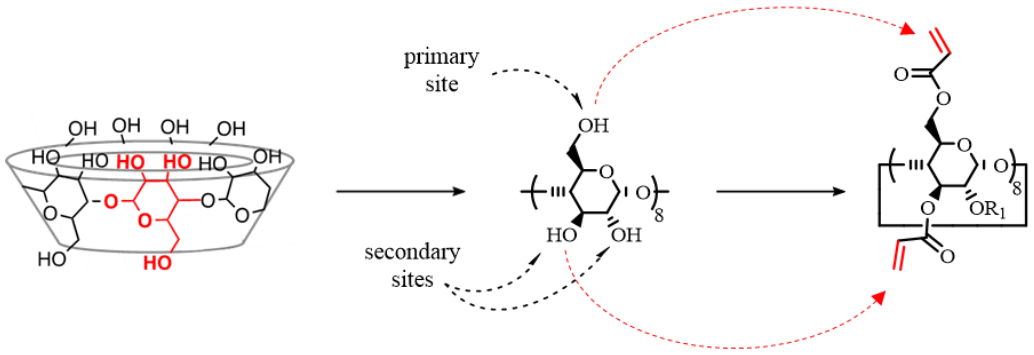

Figure 3.5. Schematic representation of the functionalization of both primary and secondary hydroxyl sites of the pristine γ-CyD with photopolymerizable acrylate functions.

3.3.2 Photoreactivity of the formulations

The multi-acrylated γ-cyclodextrin derivative was then tested as macromer in novel photocurable formulations. Two different strategies were followed: 1) Ac-γ-CyD tested as building block of all CyD-based thermosets (Ac-γ-CD dissolved in propylene carbonate to get liquid formulations, strategy 1); 2) Ac-γ-CyD used as crosslinker in combination with a monofunctional monomer, poly(ethylene glycol) methyl ether methacrylate (PEGMEMA), which serves also as reactive diluent (strategy 2). Detailed information on the composition and preparation of the two sets of formulations, namely Ac-γ-CD-X and PEG-AcγCD-X (X corresponds to the wt% of Ac-γ-CD used: 5, 10, 20, 30 %) are given in the experimental procedures (see subsection 3.2.2).

The photoreactivity of the formulations was studied by means of real-time photorheology. The resulting photorheology curves show that thermosetting networks can be generated after a short irradiation time (delay time < 2 s) when Ac-γ-CyD is used as building block for an all CyD-based thermoset (strategy 1), independently from the macromer concentration, while the storage modulus (G′) at plateau gradually increases with increasing content of Ac-γ-CyD (**Figure 3.6a**). These data indicate that, as soon as the initiating radicals are generated upon the photolysis of the PI, the homopolymerization of the macromer is rapidly activated leading to the generation of crosslinked networks in few seconds.

Instead, the photoreology curves of the formulations prepared by using Ac-γ-CyD as crosslinker of PEGMEMA (strategy 2) are given in Figure 3.6b. In this case the UV irradiation activates both the copolymerization of Ac-γ-CyD with PEGMEMA and their homopolymerization. Note that no crosslinking occurs by irradiating PEGMEMA in the absence of Ac-γ-CyD, as expected when using only monofunctional monomers. As becomes clear from the G' curves, thermosetting networks are generated at a rapidly increasing rate with increasing Ac-γ-CyD content in the precursor formulation. Indeed, the photopolymerization starts earlier (onset of crosslinking decreases from 15 s for PEG-AcγCD-5 to < 1 s for PEG-AcγCD-30) and the kinetic is fastened (slope of G' curves result ever steeper), due to both the higher reactivity of the multiple acrylate functions of Ac-γ-CyD with respect to the methacrylate ones of PEGMEMA and to the "autoacceleration" phenomenon, typical for those polymerizations involving multiunsaturated monomers.

Indeed, the restricted diffusions of the active species in a highly crosslinked network, as the one generated in the presence of multiunsaturated monomers, lead

to a reduction of termination mechanisms. Therefore, the local concentration of radicals increases and the kinetic is accelerated in the first stages of polymerization. In this sense, the photopolymerization of multiunsaturated monomers could be considered as an autocatalytic process, even if the speeding-up of the reaction rate is not ascribable to the generation of intermediate species (as for the typical autocatalytic mechanisms) but to complex diffusion processes that occur in the growing polymer network.[157,158,213,214]

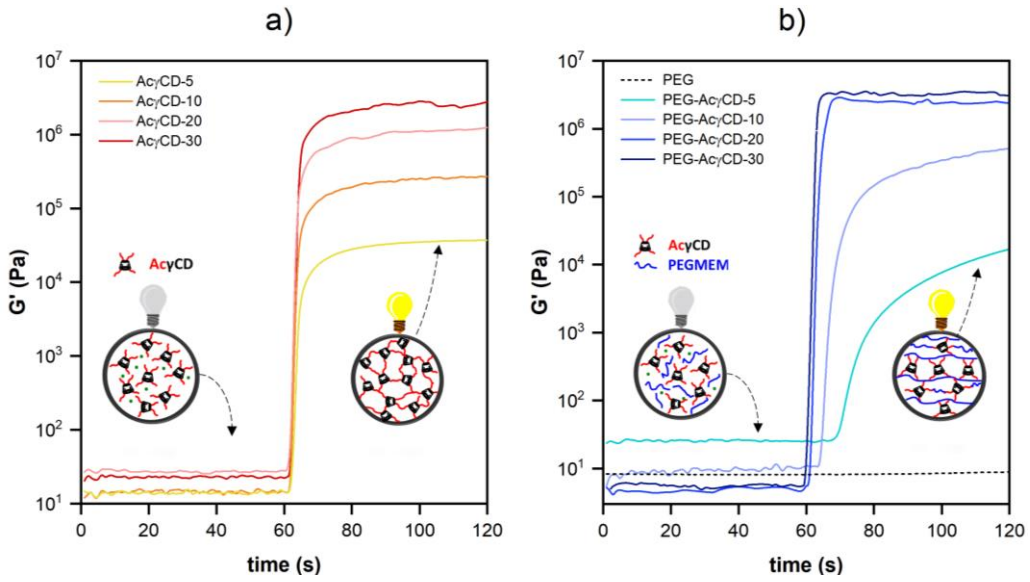

Figure 3.6. Photorheology characterization of the two different sets of formulations using Ac-γ-CyD as a) building block or as b) crosslinker of monofunctional PEGMEMA and corresponding photopolymerization mechanisms: homopolymerization of Ac-γ-CyD and copolymerization with PEGMEMA, respectively.

Based on these photorheology data, both sets of formulations can be considered as interesting candidates for DLP-printing. As evidence of this, the printability will be assessed in the following subsection, with a particular focus on those formulations containing either 20 or 30 wt% of Ac-γ-CyD because of the faster kinetic and higher mechanical stability displayed by the cured samples (i.e. higher G' values at plateau monitored via photorheology).

3.3.3 DLP-printing of CyD-based thermosets

The AcγCD-X and PEG-AcγCD-X formulations were tested as innovative inks for DLP-printing.

The printing parameters were optimized for each formulation. In particular, the layer thickness was fixed to 50 μm and the UV-light intensity was set at 30.66 mW/cm^2, while the exposure time was ranged between 1.5 and 2.5 s/layer depending on the specific reactivity of the precursor formulation monitored via the preliminary photorheology tests.

Complex 3D-geometries (**Figure 3.7**, detailed features in the order of hundreds of μm) were successfully printed with high resolution, as confirmed by optical microscopy (**Figure 3.8a**). The high printing fidelity to the original CAD models was further proved by 3D-scanning analysis. This technique allows to get a point-cloud map from the scan of the printed structures, which is then used to prepare a digitalized model to be virtually overlaid to the original CAD file for a comparative analysis. The results of the comparison are displayed as a colored 3D-map which shows the geometrical deviation from the reference model, where the red zones represent the "material-excess" and the blue ones correspond to areas with a "material-deficit".[118,133] From the 3D-inspection of the diamond-shaped printed part (see Figure 3.7f) it has been calculated that the dimensional variations between positive and negative values was about ± 0.19 mm (Figure 3.8b).

These results confirmed that these novel bio-based formulations can be successfully used to fabricate complex 3D-microarchitectures with a high resolution.

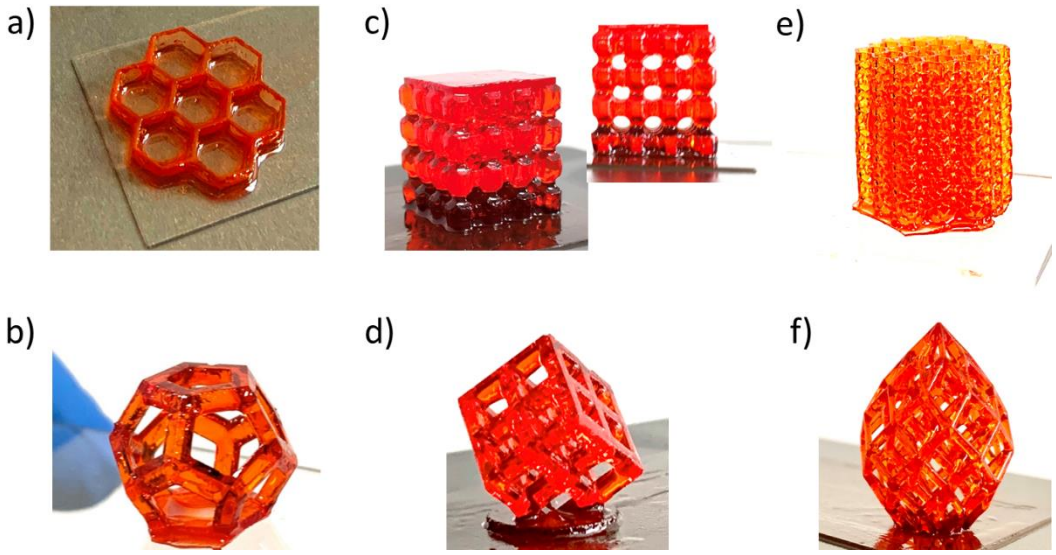

Figure 3.7. Photographs of 3D-printed structures prepared from AcγCD-30 (a, b) and PEG-AcγCD-20 (c-f).

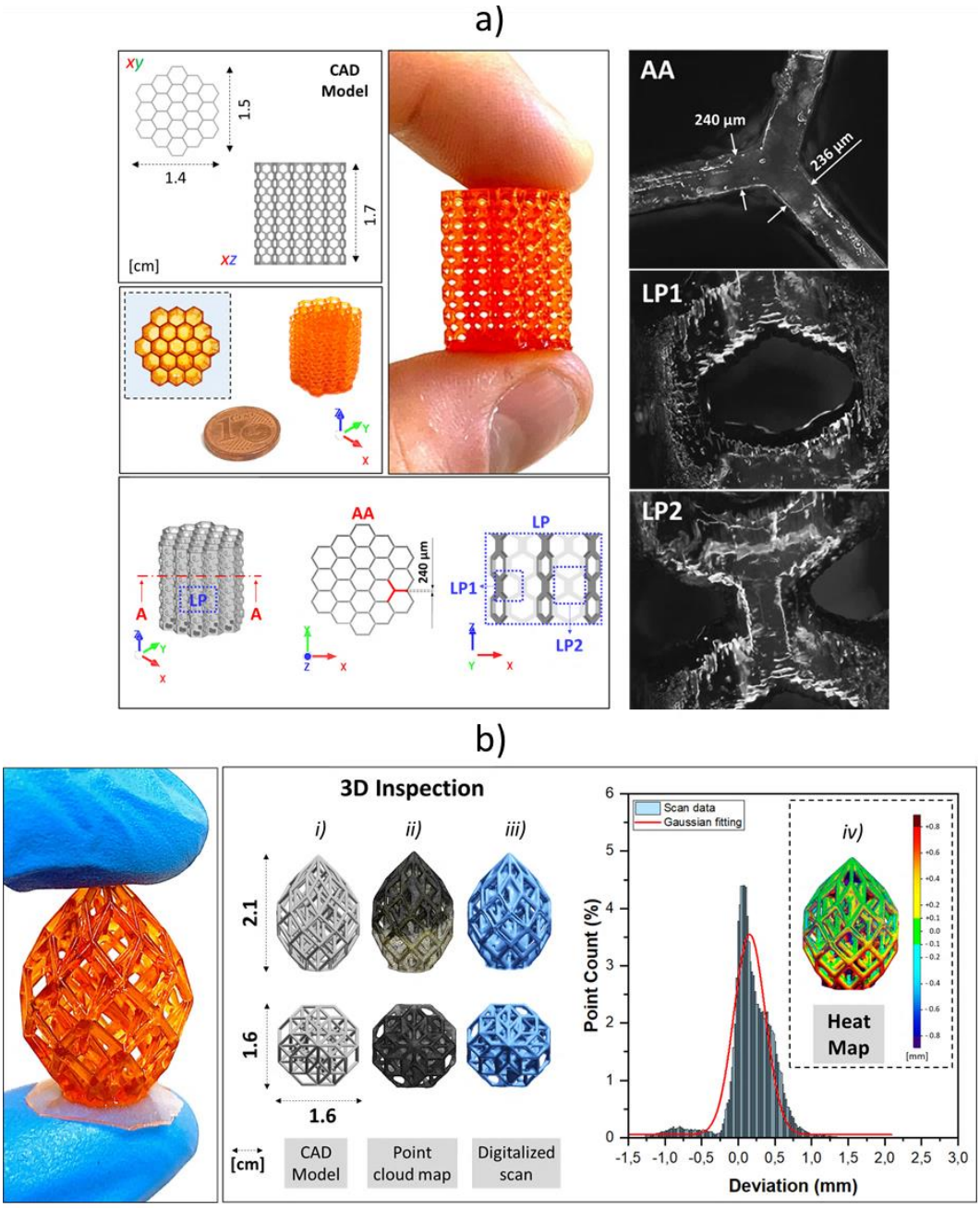

Figure 3.8. Analysis of the resolution and fidelity to the original CAD files of the printed a) honeycomb-like and b) diamond-shaped structures. The investigations were carried out by means of optical microscopy 3D scanning, respectively.

However, despite the good printability, those structures fabricated from all-CyD based inks result much more brittle than the ones obtained from the set of

formulation wherein Ac-γ-CD acts as crosslinker of monofunctional PEGMEMA. This can be ascribed to the development of high stress inside the AcγCD-X network generated upon irradiation, as reported in the literature for the UV-induced free-radical polymerization of multiunsaturated acrylates.[156,162,163,215] Whereas, the presence of PEGMEMA limits the brittleness of the printed PEG-AcγCD-X structures, given that monofunctional monomers are typically used as plasticizers. Therefore, in the following subsection, we decided to further investigate the properties of the thermosetting polymers prepared just from the second set of formulations (PEG-AcγCD-X), since we truly believe that the accurate combination of the crosslinking efficiency of Ac-γ-CyD with the plasticizing effect of PEGMEMA, would allow to prepare thermosetting polymers with tailorable thermomechanical properties.

3.3.4 Properties of the PEG-AcγCD-X thermosets

As previously discussed, when Ac-γ-CyD is used in combination with the monofunctional monomer PEGMEMA it behaves as crosslinking agent. Therefore, solvent extraction measurements were performed on the cured PEG-AcγCD-X samples to evaluate the crosslinked fraction of the polymers. The results revealed that the gel content (GC) increases with increasing concentration of Ac-γ-CyD in the precursor formulations, reaching a maximum value of approximately 90% for PEG-AcγCD-30 (**Figure 3.9**).

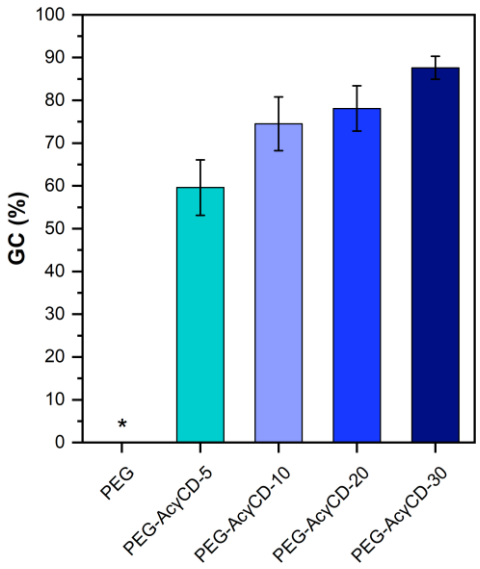

Figure 3.9. Results of the solvent extraction measurements carried out to evaluate the crosslinked fraction (gel content, GC) of the PEG-AcγCD-X thermosets obtained upon irradiation.

This confirm the high crosslinking efficiency of the multi-acrylated macromer since ever more covalently crosslinked networks are generated upon irradiation. Note that no chemical crosslinking occurs by irradiating PEGMEMA itself (GC = 0%) without the addition of the crosslinker, since the linear thermoplastic chains generated upon irradiation of a monofunctional monomer rapidly dissolve when immersed in the solvent.[143]

The thermomechanical properties of the PEG-AcγCD-X thermosets were then evaluated by means of DMTA. Note that the samples prepared with the lowest content of crosslinker (5% of Ac-γ-CyD) have the consistency of a very soft gel. This makes the investigation of PEG-AcγCD-5 extremely challenging, because the samples bend significantly once above the glass transition temperature (T_g) and break when approaching the plateau region. For this reason, the curves of PEG-AcγCD-5 appear incomplete, but they are shown anyway by way of comparison with the other PEG-AcγCD-X samples (with a particular focus on the tanδ plot, as will be discussed later). The DMTA curves are given in **Figure 3.10**, while the main data resulting from the thermomechanical investigation are given in **Table 3.1.**

The E' plots (Figure 3.10a) revealed that the drop of the storage modulus in the T_g region becomes lower as the amount of the multi-acrylated crosslinker is increased. In other words, the modulus at the plateau in the so-called rubbery region, increased with increasing amount of Ac-γ-CD, ranging from 4.5 x 10^6 up to 1.4 x 10^8 Pa. This suggests the generation of ever-more rigid and crosslinked networks. Indeed, the value of rubbery modulus has been related to the crosslinking density (ν_e) of a polymer,[157,216] that is the higher the modulus in the rubbery region, the higher the ν_e. As evidence of that, the average ν_e of the PEG-AcγCD-X polymers calculated according to the statistical theory of rubber elasticity increases from 0.0025 up to 0.0768 mmol/mm^3 by increasing the amount of Ac-γ-CyD. Furthermore, the increase of ν_e reflects into higher T_g, as confirmed by the shift of the tanδ curves toward higher temperatures with increasing amount of Ac-γ-CyD (Figure 3.10b).

However, the broadening of the curve suggests that the T_g is more likely spread over a region of temperatures due to a wide distribution of the mobility or relaxation times of the polymer chains.[217–219] Generally, this is an indication of a structural inhomogeneity of the material and typically occurs when thermosetting networks are generated upon UV-irradiation of multifunctional monomers, due to complex polymerization mechanisms.[217,220] Indeed, the polymerization of multifunctional monomers may involve both intermolecular and intramolecular radical reactions. Intramolecular crosslinking is enhanced in the early stage of

polymerization due to the higher concentration of pendant double bonds in the proximity of the radical site, and it is also evident for the copolymerization with monounsaturated monomers. This phenomenon leads to the generation of highly crosslinked regions, named microgels, with locally reduced chain mobility, wherein unreacted double bonds remain entrapped. Accordingly, the formation of more or less crosslinked regions is the reason for a structural inhomogeneity of the growing polymer network.[158,159,213,219–221]

Therefore, the experimental observations are in good agreement with these findings, since it is reasonable to assume that the broadening of the tanδ curves of the PEG-AcγCD-X samples may reflect an increasing inhomogeneity of the network due to a wider distribution of the mobility of the PEGMEMA chains with increasing content of the multifunctional Ac-γ-CyD. Furthermore, ever-lower damping factors were observed when the concentration of Ac-γ-CyD is increased in the formulations, as confirmed by the flattening of the tanδ plots. As reported in the literature, the intensity of the tan δ peak at the T_g reflects the extent of mobility of the polymeric chains at this specific temperature.[220,222] In this context, the increase of the crosslinking density would reflect into a decreased intensity of the tanδ peak, since crosslinks significantly restrict the mobility of the chains giving to the polymer an ever-lower viscous behavior.[220] This is consistent with the trend observed for the PEG-AcγCD thermosets, since the increase in the crosslinking density leads to a reduction in the mobility of the polymer chain in the T_g region (i.e. lower values of tanδ).

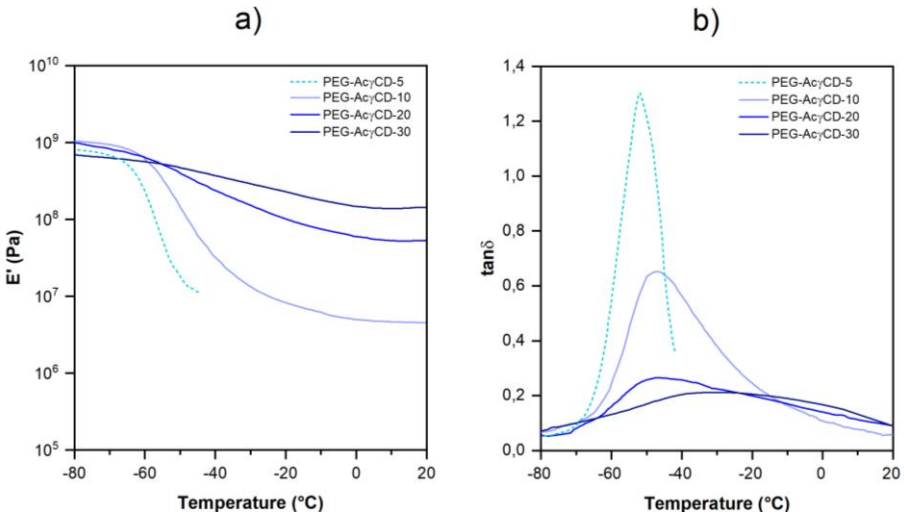

Figure 3.10. a) E' and b) tanδ curves resulting from the DMTA measurements of the cured PEG-AcγCD-X thermosets.

Table 3.1 Thermomechanical properties of the PEG-AcγCD thermosets.

Sample	E'_{RT} (Pa)	ν_e (mmol/mm^3)	T_g (°C)	tanδ
PEG-AcγCD-5	NA	NA	- 52	1.31
PEG-AcγCD-10	4.5 x 10^6	0.0025	- 48	0.66
PEG-AcγCD-20	5.1 x 10^7	0.0280	- 45	0.26
PEG-AcγCD-30	1.4 x 10^8	0.0768	- 30	0.21

The mechanical properties of the cured PEG-AcγCD-X samples were also investigated by means of frequency and amplitude sweep measurements.

The former further confirm the increase of the rigidity of the thermosets since the recoded G' increases with increasing content of Ac-γ-CD (**Figure 3.11a**), in good agreement with the E' trend observed in the DMTA curves. Whereas the latter revealed a great difference in the viscoelastic properties of the thermosets under increasing oscillation amplitude, since the samples can endure an ever-lower strain amplitude before breaking, as the content of Ac-γ-CyD increased (Figure 3.11b). It is therefore evident that the accurate compounding of the formulations allows to tailor the thermomechanical properties of the resulting thermosetting networks by merging the crosslinking efficiency of Ac-γ-CyD with the plasticizing effect of PEGMEMA.

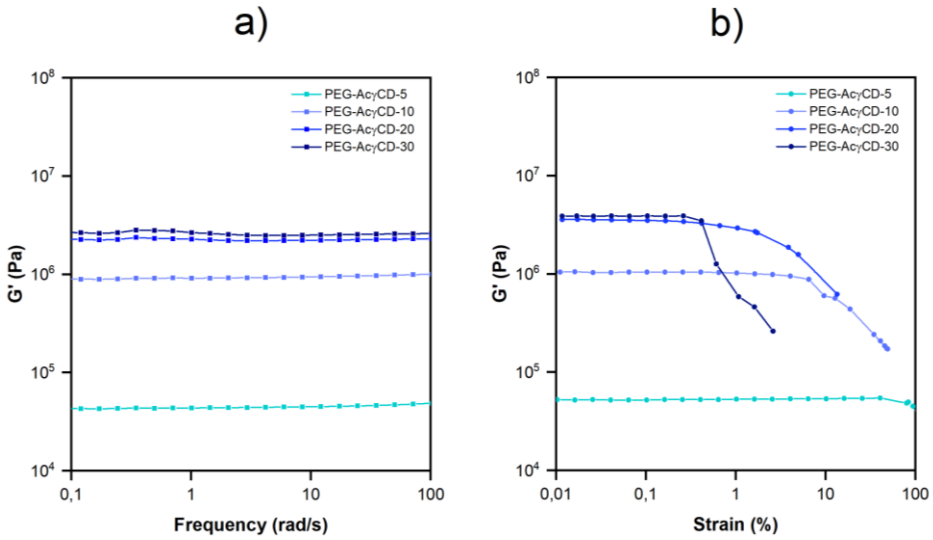

Figure 3.11. a) Frequency and b) amplitude sweep measurements performed with the rheometer apparatus on fresh irradiated PEG-AcγCD-X samples.

Finally, the thermal stability of the PEG-AcγCD-X thermosets was investigated by means of TGA. The resulting thermograms (**Figure 3.12**) revealed that all the samples are stable up to 250-300 °C, with a slight shift of the onset of degradation to higher temperatures and a gradual increase of the char residue with increasing content of Ac-γ-CyD. Both these findings can be related to the increase in the crosslinking densities of the thermosets.[223]

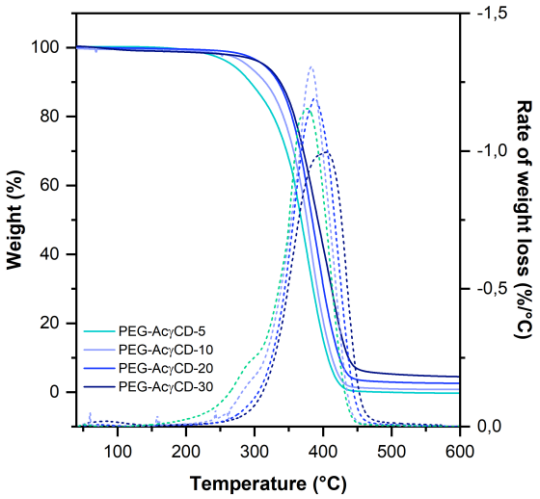

Figure 3.12. TGA curves (solid lines) of the PEG-AcγCD-X thermosets. The rate of weight loss (dashed lines) was calculated as the derivative of the weight curves.

3.4 Conclusions

In this chapter, a multifunctional cyclodextrin derivative is proposed as a novel bio-based macromer for DLP-printing. The target molecule was prepared following an acrylation protocol designed to substitute the original hydroxyl groups with photopolymerizable functionalities. The successful functionalization was confirmed by means of ^{1}H- and ^{13}C-NMR spectroscopy, as well as by ATR-FTIR spectroscopy and mass spectrometry. Real-time photorheology measurements revealed the high reactivity of the multi-acrylated macromer Ac-γ-CyD, suggesting its use to prepare novel bio-based photoresins for DLP-printing. This has been demonstrated since complex 3D-structures were successfully printed with high resolution by using Ac-γ-CyD either as neat building block for an all cyclodextrins-based thermoset or as crosslinking agent in combination with a monofunctional methacrylate oligomer. The latter strategy seemed to be the most promising since the combination of the high crosslinking efficiency of Ac-γ-CD and the plasticizing

effect induced by PEGMEMA easily allows to modulate the properties of the resulting thermosetting polymers, as confirmed by the results of the thermomechanical investigations. However, the versatility of such a system, that is the possibility to tailor the mechanical properties by simply varying the composition of the precursor formulation, is likely counterbalanced by the occurrence of network inhomogeneities which are due to the use of a multiunsaturated monomer in a multicomponent formulation, as reported elsewhere.

In conclusion, the results provided further evidence that bio-based molecules can be successfully used to develop valuable and greener alternatives to the commercially available photopolymers obtained from petroleum-based resources. Moreover, the strategy followed to modify the starting material making it suitable for photopolymerization process could be reasonably used in the future to further enlarge the printable materials palette with other natural molecules.

4. Strategies of post-printing surface modification of PEGDA-AcγCyD structures

4.1 Motivation and outline

As briefly introduced in subsection 1.1, the modification of polymeric surfaces is a powerful approach to further expand the possibilities given by 3D-printing, since it allows to impart to the printed parts superior functionalities while retaining their bulk properties.[40,224,225] Looking at DLP-printing, chemical moieties with suitable reactive groups can be directly introduced in the photocurable formulations to be later exploited for further functionalization via a wide range of reactions.[127,226,227] Besides, also pendant unsaturated functions remained unreacted after the printing step can provide potential reactive sites for surface modification.[228] In this context, the residue of C=C double bonds arising from the photopolymerization of multifunctional acrylates [157,158,213] can turn into a potential advantage.

Within this framework, this chapter is devoted to show the results of preliminary investigations on the use of surface-functionalization strategies to benefit from unreacted acrylate functions in structures printed from a photocurable system containing the multi-acrylated cyclodextrin derivative Ac-γ-CyD presented in chapter 3. First, the residual amount of C=C bonds on the surface of DLP-printed parts was evaluated. Then, thiol- and aza-Michael additions are proposed as versatile reactions to tune the wettability of the printed structures via the selective grafting of hydrophobic/hydrophilic polymeric brushes. ATR-FTIR spectroscopy was used to confirm the chemical grafting, while water contact angle measurements were carried out to monitor the wettability evolution. Moreover, thiolated surfaces were further exploited as active substrates for the immobilization of photogenerated silver nanoparticles, which was monitored by means of X-ray photoelectron spectroscopy (XPS) and field-emission scanning electron microscopy (FESEM).

4.2 Experimental

4.2.1 Materials and chemicals

Polyethylene glycol diacrylate (PEGDA, M_n = 250 g/mol), poly(dimethylsiloxane) bis(3-aminopropyl) terminated (A-PDMS, M_n = 2500 g/mol), pentaerythritol tetrakis(3-mercaptopropionate) (PETMP), acrylic acid (AA), silver nitrate ($AgNO_3$, > 99.0 %), ethanol (EtOH), isopropanol (IPOH), acetonitrile (MeCN), phenylbis(2,4,6-trimethylbenzoyl)phosphine oxide (Omnirad 819) and 2-hydroxy-4′-(2-hydroxyethoxy)-2-methylpropiophenone (Irgacure 2959) were purchased from Sigma Aldrich and used as received. Ac-γ-CyD was prepared according to the synthetic protocol reported in chapter 3.

4.2.2 Procedures

Preparation of the DLP-printable formulation

Ac-γ-CyD (20 wt.%) was dissolved in PEGDA, which serves simultaneously as reactive diluent and as comonomer, while Omnirad 819 (0.2 phr) was added as PI. The formulation was stirred until becoming homogeneous.

DLP-printing

The precursor formulation was 3D-printed using a MAX X27 DLP-printer from ASIGA (for more information about the printer, refer to subsection 3.2.2). The layer thickness was set to 50 μm, while the light intensity and the exposure time/layer were set to 40 mW/cm^2 and 0.8 s, respectively. The printed samples (diameter = 12 mm; thickness = 1 mm), named PCyD20, were washed in EtOH to remove the excess of resin before being used for post-printing functionalization purposes.

Surface grafting of A-PDMS brushes

The surface functionalization was performed by immersing the printed sample into an amino-solution of A-PDMS diluted in IPOH (10 wt.%) for 24h at RT. The samples were then removed from the reaction bath and rinsed three times in IPOH.

Photo-induced grafting of PETMP brushes

The photo-induced grafting was performed as follows: few drops of a solution consisting of PETMP diluted in MeCN (50 wt.%), with Omnirad 819 added as PI (2 wt.%, concerning the PETMP amount), were spread on the printed sample and irradiated for 1 min using a high-pressure mercury Dymax ECE lamp (100 mW/cm^2) to activate a thiol-ene reaction at the surface. Then, the samples were rinsed in EtOH for 30 min to remove unlinked PETMP from the surface. Note that

PETMP was appositely used to leave unreacted thiols (-SH) on the surface for further functionalization purposes.

Photo-induced grafting of AA brushes

The photo-induced grafting was performed as follows: few drops of a solution of AA diluted in water (10 wt.%) were spread on the surface of the samples previously functionalized with PETMP and irradiated for 10 min using a high-pressure mercury Dymax ECE lamp (70 mW/cm^2). This allows to activate a thiol-ene reaction via the -SH groups remained on the surface after the first functionalization with PETMP. Then, the samples were triply rinsed in H_2O to remove the unlinked AA.

Surface grafting of photoreduced silver nanoparticles (AgNPs)

The surface-anchoring of AgNPs was performed as follows: the samples previously functionalized with PETMP were immersed in a grafting solution consisting of $AgNO_3$ dissolved in distilled H_2O (100 mg/mL), with Irgacure 2959 added as PI (0.5 wt.%). Then, the solution was irradiated for 15 min using a Hamamatsu LC8 lamp equipped with an 8 mm light guide (70 mW/cm^2), to activate the photogeneration of AgNPs and their spontaneous grafting on the residual -SH groups on the surface. During the photoreduction process, the solution was magnetically stirred. Finally, the samples were rinsed in H_2O for 90 min under sonication.

4.2.3 Characterization methods

Gel content measurements

Gel content measurements were performed to evaluate the covalently crosslinked fraction of the printed polymers. The GC values were calculated by following the same experimental procedure already reported in chapter 3, subsection 3.2.3.

IR spectroscopy

ATR-FTIR spectroscopy was used to investigate the double bond conversion (DBC, that is the conversion of the C=C bonds of the acrylate functions) in the 3D-printed parts and the effective anchoring of the polymer brushes grafted by following the abovementioned strategies. The measurements were performed using a Nicolet iS50 FT-IR spectrometer equipped with an attenuated total reflectance (ATR) accessory (Smart iTX). ATR Spectra were collected with a resolution of 4 cm^{-1} between 600 and 4000 cm^{-1}, averaging 32 scans for each spectrum. The surface-DBC of the printed samples was calculated from the decrease of the area of the peak

at about 1633 cm^{-1} (corresponding to the vibration of C=C bonds of acrylates) normalized by the constant signal centered at 1730 cm^{-1} (corresponding to the stretching vibration of C=O groups).

Contact angle measurements

Water contact angles measurements were performed to monitor the wettability-evolution of the printed samples upon the different post-functionalizations. The tests were carried out at RT using a Kruss DSA100 drop shape analyzer, equipped with a video camera and an image software. First, small water droplets (≈15 μL) were applied onto a leveled surface of the printed sample. Then, the static contact angles were measured using the sessile drop technique. The results were averaged over six measurements randomly performed in different area of each sample.

XPS analyses

XPS was used to confirm the photografting of AgNPs onto the surface of the printed sample. The measurements were performed using a PHI Versaprobe 5000 (Physical Electronics – Chanhassen, MN – USA), equipped with a monochromatic Al k-alpha source (1486.6 eV). Both survey and high resolution (HR) spectra were collected for each sample. The core-level energy shifts were referred to C 1s peak (C-C) at 284.5 eV. Omnic software was used for data analysis and for further peak-fitting procedure.

Morphological investigation

The morphology of the metallic NPs grafted on the surface of the printed samples were analyzed by means of FESEM investigations using a MERLIN-FESEM from Carl Zeiss. The measurements were carried out without any previous metallization of the samples.

4.3 Results and discussion

4.3.1 Unreacted acrylate functions as sites for surface functionalization

Although the photopolymerization of multiunsaturated acrylates enables the fast generation of highly crosslinked polymer networks, it also entails anomalous behaviors, such as a structural heterogeneity (as already discussed in subsection 3.3.4) and, especially, an incomplete conversion of the acrylate groups.[157,158,213] Nevertheless, the residual unsaturated functionalities can be attractive candidates for functionalization purposes exploiting Michael-reactions,

giving the high selectivity of the latter towards C=C bonds and their ability to yield regiospecific products under rather facile conditions.[100,229–231] In this sense, the unavoidable residue of unreacted C=C bonds when DLP-printing multifunctional acrylates can be turn to an advantage to give new functionalities to the printed parts via a post-printing surface modification.

To prove the feasibility of this strategy, structures were first DLP-printed from a photocurable formulation containing the multi-acrylated cyclodextrin derivative Ac-γ-CyD and PEGDA (as reactive diluent), and then used as platform to explore strategies of post-functionalization involving the residual acrylate functions located at the surface. Indeed, preliminary investigations confirmed that, despite the generation of densely crosslinked thermoset (GC = 96.9 ± 0.3 %, measured by gel content experiments), a significant amount of C=C bonds did not polymerize during the printing step (DBC = 60.5 ± 1.8 %, measured by ATR-FTIR spectroscopy). As evidence of that, the signals corresponding to the stretching and bending vibrations of C=C bonds can be still clearly observed at around 809, 1410 and 1633 cm^{-1} in the ATR spectrum of the printed samples (named PCyD20) shown in **Figure 4.1**.

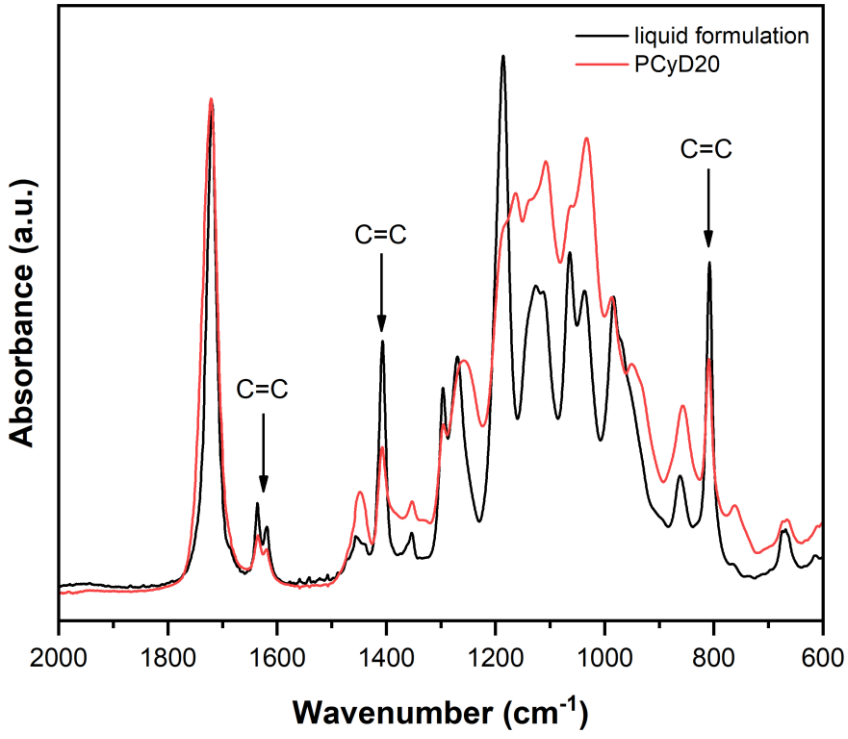

Figure 4.1. Comparison between the ATR-FTIR spectra of the liquid formulation and of the DLP-printed sample PCyD20. The signals of unreacted C=C bonds can be observed at around 809, 1410 and 1633 cm^{-1} in the spectrum of PCyD20.

The high residue of unreacted C=C bonds can be ascribed to the complex mechanisms of the photopolymerization of multiunsaturated monomers. Indeed, as the reaction proceeds, an ever-higher number of polymer chains become crosslinked and the segmental mobility is so dramatically reduced that diffusion becomes the dominating termination mechanism already from low values of DBC.[232] This means that, as the mobility of the functional groups is reduced, an ever-growing number of radicals tend to get trapped [233] and the reactivity of the system drops down until the reaction stops due to vitrification.[158] As a result, despite highly crosslinked thermosets are generated, the final DBC stands at values well below 100%, i.e. a large amount of unreacted pendant C=C bonds remained entrapped in the network.

However, as previously introduced, the incomplete DBC may be exploited for post-printing functionalization. Following this strategy, the next subsections are focused on presenting the preliminary results of surface modification of PcyD20 structures employing the surface-localized unreacted acrylate groups for Michael-addition reactions. More specifically, two different grafting methodologies were investigated:

1) Residual C=C bonds used as active sites for the direct anchoring of amino-terminated polysiloxane brushes (A-PDMS) to generate hydrophobic surfaces. This strategy follows a *grafting-to* approach,[234,235] since it involves only a chemical coupling of surface-bound moieties with a suitable end-functionalized pre-polymerized chain.

2) residual C=C bonds used as substrate for the generation a versatile interface bearing pendant -SH groups which are subsequently exploited to: a) activate the surface-initiated photopolymerization of hydrophilic brushes of acrylic acid (AA) (*grafting-from* approach [234,235]) or b) immobilize on the surface photoreduced silver nanoparticles (AgNPs).

4.3.2 Post-printing surface grafting of hydrophobic/hydrophilic polymer brushes

In a first set of experiments, polysiloxane brushes were anchored onto the surface of the printed PCyD20 following the path of an aza-Michael reaction. The sample was immersed in a grafting solution wherein the amino-terminated A-PDMS was used as Michael-donor to activate the nuchleophilic addition onto the β-carbon atom of the C=C bond of the residual acrylate functions (i.e. the Michael-acceptors).[231,236] The reaction is schematically represented in **Figure 4.2**.

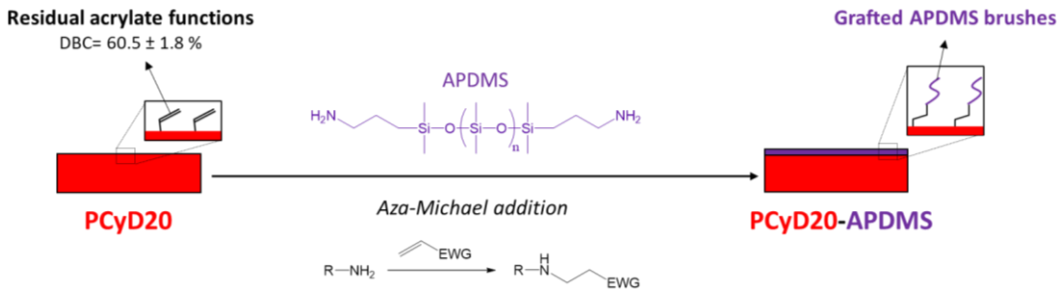

Figure 4.2. Schematic representation of the surface-grafting of A-PDMS brushes onto PCyD20 following the path of an aza-Michael reaction.

The effective anchoring of A-PDMS brushes onto PCyD20 was first proved by ATR-FTIR spectroscopy. The ATR spectrum of PCyD20 after the functionalization, named PCyD20-APDMS, is shown in **Figure 4.3**. The spectra of PCyD20 and A-PDMS are reported as reference.

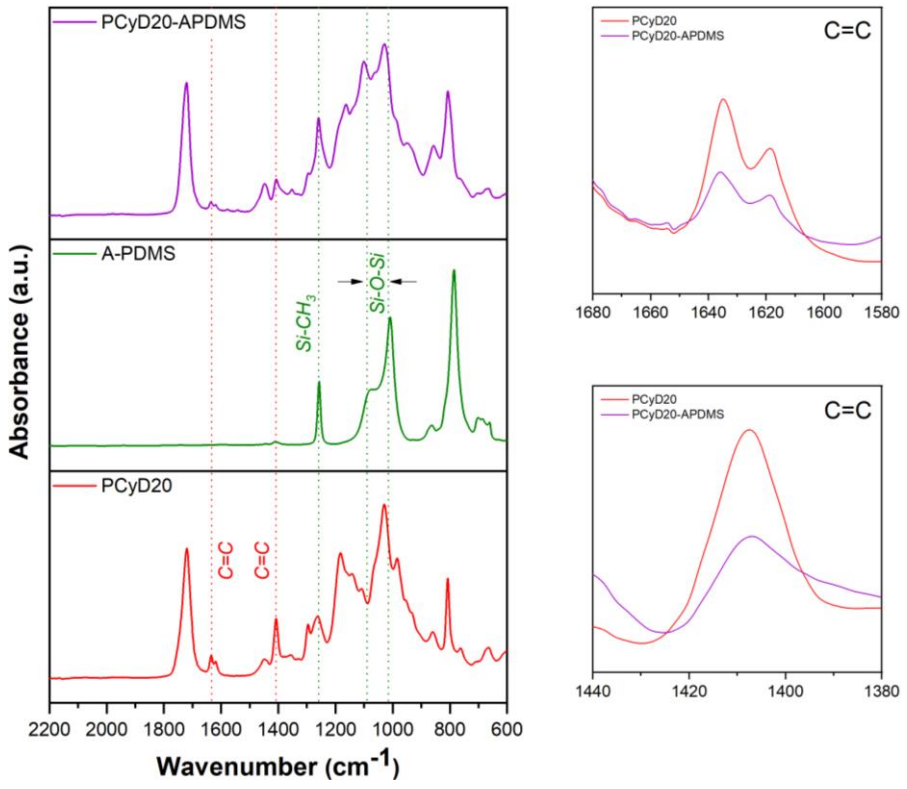

Figure 4.3. ATR spectra of PCyD20, A-PDMS and PCyD20 after the functionalization (PCyD20-APDMS) and detailed view of the absorption ranges corresponding to C=C vibrations before and after the aza-Michael reaction.

The lower intensity of the peaks centered at 1410 and 1633 cm^{-1} (C=C stretching vibrations, see detailed views given in Figure 4.3) in the ATR spectrum of PCyD20-APDMS confirmed that the aza-Michael addition occurred on the surface of PCyD20 leaving a lower amount of unreacted double bonds.[236] In this sense, a complete conversion of the residual acrylate functions was not achieved even under forcing the reaction conditions using higher amount of A-PDMS in the grafting solution, due to the steric hindrance of the high molecular weight polysiloxane chains. The effective grafting was further proved by the appearance in the PCyD20-APDMS spectrum of the characteristic peaks corresponding to the asymmetric stretching vibration of Si-O-Si (absorption band between 1000 and 1100 cm^{-1}) and to the structural vibration of $Si-CH_3$ (1260 cm^{-1}) [237].

Finally, wettability measurements confirmed the generation of a hydrophobic surface since the water contact angle increases from 61° to 96° after the grafting of A-PDMS (**Figure 4.4**).

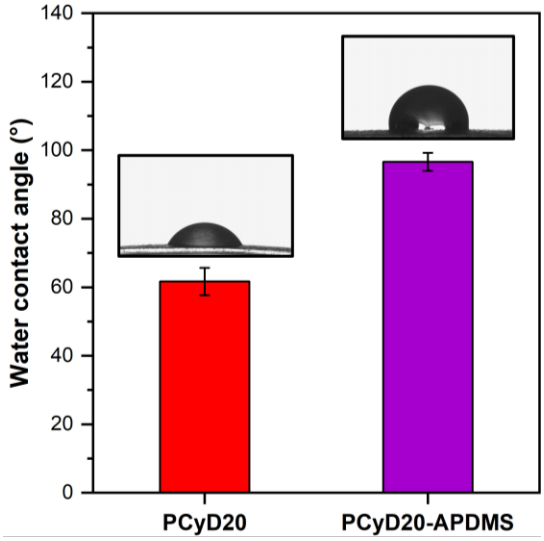

Figure 4.4. Water contact angles on the surface of the printed sample before (PCyD20) and after the grafting of A-PDMS (PCyD20-APDMS).

On the contrary, the goal of a second set of experiments was to increase the wettability of PCyD20. To do this, thiol-ene click chemistry [100,229,230] was first employed to photogenerate on PCyD20 an active interface bearing free -SH groups. Then, the pendant -SH were employed in a subsequent Michael-addition to activate the grafting of hydrophilic AA brushes.

It follows that the choice of the tetrafunctional monomer PETMP as functionalizing agent was dictated by the need to exploit part of its terminal -SH groups to generate the thiolated interface (named PCyD20-PETMP) converting the residual C=C into C-S bonds (**Figure 4.5a**), while the remained thiols were used to graft AA chains (Figure 4.5b).

Remarkably, the functionalization routes previously reported consist of the chemical reaction of surface-bound functionalities (residual C=C) with polymeric end-groups (amines of A-PDMS, or thiols of PETMP) which not undergo further polymerization (*grafting-to* strategy). On the contrary, the grafting of AA brushes involves not only a chemical coupling but also a surface-initiated radical photopolymerization of the monomer (*photografting-from* strategy), which is activated by the generation of thiyl radicals upon UV-irradiation of the PCyD20-PETMP interface (for more information, see chapter 2, subsection 2.2). Note that, the photo-induced grafting of AA was carried out without using any radical PI to limit the homopolymerization of AA-chains which would happen in competition with the thiol-ene reaction with the thiolated interface.

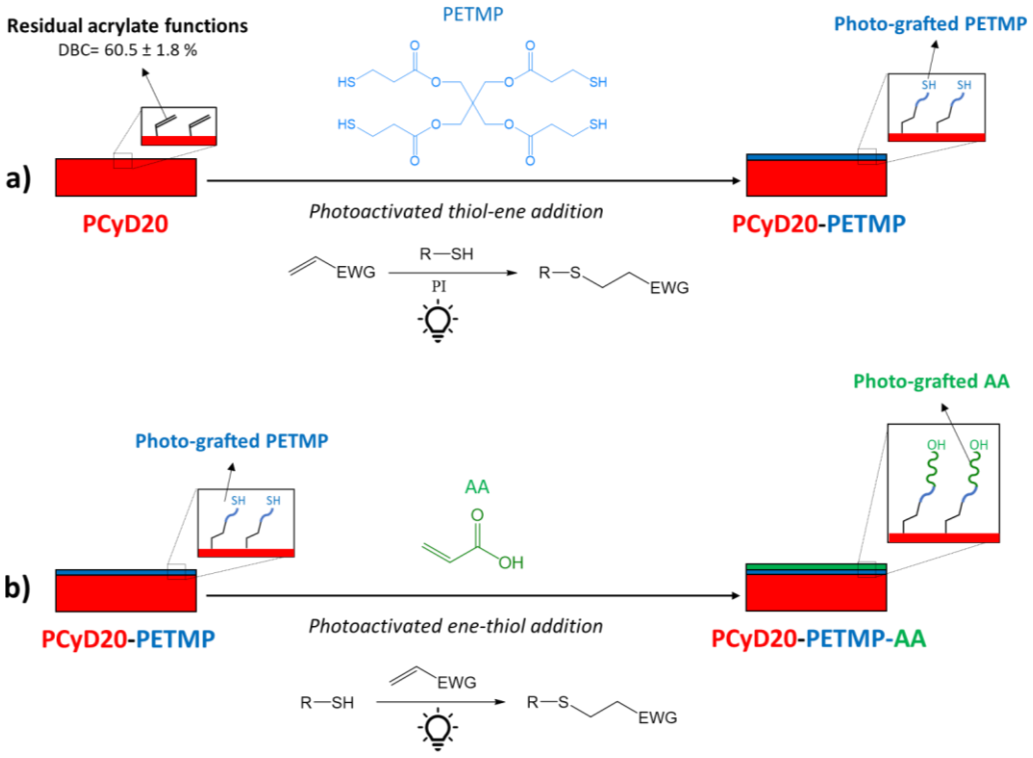

Figure 4.5. Schematic representation of the surface-grafting of PETMP onto PCyD20 (a) followed by the surface initiated photopolymerization of AA from the thiolated PCyD20-PETMP interface (b).

The successful grafting of PETMP onto PCyD20 was confirmed by ATR-spectroscopy. The ATR spectrum of PCyD20 after the functionalization, named PCyD20-PETMP, is shown in **Figure 4.6**. The spectra of PCyD20 and PETMP are reported as reference.

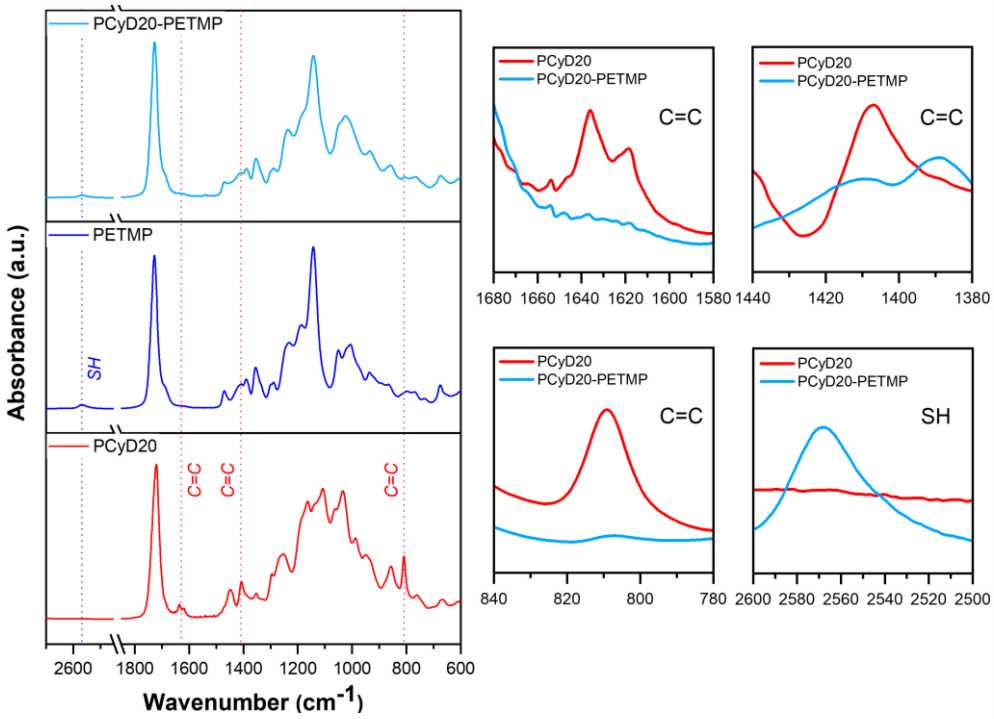

Figure 4.6. ATR spectra of PCyD20, PETMP and PCyD20 after the functionalization (PCyD20-PETMP) and detailed view of the absorption ranges corresponding to C=C vibrations before and after the thiol-ene reaction.

The ATR-spectrum of PCyD20-PETMP revealed the total conversion of residual C=C bonds into C-S moieties, since the characteristic peaks corresponding to the C=C vibration of the residual acrylate functions of PCyD20 (809, 1410 and 1633 cm^{-1}) disappeared after the thiol-ene reaction (see detailed views of the C=C stretching regions given in Figure 4.6). Moreover, the peak at around 2560 cm^{-1}, attributed to the stretching vibration of free -SH,[238] confirmed the presence of pendant -SH not involved in the generation of C-S bonds, as expected due to the choice of the tetrafunctional PETMP as functionalizing agent.

As discussed above, these free thiols were then exploited in another Michael-reaction, to activate the photopolymerization of AA brushes from the PCyD20-PETMP interface. The effectiveness of the new thiol-ene reaction was confirmed

since the characteristic peak corresponding to the vibration of the C=C bonds of the acrylate functions of AA disappeared from the ATR spectrum of the interface after the photografting (named PCyD20-PETMP-AA, see **Figure 4.7a**), as well as the signal of the residual -SH. Moreover, the new broad band centered at around 3000 cm^{-1} evidenced the presence of pendant -OH groups after the functionalization. This further proved the grafting of AA chains.

Finally, wettability measurements confirmed the increased hydrophilicity of the surface since the water contact angle decrease from 61° to 32° (Figure 4.7b) after the grafting of the AA brushes.

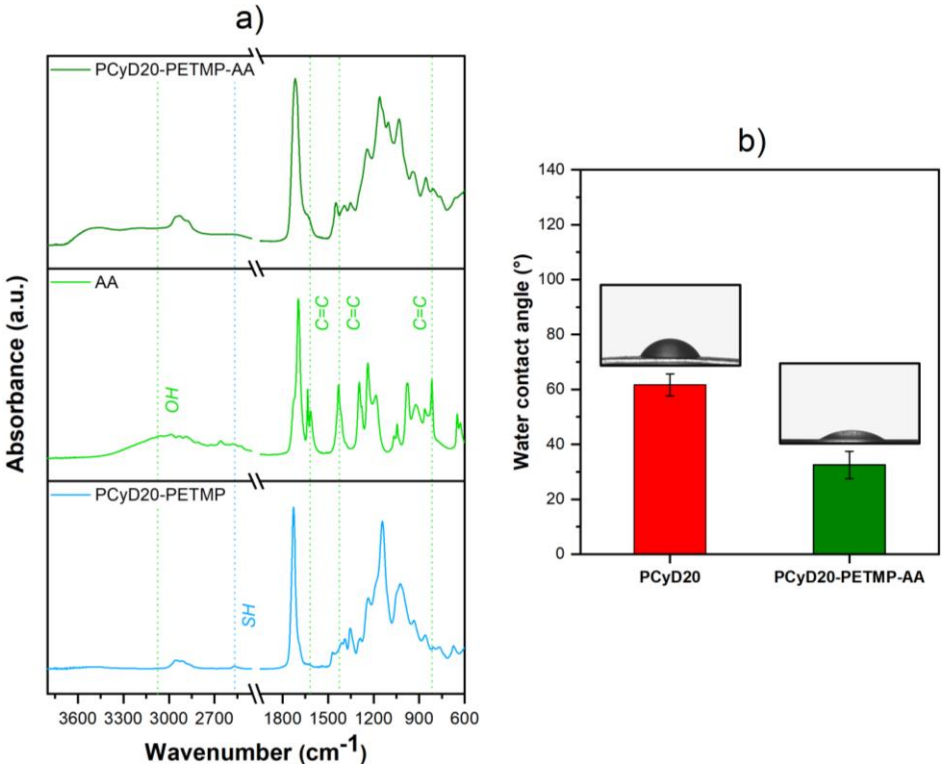

Figure 4.7. a) ATR spectra of PCyD20-PETMP, AA and PCyD20-PETMP-AA and b) water contact angles on the surface of the printed sample before (PCyD20) and after the grafting of AA brushes (PCyD20-PETMP-AA).

4.3.2 Post-printing surface patterning with silver nanoparticles

The thiolated interface generated onto PCyD20 (see Figure 4.5a) was further exploited as active substrate for the anchoring of silver nanoparticles (AgNPs). Indeed, as reported in the literature, thiols can serve for the immobilization of NPs

generated upon the UV-induced photoreduction of transition-metals.[239–241] Therefore, the pendant -SH sites which were not involved in the generation of the PCyD20-PETMP interface via C-S bonds were subsequently exploited to create S-Ag anchoring sites for the AgNPs generated upon the photoreduction of Ag^+ ions dispersed in a water solution of $AgNO_3$. To do this, the samples previously functionalized with PETMP were immersed in the grafting solution and the photoreduction of Ag^+ to Ag^0 onto the free -SH groups was activated by UV-light using Irgacure 2959 as reducing agent (**Figure 4.8a**). Indeed, it has been demonstrated that the long-lived ketyl radicals (lifetime in the order of ms) generated upon photolysis of this PI (Norrish type I mechanism: see chapter 2, subsection 2.1) are capable to promote the in-situ reduction of transition metals, including Ag.[242–245] Simultaneously, the oxidation of the photogenerated benzoyl radicals leads to the production of benzoic acid which contributes to significantly increase the stability of the generated metal NPs.[245] The UV-induced reduction of metal ions upon photodecomposition of Irgacure 2959 is schematically represented in Figure 4.8b.

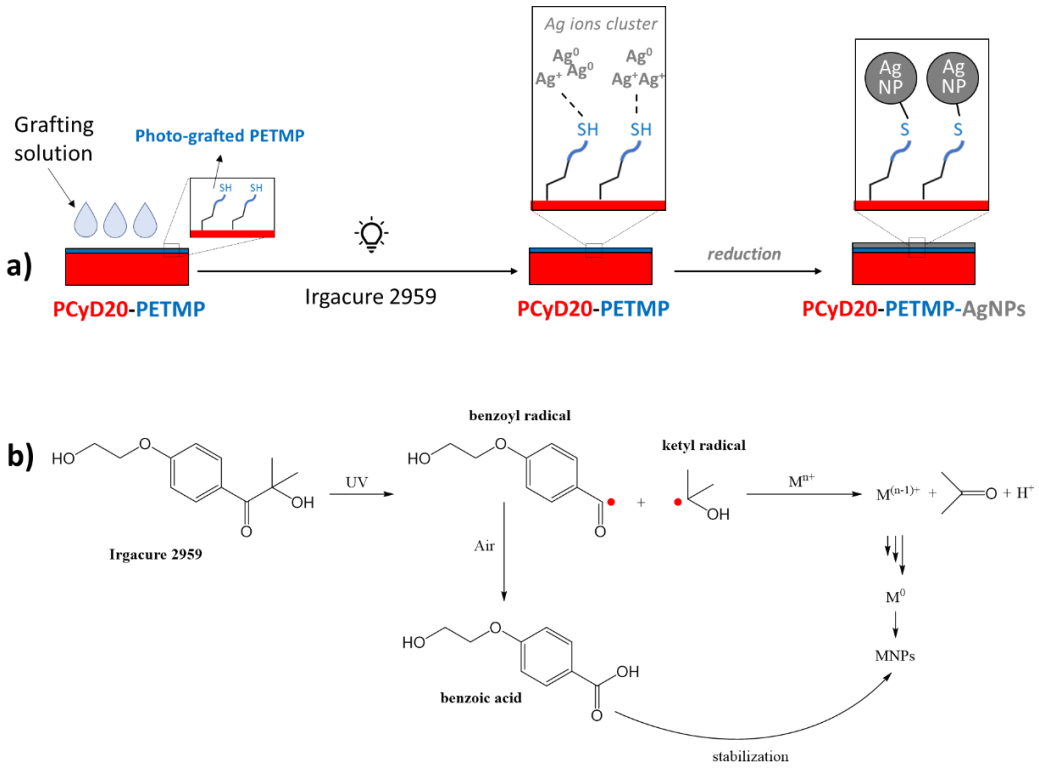

Figure 4.8. a) Schematic representation of the photoreduction of Ag^+ ions on the thiolated PCyD20-PETMP interface and immobilization of the generated AgNPs onto the pendant -

SH groups via S-Ag bridging-bonds; b) photoreduction of transition metal activated and stabilized by the radicals generated upon the photolysis of Irgacure 2959.

The photochemical grafting of AgNPs onto the thiolated PCyD20-PETMP interface was investigated by means of XPS analyses. The survey spectra of PCyD20 before and after the grafting are shown in **Figure 4.9a**. The S2p and Ag3d high resolution spectra of the functionalized surface, along with the results of the peak-fitting procedure, are given in Figure 4.9b-c, respectively.

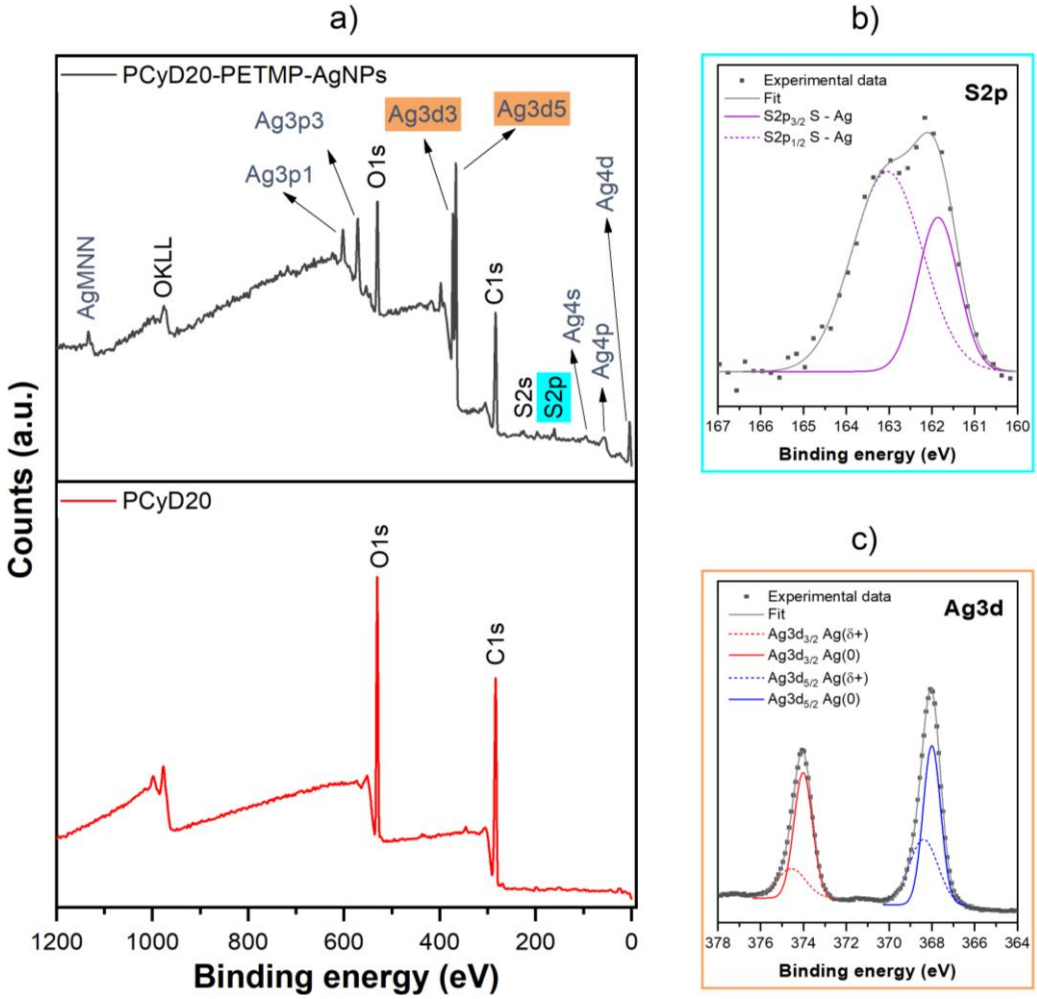

Figure 4.9. a) Survey XPS spectra of the printed sample before (PCyD20) and after the photografting of AgNPs (PCyD20-PETMP-AgNPs); and high resolution S2p (b) and Ag3d (c) spectra showing the experimental data, the best fitting analysis and the peaks contributions obtained from the deconvolution procedure.

The reduction of the Ag^{+} ions to Ag^{0} was confirmed by the appearance in the XPS spectrum of PCyD20 after the photografting (named PCyD20-PETMP-AgNPs) of the typical peaks corresponding to the binding energy (BE) of Ag atoms in their zerovalent state ($Ag3d_{5/2}$ and $Ag3d_{3/2}$ at 368.1 eV and 374.1 eV).[239,240,240,241] Moreover, the fitting analyses of the Ag3d core-level proved that Ag atoms at the surface of the photogenerated NPs are covalently bonded to the active -SH sites of the PCyD20-PETMP interface. Indeed, the deconvolution of the Ag3d spectrum shows two spin-orbit doublets (splitting of about 0.5 eV): the peak contributions with higher BE are conventionally assigned to unperturbed Ag^{0} atoms in the NPs core, while the ones with lower BE can be attributed to positively charged Ag atoms ($Ag\delta^{+}$) coupled with the thiolated surface via S-Ag bridging-bonds.[239]

The fitting-procedure of the S2p spectrum further confirmed the generation of S-Ag anchoring sites. Indeed, the peak-deconvolution revealed a spin-orbit doublet ($S2p_{3/2}$ and $S2p_{1/2}$; splitting of 1.21 eV), whose contribute at 161.85 eV ($S2p_{3/2}$) is conventionally attributed to S atoms chemically bonded to metals.[239,240]

The effective patterning of the surface with AgNPs was further confirmed by FESEM investigations. The micrographs given in **Figure 4.10** clearly show the presence of cluster of AgNPs grafted onto the surface of the thiolated PCyD20-PETMP interface.

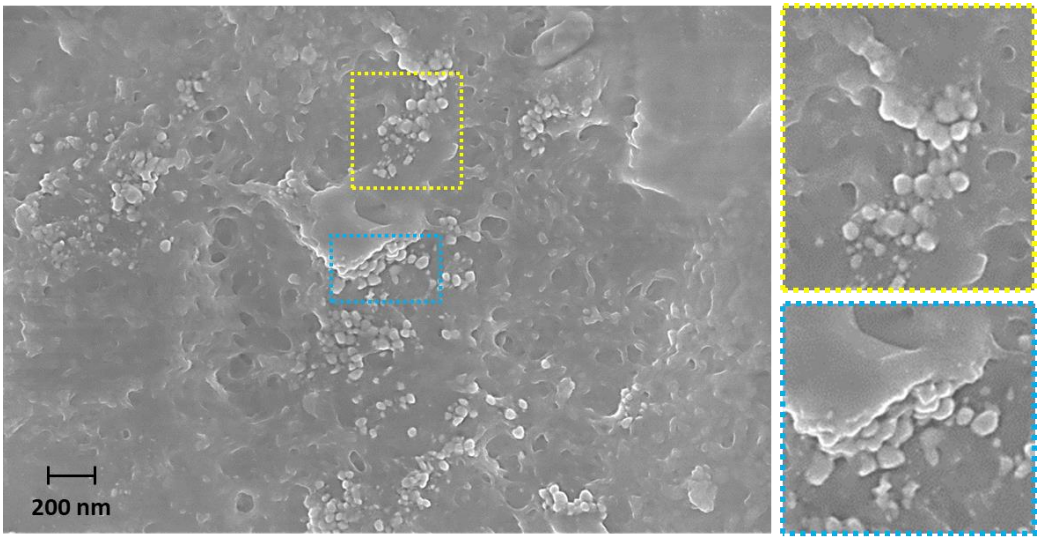

Figure 4.10. Representative FESEM micrographs of cluster of AgNPs grafted onto the surface of the thiolated PCyD20-PETMP interface.

4.4 Conclusions

In this chapter, the incomplete double bond conversion derived from the DLP-printing of multiunsaturated monomers was explored as a potential advantage. Giving the high selectivity towards C=C bonds and the ability to yield regiospecific products under facile conditions, Michael-addition reactions were successfully used to implement special features to PEGDA-AcγCyD printed parts by simply exploiting the unreacted acrylate functionalities located on the surface. Different modification methodologies were followed to tune the wettability of the surface by either grafting hydrophobic polysiloxane brushes via an aza-Michael addition, or by activating the surface-initiated photopolymerization of hydrophilic chains of acrylic acid via two consecutive thiol-ene reactions. The successful functionalizations were confirmed by ATR-spectroscopy and water contact angle measurements. Moreover, the generation of a thiolated interface onto the surface of the printed samples was successfully used to immobilize photogenerated AgNPs, as demonstrated by XPS and FESEM investigations.

In conclusion, the preliminary results here reported proved that the residue of unsaturated functionalities can be successfully used for post-modification purposes aiming to implement special functions to the printed parts without the need to add any specific chemical component in the printable formulation. Moreover, the versatility given by Michael-reactions would allow to explore further strategies for the ease surface modification, especially in those fields where surface properties are critical, such as microfluidic and biomedicine. In this sense, future studies may be focused on the development of smart microfluidic devices with selectively tuned wettability or to the design of components for biomedical applications exploiting the well-known antibacterial properties of surfaces patterned with AgNPs.

5. Multi-photoactive BAPO-cyclodextrin: a *two-in-one* PI and crosslinking agent

5.1 Motivation and outline

As discussed in subsection 2.3.2.1, BAPOs stand out as highly reactive NT1 PIs due to their high reactivity, long-wavelength absorption and fast photobleaching.[246–251] By virtue of such unique properties, functionalized BAPOs have found applications in many fields ranging from surface modifications [141,252–255] and the synthesis of star-shaped polymers;[256] to photopolymerization and 3D-printing in organic and aqueous media,[143,144,257] atom transfer radical polymerization[258] and others.[142,259,260] In this sense, one of the most powerful strategies to prepare carbon-substituted BAPOs is the phospha-Michael addition of bis(mesitoyl)hydrogen phosphane ($HP(COMes)_2$) onto activated olefins in the presence of catalytic amount of amines.[139,140]

Continuing to explore this strategy, a novel bis(acyl)phosphane oxide γ-cyclodextrin derivative (BAPO-γ-CyD) is proposed in this chapter as a multifunctional photoinitiator (MFPI)[261,262] serving simultaneously as photo-crosslinking agent. The target MFPI was prepared by grafting multiple BAPO units on a γ-CyD, which serves as well-defined core molecule. More specifically, the multi-acrylated Ac-γ-CyD presented in chapter 3 was used as the active substrate for the P-addition of $HP(COMes)_2$, given that the acrylate functions behave as efficient Michael acceptor.

The novel MFPI was characterized by means of ^{1}H-, ^{13}C- and ^{31}P-NMR, ATR-FTIR and UV-Vis spectroscopy, as well as by mass spectrometry. Photo-differential scanning calorimetry and photorheology measurements were then carried out to investigate its photoinitiating activity. Moreover, its use for DLP-printing applications was assessed.

Finally, the *two-in-one* photoinitiating and crosslinking efficiency of BAPO-γ-CyD for the conversion of monounsaturated monomers into thermosetting polymers was deeply evaluated to prove its superior performance over molecular PIs. For this purpose, the photopolymerization kinetic of a commercial monofunctional methacrylate oligomer was monitored via photorheology and the properties of the polymers obtained upon irradiation were assessed by means of gel content measurements, swelling tests and amplitude sweep experiments.

Part of the work described in this chapter has been already published and it is available at the reference[263]:
Cosola, A.; Conti, R.; Rana, V. K.; Sangermano, M.; Chiappone, A.; Levalois-Grützmacher, J., Grützmacher H. Synthesis of γ-cyclodextrin substituted bis(acyl)phosphane oxide derivative (BAPO-γ-CyD) serving as multiple photoinitiator and crosslinking agent. *Chem. Commun.* **2020**, 56, 4828, doi:10.1039/d0cc01732a.

5.2 Experimental

5.2.1 Materials and chemicals

γ-Cyclodextrin (γ-CyD) was purchased from ABCR and used as received. Acryloyl chloride, anhydrous n-methyl pyrrolidone (NMP), tetramethylguanidine (TMG), hydrogen chloride in diethyl ether solution (HCl in DEE), hydrogen peroxide (H_2O_2 35%), phenylbis(2,4,6-trimethylbenzoyl)phosphineoxide (registered trade name Omnirad 819 or Irgacure 819), hexanediol diacrylate (HDDA), poly(ethylene glycol) methyl ether methacrylate (PEGMEMA, M_n = 500 g/mol), methyl red (MR), deuterated dimethyl sufoxide (DMSO-d6) and dichloromethane (DCM) were obtained from Sigma Aldrich and used without further purification. Dimethoxyethane (DME) and toluene were degassed and purified using an Innovative Technologies PureSolv System. Bis(mesitoyl)hydrogen phosphane ($HP(COMes)_2$, reported in the text as BAP-H) was kindly provided by the Grützmacher group of ETH Zürich.

5.2.2 Procedures

Synthesis of the bis(acyl)phosphane oxide γ-cyclodextrin derivative (BAPO-γ-CD)

First, acrylated γ-Cyclodextrin (Ac-γ-CD) was prepared following the protocol given in chapter 3 (see subsection 3.2.2). Then, Ac-γ-CD (2 g, 0.81 mmol) and BAP-H (2.93 g, 8.9 mmol) were dissolved in 90 mL of DME using a 250 ml Schlenk flask and TMG (0.11 mL, 0.89 mmol) was added as catalyst. After 1 h

stirring at 300 rpm and 50 °C, DME was removed under reduced pressure. The yellow oily residue was dissolved in 90 mL of toluene. After the addition of HCl (HCl in DEE, 0.45 mL, 0.89 mmol) at RT, the mixture was left to stir for 1 h and then filtered over celite. Subsequently, aq. H_2O_2 (0.84 mL, 9.8 mmol, 35%) was added dropwise in the dark at 0 °C and the mixture was left to stir vigorously at RT for 1 h. Finally, the solvent was removed under reduced pressure yielding the phosphanoxide BAPO-γ-CD as a light-yellow powder. The product was dried for two days under high vacuum and then stored in the dark at 4 °C.

Preparation of the photocurable formulations

Two set of photocurable formulations (a, b) were prepared for different purposes:

a) formulations containing HDDA as diacrylate monomer and either BAPO-γ-CD or Omnirad 819 as PI at different molar concentrations (details in the results section, formulations containing Omnirad 819 used as reference). This set of formulations was used to investigate the photoreactivity of BAPO-γ-CD by means of photo-differential scanning calorimetry (Photo-DSC) and photorheology, and for DLP-printing (MR was added as dye absorber to limit the light diffusion in the resin vat, thus increase the printing resolution)
b) formulations containing PEGMEMA as monofunctional monomer and either BAPO-γ-CD or Omnirad 819 as PI at different concentrations (details in the results section, formulations containing Omnirad 819 used as reference). This set of formulations was used to investigate the crosslinking efficiency of BAPO-γ-CD, that is the ability of such MFPI to behave as crosslinker of a monofunctional monomer for the generation of a thermosetting polymer upon irradiation.

DLP-printing

The photocurable formulations from set a were 3D printed using a UV-MAX X27 DLP printer from ASIGA (layer thickness = 50 μm; light intensity = 32 mW/cm^2 ; exposure time = 3 s/layer; for more information on the printer see subsection 3.2.2). The printed samples were washed in EtOH before being post-cured using a medium-pressure mercury lamp provided by Robot Factory (2 min, 12 mW/cm^2).

UV-curing

Cylindrical samples were prepared by casting the photocurable formulations from set b in a polydimethylsiloxane mold (0.75 cm diameter, 0.5 cm thick) and irradiating 4 min using a Hamamatsu LC8 (8 mW/cm^2) equipped with an optical

fiber. All the samples were then postcured in a medium-pressure mercury lamp provided by Robot Factory (2 min, 12 mW/cm^2) and finally removed from the mold.

5.2.3 Characterization methods

NMR spectroscopy

^{1}H-, ^{13}C- and ^{31}P-NMR spectroscopy were used to confirm the successful phospha-Michael addition of BAPO units onto Ac-γ-CyD. NMR spectra were recorded on a Bruker 500 spectrometer. Chemical shifts δ were measured according to IUPAC and are given in parts per million (ppm) relative to TMS for ^{1}H and ^{13}C and to H_3PO_4 for ^{31}P.

IR spectroscopy

IR spectroscopy was used to further confirm the successful grafting of BAPO units onto Ac-γ-CD. FTIR spectra were recorded by using a Perkin Elmer Spectrum 2000 FTIR spectrometer (Perkin Elmer, Norwalk, CT, USA) equipped with a single reflection attenuated total reflectance (ATR) accessory. 32 scans were recorded for each sample from 4000 to 500 cm^{-1} with a resolution of 4 cm^{-1}. The results were reported in transmittance mode.

Mass spectrometry

Maldi MS was used to estimate the number of BAPO units grafted to Ac-γ-CD. The measurements were carried out by the MS Service of the Laboratory of Organic Chemistry at ETH Zürich.

UV-is spectroscopy

UV-Vis spectroscopy was used to evaluate the absorption of the MFPI BAPO-γ-CD as compared to the one of the molecular PI Omnirad 819. UV-vis spectra were recorded on a UV/vis/NIR lambda-19-spectrometer (range 200 - 600 nm) in 10 mm Quartz cells. The molar extinction coefficients (ε) were calculated using the Beer-Lambert equation (Eq. 5.1):

$$\varepsilon = \frac{A}{cl} \qquad \text{Eq. 5.1}$$

where c is the concentration, l the extinction pathway and A is the absorption measured at 365 nm. Moreover, UV-Vis spectroscopy was used to study the photolysis of BAPO-γ-CD. The MFPI was dissolved in DMSO (c = 0.5 x 10^{-3} mol/L) and irradiated with a Hamamatsu LC8 lamp (60 mW/cm^2). UV-Vis spectra were recorded at different irradiation times.

Photo-DSC

Photo-DSC measurements were carried out to evaluate the photoreactivity of the MFPI BAPO-γ-CD as compared to the one of the molecular PI Omnirad 819. For this purpose, we investigated the photopolymerization of standard diacrylate formulations (set a). The tests were performed at 25 °C under N_2 atmosphere (30 mL/min), using a Mettler Toledo DSC. The light source was provided by a Hamamatsu LC8 lamp (cutoff filter under 400 nm, 0.6 mW/cm^2) equipped with an 8 mm light guide. At the beginning of the measurements, an isothermal period of 120 s was scheduled before the irradiation was activated for 240 s. Subsequently, another isothermal period of 120 s was observed before the second irradiation period of 240 s. The heat flux from the second irradiation period was subtracted from the first one to exclude all thermal effects due to light dissipation. From the resulting DSC curves, t_{onset}, the time to start the polymerization, t_{max}, the time to reach the maximum of heat flux, the double bond conversion (DBC, Eq. 5.2) and the rate of conversion (Rp, Eq. 5.3) were obtained.[144]

$$\mathrm{DBC} = \frac{\Delta H_p \times M_w}{\Delta H_t} \qquad \text{Eq. 5.2}$$

$$\mathrm{Rp}\ (s^{-1}) = \frac{d(DBC)}{dt} \qquad \text{Eq. 5.3}$$

where M_w and ΔH_t are the molecular weight and the theoretical heat of polymerization of the monomer, while ΔH_p is the heat of polymerization measured experimentally ($M_{w,\,HDDA}$ = 226.27 g/mol and $\Delta H_{t,\,HDDA}$ = 172 kJ/mol[264,265]).

Real-time photorheology

Real time photorheology was first used to further investigate the photoreactivity of the MFPI BAPO-γ-CD as compared to the one of the molecular PI Omnirad 819. For this purpose, we tested the same HDDA-based formulations (set a) used for the photo-DSC measurements. Likewise, we investigated also the photopolymerization kinetic of the formulations containing PEGMEMA (set b) to study the efficiency of BAPO-γ-CD as photo-crosslinking agent for monofunctional monomers. The measurements were performed using an Anton PAAR Modular Compact Rheometer (Physica MCR 302) in parallel-plate mode (25 mm diameter, gap between the plates set to 0.2 mm, frequency of 6.2 rad/s and strain amplitude of 1%). The light irradiation was provided by a Hamamatsu LC8 lamp (6 mW/cm^2, light switched on after 60s). Both the delay time and the curing rate (measured as the slope of the G' curves) were extrapolated from the measured data. For more information on the instrumental set up, see chapter 3, subsection 3.2.3.

Gel content measurements

With the aim to evaluate the efficiency of BAPO-γ-CD to serve as crosslinker for the conversion of monofunctional monomers into thermosetting polymers, GC measurements were carried out on the samples obtained by irradiating the photocurable formulations from set b to evaluate the crosslinked fraction of the cured PEGMEMA.[143] The final GC values were calculated gravimetrically by following the same experimental procedure already reported in chapter 3 (see subsection 3.2.3).

Swelling ratio

To further prove the effectiveness of chemical crosslinking while using BAPO-γ-CD as crosslinker for monofunctional monomer, we investigated the water-swelling capability of the samples obtained by irradiating the photocurable formulations from set b. The samples were placed in a deionized water bath at RT. Then, they are removed from the bath at different time interval (until no further mass variation was detected) and weighed after having wiped off the surface droplets with wet paper. The swelling degree and the water content at equilibrium (SW_{eq}% and WC_{eq}%, respectively) were measured gravimetrically using the following equations (Eq. 5.4 and Eq. 5.5, respectively):

$$SW_{eq}\ (\%) = \frac{W_t - W_0}{W_0} \times 100 \qquad \text{Eq. 5.4}$$

$$WC_{eq}\ (\%) = \frac{W_t - W_0}{W_t} \times 100 \qquad \text{Eq. 5.5}$$

where W_t is the weight of the soaked sample and W_0 is the initial weight of the dried sample.

Amplitude sweep measurements

Amplitude sweep measurements were performed to evaluate the viscoelastic properties of the fresh-cured polymers obtained by irradiating the PEGMEMA-based formulations (set b) in the rheometer apparatus. The measurements were performed at RT on flat specimens (thickness 0.2 mm) setting a constant shear frequency (6.2 rad/s) and a strain amplitude range of 0.01-1000%.

5.3 Results and discussion

5.3.1 Synthetic strategy and chemical characterization of BAPO-γ-CyD

BAPO-γ-CyD was prepared by grafting photoactive BAPO units onto a γ-CyD core molecule following a synthetic route developed by the Grützmacher group, which consists on the preparation of carbon-substituted BAPO derivatives via the phospha-Michael addition of bis(acyl)phosphanes onto activated olefines (see subsection 2.3.2.1).[139,140] In this sense, the substitution of the hydroxyl groups of γ-CyD with acrylate functions is crucial to get an activated substrate that can be used as efficient Michael acceptor.

Therefore, BAPO-γ-CyD was obtained following a three-step reaction (**Figure 5.1)**, namely 1) synthesis of the multi-acrylated γ-cyclodextrin derivative Ac-γ-CyD following the acrylation protocol already reported in chapter 3; 2) regiospecific P-Michael addition[266] of BAP-H, which is in equilibrium with its tautomer (MesCO)P=C(OH)Mes,[144,267] onto the terminal carbon center of the vinyl bond of Ac-γ-CyD in the presence of a catalytic amount of TMG and 3) subsequent oxygenation of the so generated phosphane derivative BAP-γ-CyD with aqueous H_2O_2, yielding the photoactive phosphaneoxide BAPO-γ-CyD.

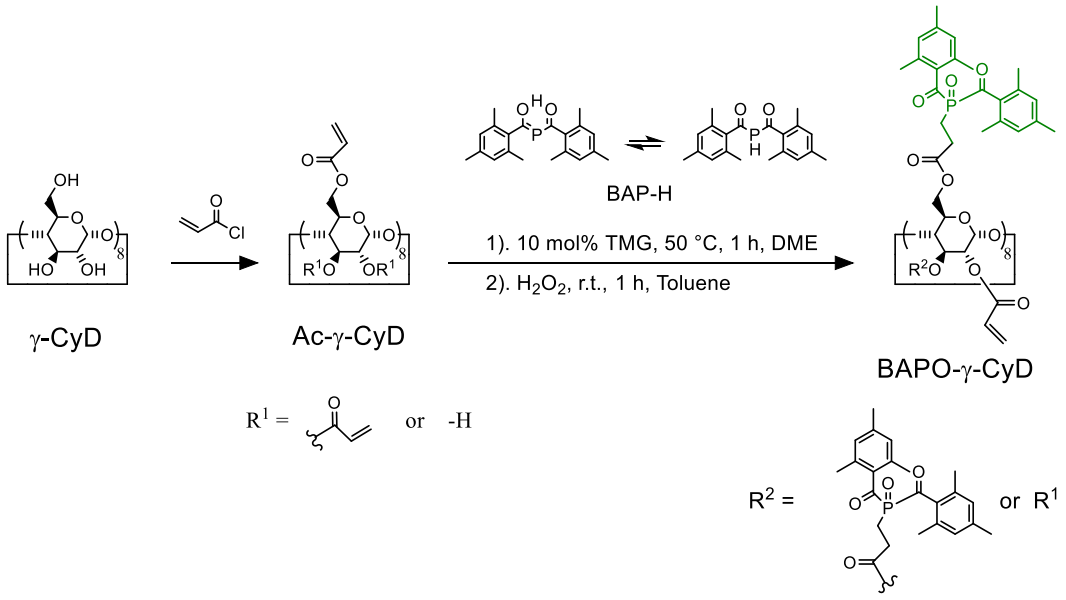

Figure 5.1. Synthetic route of the multifunctional photoinitiator BAPO-γ-CyD.

Preliminary studies were carried out to optimize the P-addition of BAP-H onto Ac-γ-CyD. In particular, the use of TMG as catalyst was preferred over Et_3N since it allows to significantly fasten the reaction from approximately 24h to 1h. Moreover, to limit the generation of undesired by-products arising from the unreacted Michael donor, only 11 equivalents of BAP-H were used. This because a fully substitution of the vinyl groups of Ac-γ-CyD cannot be achieved, even forcing reaction conditions using an excess of BAP-H, likely due to the steric hindrance of the bisacylphosphane oxide photoactive groups (-$PO(COMes)_2$) which are rather bulky (about 410 Å).

The successful grafting of BAPO units onto Ac-γ-CyD was first confirmed by $^{31}P\{^1H\}$-NMR. Two close ^{13}P signals at δ = 25.04 and 25.51 ppm (**Figure 5.2**), suggest that the P-addition of BAP-H occurred on both vinyl acceptor groups located at the primary and secondary sites of Ac-γ-CyD (**Figure 5.3**). This means that the multifunctional γ-cyclodextrin derivative results decorated with BAPO units on both its upper and lower rim.

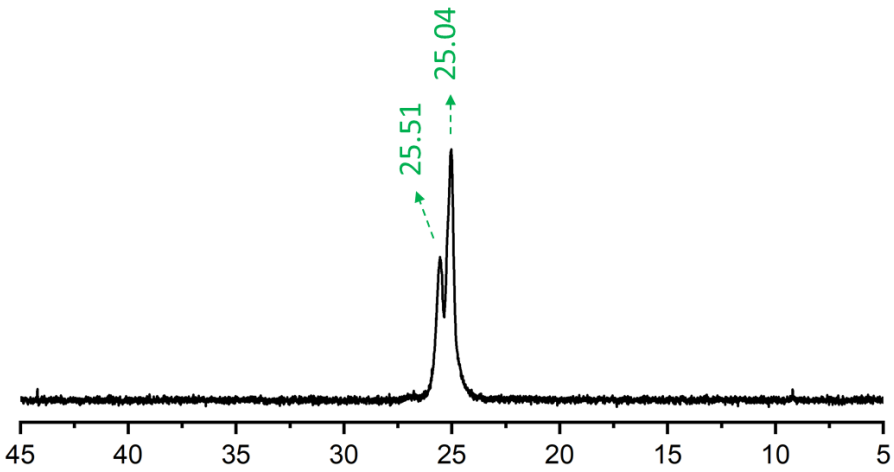

Figure 5.2. $^{13}P\{^1H\}$-NMR of BAPO-γ-CyD.

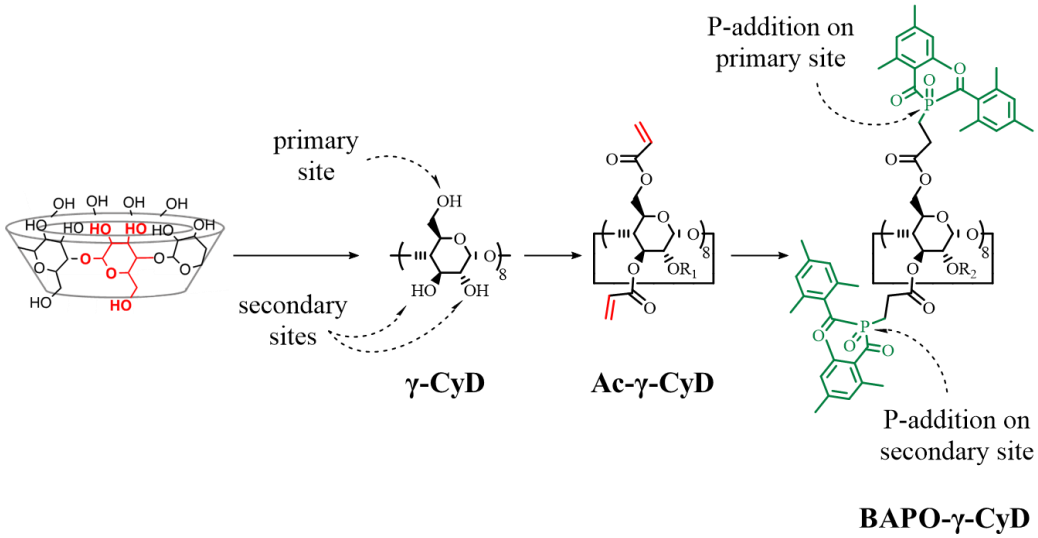

Figure 5.3. Structure of γ-CyD with detailed view of the functionalizable -OH groups and schematic representation of the P-addition of BAP-H on both the vinyl acceptor groups located at the primary and secondary sites of Ac-γ-CyD.

The grafting was further proved by ^{1}H-NMR, ^{13}C{^{1}H}-NMR and ATR-FTIR. Indeed, the characteristic ^{1}H chemical shifts for the methyl and aromatic protons of the mesityl groups (CH_3^{Mes} and H_{ar}^{Mes}) are clearly identified at δ = 2.13–2.23 and 6.87 ppm, respectively (**Figure 5.4a**), as well as the ^{13}C shifts for the carbonyl carbons (CO^{Mes}) at δ = 216.5 ppm, mesityl carbons between 127.60 and 142.50 ppm and methyl carbons (*o*-CH_3^{Mes} and *p*-CH_3^{Mes}) at δ = 19.62 and 20.70 ppm (Figure 5.4b), in good agreement with those of other BAPO derivatives.[139,143,252,255,256,267] Likewise, the typical stretching vibrations of ν(CO^{Mes}), ν(C_{ar}=C_{ar}) and ν(P=O) can be observed in the ATR-FTIR spectrum of BAPO-γ-CyD (**Figure 5.5**) at 1678, 1608 and 1143 cm^{-1} respectively, as well as the ν($oop_{bending}$) at 853 cm^{-1}, the ν($CH_{bending}$) at 735 cm^{-1} and the ν(P-C) at 634 cm^{-1}.

Mass spectrometry was then used to determine the number of photoactive (-PO(COMes)$_2$) groups bound to Ac-γ-CyD. The results revealed that about 10 BAPO units per molecule can be successfully grafted on average ($M_{w,\ BAPO\text{-}\gamma\text{-}CyD}$ = 5800 g/mol). This means that about half of the 21 vinyl groups of Ac-γ-CyD (see subsection 3.3.1) were phosphorylated while the rest remain intact, as evidenced by ^{1}H-NMR (signals from residual vinyl protons at δ = 5.95, 6.18, and 6.32 ppm, see Figure 5.4a), ^{13}C{^{1}H}-NMR (signals from residual vinyl carbons at δ = 128.39 and 132.06 ppm, see Figure 5.4b) and ATR-FTIR (C=C stretching vibrations still observable at 1410 and 809 cm^{-1}, see Figure 5.5).

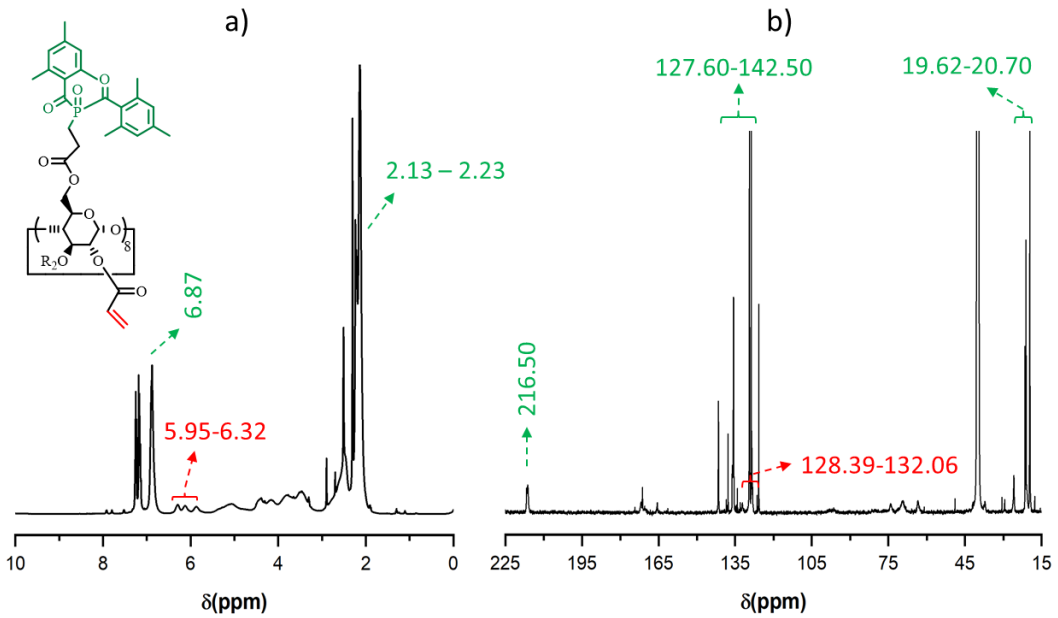

Figure 5.4. a) ^{1}H-NMR and b) ^{13}C{^{1}H}-NMR of BAPO-γ-CyD. The characteristic chemical shifts corresponding to the BAPO units are shown in green, while the signals coming from the residual acrylate functions are given in red.

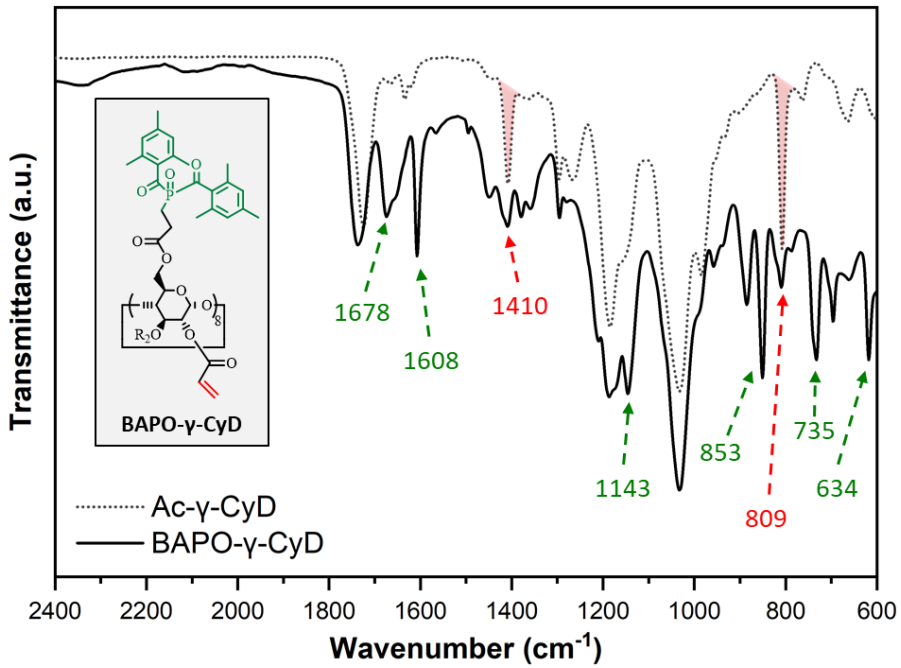

Figure 5.5. ATR-FTIR spectra of BAPO-γ-CyD and Ac-γ-CyD (taken as reference): the main stretching vibrations of the BAPO units are shown in green, while the signals coming from the acrylate functions which were not phosphorylated are given in red.

Remarkably, the simultaneous presence of photoactive -PO(COMes)$_2$ and acrylate groups can make BAPO-γ-CyD an intriguing multifunctional molecule capable of serving as a *two-in-one* photoinitiator and crosslinking agent. This behavior will be further discussed in subsection 5.3.3.

Then, the absorption properties of BAPO-γ-CyD were investigated by means of UV-Vis spectroscopy. The UV-Vis spectrum of our BAPO-derivative (c = 0.1 x 10^{-3} mol L^{-1}) was measured and compared to that of commercial Omnirad 819 taken as reference PI. As can be observed in **Figure 5.6**, BAPO-γ-CyD has a long-wave absorption band above 360 nm corresponding to the n-p* excitation of the CO chromophore similar to that of commercial BAPOs and in line with the typical values already reported for BAPO derivatives.[143,144,255] Notably, BAPO-γ-CyD has a significantly stronger absorption than equimolar amount of the commercial Omnirad 819 (Figure 5.6a). But, increasing ten times the concentration of the latter (c = 1 x 10^{-3} mol L^{-1}), the spectra appear quite similar (Figure 5.6b). Based on these data, the comparison of the molar extinction coefficients (ε) can further prove the effective grafting of about 10 BAPO units, since BAPO-γ-CyD exhibits an ε almost ten times higher than Omnirad 819 (ε = 5484 L mol^{-1} cm^{-1} and 530 L mol^{-1} cm^{-1}, respectively).

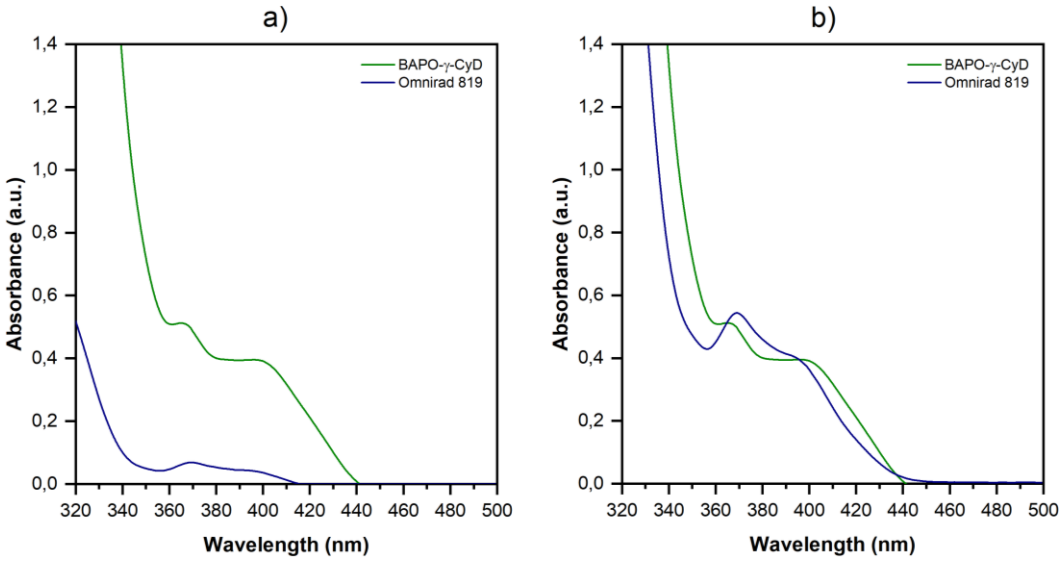

Figure 5.6. Comparison of the UV-Vis spectra of BAPO-γ-CyD and Omnirad 819 in DCM: a) equimolar concentration (c = 0.1 x 10^{-3} mol L^{-1}) and b) molar concentration of Omnirad 819 increased tenfold (c = 1 x 10^{-3} mol L^{-1}) than that of BAPO-γ-CyD.

Furthermore, photolysis experiments revealed the fast photobleaching of BAPO-γ-CyD, as typical for acylphosphine oxides,[4,5,73] since the nπ* transition band absorption above 360 nm decreased gradually with increasing irradiation times with residual absorption of photoproducts limited up to 400 nm (**Figure 5.7**).

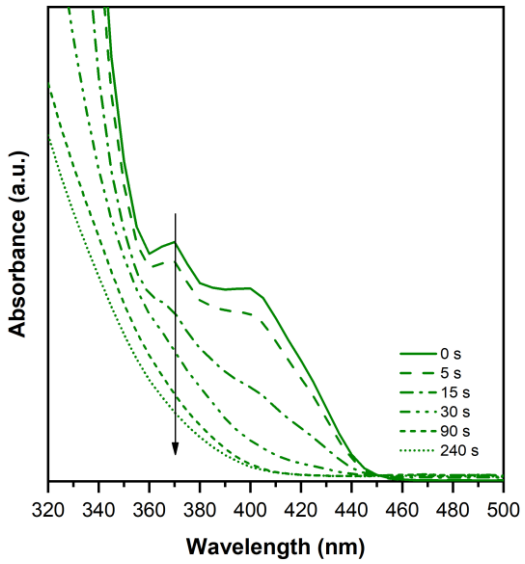

Figure 5.7. UV–vis spectral changes during irradiation of BAPO-γ-CyD in DMSO (0.5 mM) under light irradiation (I = 70 mW/cm^2).

5.3.2 Efficiency of BAPO-γ-CyD as multiple PI for free-radical polymerization

Photo-DSC experiments were carried out to investigate the activity of BAPO-γ-CyD as multiple photoinitiator for free radical polymerization. Indeed, this technique can be used to calculate the double-bond conversion (DBC) of unsaturated monomers, the rate of polymerization (Rp) and other reaction parameters, such as the time at which the maximum heat of polymerization is reached (t_{max}). The measurements were performed using photocurable formulations prepared by dissolving either BAPO-γ-CyD (c = 0.2 mM) or Omnirad 819 (in equimolar amount or tenfold the molar amount of BAPO-γ-CyD) in 1,6 hexanediol diacrylate (HDDA). The photocuring was carried out under N_2 atmosphere to limit oxygen inhibition.

The photo-DSC plots revealed that, when equimolar PI concentrations are compared (**Figure 5.8a-b**), the MFPI BAPO-γ-CyD is much more reactive than the molecular PI Omnirad 819, as indicated by shorter t_{max} = 34 s, and faster Rp_{max} =

0.027 s^{-1} and an overall DBC of HDDA of 67%. Compared to this, the performance of Omnirad 819 is much lower with t_{max} = 120 s, Rp_{max} = 0.007 s^{-1} and a DBC below 50%. Thereafter, under the assumption that BAPO-γ-CyD contains ten BAPO units on average (see section 5.3.1), we performed new measurements adjusting the concentration of Omnirad 819 (i.e. tenfold the molar amount of BAPO-γ-CyD) so that the formulations contained equimolar amounts of photoactive groups (i.e. equal number of BAPO units). The photo-DSC curves shown in Figure 5.8c-d revealed that, under these new conditions, the two PI have an almost equal activity (t_{max} = 31 s, $Rp_{,max}$ = 0.029 s^{-1} and DBC = 65%).

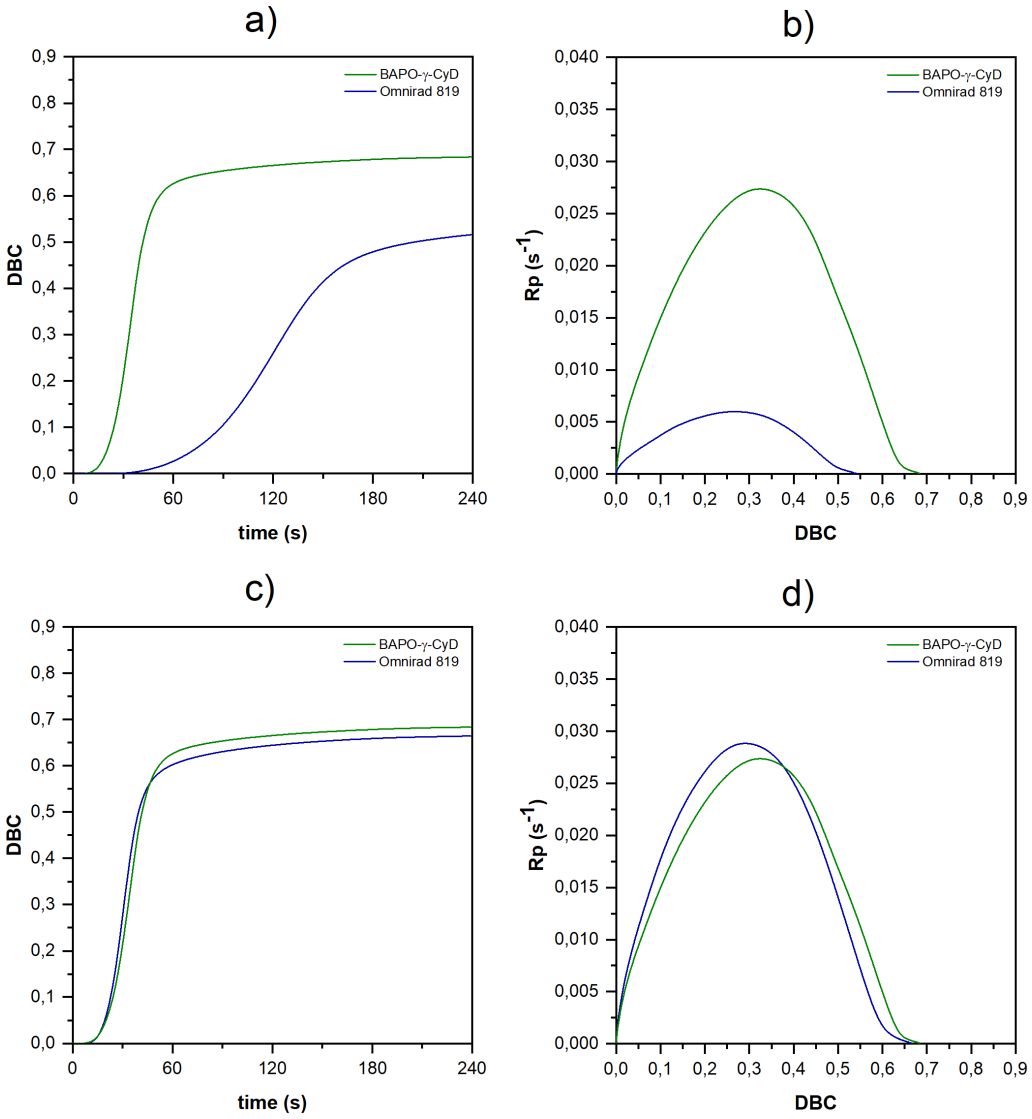

Figure 5.8. Double bond conversion (DBC) and conversion rate (Rp) resulting from the investigation of the photopolymerization of HDDA using either a) equimolar PI

concentration or b) comparing equal amount of radically cleavable groups using Omnirad 819 in ten times higher concentration than BAPO-γ-CyD.

Real time photorheology measurements were carried out to further investigate the photopolymerization kinetic of the same abovementioned formulations. The results are in good agreement with photo-DSC data. Indeed, when comparing the kinetic of formulations that contain equimolar PI concentrations (**Figure 5.9a**), longer irradiation times are required to reach the onset of crosslinking when using the commercial Omnirad 819 (t_d > 90 s) and the photopolymerization proceeds significantly slower ($\Delta G'/\Delta t < 0.06$ kPa s^{-1}). But, employing PI concentrations with equimolar amounts of radically cleavable groups (Figure 5.9b), almost identical delay times were observed ($t_{d,\ BAPO\text{-}\gamma\text{-}CyD} = 8.75 \pm 0.5$ s and $t_{d,\ Omnirad\ 819} = 7.50 \pm 0.6$ s). Likewise, the slopes of the curves suggest comparable curing rates ($\Delta G'/\Delta t >$ 24 kPa s^{-1} in both cases).

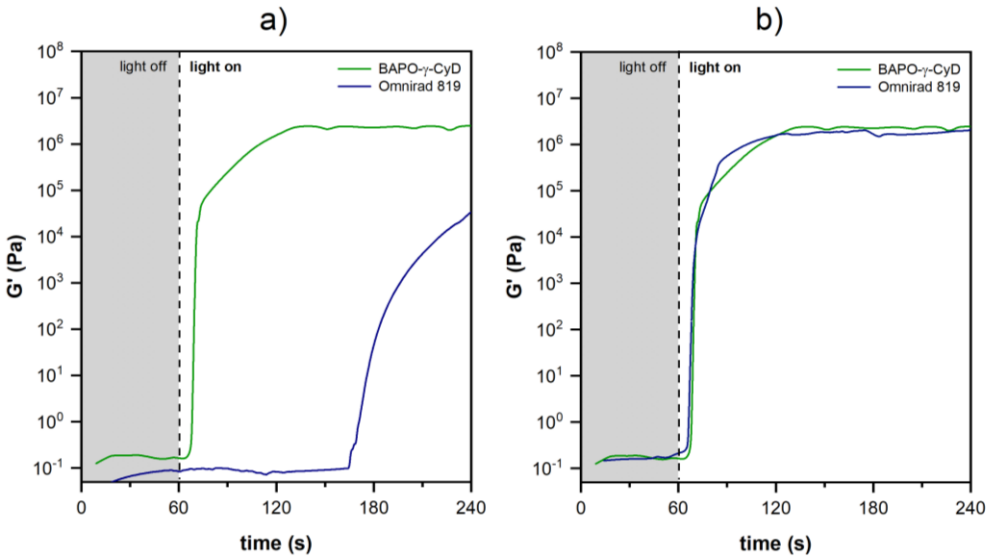

Figure 5.9. Photorheology curves resulting from the investigation of the photopolymerization of HDDA using either a) equimolar PI concentration or b) comparing equal amount of radically cleavable groups using Omnirad 819 in ten times higher concentration than BAPO-γ-CyD.

Therefore, both photo-DSC and photorheology data proved that BAPO-γ-CyD can be used as efficient NT1 PI even at much lower molar concentrations than the conventional molecular PI without any loss of initiating activity. This feature is of particular interest for those applications wherein PIs with a high-molecular weight

must be used to guarantee low migration in the formulation without loss of photoactivity.

Finally, the formulation prepared with BAPO-γ-CyD (0.2 mM in HDDA) was tested on a DLP-printer. Methyl red was added (0.01 wt%) as a light absorber to limit light diffusion phenomena in the resin vat, thus increasing the printing resolution. Highly complex lattice structures were successfully printed (**Figure 5.10a**) with an outstanding definition on both xy plane and z direction, as confirmed by 3D scanning analysis which revealed an average deviation from the original CAD models of about ± 60 μm (see the results of the 3D inspection of the printed part iv, given in Figure 5.10b). This proved that BAPO-γ-CyD can be used at very low molar concentration for DLP-printing applications.

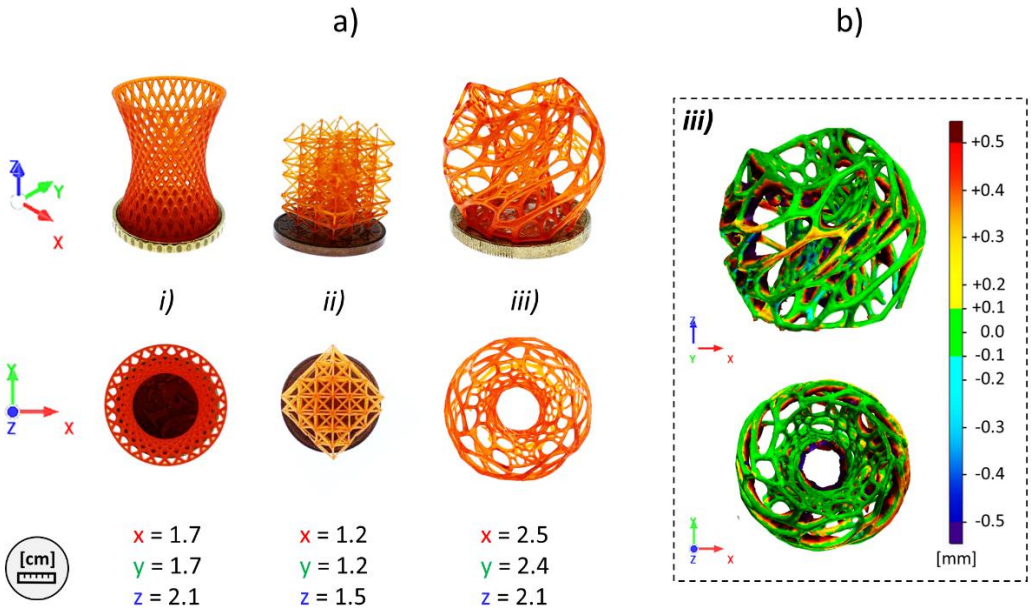

Figure 5.10. a) Photograph of several DLP-printed lattice structures with corresponding dimensions and b) results of the 3D inspection of structure iii.

5.3.3 BAPO-γ-CyD as multiple photoinitiator and crosslinking agent

As previously stated, BAPO-γ-CyD should serve simultaneously as multiple PI and crosslinking agent exploiting both the photoactive BAPO units and the acrylate functions which remain unsubstituted after the P-addition of the Michael donor BAP-H on the vinyl bonds of Ac-γ-CyD (see subsection 5.3.1). This intriguing

behavior was assessed by evaluating the photopolymerization of a commercial monounsaturated monomer in the presence of either the MFPI BAPO-γ-CyD or the molecular PI Omnirad 819, used once again as reference. Four different formulations were prepared by dissolving either Omnirad 819 (2 mM, formulation F1) or BAPO-γ-CyD (0.2 - 2 - 20 mM, formulations F2, F3 and F4, respectively) in poly(ethylene glycol) methyl ether methacrylate (PEGMEMA) and their photopolymerization was monitored via photo-rheology.

The photorheology plots (**Figure 5.11)** show that shorter delay times (t_d < 40 s) and faster kinetics were obtained when using BAPO-γ-CyD as PI. Moreover, polymers with higher G' are obtained upon curing, suggesting the generation of covalently cross-linked networks. Notably, increasing the content of BAPO-γ-CyD in the formulations results in faster photopolymerization kinetic and higher G' values. These results suggest that BAPO-γ-CyD has not only a positive effect on the kinetics, but it also affects the final mechanical properties of the cured polymers leading to a higher crosslinking density.

On the contrary, when using Omnirad 819 as PI, the variation of G' after long exposure times (t_d > 90 s) reflects the generation of a viscous and sticky paste which stems from the increase of the molecular weight of the growing thermoplastic polymer. This is typical for linear polymerization processes of a monofunctional monomer.[143]

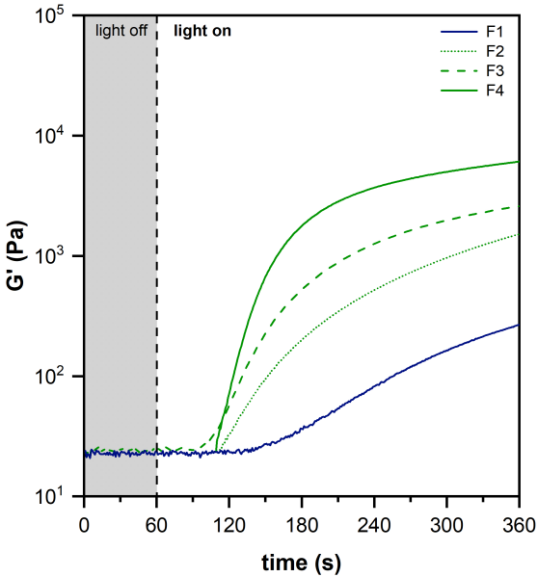

Figure 5.11. Photorheology curves of formulations F1, F2, F3 and F4 prepared by dissolving either Omnirad 819 (2 mM, formulation F1) or BAPO-γ-CyD (0.2 - 2 - 20 mM, formulations F2, F3 and F4, respectively) in PEGMEMA.

Gel content measurements were performed to confirm that the monofunctional PEGMEMA can be converted into a stable thermoset just when using BAPO-γ-CyD. For this purpose, small cylindrical samples (P1, P2, P3 and P4) were first prepared by irradiating the abovementioned formulations (F1, F2, F3 and F4, respectively) and then immersed in water to separate the soluble (not crosslinked) and insoluble (crosslinked) fractions of the polymeric materials obtained upon photocuring. Note that self-standing and mechanically stable samples were obtained just from F2, F3 and F4 (BAPO-γ-CyD used as PI), while the irradiation of F1 (Omnirad 819 as PI) leads to the generation of a viscous paste, as previously reported.

The results of the water extraction experiments are shown in **Figure 5.12**. As expected, the sticky polymer paste (P1, Omnirad 819 used as PI) rapidly dissolves when immersed in water indicating the absence of crosslinking (GC = 0) and the generation of a water-soluble thermoplastic polymer upon irradiation.

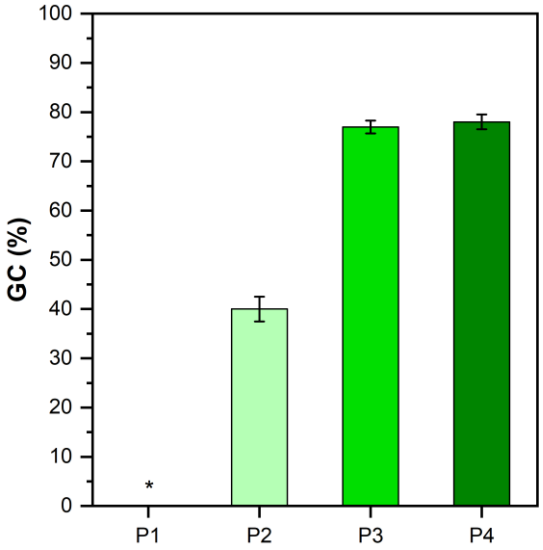

Figure 5.12. Gel content values obtained from the water-extraction experiments performed on the polymeric samples P1, P2, P3 and P4 obtained upon photopolymerization of F1, F2, F3 and F4 (*P1 rapidly dissolves when immersed in water indicating the generation of a water-soluble thermoplastic polymer upon light irradiation).

On the contrary, the ever-higher gel content values obtained for P2, P3 and P4 (GC up to 78%) confirmed that the multifunctional BAPO-γ-CyD serves efficiently both as PI and crosslinking agent for the generation of thermosets in which the polymer chains of PEGMEMA can be crosslinked either via the phosphorylated γ-

CyD units generated under photolysis (γCyD-PO•) or via the residual acrylate functions.

Instead, the water-soluble fractions of P2, P3 and P4 (non-crosslinked polymer) are assumed to be the homopolymers of PEGMEMA generated by free mesityl radicals (MesCO•) (see **Figure 5.13**).[143,255]

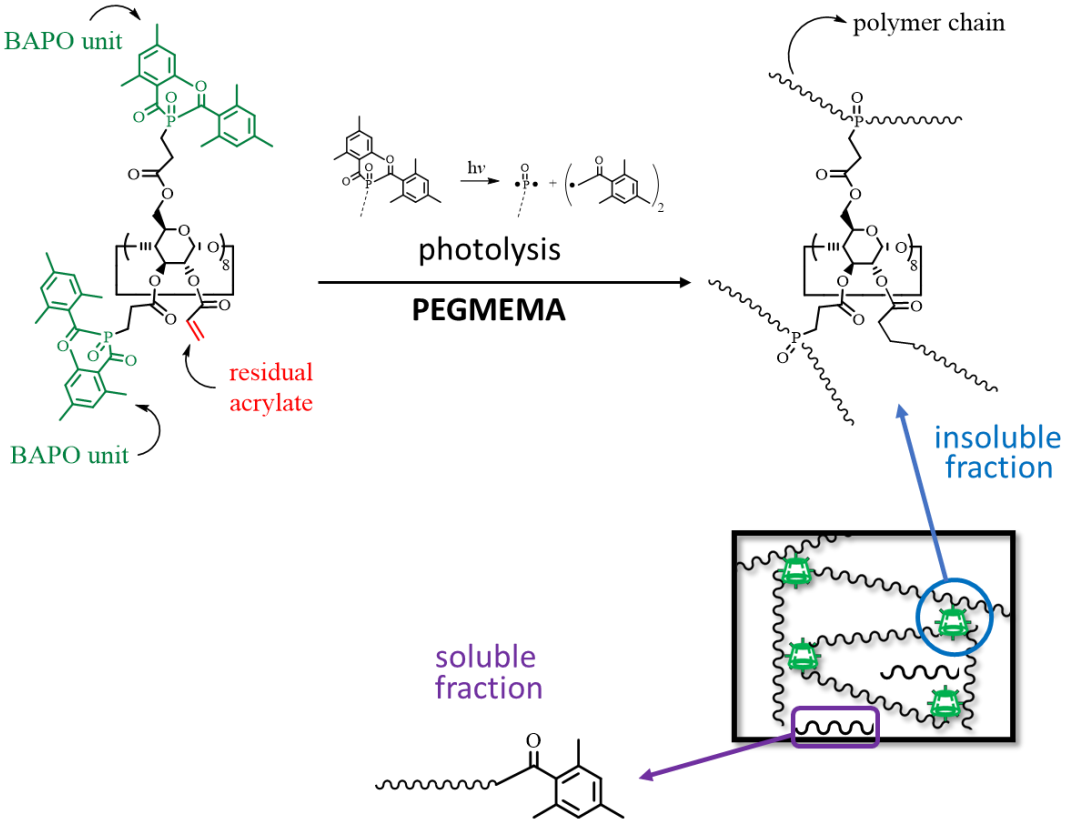

Figure 5.13. a) Chemical structure of BAPO-γ-CyD with detailed view of the BAPO units and residual acrylates functions; b) generation of the PO• and MesCO• radicals after the photolysis of a BAPO units and c) schematic representation of the crosslinked and not-crosslinked fractions of the polymer obtained after irradiation of the monofunctional monomer PEGMEMA in the presence of BAPO-γ-CyD as PI and crosslinking agent.

Once confirmed the effectiveness of chemical crosslinking when using BAPO-γ-CyD as photoinitiator and crosslinker, hence proving the superior performance of this MFPI over the standard molecular PIs, a last set of water absorption measurements were performed on the samples P2, P3 and P4.

The experiments revealed that all the cured polymers extensively absorb water (**Figure 5.14a**) reaching high swelling degree and water content at equilibrium (SW_{eq} and WC_{eq} up to 900% and 90%, respectively).

The high swelling degrees can be ascribed to the flexible nature of the network generated upon irradiation. Indeed, since a monofunctional monomer was used without adding any crosslinker except for the MFPI BAPO-γ-CyD, the polymer chains have enough mobility for extensive expansion in water. Remarkably, both SW_{eq} and WC_{eq} gradually decrease with increasing BAPO-γ-CyD content in the precursor formulations (see Figure 5.14b). This further confirmed the assumption that a higher concentration of BAPO-γ-CyD leads to a higher density of crosslinking, which in turns entails more stable and stronger network less prone to swell when immersed in water.

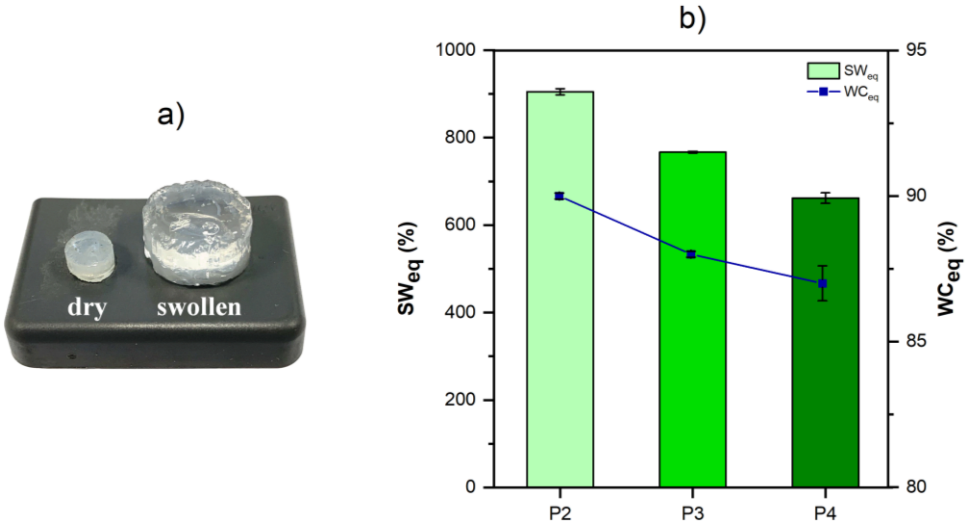

Figure 5.14. a) Photograph of a sample obtained from the photopolymerization of PEGMEMA in the presence of BAPO-γ-CyD as PI and crosslinking agent, before and after swelling in water at RT; b) SW_{eq} and WC_{eq} values obtained from the water absorption experiments performed on the samples P2, P3 and P4.

Amplitude sweep measurements carried out on fresh-photocured samples definitely proved that BAPO-γ-CyD influences the mechanical properties of the cured thermosets. Indeed, besides showing that all the samples (i.e. P2, P3 and P4) can stand strain amplitudes higher than 100% before breaking, the results revealed an increase of the storage modulus (G') from 1.8 kPa to 6.7 kPa, which is in good agreement with the generation of more densely crosslinked materials with increasing BAPO-γ-CyD contents (**Figure 5.15**).

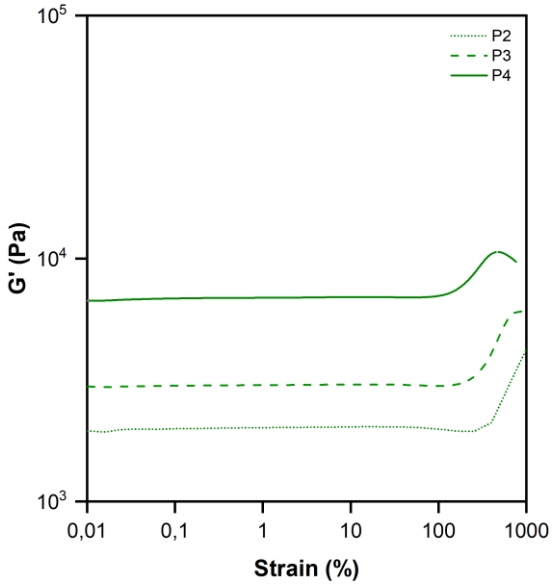

Figure 5.15. Amplitude sweep measurements performed on fresh-photocured samples P2, P3 and P4.

5.4 Conclusions

In this chapter, γ-cyclodextrins were used as building blocks for the synthesis of a well-defined multifunctional photoinitiator. Indeed, the versatility of this oligosaccharide allowed to get the target molecule BAPO-γ-CyD via a hydroxyl group substitution followed by a regiospecific phospha-Michael addition and a final oxidation.

BAPO-γ-CyD behaves as highly efficient NT1 radical photoinitiator, as confirmed by the in-depth investigation of the photopolymerization kinetic of a commercial diacrylate monomer and can be successfully used for DLP-printing applications. The superior performance of this novel MFPI over the conventional molecular PIs was demonstrated, since BAPO-γ-CyD can be simultaneously used photo-crosslinking agent to convert monounsaturated monomers into self-standing thermosets without the need of any additional crosslinkers. Moreover, it was shown that the properties of the network obtained upon irradiation can be tailored by varying the concentration of BAPO-γ-CyD in the precursor formulation. This confirmed the effect of BAPO-γ-CyD on the crosslinking density of the cured polymers.

In conclusion, the results provided in this work proved the possibility to prepare a MFPI with a defined number of photoactive groups by exploiting the strategy of grafting BAPO units on a core molecule having a well-defined structure. This route could be followed in the future to prepare a new set of multifunctional photoinitiators. Moreover, the results of a comparative analysis with a molecular BAPO revealed that BAPO-γ-CyD can be used at much lower molar concentrations without any loss of photo-initiating activity. This feature might be very useful for those applications wherein PIs with a high-molecular weight must be used to assure low migration of the radicals in the formulation without losing efficiency in terms of reactivity.[268] Remarkably, the *two-in-one* photoinitiating and crosslinking efficiency of such type of MFPI could be exploited to develop innovative DLP-printable formulations containing just monofunctional monomers without using any of the conventional crosslinkers. This aspect will be discussed in chapter 6.

6. DLP 4D-printing of thermoresponsive SMPs from monofunctional methacrylates

6.1 Motivation and outline

Stimuli-responsive polymers have spurred increasing attention in biomedicine,[269–271] aerospace,[272,273] automotive,[274] microfluidics,[275,276] and microelectronics;[277,278] and their recent implementation in AM led to the exciting advancement of 4D-printing.[47] Indeed, as already mentioned in subsections 1.1 and 2.3.3.2, the processing of materials capable of transforming when exposed to an enviromental stimulus has given the opportunity to overcome the static nature of the traditional 3D-printed parts.[197,199,279–281] Among all stimuli-responsive polymers, shape memory polymers (SMPs) are of particular interest, due to their ability to fix a temporary shape (TS) and then retrieve their original configuration (i.e. permanent shape, PS) when immersed in water,[42,46] or exposed to light,[282] pH variation,[283] and, heat, which remains the most investigated triggering mechanism.[196,197,284,285]

To display a heat-activated shape memory behavior, polymers must meet specific requirements, namely a molecular architecture consisting of chemical or physical crosslinking net-points, to set a mechanically-stable PS and drive the recovery, and a reversible switching phase governed by a transition temperature (T_{trans}), to program a TS.[279,286–288] Accordingly, thermoresponsive SMPs can be deformed under the application of a stress when heated to above their T_{trans}, which can be a melting temperature (T_m) or a T_g, depending on whether the polymer has a semi-crystalline phase or it is amorphous. The TS is then fixed once cooling below T_{trans} under fixed strain conditions, while the PS is finally recovered via an entropy-driven process when reheating to above $T_{trans.}$

Looking at the fabrication of thermoresponsive SMPs by means of DLP-printing, the typical strategy relies on using formulations containing semi-crystalline polymers, such as poly(caprolactone) (PCL) photocurable derivatives.

Therefore, the TS is stabilized below T_m (more precisely below a crystallization temperature) by the generation of crystalline domains, while the recovery is activated by reheating to above T_m, where the chain mobility is regained once the crystalline phase has been destroyed.[289–292] In this sense, Zarek et al. printed thermoresponsive devices for both flexible electronics [197] and biomedical applications [196], using a photocurable methacrylated-PCL. Likewise, Invernizzi et al. prepared soft actuators with both shape memory and self-healing behavior, combining methacrylated-PCL with ureido-pyrimidinone (UPy) moieties.[202]

But, rather than following this approach, the use of amorphous polymers bearing reversible binding groups (RBGs), has emerged as an alternative strategy to prepare thermoresponsive SMPs.[288] Among all the RBGs, non-convalent hydrogen bonds are particularly appealing due to their thermoreversibility, that is H-bonds between a donor and acceptor group constantly break and reform within a dynamic supramolecular network depending on the temperature. The reassociation of H-bonds at $T < T_{trans}$ allows to generate temporary non-covalent networks serving to stabilize the TS.[293–296] Recently, Li et al. developed a polyimides-based system to prepare smart grippers with excellent shape memory properties.[203]

Within this framework, a novel and versatile photopolymerizable system based on monofunctional methacrylates bearing H-bonding groups has been developed to fabricate thermoresponsive SMPs via DLP-printing. In such a system, 2-hydroxyethyl methacrylate (HEMA) and poly(ethylene glycol) methyl ether methacrylate (PEGMEMA) were used as photopolymerizable monomer and oligomer. Remarkably, multifunctional crosslinkers typically used to get thermosetting polymers upon photopolymerization are not included in the printable formulations since the multifunctional phosphaneoxide derivative BAPO-γ-CyD presented in chapter 5 was used as a *two-in-one* photoinitiator and photocrosslinking agent. Preliminary real-time photorheology investigations were performed before DLP-printing, both to optimize the content of BAPO-γ-CyD and evaluate the photopolymerization kinetics of the final formulations chosen for further DLP-printing investigations. DMTA were carried out to investigate the influence of the composition of the methacrylates-based photocurable system on the thermo-mechanical properties of the cured PHEMA-*co*-PEGMEMA thermosets. Then, the shape memory behavior was investigated by studying the response of the thermosets upon the application of properly designed thermo-mechanical cycles. Likewise, the shape memory properties were also confirmed qualitatively, by simply monitoring the ability of different DLP-printed structures to return to their original shape from a deformed configuration when exposed to a thermal trigger. At last, to demonstrate the potential integration of such SMPs in

the fabrication of a smart device, a prototype of thermoresponsive airflow diverter has been developed.

The work described in this chapter has been already published and it is available at the reference [297]:
Cosola, A.; Sangermano, M.; Terenziani, D.; Conti, R.; Messori, M.; Grützmacher, H.; Pirri, C. F.; Chiappone, A. DLP 3D-printing of shape memory polymers stabilized by thermoreversible hydrogen bonding interactions. *Appl. Mater. Today* **2021**, 23, 101060, doi:10.1016/j.apmt.2021.101060.

6.2 Experimental

6.2.1 Materials and chemicals

2-Hydroxyethyl methacrylate (HEMA, ≥ 99%), poly(ethylene glycol) methyl ether methacrylate (PEGMEMA, M_n = 500 g/mol), poly(ethylene glycol) diacrylate (PEGDA, M_n = 250 g/mol), phenylbis(2,4,6-trimethylbenzoyl)phosphineoxide (Omnirad 819), 2-(4-dimethylaminophenylazo)benzoic acid (Methyl red), brilliant green and EtOH were received from Sigma Aldrich. BAPO-γ-CyD was prepared according to the synthetic route reported in chapter 5.

6.2.2 Procedures

Preparation of the photocurable formulations

Different photocurable formulations were prepared by using HEMA and PEGMEMA as photopolymerizable monomer and oligomer, respectively, and BAPO-γ-CyD as MFPI and photocrosslinking agent. MR dye was added to increase the printing resolutions. The composition of the photocurable system was tuned by varying the HEMA:PEGMEMA weight ratio, aimed to tailor the thermo-mechanical properties of the resulting polymers. The final compositions will be given in the results section (subsection 6.3.1). A second set of formulations was prepared by using PEGDA as reactive oligomer, Omnirad 819 as PI (0.5 phr) and MR as dye (0.025 phr) and used to fabricate some structural components of the smart device (some parts were printed appositely without using the dye), as it will be discussed in subsection 6.3.4.

DLP-printing

Digital 3D-models (including the prototype of smart device), were designed with Solidworks 2019 CAD software, converted in STL file formats and DLP-printed from the different photocurable formulations being investigated using a MAX X27 printer form ASIGA (for more information on the printer, refer to chapter 3,

subsection 3.2.2). The surface of the vat was wetted with silicon oil to avoid the adhesion of the photocured methacrylates. The layer thickness and the light intensity were fixed at 25 μm and 28 mW/cm^2, while the exposure time was optimized for each formulation, based on the kinetic data obtained via preliminary photorheology measurements. Lastly, the printed objects were washed in EtOH and post-cured using a medium-pressure mercury lamp provided by Robot Factory (3 min, 12 mW/cm^2).

6.2.3 Characterization methods

Real-time photorheology

Real-time photorheologies were performed with an Anton PAAR Modular Compact Rheometer Physica MCR 302 (parallel-plate mode, plate diameter 25 mm, gap set to 0.2 mm, frequency of 6.2 rad/s, strain amplitude of 1%, light provided by a Hamamatsu LC8 lamp: 30 mW/cm^2) to evaluate the photopolymerization kinetic of the photocurable formulations. Both the delay time and the curing rate ($\Delta G'/\Delta t$, measured as the slope of the G' curves) were extrapolated from the measured data. For more information on the instrumental set up and procedure, see chapter 3, subsection 3.2.3.

Gel content measurements

Gel content measurements were carried out to evaluate the crosslinked fraction of the printed PHEMA-*co*-PEGMEMA thermosets. The GC values were calculated by following the same experimental procedure already reported in chapter 3, subsection 3.2.3.

DMTA

Thin rectangular samples were prepared by UV-curing and used for the thermo-mechanical characterization. The precursor formulations were casted into silicon molds and irradiated for 5 min at RT with UV light (Hamamatsu LC8 lamp equipped with an 8 mm optical fiber, 130 mW/cm^2). DMTA were carried out using a Tritec 2000 machine (Triton Technology Ltd, London UK, temperature ramp of 3°C/min, frequency of 1 Hz, displacement of 20 μm) to monitor the evolution of E' with temperature. The T_g was taken as the temperature corresponding to the tanδ peak.

IR spectroscopy

ATR-FTIR spectroscopy was used to investigate the H-bonding interactions in the PHEMA-*co*-PEGMEMA thermosets. The measurements were performed on dried

thin films (5 min photocuring with a Dymax ECE 5000-UV lamp), using a Thermo Scientific Nicolet iS50 FTIR spectrometer equipped with a diamond crystal ATR accessory. 64 spectra were collected for each sample, in the range of 4000 – 600 cm^{-1}, with a resolution of 4 cm^{-1}. The spectra were acquired with Omnic software and processed to calculate the second derivative spectra (smoothed with the Savitzky-Golay method) in the regions of the -OH and C=O stretching vibrations (3700 – 3300 and 1700 – 1730 cm^{-1}, respectively), and to identify the specific spectral contributes by means of peak deconvolution and Gaussian fitting.

Shape memory investigation

The shape memory behavior was evaluated with a DMA Q800 (Thermal Analysis Inc.) used in tensile configuration, by monitoring the strain evolution of thin rectangular specimens upon the application of suitably designed thermo-mechanical cycles that involve a programming step followed by a recovery stage. The detailed description of the shape memory cycle is given in the result section (see subsection 6.5.3). The strain fixity ratio (R_f) and the strain recovery ratio (R_r), defined as the ability of the material to hold the strained TS and to recover the PS respectively,[287,288] are calculated as follows:

$$R_f = \frac{\varepsilon_u(N)}{\varepsilon_l(N)} \qquad \text{Eq. 6.1}$$

where ε_l (N) is the strain achieved after cooling at low temperature and ε_u (N) is the strain after unloading for the N^{th} cycle.

$$R_R = \frac{\varepsilon_l(N) - \varepsilon_r(N)}{\varepsilon_l(N) - \varepsilon_r(N-1)} \qquad \text{Eq. 6.2}$$

where ε_r (N) and ε_r (N-1) are the residual strains after the recovery step for two consecutive thermo-mechanical cycles. The parameters R_f and R_r were averaged over three measurements. Furthermore, the recovery rate was calculated as the first derivative of the strain recovery curve.

TGA

TGA were conducted using a Mettler Toledo TGA/SDTA 851e to evaluate the thermal stability of the PHEMA-*co*-PEGMEMA thermosets. The measurements were performed from 25 °C to 700 °C under nitrogen atmosphere (50 mL/min), setting a heating rate of 10 °C/min.

6.3 Results and discussion

6.3.1 Photocurable system: composition, photoreactivity and DLP-printability

As previously mentioned, differently from the rather conventional approach of using semicrystaline polymers suitably modified with photopolymerizable functionalities, the purpose of this work was to develop a novel DLP-printable system for the fabrication of amorphous SMPs stabilized by RBGs.

The chosen molecular system consists of three components: two monofunctional monomers, HEMA and PEGMEMA, as photopolymerizable ingredients to design an amorphous matrix governed by a tailorable T_g, and the phosphaneoxide derivative BAPO-γ-CyD presented in chapter 5 as a *two-in-one* photoinitiator and crosslinker. Indeed, as already discussed (see subsection 5.3.3), this MFPI stands out over molecular PIs by serving simultaneously as photocrosslinking agent to generate thermosets from monofunctional methacrylates without the need of additional crosslinker. Accordingly, branched thermosets are expected to be formed by radical copolymerization of HEMA and PEGMEMA either via the PO-γCyD groups formed during the photolysis of the MFPI or via its residual acrylate functions. Moreover, the presence of side-terminal hydroxyl RBGs on the HEMA chains leads to the generation of multiple H-bonding motifs, which may occur between the same -OH groups, acting as both proton donor and proton acceptor, or via the interaction between proton donating -OH and proton accepting carbonyl groups (C=O). These non-covalent interactions serve to generate additional physical net-points which may ultimately stabilize the shape memory properties of the polymers, as will be discussed later.

A schematic representation of the PHEMA-*co*-PEGMEMA network is given in **Figure 6.1**, with a detailed view of the two types of interactions previously mentioned.

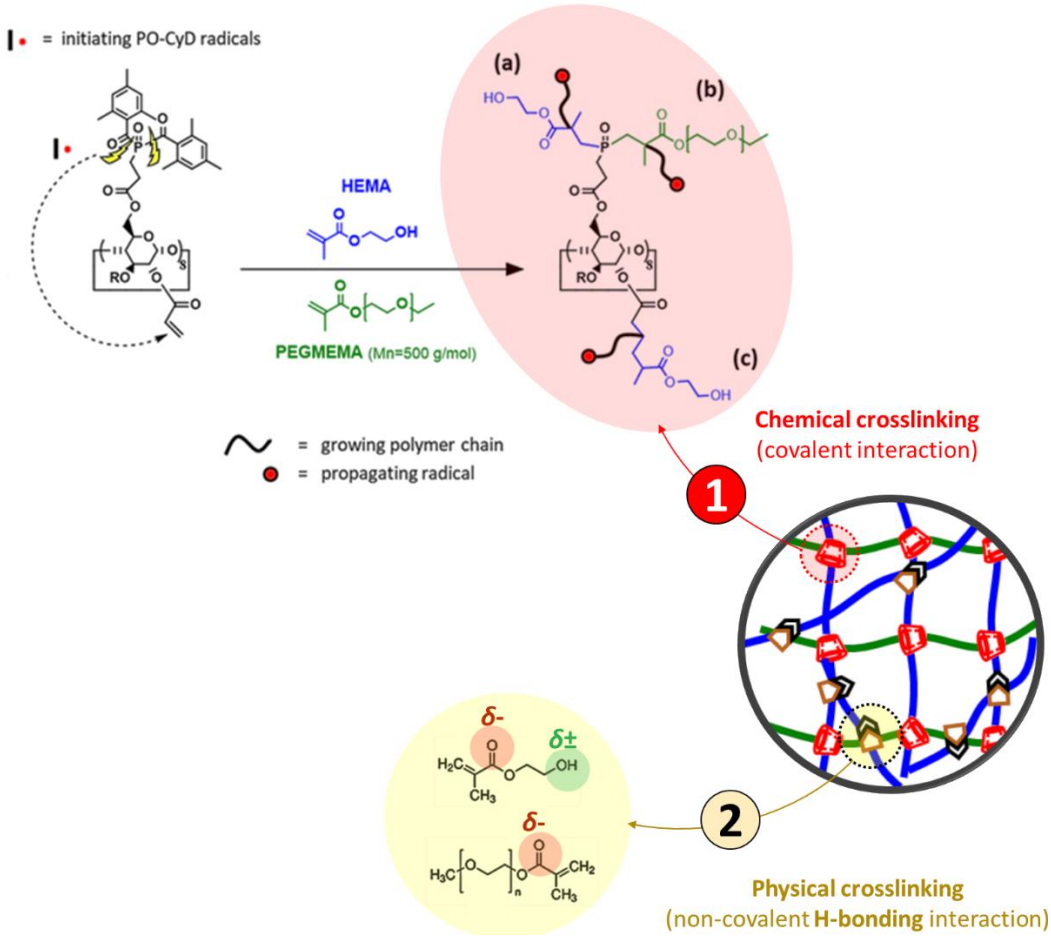

Figure 6.1. Schematic representation of the molecular structure of the PHEMA-*co*-PEGMEMA thermosets investigated in this study. 1) Three possible scenarios for the photoinduced polymerization and chemical crosslinking of HEMA and PEGMEMA either via the multiple photoactive groups of the multifunctional photoinitiator BAPO-γ-CyD: polymerization of a) HEMA or b) PEGMEMA via PO-CyD initiating radicals generated upon photolysis; c) involvement of acrylate functions of the MFPI in PHEMA chain formation. 2) Non-covalent H-bonding interactions occurring between side terminal -OH groups of PHEMA, or between proton donating -OH of PHEMA and the proton accepting (C=O) of both PHEMA and PEGMEMA.

Several photocurable formulations, denoted as HxPy (x and y correspond to the weight concentration of HEMA and PEGMEMA, respectively) were prepared and tested via real-time photorheology prior to DLP-printing. Preliminary studies were carried out to investigate the influence of different amount of BAPO-γ-CyD on the irradiation time required to induce both the crosslinking (t_{ind}) and the gelation (t_{gel}, calculated as the crossover between the loss and the storage moduli curves) of the

methacrylates-based system. In this sense, t_{gel} is particularly relevant in view of DLP-printing, because it gives an indication on how to tune the main printing parameters (i.e. exposure time and layer thickness) to get mechanically-stable thermosets which not solubilize while coming repetitively in contact with the liquid resin during the layer-by-layer fabrication (for more information on gelation, refer to chapter 2, subsections 2.2).

For this purpose, a reference formulation (H50P50) was prepared by keeping the HEMA:PEGMEMA weight ratio at 1:1, while the concentration of the MFPI was varied between 0.1 and 2.0 phr. The photorheology data reveal that both t_{ind} and t_{gel} decrease from 29 to 16 s and from 106 to 35 s, respectively, when the content of the MFPI is increased. However, since the values seems to reach a plateau when using the MFPI above 1.5 phr (**Figure 6.2a**), the concentration of MFPI was set at this value for further investigations. Accordingly, three different formulations were prepared by varying the HEMA:PEGMEMA weight ratio and tested once again via photorheology. The final composition of this last set of formulations is given in **Table 6.1**. The results revealed that both t_{ind} and t_{gel} decrease while the curing rate ($\Delta G'/\Delta t$) increases (as evidenced by the steeper slopes of the G' curves shown in Figure 6.2b) by increasing the concentration of HEMA in the precursor formulation. This is consistent with the higher reactivity of HEMA with respect to PEGMEMA, which was confirmed by monitoring the photopolymerization kinetics of reference formulations prepared with either 100% HEMA or PEGMEMA.

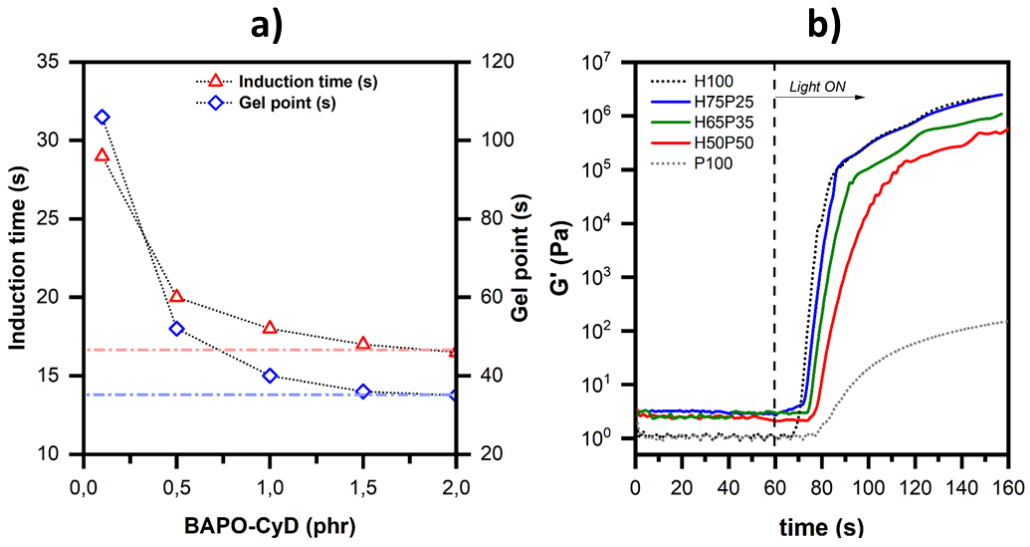

Figure 6.2. a) Evolution of t_{ind} and t_{gel} with increasing content of BAPO-γ-CyD (photopolymerization kinetic of H50P50 taken as reference) and b) photorheology curves of the final photocurable formulations prepared by keeping constant the content of BAPO-

γ-CyD (1.5 phr) and varying the HEMA:PEGMEMA weight ratio (the dotted lines refer to the kinetic of formulations prepared with either 100% HEMA or 100% PEGMEMA and 1.5 phr of BAPO-γ-CyD, H100 and P100, respectively, and reported just for comparison). The light was switched on after 60 s for all the measurements to let the system stabilize before the onset of photocrosslinking.

Table 6.1 Composition and photorheological properties of the final precursor formulations selected for DLP-printing and further investigations (*data of H100 and P100 reported just for comparison).

Formulation code	Composition			Photorheology data		
	HEMA [wt%]	PEGMEMA [wt%]	BAPO-γ-CyD [phr]	t_{ind} [s]	t_{gel} [s]	ΔG'/Δt [kPa/s]
*P100	-	100	1.5	24.0 ± 2.6	84.0 ± 2.0	(0.14 ± 0.03) 10^{-2}
H50P50	50	50	1.5	16.0 ± 1.0	35.0 ± 1.0	0.8 ± 0.1
H65P35	65	35	1.5	13.7 ± 0.6	25.3 ± 2.5	2.7 ± 0.3
H75P25	75	25	1.5	12.3 ± 0.6	21.7 ± 1.2	6.6 ± 0.8
*H100	100	-	1.5	9.7 ± 0.7	17.3 ± 0.6	7.3 ± 0.4

Once evaluated the photopolymerization kinetic, the last set of HxPy formulations given in Table 6.1, i.e. H50P50, H65P35 and H75P25, was tested for DLP-printing. MR dye (0.025 phr) was added to increase the printing resolution. The printing parameters were optimized for each formulation. In this sense, based on the trend observed in both t_{ind}, t_{gel} and curing kinetic when increasing the amount of HEMA in the precursor formulation, the best printing accuracy was achieved by setting the exposure time/layer at 10, 7 and 5 s for H50P50, H65P35 and H75P25 respectively, while keeping the layer thickness at 25 μm. As shown in **Figure 6.3**, different CAD models, ranging from honeycomb-like to hollow cube and net-shaped structures, were successfully reproduced with a good resolution from all the above-mentioned formulations.

Remarkably, the analysis of the insoluble fraction of the printed polymers (denoted from now on as PHEMA-*co*-PEGMEMA x:y, where x and y refer to the weight concentration of HEMA and PEGMEMA in the corresponding precursor formulation HxPy) proved that highly crosslinked thermosets can be successfully obtained using BAPO-γ-CyD as the only crosslinker (GC up to 94%). This means that, when using the chosen photocurable system, none of the multifunctional monomers typically used to prepare DLP-printable formulations is needed. The GC values of the DLP-printed thermosets are shown in **Figure 6.4**.

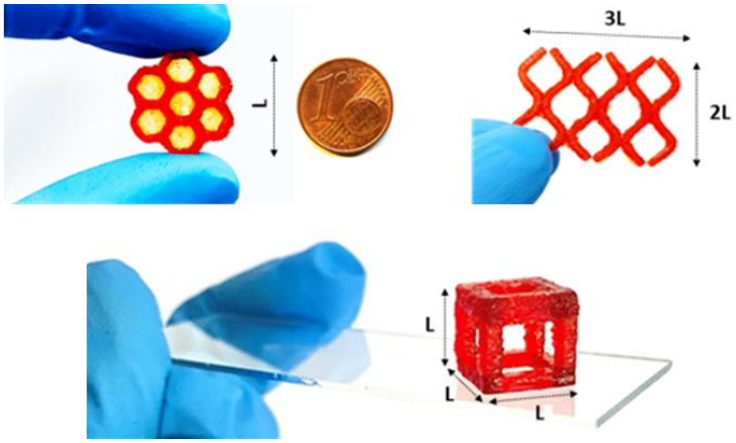

Figure 6.3. Photographs of different structures DLP-printed from the final set of formulations (L=1 cm).

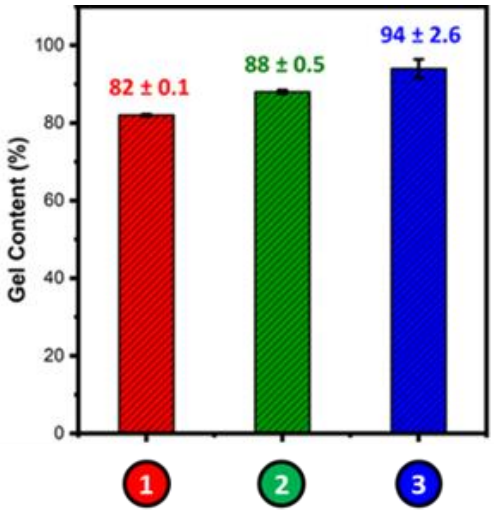

Figure 6.4. GC values of the PHEMA-*co*-PEGMEMA thermosets DLP-printed from 1) H50P50; 2) H65P35 and 3) H75P25.

6.3.2 Thermomechanical properties of the PHEMA-*co*-PEGMEMA thermosets

The influence of the composition of the molecular system on the thermomechanical properties of the thermosets was then evaluated by means of DMTA measurements. The results shown in the following **Figure 6.5** proved that the T_g of the PHEMA-*co*-PEGMEMA polymers increases by increasing the concentration of HEMA in

the precursor formulation, as evidenced by the gradual shift of the tanδ peak from 12°C to 63°C. Moreover, a significant drop of E' was observed between the glassy and rubbery region, resulting in elasticity ratio (i.e. E_g/E_r, being these the glassy and rubbery modulus, respectively) higher than 10^3.

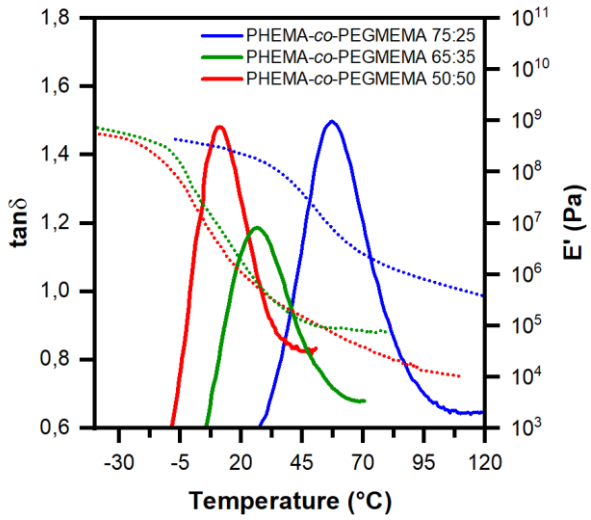

Figure 6.5. Tan(δ) and E′ curves obtained from DMTA measurements for all the PHEMA-*co*-PEGMEMA thermosets being investigated.

The trend observed for the T_g can be ascribed to the generation of thermosets with an ever-higher content of PHEMA chains, whose macromolecular properties imply non-covalent H-bonding interactions (e.g. inter-macromolecular, intra-macromolecular, inter-neighboring-side-chain) that give to the polymer a glassy consistence.[298] Indeed, H-bonding may play an active role in determining the T_g of a polymer, since it has been proven that the T_g increases linearly with the concentration of either strong or weak H-bonds, which behave as temperature-dependent physical crosslinks of a supramolecular network.[299,300] Therefore, it is reasonable to suppose that the thermomechanical properties of the PHEMA-*co*-PEGMEMA thermosets being investigated in this study could be affected by the multiple H-bonding interactions which can occur via the side terminal -OH groups of PHEMA, as already mentioned in subsection 6.3.1 (see Figure 6.1).

The effective generation of H-bond motifs was investigated by means of vibrational spectroscopy, which is one of the most effective strategy to study such a type of non-covalent interaction in amorphous polymers.[301] In the present case, the analysis of the absorption bands corresponding to both the -OH and -C=O

stretching regions (νOH: 3700 – 3000 cm^{-1}; νC=O: 1730 – 1700 cm^{-1}) is an effective tool to evaluate the generation of a H-bonding network via the side terminal -OH groups of PHEMA. In particular, specific H-bonding vibrations can be identified in the aforementioned spectral regions evaluating the second derivative spectra and via Gaussian fitting.[298,302,303] Indeed, three spectral components can be observed upon fitting the OH stretching bands, which correspond to the specific vibrations of O-H···O=C and O-H···O-H aggregates at around 3530 and 3320 cm^{-1}, and to the first overtone of C=O stretching at 3430 cm^{-1}. Likewise, the CO absorption band is deconvoluted into two stretching vibrations, which can be assigned to free C=O and H-bonded C=O groups (at 1730 cm^{-1} and 1703 cm^{-1}, respectively).

Based on that, the H-bonding interactions in the PHEMA-*co*-PEGMEMA polymers are confirmed, since the characteristic bands corresponding to the vibration of both O-H···O=C and O-H···O-H aggregates can be easily identified in all the second derivative spectra and in the spectra obtained after Gaussian fitting (**Figure 6.6**).

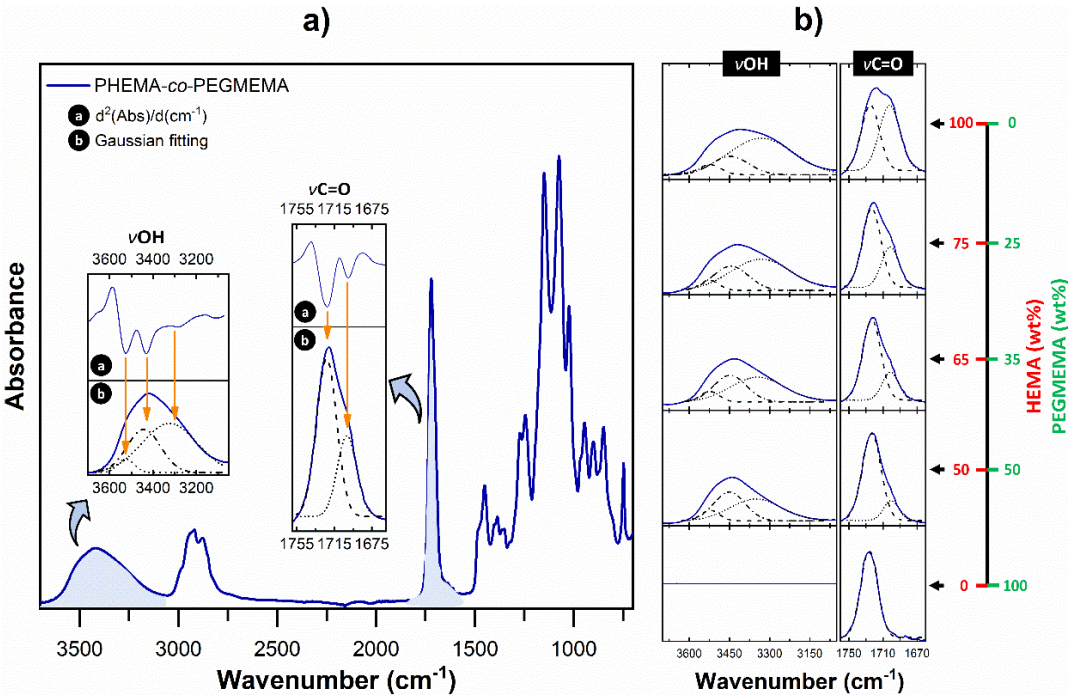

Figure 6.6. a) IR spectrum of a PHEMA-*co*-PEGMEMA thermoset with two insets corresponding to the second derivate spectra and the spectral components resulting from the Gaussian fitting of both the -C=O an -OH stretching regions; b) influence of the composition of the methacrylates-based photocurable system on the spectral components

corresponding to the specific H-bonding vibrations identified via Gaussian fitting (crosslinked polymers prepared from precursor formulations containing 100% of either HEMA or PEGMEMA are used as reference).

Moreover, the fraction of H-bonded C=O increases with increasing content of HEMA within the precursor formulation, as evidenced by the ever-higher intensity of the absorption band of the H-bonded C=O at 1703 cm^{-1}. Likewise, also the intensity of the bands at around 3320 cm^{-1} increases, suggesting an ever-higher density of O-H···O-H aggregates. Note that the latter are considered to be mainly responsible for the suppression of chain mobility in PHEMA and to the generation of a rigid amorphous polymer.[298]

These findings are in good agreement with the trend observed in the DMTA plots, since the higher density of H-bonds with increasing concentration of HEMA in the PHEMA-*co*-PEGMEMA polymers is reflected by ever-higher glass transition temperatures. In other words, this means that the T_g can be tuned by adding PEGMEMA, which serves as flexible spacer to soften the network while reducing the local density of -OH groups available to form H-bonded aggregates.

6.3.3 Thermally triggered shape memory behavior

The significant drop of E' over the T_g region, along with the presence of chemical net-points and additional physical interactions via side terminal RBGs, make these PHEMA-*co*-PEGMEMA thermosets promising thermoresponsive SMP candidates. Indeed, the high elasticity ratio ($E_g/E_r > 10^3$) would allow an acceptable stretchability at $T > T_g$ and a good resistance to deformation at $T < T_g$.[304–306] Likewise the covalent crosslinking generated by using BAPO-γ-CyD should provide dimensional stability, thermal resistance and prevent chain slippage upon deformation at $T > T_g$.[47,280,287] Moreover, the multiple H-bonding interactions can serve to stabilize the TS during the programming stage.[288]

To validate this expectation, the response of the PHEMA-*co*-PEGMEMA upon the application of specifically designed thermo-mechanical cycles was monitored via additional DMA investigations and the shape memory parameters R_f and R_r were calculated based on the quantitative analysis of the strain evolution (see subsection 6.2.2, shape memory). As already mentioned, the thermo-mechanical cycle involves a programming step followed by a recovery stage. First the sample is heated at T_g + 50°C and kept unloaded at this temperature for 5 min before being deformed under a stress of 0.02 MPa for 10 min. Subsequently, the sample is cooled down to T_g - 50°C (- 40 °C/min) under fixed strain conditions to fix the TS. Then,

the load is removed. Finally, the sample, fixed in its TS, is reheated up to T_g + 50°C (+ 40 °C/min) under quasi stress-free conditions (0.2 kPa) to promote the recovery of the PS. Note that, the programming temperatures, i.e. deforming temperature, (T_D) and fixing temperature (T_F) were set at T_g ± 50°C, respectively, for all the PHEMA-*co*-PEGMEMA X:Y samples, to maximize the elasticity ratio in accordance to the drop of E' observed in the DMTA curves (see Figure 6.5). In this sense, setting the heating stages (both deformation and recovery) at T_g + 50°C never bothers the thermal stability of the PHEMA-*co*-PEGMEMA thermosets, since no degradation was observed up to about 250°C according to preliminary TGA measurements.

The 3D-plot given in **Figure 6.7a** shows the stress/strain evolution during the shape memory cycle of a PHEMA-*co*-PEGMEMA 75:25 specimen: (A) heating of the PS up to T_D; (A → B) deforming stage; (B → C) fixing of the TS; (C → D) load removal and (D → A) recovery of the PS. The thermomechanical cycling resulted in R_f and R_r ratios near to 99%, in good agreement with the values already reported in the literature for thermoresponsive SMPs prepared via DLP-printing from different polymeric systems.[202,203] These results confirmed that the PHEMA-*co*-PEGMEMA 75:25 thermosets can both efficiently hold a temporary strained configuration and memorize their original shape, being able to recover it from mechanical deformation. In this sense, the in-depth analysis of the recovery stage (strain recovery and recovery rate curves reported in Figure 6.7b**)** proved that the sample starts to regain its PS when heated to above its T_g, as expected for amorphous SMPs.

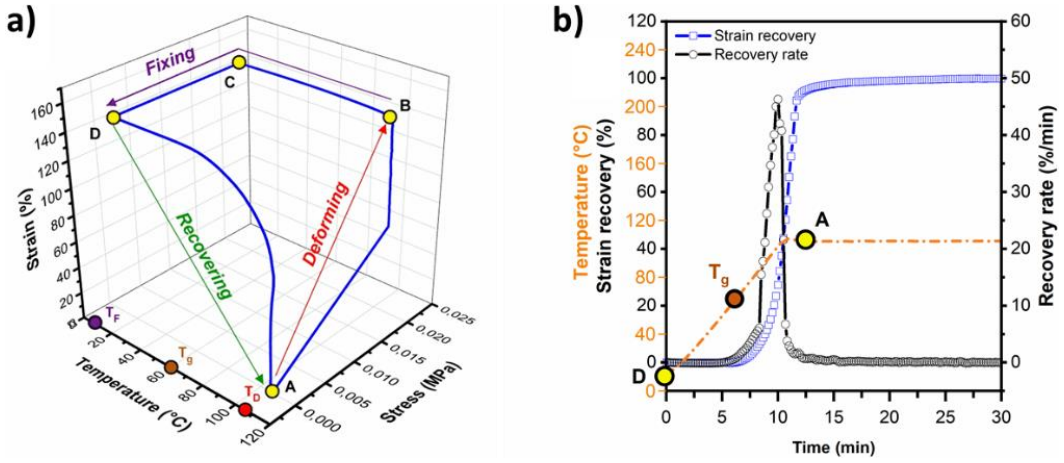

Figure 6.7. a) Shape memory cycle for a sample from PHEMA-*co*-PEGMEMA 75:25. A-B: heating at T_D = T_g + 50°C and deformation upon load application (0.02 MPa); B-C: cooling down at T_F = T_g - 50°C under fixed strain condition; C-D unloading; D-A shape

recovery under quasi stress-free conditions (0.2 kPa). b) strain recovery and recovery rate during (D-A).

Notably, both R_f and R_r remain stable after three consecutive thermo-mechanical cycles, which means the sample can hold a TS and recover its PS with high repeatability. Similar R_f and R_r ratios were measured for the other PHEMA-*co*-PEGMEMA X:Y samples (**Table 6.2**), proving definitively the excellent shape memory behavior of these novel DLP-printable thermosets.

Table 6.2 Results of the shape memory investigation performed on the PHEMA-*co*-PEGMEMA X:Y thermosets (X and Y refer to weight concentration of the two photopolymerizable species in the precursor formulation); the given R_f and R_r ratios are obtained after three thermo-mechanical cycles.

Sample code	T_g [°C]	Shape memory parameters	
		R_f [%]	R_r [%]
PHEMA-*co*-PEGMEMA 50:50	12 ± 2	98.6 ± 0.3	98.7 ± 0.5
PHEMA-*co*-PEGMEMA 65:35	27 ± 2	98.4 ± 0.3	99.0 ± 0.6
PHEMA-*co*-PEGMEMA 75:25	63 ± 4	98.8 ± 0.1	98.8 ± 0.4

The proposed mechanism behind the thermoresponsive shape memory behavior of these novel SMPs is schematically represented in **Figure 6.8**, where the thermomechanical cycling of a DLP-printed structure from PHEMA-*co*-PEGMEMA 75:25 is analyzed at a molecular level. As you can see, the printed part displays a high resistance to deformation at RT (i.e. at $T < T_g$), being able to efficiently hold its shape while in its glassy state ($T_g = 63$°C), when loaded with a weight of 50 g. But when the temperature is increased above the T_g, the structure can be easily deformed. This is because the polymer softens while in its elastomeric state ($T > T_g$). Notably, intermolecular H-bonding motifs dissociate via fast exchange mechanisms upon heating, so that the physical net-point are destroyed and the polymer gains additional stretchability, while the chemical net-points (i.e. the one generated by using BAPO-γ-CyD as crosslinker) prevent chains slippage.[288] Then, the mobility of the chains is frozen out by cooling below the T_g. This allows to fix the strained configuration (i.e. TS), which is further stabilized by the dynamic re-association of multiple H-bonds serving as newly formed physical net-points of a supramolecular network.[287,293,295,299] Finally, reheating under stress-free conditions to above the T_g leads the H-bonds to newly dissociate, so that the molecular chains move back to their thermodynamically preferred highest entropy state and the printed structure recovers its PS.[287,288]

The subsequent cooling to room temperature allows to regain the mechanical properties due to a final H-bond reassociation.

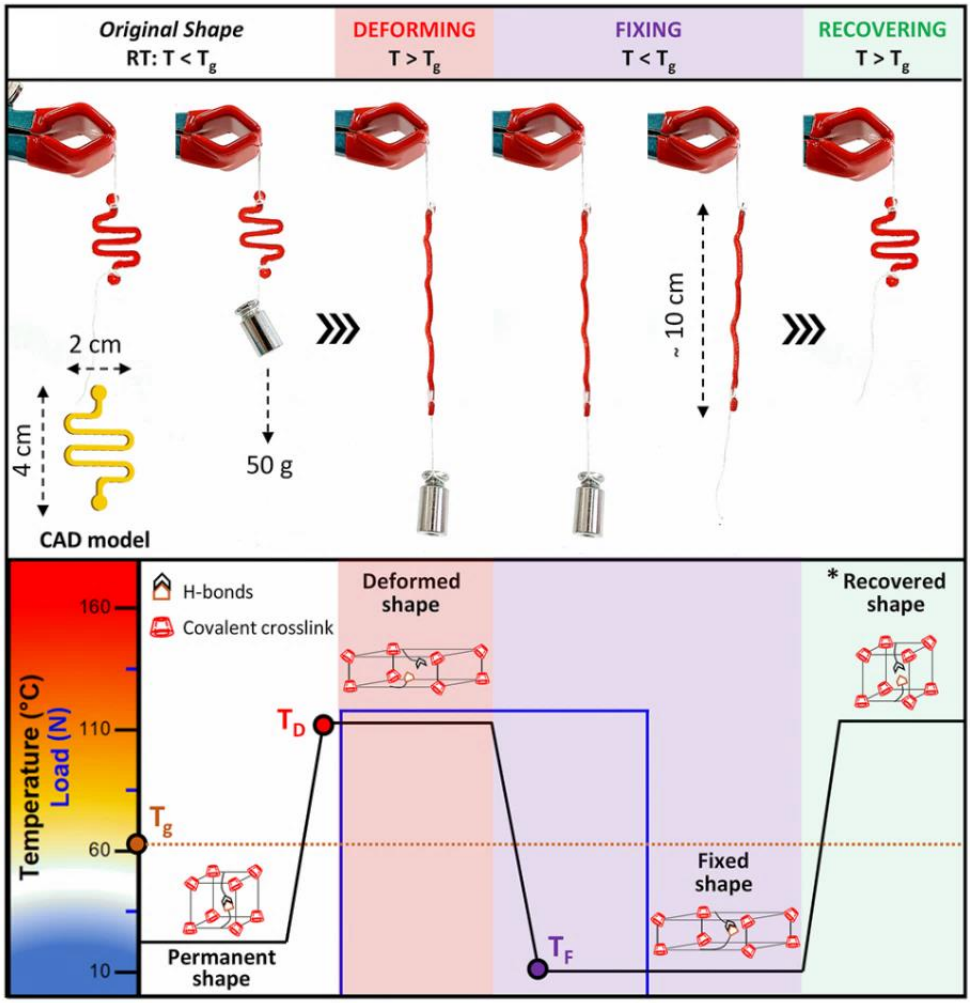

Figure 6.8. Proposed molecular mechanism behind the shape memory behavior of a DLP-printed structure from PHEMA-*co*-PEGMEMA 75:25 (*the thermodynamically stable permanent shape is recovered by reheating above the T_g, while the original mechanical properties are regained after cooling to RT, due to H-bonds reassociation).

The shape memory behavior was also confirmed qualitatively, by monitoring the capability of different DLP-printed structures to recover their original shape from a programmed configuration when exposed to a thermal trigger (**Figure 6.9**).

Remarkably, one of the main advantages of the system here described is the opportunity to suitably design the T_g of the SMP by tuning the concentration of the photopolymerizable methacrylates in the precursor formulations. This can

ultimately enable to fabricate structures having a multiple shape memory response by just changing the composition of the photocurable system during the printing stage.

As evidence of this, the flower-shaped structure shown in Figure 6.9 (CAD model 4) was prepared using two different formulations for the fabrication of the stem and the petals, each one having different concentrations of HEMA and PEGMEMA, and using different dyes (MR and brilliant green). The structure is obtained by simply changing the resin vat during the printing process. Hence, after being fixed into a bended TS, the flower shows a sequential recovery upon heating: the stem regains its permanent shape first because of the lower T_g of the photocured resin being used (Resin 2, PHEMA-*co*-PEGMEMA 65:35, T_g = 27°C), while the petals open up at higher temperatures (Resin 1, PHEMA-*co*-PEGMEMA 75:25, T_g = 63°C).

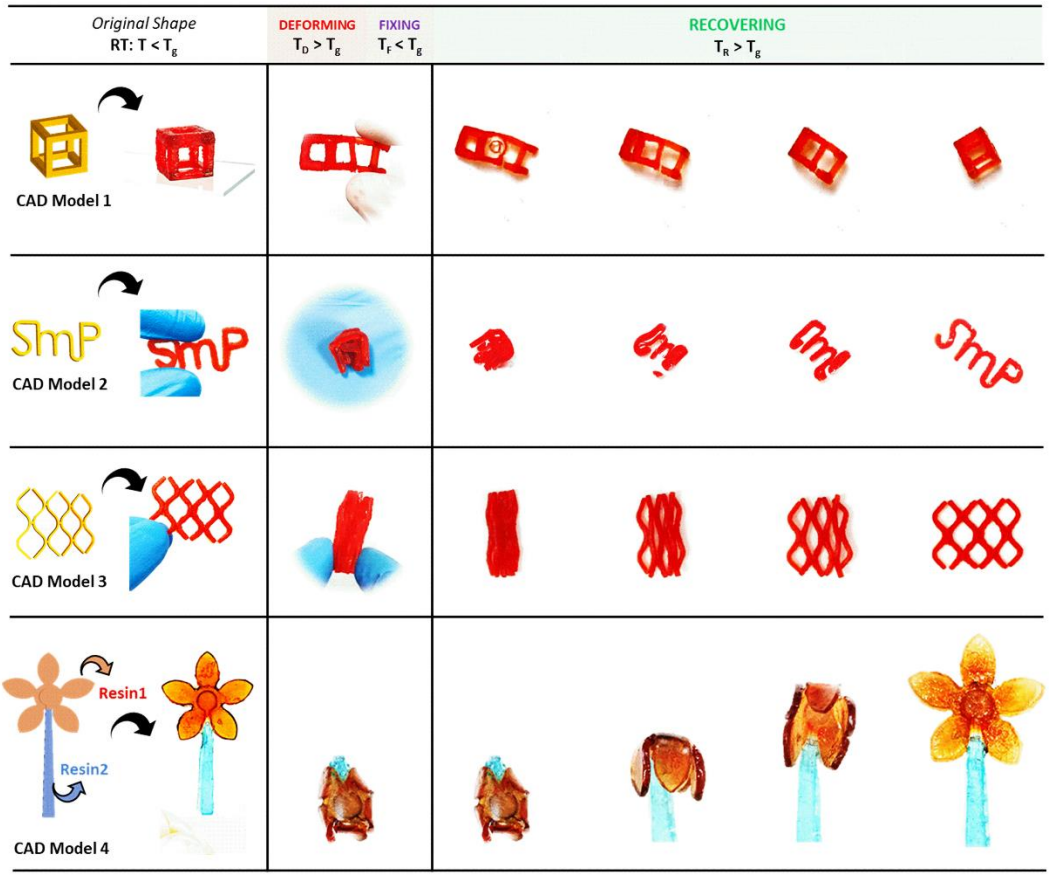

Figure 6.9. Shape memory cycles of different DLP-printed PHEMA-*co*-PEGMEMA structures. TS programmed by deforming the structures at $T_D = T > T_g$ and fixed by rapid cooling below at $T_F = T < T_g$. The shape recovery is carried out at $T_R = T > T_g$.

6.3.4 DLP 4D-printing of a smart thermoresponsive device

As already mentioned, the implementation of SMPs in AM gave the opportunity to fabricate highly complex structures with time-programmable and stimuli-responsive properties. Therefore, aimed to demonstrate the potential integration of such PHEMA-*co*-PEGMEMA SMPs to develop DLP-printed smart devices, we fabricate a prototype of a structure (**Figure 6.10**) able to divert an airflow depending on its temperature.

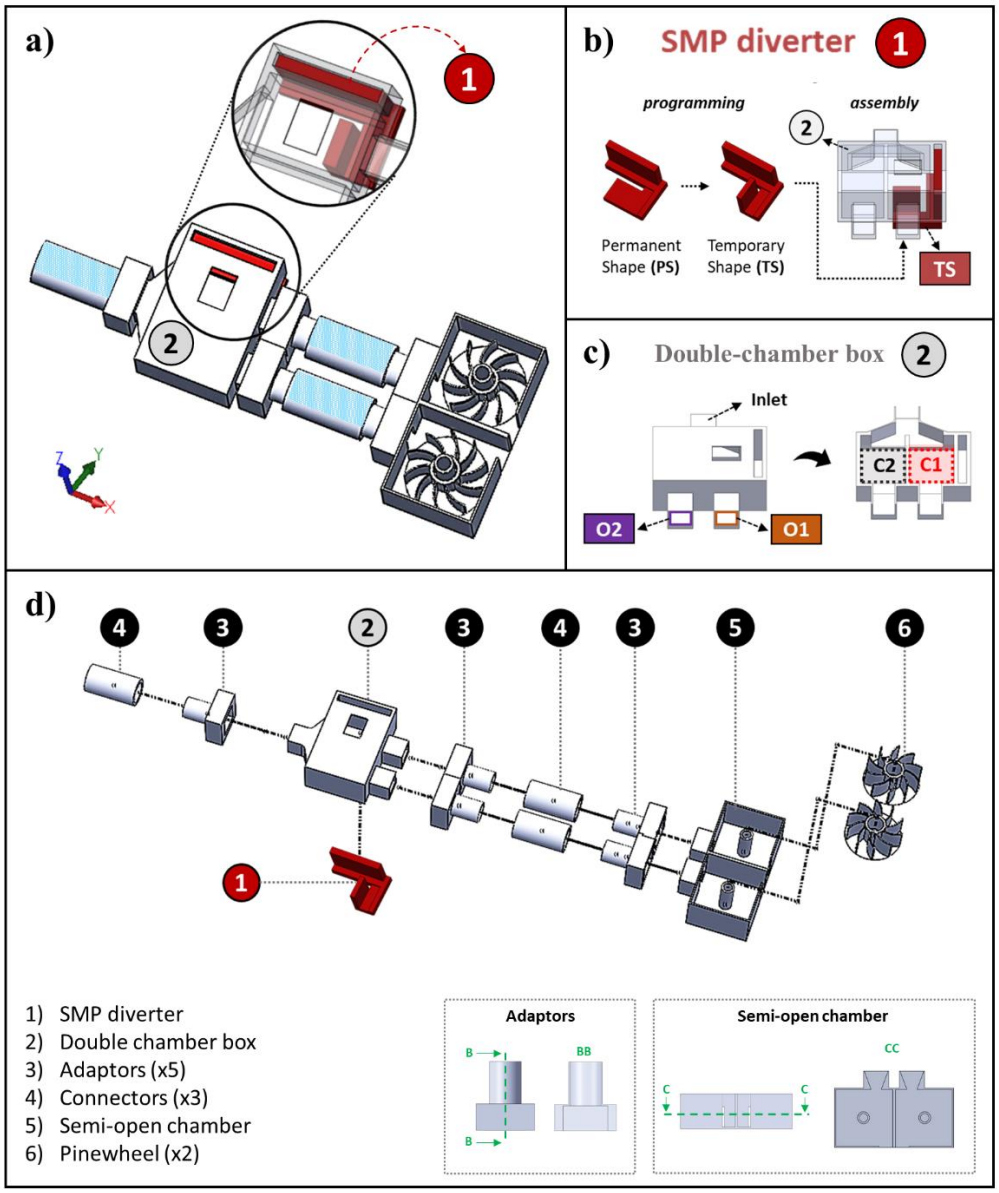

Figure 6.10. a) CAD model of the prototype; detailed views of b) component 1 (SMP), with relative programming of the vertical configuration (TS) and final assembly into C1

and c) component 2 (double chamber box); d) exploded view of the final assembly with section views of the adaptors and the semi-open chamber (component 3 and 5, respectively).

The designed device (Figure 6.10a) consists of a SMP element (component 1, Figure 6.10b) assembled in a double chamber box (component 2) having a single inlet and two separate outlets (O1 and O2, see the section view given in Figure 6.10c). Adaptors (components 3) and tubes (components 4) are used to connect the output channels of component 2 to two semi-open chambers (component 5), where two pinwheels (component 6) are positioned. The exploded view of the assembly is given in Figure 6.10d). All the elements of the device were DLP-printed, except for the connecting tubes made of PVC (components 4). More specifically, the SMP element is fabricated from H75P25 since the resulting PHEMA-*co*-PEGMEMA thermoset can efficiently store a mechanically stable temporary-strained configuration at RT. Whereas the other structural elements (components 2, 3, 5 and 6) were prepared using PEGDA-based formulations (see subsection 6.2.2). A photograph of the final assembled device is shown in **Figure 6.11**.

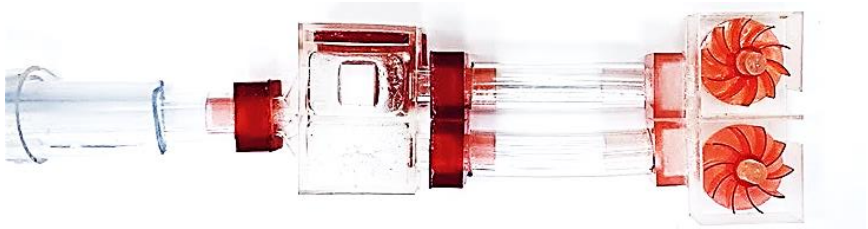

Figure 6.11. Photograph of the device after final assembly.

The device functioning can be described as follows. First the SMP component is programmed in a temporary vertical configuration. In particular, the cantilever-shaped element is deformed when heating the structure up to the T_g of PHEMA-*co*-PEGMEMA 75:25 and the TS is subsequently fixed by rapid cooling below T_g, following a programming cycle similar to those previously reported in subsection 6.3.3. Then, once the SMP component in its TS has been inserted into the first chamber (C1) of component 2 (see Figure 6.10b) and the assembly of the device is completed, air is blown from the inlet channel (air speed = 4.5 m/s).

Hence, when the temperature of the airstream is lower than the T_g of PHEMA-*co*-PEGMEMA 75:25 (case study A: T_1 = 15°C), the cantilever retains its temporary-strained vertical configuration locking O1. This means the air can freely

flow just through O2 making only one pinwheel spin, while the airflow through O1 is blocked so that the other pinwheel stands still (**Figure 6.12-top**). Note that the geometry of the inlet channels of component 5 was suitable designed with a pronounced flare to increase the pressure of the incoming airstream (see detailed view of the semichamber box given in Figure 6.10d), while the pressure buildup in C1 is released from the hole positioned on the upper wall of the chamber (see detailed view of component 2 in Figure 6.10c).

On the contrary, when the temperature of the airstream is increased to above the T_g of PHEMA-*co*-PEGMEMA 75:25 (case study B: $T_2 = 85°C$), the cantilever starts to lower against the airflow gradually recovering its horizontal PS. Therefore, O1 is unlocked, the airstream can flow through both the outlet channel and both the pinwheels spin (**Figure 6.12-bottom**).

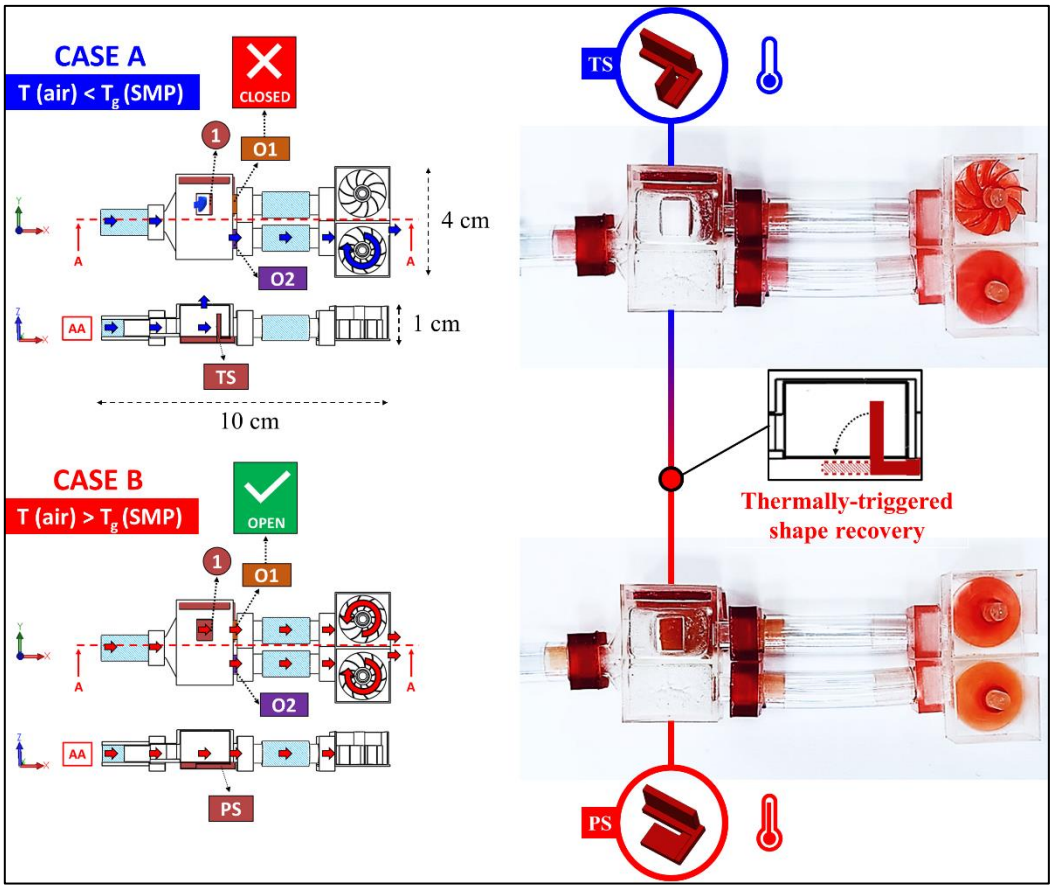

Figure 6.12. Functioning of the device depending on the inlet air temperature.

6.4 Conclusions

In this chapter, a novel photocurable system based on monofunctional methacrylates (HEMA and PEGMEMA) and the phosphaneoxide BAPO-γ-CyD, is proposed to prepare thermoresponsive SMPs via DLP-printing. Preliminary photorheology investigations served to optimize the concentration of BAPO-γ-CyD and proved the high reactivity of the photocurable system, suggesting its potential use to prepare DLP-printable formulation. The printability was then assessed, since different 3D-models were successfully reproduced with a good resolution. Besides, this proved the possibility to print stable thermosets (GC values up to 94%) using just BAPO-γ-CyD as a *two-in-one* photoinitiator and crosslinking agent, without the need of any of the multifunctional crosslinkers typically added to DLP-printable formulations to get thermosetting polymers upon photopolymerization. DMTA revealed that the thermomechanical properties of the PHEMA-*co*-PEGMEMA thermosets can be tailored by tuning the concentration of the photopolymerizable methacrylates in the precursor formulation. This allowed to prepare DLP-printable materials whose T_g can be easily designed by simply adjusting the formulation compounding. The excellent shape memory response confirmed that the printed PHEMA-*co*-PEGMEMA thermosets can efficiently memorize their shape, being able to recover their original configuration from a mechanical deformation (strain recovery near 99%). Moreover, the presence of side terminal -OH groups which thermoreversibly associate into an H-bonding network allows to stabilize the thermodynamically-unfavorable temporary shapes below the T_g, as confirmed by the high strain fixity values observed (close to 99%). Finally, a smart airflow diverter was successfully fabricated as a proof of concept, envisaging the potential implementation of these PHEMA-*co*-PEGMEMA SMPs for the development of thermoresponsive devices.

In conclusions the results reported here, besides proving the versatility of the chosen monomethacrylates-based system for the preparation of SMPs with tunable properties, further confirmed the effectiveness of using amorphous polymers bearing RBGs as valuable alternatives to fabricate thermoresponsive SMPs via DLP-printing. In particular, the possibility to develop SMPs with a tailorable T_g allowed to not be strictly bound to the specific T_m of a crystalline phase and to suitably design a transition temperature for specific application purposes. Future studies may be focused on alternative and non-thermal shape triggering strategies inherently entailed when using RBGs, such as those based on changes in chemical environment or light, which may ultimately allow to develop multifunctional materials.

General conclusions

Throughout this dissertation, γ-cyclodextrins are presented as interesting building blocks for the synthesis of bio-based multifunctional derivatives for DLP-printing applications. Indeed, the predisposition of these macrocyclic oligosaccharides to undergo many different chemical modifications by means of hydroxyl groups substitution was exploited to prepare molecularly well-defined photopolymerizable and photoactive derivatives.

A multi-substituted photopolymerizable cyclodextrin derivative is presented in the first experimental contribution (chapter 3) as a novel bio-based macromer for DLP-printing. The target molecule was successfully synthetized by following one of the main strategies used to impart photopolymerizable functionality to natural molecules, i.e. the conversion of hydroxyl groups into acrylate functions. The high photoreactivity displayed by the so obtained multi-acrylated macromer reflected into an excellent DLP-printability, as confirmed when using it either to prepare all CyD-based thermosets or as crosslinker of a monofunctional methacrylate oligomer. In this sense, the latter strategy was found to be the most interesting, since it allows to modulate the thermomechanical properties of the printed thermosets by merging the high crosslinking efficiency of the macromer and the plasticizing effect of the monofunctional methacrylate. In the framework of an ever-growing interest for a greener and sustainable manufacturing, these findings gave further evidence that bio-based molecules can be successfully used to prepare valuable alternatives to the current palette of printable photopolymers. Remarkably, the synthetic route here presented could provide a defined trail to follow in the future to prepare other DLP-printable natural photopolymers.

Nevertheless, the use of a multi-acrylated monomer for the preparation of DLP-printable photoresins entails anomalous behaviors, above all the incomplete conversion of the acrylate functions upon photopolymerization. However, preliminary investigations carried out in the second experimental contribution (chapter 4), demonstrated that those C=C bonds which inevitably remained unreacted after the printing step can be successfully exploited for post-printing surface modification. In this sense, Michael-addition reactions were proved to be particularly effective to tune the surface-wettability of PEGDA-AcγCyD printed

parts enabling the *grafting-to* or *photografting-from* of hydrophobic/hydrophilic polymeric brushes. Moreover, the surface grafting of a thiolated interface was successfully exploited to immobilize on the surface photoreduced AgNPs. It is important to emphasize that the possibility to take advantage of residual unsaturated functionalities for further reactions might give a boost to the development of functionalized 3D-printing since it allows to implement special properties to the printed parts without the need to add specific chemicals in the printable formulation.

In the third experimental contribution (chapter 5), γ-cyclodextrins were exploited as core molecule for the grafting of multiple photoactive BAPO units. This allowed to prepare a molecularly well-defined MFPI (BAPO-γ-CyD) having a high photoinitiating efficiency even when used at much lower molar concentrations than molecular PIs. But mostly, BAPO-γ-CyD stand out over the conventional molecular PIs serving simultaneously as photo-crosslinking agent to convert monounsaturated monomers into mechanically stable thermosets without the need of any additional crosslinkers. Notably, this unique feature can be exploited to develop innovative printable formulations using just monofunctional monomers.

The feasibility of this strategy has been confirmed in the last experimental contribution (chapter 6), wherein BAPO-γ-CyD was successfully employed as a *two-in-one* PI and crosslinking agent to enable the DLP-printing of mechanically stable thermosets from a photocurable system containing only the monofunctional HEMA and PEGMEMA. As demonstrated, by virtue of 1) the covalently crosslinked net-points generated by BAPO-γ-CyD, which impart dimensional stability at $T > T_g$, 2) the significant elasticity ratio in the T_g region, which allows an acceptable stretchability at $T > T_g$, and 3) the presence of side terminal hydroxyl RBGs, which serve to stabilize the temporary strained configurations at $T < T_g$, the PHEMA-*co*-PEGMEMA thermosets displayed excellent shape memory properties and were successfully implemented in the development of a smart device via DLP 4D-printing.

Appendix A

A1 List of abbreviations

^{13}C-NMR	Carbon NMR
^{1}H-NMR	Proton NMR
2PP	Two photon polymerization
^{31}P-NMR	Phosphorous NMR
3D	Three dimensional
4D	Four dimensional
AA	Acrylic acid
Ac-γ-CyD	Acrylated-γ-cyclodextrin
$AgNO_3$	Silver nitrate
AM	Additive manufacturing
A-PDMS	Poly(dimethylsiloxane) bis(3-aminopropyl) terminated
ATR	Attenuated total reflectance
BAPO	Bis(acyl)phosphane oxide
BE	Binding energy
CAD	Computer aided design
CAL	Computer axial lithography
C_d	Curing depth
CLIP	Continuous interface liquid production
CyD	Cyclodextrin
DBC	Double bond conversion
DEE	Diethyl ether

DI-H_2O	Deionized water
DLP	Digital light processing
DMD	Digital micromirror device
DME	Dimethoxyethane
DMSO	Dimethyl sulfoxide
DMTA	Dynamic mechanical thermal analysis
D_p	Penetration depth
DSC	Differential scanning calorimetry
E’	Storage modulus
E_c	Critical energy exposure
E_g	Glassy modulus
E_r	Rubbery modulus
EtOH	Ethanol
E_x	Excess energy exposure
ε	Molar extinction coefficient
FESEM	Field emission scanning electron microscopy
FTIR	Fourier-transform infrared spectroscopy
GC	Gel content
H_2O_2	Hydrogen peroxide
HCl	Hydrogen chloride
HDDA	hexanediol diacrylate
HEMA	2-Hydroxyethyl methacrylate
$HP(COMes)_2$	Bis(mesitoyl)hydrogenphosphane
HR	High resolution
I_A	Absorbed light intensity
IPOH	Isoprophanol
Irgacure 2959	2-Hydroxy-4′-(2-hydroxyethoxy)-2-methylpropiophenone
ISC	Intersystem crossing
LED	Light emitting diodes

MeCN	Acetonitrile
MFPI	Multifunctional photoinitiator
M_w	Molecular weight
MR	Methyl red
MS	Mass spectrometry
NMP	N-methyl pyrrolidone
NMR	Nuclear magnetic NMR spectroscopy
NT1	Norrish type 1
NT2	Norrish type 2
OH	Hydroxyl group
Omnirad 819/Irgacure 819	Phenylbis(2,4,6-trimethylbenzoyl)phosphine oxide
OPA	One photon absorption
PAG	Photoacid generator
PEGDA	Poly(ethylene glycol) diacrylate
PEGMEMA methacrylate	Poly(ethylene glycol) methyl ether
PETMP	Pentaerythritol tetrakis(3-mercaptopropionate)
phr	Per hundred resin
PI	Photoinitiator
ppm	Part per million
PS	Permanent shape
R^*	Initiating radical
RBG	Reversible binding group
R_f	Strain fixity
R_i	Reaction rate
RM^*	Chain carrier/propagating radical
RP	Rapid prototyping
R_r	Strain recovery

RT	Room temperature
S_0	Ground state
S_1	Singlet state
SH	Thiol group
SLA	Stereolithography
SMP	Shape memory polymer
STL	Standard triangulation language
SW_{eq}	Equilibrium swelling
T_1	Triplet state
tanδ	Damping factor
T_c	Crystallization temperature
T_g	Glass transition temperature
TGA	Thermogravimetric analysis
t_{gel}	Gel time
t_{ind}	Induction time
T_m	Melting temperature
TMG	Tetramethylguanidine
TPA	Two photon adsorption
TS	Temporary shape
T_{trans}	Transition temperature
UV	Ultraviolet
ν_e	Crosslinking density
Vis	Visible
VP	Vat polymerization
WC_{eq}	Equilibrium water content
XPS	X-ray photoelectron spectroscopy
φ	Quantum yield

A2 List of figures

A3 List of tables

Appendix B

B1 List of publications from the author

Related to the PhD research topic

Cosola, A.; Conti, R.; Rana, V. K.; Sangermano, M.; Chiappone, A.; Levalois-Grützmacher, J., Grützmacher H. Synthesis of γ-cyclodextrin substituted bis(acyl)phosphane oxide derivative (BAPO-γ-CyD) serving as multiple photoinitiator and crosslinking agent. *Chem. Commun.* **2020**, 56, 4828, doi:10.1039/d0cc01732a.

Cosola, A.; Conti, R.; Grützmacher, H.; Sangermano, M.; Roppolo, I.; Pirri, C. F.; Chiappone, A. Multiacrylated Cyclodextrin: A Bio-Derived Photocurable Macromer for VAT 3D printing. *Macromol. Mater. Eng.* **2020**, 305, 2000350, doi: 10.1002/mame.202000350.

Cosola, A.; Sangermano, M.; Terenziani, D.; Conti, R.; Messori, M.; Grützmacher, H.; Pirri, C. F.; Chiappone, A. DLP 3D-printing of shape memory polymers stabilized by thermoreversible hydrogen bonding interactions. *Appl. Mater. Today* **2021**, 23, 101060, doi:10.1016/j.apmt.2021.101060.

Cosola, A.; Sangermano, M.; Terenziani, D.; Conti, R.; Messori, M.; Grützmacher, H.; Pirri, C. F.; Chiappone, A. H-bond stabilized shape memory polymers: from 3D to 4D printing. in: *6th Virtual European Symposium of Photopolymer Science* **2021**, online, pp 101-101, ISBN: 978-3-950-48093-1

Related to side projects

Grinic, D.; Giagnorio, M.; **Cosola, A.**; Ricceri, F.; Zanetti, M. C.; Sangermano, M.; Tiraferri, A. Maximizing the Degree of Sulfonation of Polysulfone Supports in TFC Membranes for Osmotically Driven Processes. *Macromol. Mater. Eng.* **2018**, 303, 1800384, doi: 10.1002/mame.201800384.

Cosola, A.; Chiappone, A.; Martinengo, C.; Grützmacher, H.; Sangermano, M. Gelatin Type A from Porcine Skin Used as Co-Initiator in a Radical Photo-Initiating System, *Polymers* **2019**, 11, 1901, doi:10.3390/polym11111901.

Cortés, A.; **Cosola, A.**; Sangermano, M.; Campo, M.; Gonzàlez Prolongo, S.; Pirri, C. F.; Jiménez-Suárez, A.; Chiappone, A. DLP 4D-Printing of Remotely, Modularly, and Selectively Controllable Shape Memory Polymer Nanocomposites Embedding Carbon Nanotubes. *Adv. Funct. Mater*. **2021**, 31, 2106774, doi:10.1002/adfm.202106774.

Cortés, A.; Aguilar, Jose L.; **Cosola, A.**; Fernàndez Sanchez-Romate, X. X.; Jiménez-Suárez, A.; Sangermano, M.; Campo, M.; Gonzàlez Prolongo, S. 4D-Printed Resins and Nanocomposites Thermally Stimulated by Conventional Heating and IR Radiation. ACS *Appl. Polym. Mat.* **2021**, 3, 10, 5207-5215, doi:10.1021/acsapm.1c00970.

Noè, C.; **Cosola, A.**; Chiappone, A.; Hakkarainen, M.; Grützmacher, H.; Sangermano, M. From polysaccharides to UV-curable biorenewable hydrogels for methylene blue removal. *Polymer* **2021**, 235, 124257, doi:10.1016/j.polymer.2021.124257.

Noè, C.; **Cosola, A.**; Tonda-Turo, C.; Sesana, R.; Delprete, C.; Chiappone, A.; Hakkarainen, M.; Sangermano, M. DLP-printable fully biobased soyben oil composites, *submitted*

B2 List of conferences attended by the author

European Symposium of Photopolymer Science 2018, September 3 – 6 2018, Mulhouse, FRA

Photopolymerization Fundamentals 2019, September 15 – 18 2019, Monterey Plaza Hotel & Spa in Monterey, CA, USA (Poster session: "*Gelatin used as co-initiator in a radical photoinitiating system*")

Virtual European Symposium of Photopolymer Science 2021, June 15 – 17 2021 (Oral presentation: "*H-bond stabilized shape memory polymers: from 3D to 4D printing*")

Italian Photochemistry Meeting 2021, December 16 – 18 2021, Turin, ITA (Oral presentation: "*Multi-photoactive BAPO-cyclodextrin: a two-in-one photoinitiator and photocrosslinking agent*")

XIII Convegno Nazionale sulla Scienza e Tecnologia dei Materiali, January 23 – 26 2022, TH Resorts Sestriere (Oral presentation: "*Pushing beyond the borders of 3D: 4D-printing of H-bond stabilized shape memory polymers*")

References

1. Hull, C.W. Apparatus for production of three dimensional objects by stereolithography. U.S. Patent 4575330, 1986.
2. Gibson, I.; Rosen, D.; Stucker, B.; Khorasani, M. Additive Manufacturing Technologies. *Addit. Manuf. Technol.* **2021**, doi:10.1007/978-3-030-56127-7.
3. Ngo, T.D.; Kashani, A.; Imbalzano, G.; Nguyen, K.T.Q.; Hui, D. Additive manufacturing (3D printing): A review of materials, methods, applications and challenges. *Compos. Part B Eng.* **2018**, *143*, 172–196, doi:10.1016/J.COMPOSITESB.2018.02.012.
4. Ligon, S.C.; Liska, R.; Stampfl, J.; Gurr, M.; Mülhaupt, R. Polymers for 3D Printing and Customized Additive Manufacturing. *Chem. Rev.* **2017**, *117*, 10212–10290, doi:10.1021/acs.chemrev.7b00074.
5. Bagheri, A.; Jin, J. Photopolymerization in 3D Printing. *ACS Appl. Polym. Mater.* **2019**, *1*, 593–611, doi:10.1021/ACSAPM.8B00165.
6. Saleh Alghamdi, S.; John, S.; Roy Choudhury, N.; Dutta, N.K. Additive Manufacturing of Polymer Materials: Progress, Promise and Challenges. *Polymers (Basel).* **2021**, *13*, 753, doi:10.3390/polym13050753.
7. Berman, B. 3-D printing: The new industrial revolution. *Bus. Horiz.* **2012**, *55*, 155–162, doi:10.1016/J.BUSHOR.2011.11.003.
8. Huang, S.H.; Liu, P.; Mokasdar, A.; Hou, L. Additive manufacturing and its societal impact: A literature review. *Int. J. Adv. Manuf. Technol.* 2013, *67*, 1191–1203.
9. Ficko, M.; Drstvenšek, I.; Brezočnik, M.; Balič, J.; Vaupotic, B. Prediction of total manufacturing costs for stamping tool on the basis of CAD-model of finished product. *J. Mater. Process. Technol.* **2005**, *164–165*, 1327–1335, doi:10.1016/J.JMATPROTEC.2005.02.013.
10. Kumar, R.; Kumar, M.; Chohan, J.S. Material-specific properties and applications of additive manufacturing techniques: a comprehensive review. *Bull. Mater. Sci.* **2021**, *44*, 181, doi:10.1007/s12034-021-02364-y.

11. Sandeep, B.; Kannan, T.T.M.; Chandradass, J.; Ganesan, M.; John Rajan, A. Scope of 3D printing in manufacturing industries-A review. *Mater. Today Proc.* **2021**, *45*, 6941–6945, doi:10.1016/J.MATPR.2021.01.394.

12. Kalyan, M.V.. S.; Kumar, H.; Nagdeve, L. Latest trends in Additive manufacturing. *IOP Conf. Ser. Mater. Sci. Eng.* **2021**, *1104*, 012020, doi:10.1088/1757-899X/1104/1/012020.

13. 3D Printing Market (2021-26) | Industry Trends, Growth, Size - Mordor Intelligence Available online: https://www.mordorintelligence.com/industry-reports/3d-printing-market (accessed on Oct 12, 2021).

14. Nickels, L. AM and aerospace: an ideal combination. *Met. Powder Rep.* **2015**, *70*, 300–303, doi:10.1016/J.MPRP.2015.06.005.

15. Kobryn, P.A.; Ontko, N.. R.; Perkins, L.. P.; Tiley, J.S. Additive Manufacturing of Aerospace Alloys for Aircraft Structures. *AVT-139 Spec. Meet. Amsterdam* **2006**, *139*, 1–14.

16. Murphy, S. V; Atala, A. 3D bioprinting of tissues and organs. *Nat. Biotechnol.* **2014**, *32*, 773–785, doi:10.1038/nbt.2958.

17. Gao, B.; Yang, Q.; Zhao, X.; Jin, G.; Ma, Y.; Xu, F. 4D Bioprinting for Biomedical Applications. *Trends Biotechnol.* **2016**, *34*, 746–756, doi:10.1016/J.TIBTECH.2016.03.004.

18. Wong, K.C. 3D-printed patient-specific applications in orthopedics. *Orthop. Res. Rev.* **2016**, *8*, 57, doi:10.2147/ORR.S99614.

19. Jardini, A.L.; Larosa, M.A.; de Carvalho Zavaglia, C.A.; Bernardes, L.F.; Lambert, C.S.; Kharmandayan, P.; Calderoni, D.; Maciel Filho, R. Customised titanium implant fabricated in additive manufacturing for craniomaxillofacial surgery. *Virtual Phys. Prototyp.* **2014**, *9*, 115–125, doi:10.1080/17452759.2014.900857.

20. Yu, D.G.; Zhu, L.M.; Branford-White, C.J.; Yang, X.L. Three-Dimensional Printing in Pharmaceutics: Promises and Problems. *J. Pharm. Sci.* **2008**, *97*, 3666–3690, doi:10.1002/JPS.21284.

21. Katakam, P.; Dey, B.; Assaleh, F.H.; Hwisa, N.T.; Adiki, S.K.; Chandu, B.R.; Mitra, A. Top-Down and Bottom-Up Approaches in 3D Printing Technologies for Drug Delivery Challenges. *Crit. Rev. Ther. Drug Carr. Syst.* **2015**, *32*, 61–87, doi:10.1615/CRITREVTHERDRUGCARRIERSYST.2014011157.

22. Prasad, L.K.; Smyth, H. 3D Printing technologies for drug delivery: a review. *Drug Dev. Ind. Pharm.* **2016**, *42*, 1019–1031, doi:10.3109/03639045.2015.1120743.

23. Goole, J.; Amighi, K. 3D printing in pharmaceutics: A new tool for designing customized drug delivery systems. *Int. J. Pharm.* **2016**, *499*, 376–394, doi:10.1016/J.IJPHARM.2015.12.071.

24. Krivec, S.; Matsko, N.; Satzinger, V.; Pucher, N.; Galler, N.; Koch, T.; Schmidt, V.; Grogger, W.; Liska, R.; Lichtenegger, H.C. Silica-Based, Organically Modified Host Material for Waveguide Structuring by Two-Photon-Induced Photopolymerization. *Adv. Funct. Mater.* **2010**, *20*, 811–819, doi:10.1002/ADFM.200901790.

25. Ishihara, J.; Komatsu, K.; Sugihara, O.; Kaino, T. Fabrication of three-dimensional calixarene polymer waveguides using two-photon assisted polymerization. *Appl. Phys. Lett.* **2007**, *90*, 033511, doi:10.1063/1.2430480.

26. Lawes, S.; Riese, A.; Sun, Q.; Cheng, N.; Sun, X. Printing nanostructured carbon for energy storage and conversion applications. *Carbon N. Y.* **2015**, *92*, 150–176, doi:10.1016/J.CARBON.2015.04.008.

27. Fu, K.; Wang, Y.; Yan, C.; Yao, Y.; Chen, Y.; Dai, J.; Lacey, S.; Wang, Y.; Wan, J.; Li, T.; et al. Graphene Oxide-Based Electrode Inks for 3D-Printed Lithium-Ion Batteries. *Adv. Mater.* **2016**, *28*, 2587–2594, doi:10.1002/ADMA.201505391.

28. Lim, S.; Buswell, R.A.; Le, T.T.; Austin, S.A.; Gibb, A.G.F.; Thorpe, T. Developments in construction-scale additive manufacturing processes. *Autom. Constr.* **2012**, *21*, 262–268, doi:10.1016/J.AUTCON.2011.06.010.

29. Xia, M.; Sanjayan, J. Method of formulating geopolymer for 3D printing for construction applications. *Mater. Des.* **2016**, *110*, 382–390, doi:10.1016/J.MATDES.2016.07.136.

30. Labonnote, N.; Rønnquist, A.; Manum, B.; Rüther, P. Additive construction: State-of-the-art, challenges and opportunities. *Autom. Constr.* **2016**, *72*, 347–366, doi:10.1016/J.AUTCON.2016.08.026.

31. Holt, C.; Edwards, L.; Keyte, L.; Moghaddam, F.; Townsend, B. Construction 3D Printing. *3D Concr. Print. Technol.* **2019**, 349–370, doi:10.1016/B978-0-12-815481-6.00017-8.

32. Korger, M.; Bergschneider, J.; Lutz, M.; Mahltig, B.; Finsterbusch, K.; Rabe, M. Possible Applications of 3D Printing Technology on Textile Substrates.

IOP Conf. Ser. Mater. Sci. Eng. **2016**, *141*, 012011, doi:10.1088/1757-899X/141/1/012011.

33. Cao, Y.; Zhang, G.; Zhang, Y.; Yue, M.; Chen, Y.; Cai, S.; Xie, T.; Feng, X. Direct Fabrication of Stretchable Electronics on a Polymer Substrate with Process-Integrated Programmable Rigidity. *Adv. Funct. Mater.* **2018**, *28*, 1804604, doi:10.1002/ADFM.201804604.

34. Chatterjee, K.; Ghosh, T.K. 3D Printing of Textiles: Potential Roadmap to Printing with Fibers. *Adv. Mater.* **2020**, *32*, 1902086, doi:10.1002/ADMA.201902086.

35. Wegrzyn, T.F.; Golding, M.; Archer, R.H. Food Layered Manufacture: A new process for constructing solid foods. *Trends Food Sci. Technol.* **2012**, *27*, 66–72, doi:10.1016/J.TIFS.2012.04.006.

36. Lipton, J.I.; Cutler, M.; Nigl, F.; Cohen, D.; Lipson, H. Additive manufacturing for the food industry. *Trends Food Sci. Technol.* **2015**, *43*, 114–123, doi:10.1016/J.TIFS.2015.02.004.

37. Godoi, F.C.; Prakash, S.; Bhandari, B.R. 3d printing technologies applied for food design: Status and prospects. *J. Food Eng.* **2016**, *179*, 44–54, doi:10.1016/J.JFOODENG.2016.01.025.

38. Liu, Z.; Zhang, M.; Bhandari, B.; Wang, Y. 3D printing: Printing precision and application in food sector. *Trends Food Sci. Technol.* **2017**, *69*, 83–94, doi:10.1016/J.TIFS.2017.08.018.

39. Zastrow, M. THE NEW 3D PRINTING. *Nature* **2020**, *578*, 20–24.

40. Jiang, P.; Ji, Z.; Wang, X.; Zhou, F. Surface functionalization – a new functional dimension added to 3D printing. *J. Mater. Chem. C* **2020**, *8*, 12380–12411, doi:10.1039/D0TC02850A.

41. Tibbits, S. 4D Printing: Multi-Material Shape Change. *Archit. Des.* **2014**, *84*, 116–121, doi:10.1002/AD.1710.

42. Raviv, D.; Zhao, W.; McKnelly, C.; Papadopoulou, A.; Kadambi, A.; Shi, B.; Hirsch, S.; Dikovsky, D.; Zyracki, M.; Olguin, C.; et al. Active Printed Materials for Complex Self-Evolving Deformations. *Sci. Rep.* **2014**, *4*, 7422, doi:10.1038/srep07422.

43. Ge, Q.; Qi, H.J.; Dunn, M.L. Active materials by four-dimension printing. *Appl. Phys. Lett.* **2013**, *103*, 131901, doi:10.1063/1.4819837.

44. Choi, J.; Kwon, O.C.; Jo, W.; Lee, H.J.; Moon, M.W. 4D printing

technology: A review. *3D Print. Addit. Manuf.* **2015**, *2*, 159–167, doi:10.1089/3DP.2015.0039/ASSET/IMAGES/MEDIUM/FIGURE1.GIF.

45. Li, Y.-C.; Zhang, Y.S.; Akpek, A.; Shin, S.R.; Khademhosseini, A. 4D bioprinting: the next-generation technology for biofabrication enabled by stimuli-responsive materials. *Biofabrication* **2016**, *9*, 012001, doi:10.1088/1758-5090/9/1/012001.

46. Sydney Gladman, A.; Matsumoto, E.A.; Nuzzo, R.G.; Mahadevan, L.; Lewis, J.A. Biomimetic 4D printing. *Nat. Mater.* **2016**, *15*, 413–418, doi:10.1038/nmat4544.

47. Kuang, X.; Roach, D.J.; Wu, J.; Hamel, C.M.; Ding, Z.; Wang, T.; Dunn, M.L.; Qi, H.J. Advances in 4D Printing: Materials and Applications. *Adv. Funct. Mater.* **2019**, *29*, 1805290, doi:10.1002/ADFM.201805290.

48. Momeni, F.; M.Mehdi Hassani.N, S.; Liu, X.; Ni, J. A review of 4D printing. *Mater. Des.* **2017**, *122*, 42–79, doi:10.1016/J.MATDES.2017.02.068.

49. Rafiee, M.; Farahani, R.D.; Therriault, D. Multi-Material 3D and 4D Printing: A Survey. *Adv. Sci.* **2020**, *7*, 1902307, doi:10.1002/ADVS.201902307.

50. The Additive Manufacturing Industry Landscape 2020: 240 Companies Driving Digital Manufacturing [Updated] - AMFG Available online: https://amfg.ai/2020/05/26/the-additive-manufacturing-industry-landscape-2020-231-companies-driving-digital-manufacturing/ (accessed on Oct 22, 2021).

51. Noorani, R. *3D printing: technology, applications, and selection*; CRC Press, 2018; ISBN 9780367781965.

52. Polymer Additive Manufacturing Market to Reach $16 billion in 2023 Available online: https://www.smartechanalysis.com/news/polymer-additive-manufacturing-market/ (accessed on Oct 22, 2021).

53. Zhou, L.-Y.; Fu, J.; He, Y. A Review of 3D Printing Technologies for Soft Polymer Materials. *Adv. Funct. Mater.* **2020**, *30*, 2000187, doi:10.1002/ADFM.202000187.

54. Chatani, S.; Kloxin, C.J.; Bowman, C.N. The power of light in polymer science: Photochemical processes to manipulate polymer formation, structure, and properties. *Polym. Chem.* **2014**, *5*, 2187–2201, doi:10.1039/c3py01334k.

55. Scott, T.F.; Kloxin, C.J.; Forman, D.L.; McLeod, R.R.; Bowman, C.N. Principles of voxel refinement in optical direct write lithography. *J. Mater. Chem.* **2011**, *21*, 14150–14155, doi:10.1039/C1JM11915J.

56. Viswanathan, N.K.; Kim, D.Y.; Shaoping Bian; John Williams; Wei Liu; Lian Li; Lynne Samuelson; Jayant Kumar; Tripathy, S.K. Surface relief structures on azo polymer films. *J. Mater. Chem.* **1999**, *9*, 1941–1955, doi:10.1039/A902424G.

57. Finkelmann, H.; Nishikawa, E.; Pereira, G.G.; Warner, M. A New Opto-Mechanical Effect in Solids. *Phys. Rev. Lett.* **2001**, *87*, 015501, doi:10.1103/PhysRevLett.87.015501.

58. Ikeda, T.; Nakano, M.; Yu, Y.; Tsutsumi, O.; Kanazawa, A. Anisotropic Bending and Unbending Behavior of Azobenzene Liquid-Crystalline Gels by Light Exposure. *Adv. Mater.* **2003**, *15*, 201–205, doi:10.1002/ADMA.200390045.

59. Peters, M.V.; Stoll, R.S.; Kühn, A.; Hecht, S. Photoswitching of Basicity. *Angew. Chemie Int. Ed.* **2008**, *47*, 5968–5972, doi:10.1002/ANIE.200802050.

60. Beharry, A.A.; Woolley, G.A. Azobenzene photoswitches for biomolecules. *Chem. Soc. Rev.* **2011**, *40*, 4422–4437, doi:10.1039/C1CS15023E.

61. Liu, D.; Bastiaansen, C.W.M.; den Toonder, J.M.J.; Broer, D.J. Photo-Switchable Surface Topologies in Chiral Nematic Coatings. *Angew. Chemie Int. Ed.* **2012**, *51*, 892–896, doi:10.1002/ANIE.201105101.

62. Dilling, W.L.; Kroening, R.D.; Little, J.C. Organic Photochemistry. VII. The Photosensitized and Thermal Cycloaddition Reactions of 1,3-Butadiene, Isoprene, and Cyclopentadiene to α-Acetoxyacrylomtrile. 1,2 vs. 1,4 Addition as a Function of Sensitizer Triplet Energy in Cross-Addition Reactions. *J. Am. Chem. Soc.* **1970**, *92*, 928–948, doi:10.1021/JA00707A033.

63. Obi, M.; Morino, S.; Ichimura, K. Reversion of Photoalignment Direction of Liquid Crystals Induced by Cinnamate Polymer Films. *Jpn. J. Appl. Phys.* **1999**, *38*, L145, doi:10.1143/JJAP.38.L145.

64. Lendlein, A.; Jiang, H.; Jünger, O.; Langer, R. Light-induced shape-memory polymers. *Nature* **2005**, *434*, 879–882, doi:10.1038/nature03496.

65. Dong, C.M.; Wu, X.; Caves, J.; Rele, S.S.; Thomas, B.S.; Chaikof, E.L. Photomediated crosslinking of C6-cinnamate derivatized type I collagen.

Biomaterials **2005**, *26*, 4041–4049, doi:10.1016/J.BIOMATERIALS.2004.10.017.

66. Crivello, J. V.; Lam, J.H.W. Diaryliodonium Salts. A New Class of Photoinitiators for Cationic Polymerization. *Macromolecules* **1977**, *10*, 1307–1315, doi:10.1021/MA60060A028.

67. Cameron, J.F.; Fréchet, J.M.J. Photogeneration of Organic Bases from O-Nitrobenzyl-Derived Carbamates. *J. Am. Chem. Soc.* **1991**, *113*, 4303–4313, doi:10.1021/JA00011A038.

68. Kloxin, A.M.; Kasko, A.M.; Salinas, C.N.; Anseth, K.S. Photodegradable Hydrogels for Dynamic Tuning of Physical and Chemical Properties. *Science (80-.).* **2009**, *324*, 59–63, doi:10.1126/SCIENCE.1169494.

69. Tasdelen, M.A.; Yilmaz, G.; Iskin, B.; Yagci, Y. Photoinduced Free Radical Promoted Copper(I)-Catalyzed Click Chemistry for Macromolecular Syntheses. *Macromolecules* **2011**, *45*, 56–61, doi:10.1021/MA202438W.

70. Fouassier, J.P.; Allonas, X.; Lalevée, J.; Dietlin, C. Photoinitiators for Free Radical Polymerization Reactions. *Photochem. Photophysics Polym. Mater.* **2010**, 351–419, doi:10.1002/9780470594179.CH10.

71. Steyrer, B.; Neubauer, P.; Liska, R.; Stampfl, J. Visible light photoinitiator for 3D-printing of tough methacrylate resins. *Materials (Basel).* **2017**, *10*, 1445, doi:10.3390/ma10121445.

72. Jasinski, F.; Zetterlund, P.B.; Braun, A.M.; Chemtob, A. Photopolymerization in dispersed systems. *Prog. Polym. Sci.* **2018**, *84*, 47–88, doi:10.1016/J.PROGPOLYMSCI.2018.06.006.

73. Arsu, N.; Kabatc, J.; Ortyl, J.; Avci, D.; Xiao, P.; Lalevee, J.; Dumur, F.; Junkers, T.; Sangermano, M.; Andrzejewska, E. *Photopolymerisation Initiating Systems*; Lalevée, J., Fouassier, J.-P., Eds.; Polymer Chemistry Series; Royal Society of Chemistry: Cambridge, 2018; ISBN 1788014944.

74. Griesser, M.; Neshchadin, D.; Dietliker, K.; Moszner, N.; Liska, R.; Gescheidt, G. Decisive Reaction Steps at Initial Stages of Photoinitiated Radical Polymerizations. *Angew. Chemie Int. Ed.* **2009**, *48*, 9359–9361, doi:10.1002/ANIE.200904473.

75. Kolczak, U.; Rist, G.; Dietliker, K.; Wirz, J. Reaction Mechanism of Monoacyl- and Bisacylphosphine Oxide Photoinitiators Studied by 31 P-, 13 C-, and 1 H-CIDNP and ESR. *J. Am. Chem. Soc.* **1996**, *118*, 6477–6489, doi:10.1021/ja9534213.

76. Wayner, D.D.M.; Clark, K.B.; Rauk, A.; Yu, D.; Armstrong, D.A. C-H bond dissociation energies of alkyl amines: Radical structures and stabilization energies. *J. Am. Chem. Soc.* **1997**, *119*, 8925–8932, doi:10.1021/ja971365v.

77. Meereis, C.T.W.; Leal, F.B.; Lima, G.S.; De Carvalho, R. V.; Piva, E.; Ogliari, F.A. BAPO as an alternative photoinitiator for the radical polymerization of dental resins. *Dent. Mater.* **2014**, *30*, 945–953, doi:10.1016/J.DENTAL.2014.05.020.

78. Cosola, A.; Chiappone, A.; Martinengo, C.; Grützmacher, H.; Sangermano, M. Gelatin type A from porcine skin used as co-initiator in a radical photo-initiating system. *Polymers (Basel).* **2019**, *11*, doi:10.3390/polym11111901.

79. Sangermano, M.; Razza, N.; Crivello, J.V. Cationic UV-Curing: Technology and Applications. *Macromol. Mater. Eng.* **2014**, *299*, 775–793, doi:10.1002/MAME.201300349.

80. Crivello, J. V The Discovery and Development of Onium Salt Cationic Photoinitiators. *J Polym Sci A Polym Chem* **1999**, *37*, 4241–4254, doi:10.1002/(SICI)1099-0518(19991201)37:23.

81. Crivello, J. V.; Reichmanis, E. Photopolymer Materials and Processes for Advanced Technologies. *Chem. Mater.* **2013**, *26*, 533–548, doi:10.1021/CM402262G.

82. Narupai, B.; Nelson, A. 100th Anniversary of Macromolecular Science Viewpoint: Macromolecular Materials for Additive Manufacturing. *ACS Macro Lett.* **2020**, *9*, 627–638, doi:10.1021/ACSMACROLETT.0C00200.

83. Tseng, S.-J.; Chien, C.-C.; Liao, Z.-X.; Chen, H.-H.; Kang, Y.-D.; Wang, C.-L.; Hwu, Y.; Margaritondo, G. Controlled hydrogel photopolymerization inside live systems by X-ray irradiation. *Soft Matter* **2012**, *8*, 1420–1427, doi:10.1039/C1SM06682J.

84. Puchleitner, R.; Riess, G.; Kern, W. X-ray induced cationic curing of epoxy-bonded composites. *Eur. Polym. J.* **2017**, *91*, 31–45, doi:10.1016/j.eurpolymj.2017.03.036.

85. Chen, Z.; Wang, X.; Li, S.; Liu, S.; Miao, H.; Wu, S. Near-Infrared Light Driven Photopolymerization Based On Photon Upconversion. *ChemPhotoChem* **2019**, *3*, 1077–1083, doi:10.1002/CPTC.201900007.

86. Li, Z.; Chen, H.; Wang, C.; Chen, L.; Liu, J.; Liu, R. Efficient photopolymerization of thick pigmented systems using upconversion nanoparticles-assisted photochemistry. *J. Polym. Sci. Part A Polym. Chem.*

2018, *56*, 994–1002, doi:10.1002/pola.28969.

87. Fouassier, J.P.; Allonas, X.; Burget, D. Photopolymerization reactions under visible lights: principle, mechanisms and examples of applications. *Prog. Org. Coatings* **2003**, *47*, 16–36, doi:10.1016/S0300-9440(03)00011-0.

88. Fantino, E.; Vitale, A.; Quaglio, M.; Cocuzza, M.; Pirri, C.F.; Bongiovanni, R. Blue and UV combined photolithographic polymerization for the patterning of thick structures. *Chem. Eng. J.* **2015**, *267*, 65–72, doi:10.1016/J.CEJ.2014.12.088.

89. Pascault, J.P.; Williams, R.J.J. Thermosetting Polymers. In *Handbook of Polymer Synthesis, Characterization, and Processing*; Marcel Dekker: New York, 2013; pp. 519–533 ISBN 9780470630327.

90. Decker, C.; Jenkins, A.D. Kinetic Approach of 02 Inhibition in Ultraviolet- and Laser-Induced Polymerizations. *Macromolecules* **1985**, *18*, 1241–1244.

91. Yagci, Y.; Jockusch, S.; Turro, N.J. Photoinitiated Polymerization: Advances, Challenges, and Opportunities. *Macromolecules* **2010**, *43*, 6245–6260, doi:10.1021/MA1007545.

92. Xu, J.; Jung, K.; Atme, A.; Shanmugam, S.; Boyer, C. A Robust and Versatile Photoinduced Living Polymerization of Conjugated and Unconjugated Monomers and Its Oxygen Tolerance. *J. Am. Chem. Soc.* **2014**, *136*, 5508–5519, doi:10.1021/JA501745G.

93. Kolb, H.C.; Finn, M.G.; Sharpless, K.B. Click Chemistry: Diverse Chemical Function from a Few Good Reactions. *Angew. Chemie Int. Ed.* **2001**, *40*, 2004–2021, doi:10.1002/1521-3773(20010601)40:11<2004::AID-ANIE2004>3.0.CO;2-5.

94. Hoyle, C.E.; Lowe, A.B.; Bowman, C.N. Thiol-click chemistry: a multifaceted toolbox for small molecule and polymer synthesis. *Chem. Soc. Rev.* **2010**, *39*, 1355–1387, doi:10.1039/B901979K.

95. Hoyle, C.E.; Bowman, C.N. Thiol-Ene Click Chemistry. *Angew. Chemie Int. Ed.* **2010**, *49*, 1540–1573, doi:10.1002/anie.200903924.

96. Kloxin, C.J.; Scott, T.F.; Bowman, C.N. Stress Relaxation via Addition−Fragmentation Chain Transfer in a Thiol-ene Photopolymerization. *Macromolecules* **2009**, *42*, 2551–2556, doi:10.1021/MA802771B.

97. Mongkhontreerat, S.; Öberg, K.; Erixon, L.; Löwenhielm, P.; Hult, A.;

Malkoch, M. UV initiated thiol-ene chemistry: A facile and modular synthetic methodology for the construction of functional 3D networks with tunable properties. *J. Mater. Chem. A* **2013**, *1*, 13732–13737, doi:10.1039/c3ta12963b.

98. Carlborg, C.F.; Haraldsson, T.; Öberg, K.; Malkoch, M.; van der Wijngaart, W. Beyond PDMS: off-stoichiometry thiol–ene (OSTE) based soft lithography for rapid prototyping of microfluidic devices. *Lab Chip* **2011**, *11*, 3136, doi:10.1039/c1lc20388f.

99. Marx, P.; Romano, A.; Roppolo, I.; Chemelli, A.; Mühlbacher, I.; Kern, W.; Chaudhary, S.; Andritsch, T.; Sangermano, M.; Wiesbrock, F. 3D-Printing of High-κ Thiol-Ene Resins with Spiro-Orthoesters as Anti-Shrinkage Additive. *Macromol. Mater. Eng.* **2019**, *304*, 1900515, doi:10.1002/MAME.201900515.

100. Lowe, A.B. Thiol-ene "click" reactions and recent applications in polymer and materials synthesis. *Polym. Chem.* **2010**, *1*, 17–36, doi:10.1039/B9PY00216B.

101. Michaudel, Q.; Kottisch, V.; Fors, B.P. Cationic Polymerization: From Photoinitiation to Photocontrol. *Angew. Chemie Int. Ed.* **2017**, *56*, 9670–9679, doi:10.1002/anie.201701425.

102. Kodama, H. Automatic method for fabricating a three-dimensional plastic model with photo-hardening polymer. *Rev. Sci. Instrum.* **1998**, *52*, 1770, doi:10.1063/1.1136492.

103. Palmara, G.; Frascella, F.; Roppolo, I.; Chiappone, A.; Chiadò, A. Functional 3D printing: Approaches and bioapplications. *Biosens. Bioelectron.* **2021**, *175*, 112849, doi:10.1016/J.BIOS.2020.112849.

104. Pagac, M.; Hajnys, J.; Ma, Q.-P.; Jancar, L.; Jansa, J.; Stefek, P.; Mesicek, J. A Review of Vat Photopolymerization Technology: Materials, Applications, Challenges, and Future Trends of 3D Printing. *Polymers (Basel).* **2021**, *13*, 598, doi:10.3390/polym13040598.

105. Stansbury, J.W.; Idacavage, M.J. 3D printing with polymers: Challenges among expanding options and opportunities. *Dent. Mater.* **2016**, *32*, 54–64, doi:10.1016/J.DENTAL.2015.09.018.

106. Bernal, P.N.; Delrot, P.; Loterie, D.; Li, Y.; Malda, J.; Moser, C.; Levato, R. Volumetric Bioprinting of Complex Living-Tissue Constructs within Seconds. *Adv. Mater.* **2019**, *31*, 1904209, doi:10.1002/ADMA.201904209.

107. Regehly, M.; Garmshausen, Y.; Reuter, M.; König, N.F.; Israel, E.; Kelly, D.P.; Chou, C.Y.; Koch, K.; Asfari, B.; Hecht, S. Xolography for linear volumetric 3D printing. *Nature* **2020**, *588*, 620–624, doi:10.1038/s41586-020-3029-7.

108. Ge, G.; Wang, Q.; Zhang, Y.-Z.; Alshareef, H.N.; Dong, X. 3D Printing of Hydrogels for Stretchable Ionotronic Devices. *Adv. Funct. Mater.* **2021**, 2107437, doi:10.1002/ADFM.202107437.

109. Han, D.; Lu, Z.; Chester, S.A.; Lee, H. Micro 3D Printing of a Temperature-Responsive Hydrogel Using Projection Micro-Stereolithography. *Sci. Rep.* **2018**, *8*, 1–10, doi:10.1038/s41598-018-20385-2.

110. Tumbleston, J.R.; Shirvanyants, D.; Ermoshkin, N.; Janusziewicz, R.; Johnson, A.R.; Kelly, D.; Chen, K.; Pinschmidt, R.; Rolland, J.P.; Ermoshkin, A.; et al. Continuous liquid interface production of 3D objects. *Science (80-.).* **2015**, *347*, 1349–1352, doi:10.1126/SCIENCE.AAA2397.

111. Janusziewicz, R.; Tumbleston, J.R.; Quintanilla, A.L.; Mecham, S.J.; DeSimone, J.M. Layerless fabrication with continuous liquid interface production. *Proc. Natl. Acad. Sci.* **2016**, *113*, 11703–11708, doi:10.1073/PNAS.1605271113.

112. Rumi, M.; Barlow, S.; Wang, J.; Perry, J.W.; Marder, S.R. Two-Photon Absorbing Materials and Two-Photon-Induced Chemistry. *Adv. Polym. Sci.* **2008**, *213*, 1–95, doi:10.1007/12_2008_133.

113. Zhou, X.; Hou, Y.; Lin, J. A review on the processing accuracy of two-photon polymerization. *AIP Adv.* **2015**, *5*, 030701, doi:10.1063/1.4916886.

114. Felipe-Mendes, C.; Ruiz-Rubio, L.; Vilas-Vilela, J.L. Biomaterials obtained by photopolymerization: from UV to two photon. *Emergent Mater.* **2020**, *3*, 453–468, doi:10.1007/s42247-020-00114-0.

115. Maruo, S.; Fourkas, J.T. Recent progress in multiphoton microfabrication. *Laser Photon. Rev.* **2008**, *2*, 100–111, doi:10.1002/LPOR.200710039.

116. Stampfl, J.; Liska, R.; Ovsianikov, A. *Multiphoton Lithography: Techniques, Materials, and Applications*; 2016; ISBN 978-3-527-33717-0.

117. Loterie, D.; Delrot, P.; Moser, C. High-resolution tomographic volumetric additive manufacturing. *Nat. Commun.* **2020**, *11*, 1–6, doi:10.1038/s41467-020-14630-4.

118. Chiappone, A.; Fantino, E.; Roppolo, I.; Lorusso, M.; Manfredi, D.; Fino, P.;

Pirri, C.F.; Calignano, F. 3D Printed PEG-Based Hybrid Nanocomposites Obtained by Sol–Gel Technique. *ACS Appl. Mater. Interfaces* **2016**, *8*, 5627–5633, doi:10.1021/ACSAMI.5B12578.

119. Warner, J.; Soman, P.; Zhu, W.; Tom, M.; Chen, S. Design and 3D Printing of Hydrogel Scaffolds with Fractal Geometries. *ACS Biomater. Sci. Eng.* **2016**, *2*, 1763–1770, doi:10.1021/ACSBIOMATERIALS.6B00140.

120. Chan, V.; Zorlutuna, P.; Jeong, J.H.; Kong, H.; Bashir, R. Three-dimensional photopatterning of hydrogels using stereolithography for long-term cell encapsulation. *Lab Chip* **2010**, *10*, 2062–2070, doi:10.1039/C004285D.

121. Chan, V.; Jeong, J.H.; Bajaj, P.; Collens, M.; Saif, T.; Kong, H.; Bashir, R. Multi-material bio-fabrication of hydrogel cantilevers and actuators with stereolithography. *Lab Chip* **2011**, *12*, 88–98, doi:10.1039/C1LC20688E.

122. Chandler, E.M.; Berglund, C.M.; Lee, J.S.; Polacheck, W.J.; Gleghorn, J.P.; Kirby, B.J.; Fischbach, C. Stiffness of photocrosslinked RGD-alginate gels regulates adipose progenitor cell behavior. *Biotechnol. Bioeng.* **2011**, *108*, 1683–1692, doi:10.1002/BIT.23079.

123. Lin, H.; Zhang, D.; Alexander, P.G.; Yang, G.; Tan, J.; Cheng, A.W.M.; Tuan, R.S. Application of visible light-based projection stereolithography for live cell-scaffold fabrication with designed architecture. *Biomaterials* **2013**, *34*, 331–339, doi:10.1016/J.BIOMATERIALS.2012.09.048.

124. Occhetta, P.; Visone, R.; Russo, L.; Cipolla, L.; Moretti, M.; Rasponi, M. VA-086 methacrylate gelatine photopolymerizable hydrogels: A parametric study for highly biocompatible 3D cell embedding. *J. Biomed. Mater. Res. Part A* **2015**, *103*, 2109–2117, doi:10.1002/JBM.A.35346.

125. Grützmacher, H.; Geier, J.; Stein, D.; Ott, T.; Schönberg, H.; Sommerlade, R.H.; Boulmaaz, S.; Wolf, J.P.; Murer, P.; Ulrich, T. A simple straightforward synthesis of phenylphosphane and the photoinitiator bis(mesitoyl)phenylphosphane oxide (IRGACURE 819). *Chimia (Aarau).* **2008**, *62*, 18–22, doi:10.2533/CHIMIA.2008.18.

126. Fouassier, J.P.; Lalevée, J. Photoinitiators for Polymer Synthesis: Scope, Reactivity and Efficiency. *Photoinitiators Polym. Synth. Scope, React. Effic.* **2012**, doi:10.1002/9783527648245.

127. Stassi, S.; Fantino, E.; Calmo, R.; Chiappone, A.; Gillono, M.; Scaiola, D.; Pirri, C.F.; Ricciardi, C.; Chiadò, A.; Roppolo, I. Polymeric 3D Printed Functional Microcantilevers for Biosensing Applications. *ACS Appl. Mater.*

Interfaces **2017**, *9*, 19193–19201, doi:10.1021/ACSAMI.7B04030.

128. Gillono, M.; Roppolo, I.; Frascella, F.; Scaltrito, L.; Pirri, C.F.; Chiappone, A. CO2 permeability control in 3D printed light responsive structures. *Appl. Mater. Today* **2020**, *18*, 100470, doi:10.1016/J.APMT.2019.100470.

129. Lantean, S.; Barrera, G.; Pirri, C.F.; Tiberto, P.; Sangermano, M.; Roppolo, I.; Rizza, G. 3D Printing of Magnetoresponsive Polymeric Materials with Tunable Mechanical and Magnetic Properties by Digital Light Processing. *Adv. Mater. Technol.* **2019**, *4*, 1900505, doi:10.1002/ADMT.201900505.

130. Lantean, S.; Roppolo, I.; Sangermano, M.; Hayoun, M.; Dammak, H.; Rizza, G. Programming the microstructure of magnetic nanocomposites in DLP 3D printing. *Addit. Manuf.* **2021**, *47*, 102343, doi:10.1016/J.ADDMA.2021.102343.

131. Cortés, A.; Cosola, A.; Sangermano, M.; Campo, M.; González Prolongo, S.; Pirri, C.F.; Jiménez-Suárez, A.; Chiappone, A. DLP 4D-Printing of Remotely, Modularly, and Selectively Controllable Shape Memory Polymer Nanocomposites Embedding Carbon Nanotubes. *Adv. Funct. Mater.* **2021**, *31*, 2106774, doi:10.1002/adfm.202106774.

132. Gonzalez, G.; Chiappone, A.; Roppolo, I.; Fantino, E.; Bertana, V.; Perrucci, F.; Scaltrito, L.; Pirri, F.; Sangermano, M. Development of 3D printable formulations containing CNT with enhanced electrical properties. *Polymer (Guildf).* **2017**, *109*, 246–253, doi:10.1016/J.POLYMER.2016.12.051.

133. Fantino, E.; Chiappone, A.; Roppolo, I.; Manfredi, D.; Bongiovanni, R.; Pirri, C.F.; Calignano, F. 3D Printing of Conductive Complex Structures with In Situ Generation of Silver Nanoparticles. *Adv. Mater.* **2016**, *28*, 3712–3717, doi:10.1002/ADMA.201505109.

134. Fantino, E.; Chiappone, A.; Calignano, F.; Fontana, M.; Pirri, F.; Roppolo, I. In situ thermal generation of silver nanoparticles in 3D printed polymeric structures. *Materials (Basel).* **2016**, *9*, 589, doi:10.3390/ma9070589.

135. Pawar, A.A.; Saada, G.; Cooperstein, I.; Larush, L.; Jackman, J.A.; Tabaei, S.R.; Cho, N.J.; Magdassi, S. High-performance 3D printing of hydrogels by water-dispersible photoinitiator nanoparticles. *Sci. Adv.* **2016**, *2*, doi:10.1126/SCIADV.1501381.

136. Park, H.K.; Shin, M.; Kim, B.; Park, J.W.; Lee, H. A visible light-curable yet visible wavelength-transparent resin for stereolithography 3D printing. *NPG Asia Mater.* **2018**, *10*, 82–89, doi:10.1038/s41427-018-0021-x.

137. Palaganas, N.B.; Mangadlao, J.D.; De Leon, A.C.C.; Palaganas, J.O.; Pangilinan, K.D.; Lee, Y.J.; Advincula, R.C. 3D printing of photocurable cellulose nanocrystal composite for fabrication of complex architectures via stereolithography. *ACS Appl. Mater. Interfaces* **2017**, *9*, 34314–34324, doi:10.1021/acsami.7b09223.

138. Noè, C.; Tonda-Turo, C.; Chiappone, A.; Sangermano, M.; Hakkarainen, M. Light processable starch hydrogels. *Polymers (Basel).* **2020**, *12*, 1359, doi:10.3390/POLYM12061359.

139. Eibel, A.; Schmallegger, M.; Zalibera, M.; Huber, A.; Bürkl, Y.; Grützmacher, H.; Gescheidt, G. Extending the Scope of Bis(acyl)phosphane Oxides: Additional Derivatives. *Eur. J. Inorg. Chem.* **2017**, *2017*, 2469–2478, doi:10.1002/EJIC.201700140.

140. Gonsalvi, L.; Peruzzini, M. Novel Synthetic Pathways for Bis(acyl)phosphine Oxide Photoinitiators. *Angew. Chemie Int. Ed.* **2012**, *51*, 7895–7897, doi:10.1002/anie.201203648.

141. Huber, A.; Kuschel, A.; Ott, T.; Santiso-Quinones, G.; Stein, D.; Bräuer, J.; Kissner, R.; Krumeich, F.; Schönberg, H.; Levalois-Grützmacher, J.; et al. Phosphorous-Functionalized Bis(acyl)phosphane Oxides for Surface Modification. *Angew. Chemie* **2012**, *124*, 4726–4730, doi:10.1002/ANGE.201201026.

142. Beil, A.; Müller, G.; Käser, D.; Hattendorf, B.; Li, Z.; Krumeich, F.; Rosenthal, A.; Rana, V.K.; Schönberg, H.; Benkő, Z.; et al. Bismesitoylphosphinic Acid (BAPO-OH): A Ligand for Copper Complexes and Four-Electron Photoreductant for the Preparation of Copper Nanomaterials. *Angew. Chemie Int. Ed.* **2018**, *57*, 7697–7702, doi:10.1002/ANIE.201800456.

143. Wang, J.; Chiappone, A.; Roppolo, I.; Shao, F.; Fantino, E.; Lorusso, M.; Rentsch, D.; Dietliker, K.; Pirri, C.F.; Grützmacher, H. All-in-One Cellulose Nanocrystals for 3D Printing of Nanocomposite Hydrogels. *Angew. Chemie Int. Ed.* **2018**, *57*, 2353–2356, doi:10.1002/ANIE.201710951.

144. Wang, J.; Stanic, S.; Altun, A.A.; Schwentenwein, M.; Dietliker, K.; Jin, L.; Stampfl, J.; Baudis, S.; Liska, R.; Grützmacher, H. A highly efficient waterborne photoinitiator for visible-light-induced three-dimensional printing of hydrogels. *Chem. Commun.* **2018**, *54*, 920–923, doi:10.1039/C7CC09313F.

145. Zanchetta, E.; Cattaldo, M.; Franchin, G.; Schwentenwein, M.; Homa, J.; Brusatin, G.; Colombo, P. Stereolithography of SiOC Ceramic Microcomponents. *Adv. Mater.* **2016**, *28*, 370–376, doi:10.1002/adma.201503470.

146. Zhang, J.; Dumur, F.; Xiao, P.; Graff, B.; Bardelang, D.; Gigmes, D.; Fouassier, J.P.; Lalevée, J. Structure design of naphthalimide derivatives: Toward versatile photoinitiators for Near-UV/Visible LEDs, 3D printing, and water-soluble photoinitiating systems. *Macromolecules* **2015**, *48*, 2054–2063, doi:10.1021/ACS.MACROMOL.5B00201.

147. Lim, K.S.; Schon, B.S.; Mekhileri, N. V.; Brown, G.C.J.; Chia, C.M.; Prabakar, S.; Hooper, G.J.; Woodfield, T.B.F. New Visible-Light Photoinitiating System for Improved Print Fidelity in Gelatin-Based Bioinks. *ACS Biomater. Sci. Eng.* **2016**, *2*, 1752–1762, doi:10.1021/ACSBIOMATERIALS.6B00149.

148. Bertlein, S.; Brown, G.; Lim, K.S.; Jungst, T.; Boeck, T.; Blunk, T.; Tessmar, J.; Hooper, G.J.; Woodfield, T.B.F.; Groll, J. Thiol–Ene Clickable Gelatin: A Platform Bioink for Multiple 3D Biofabrication Technologies. *Adv. Mater.* **2017**, *29*, 1703404, doi:10.1002/ADMA.201703404.

149. Lee, H.; Shin, D.; Shin, S.; Hyun, J. Effect of gelatin on dimensional stability of silk fibroin hydrogel structures fabricated by digital light processing 3D printing. *J. Ind. Eng. Chem.* **2020**, *89*, 119–127, doi:10.1016/J.JIEC.2020.03.034.

150. Al Mousawi, A.; Garra, P.; Schmitt, M.; Toufaily, J.; Hamieh, T.; Graff, B.; Fouassier, J.P.; Dumur, F.; Lalevée, J. 3-Hydroxyflavone and N-Phenylglycine in High Performance Photoinitiating Systems for 3D Printing and Photocomposites Synthesis. *Macromolecules* **2018**, *51*, 4633–4641, doi:10.1021/ACS.MACROMOL.8B00979/SUPPL_FILE/MA8B00979_SI_001.PDF.

151. Na, K.; Shin, S.; Lee, H.; Shin, D.; Baek, J.; Kwak, H.; Park, M.; Shin, J.; Hyun, J. Effect of solution viscosity on retardation of cell sedimentation in DLP 3D printing of gelatin methacrylate/silk fibroin bioink. *J. Ind. Eng. Chem.* **2018**, *61*, 340–347, doi:10.1016/j.jiec.2017.12.032.

152. Ahn, D.; Stevens, L.M.; Zhou, K.; Page, Z.A. Rapid High-Resolution Visible Light 3D Printing. *ACS Cent. Sci.* **2020**, *6*, 1555–1563, doi:10.1021/acscentsci.0c00929.

153. Mousawi, A. Al; Dumur, F.; Garra, P.; Toufaily, J.; Hamieh, T.; Goubard, F.; Bui, T.-T.; Graff, B.; Gigmes, D.; Fouassier, J.P.; et al. Azahelicenes as visible light photoinitiators for cationic and radical polymerization: Preparation of photoluminescent polymers and use in high performance LED projector 3D printing resins. *J. Polym. Sci. Part A Polym. Chem.* **2017**, *55*, 1189–1199, doi:10.1002/POLA.28476.

154. Petko, F.; Galek, M.; Hola, E.; Popielarz, R.; Ortyl, J. One-Component Cationic Photoinitiators from Tunable Benzylidene Scaffolds for 3D Printing Applications. *Macromolecules* **2021**, *54*, 7070–7087, doi:10.1021/ACS.MACROMOL.1C01048.

155. Mendes-Felipe, C.; Oliveira, J.; Etxebarria, I.; Vilas-Vilela, J.L.; Lanceros-Mendez, S. State-of-the-Art and Future Challenges of UV Curable Polymer-Based Smart Materials for Printing Technologies. *Adv. Mater. Technol.* **2019**, *4*, 1800618, doi:10.1002/ADMT.201800618.

156. Wen, M.; Scriven, L.E.; McCormick, A. V. Differential scanning calorimetry and cantilever deflection studies of polymerization kinetics and stress in ultraviolet curing of multifunctional (meth)acrylate coatings. *Macromolecules* **2002**, *35*, 112–120, doi:10.1021/ma010310h.

157. Anseth, K.S.; Wang, C.M.; Bowman, C.N. Reaction behaviour and kinetic constants for photopolymerizations of multi(meth)acrylate monomers. *Polymer (Guildf).* **1994**, *35*, 3243–3250, doi:10.1016/0032-3861(94)90129-5.

158. Andrzejewska, E. Photopolymerization kinetics of multifunctional monomers. *Prog. Polym. Sci.* **2001**, *26*, 605–665, doi:10.1016/S0079-6700(01)00004-1.

159. Kannurpatti, A.R.; Anseth, J.W.; Bowman, C.N. A study of the evolution of mechanical properties and structural heterogeneity of polymer networks formed by photopolymerizations of multifunctional (meth)acrylates. *Polymer (Guildf).* **1998**, *39*, 2507–2513, doi:10.1016/S0032-3861(97)00585-5.

160. Liska, R.; Schuster, M.; Inführ, R.; Turecek, C.; Fritscher, C.; Seidl, B.; Schmidt, V.; Kuna, L.; Haase, A.; Varga, F.; et al. Photopolymers for rapid prototyping. *J. Coatings Technol. Res.* **2007**, *4*, 505–510, doi:10.1007/s11998-007-9059-3.

161. Zhao, Z.; Mu, X.; Wu, J.; Qi, H.J.; Fang, D. Effects of oxygen on interfacial

strength of incremental forming of materials by photopolymerization. *Extrem. Mech. Lett.* **2016**, *9*, 108–118, doi:10.1016/J.EML.2016.05.012.

162. Ligon-Auer, S.C.; Schwentenwein, M.; Gorsche, C.; Stampfl, J.; Liska, R. Toughening of photo-curable polymer networks: a review. *Polym. Chem.* **2015**, *7*, 257–286, doi:10.1039/C5PY01631B.

163. Boddapati, A.; Rahane, S.B.; Slopek, R.P.; Breedveld, V.; Henderson, C.L.; Grover, M.A. Gel time prediction of multifunctional acrylates using a kinetics model. *Polymer (Guildf).* **2011**, *52*, 866–873, doi:10.1016/J.POLYMER.2010.12.024.

164. Kim, L.U.; Kim, J.W.; Kim, C.K. Effects of molecular structure of the resins on the volumetric shrinkage and the mechanical strength of dental restorative composites. *Biomacromolecules* **2006**, *7*, 2680–2687, doi:10.1021/bm060453h.

165. McNair, O.D.; Janisse, A.P.; Krzeminski, D.E.; Brent, D.E.; Gould, T.E.; Rawlins, J.W.; Savin, D.A. Impact Properties of Thiol–Ene Networks. *ACS Appl. Mater. Interfaces* **2013**, *5*, 11004–11013, doi:10.1021/AM403238G.

166. Oesterreicher, A.; Wiener, J.; Roth, M.; Moser, A.; Gmeiner, R.; Edler, M.; Pinter, G.; Griesser, T. Tough and degradable photopolymers derived from alkyne monomers for 3D printing of biomedical materials. *Polym. Chem.* **2016**, *7*, 5169–5180, doi:10.1039/C6PY01132B.

167. Sycks, D.G.; Wu, T.; Park, H.S.; Gall, K. Tough, stable spiroacetal thiol-ene resin for 3D printing. *J. Appl. Polym. Sci.* **2018**, *135*, 46259, doi:10.1002/APP.46259.

168. Senyurt, A.F.; Hoyle, C.E.; Wei, H.; Piland, S.G.; Gould, T.E. Thermal and mechanical properties of cross-linked photopolymers based on multifunctional thiol-urethane ene monomers. *Macromolecules* **2007**, *40*, 3174–3182, doi:10.1021/ma0626463.

169. Decker, C.; Nguyen Thi Viet, T.; Decker, D.; Weber-Koehl, E. UV-radiation curing of acrylate/epoxide systems. *Polymer (Guildf).* **2001**, *42*, 5531–5541, doi:10.1016/S0032-3861(01)00065-9.

170. Batch, G.L.; Macosko, C.W. Oxygen inhibition in differential scanning calorimetry of free radical polymerization. *Thermochim. Acta* **1990**, *166*, 185–198, doi:10.1016/0040-6031(90)80180-7.

171. Gastaldi, M.; Cardano, F.; Zanetti, M.; Viscardi, G.; Barolo, C.; Bordiga, S.; Magdassi, S.; Fin, A.; Roppolo, I. Functional Dyes in Polymeric 3D Printing:

Applications and Perspectives. *ACS Mater. Lett.* **2020**, *3*, 1–17, doi:10.1021/ACSMATERIALSLETT.0C00455.

172. Lee, M.P.; Cooper, G.J.T.; Hinkley, T.; Gibson, G.M.; Padgett, M.J.; Cronin, L. Development of a 3D printer using scanning projection stereolithography. *Sci. Rep.* **2015**, *5*, 1–5, doi:10.1038/srep09875.

173. Peng, B.; Yang, Y.; Gu, K.; Amis, E.J.; Cavicchi, K.A. Digital Light Processing 3D Printing of Triple Shape Memory Polymer for Sequential Shape Shifting. *ACS Mater. Lett.* **2019**, *1*, 410–417, doi:10.1021/ACSMATERIALSLETT.9B00262.

174. Frascella, F.; González, G.; Bosch, P.; Angelini, A.; Chiappone, A.; Sangermano, M.; Pirri, C.F.; Roppolo, I. Three-Dimensional Printed Photoluminescent Polymeric Waveguides. *ACS Appl. Mater. Interfaces* **2018**, *10*, 39319–39326, doi:10.1021/ACSAMI.8B16036.

175. Roppolo, I.; Chiappone, A.; Angelini, A.; Stassi, S.; Frascella, F.; Pirri, C.F.; Ricciardi, C.; Descrovi, E. 3D printable light-responsive polymers. *Mater. Horizons* **2017**, *4*, 396–401, doi:10.1039/C7MH00072C.

176. Wang, F.; Chong, Y.; Wang, F.; He, C. Photopolymer resins for luminescent three-dimensional printing. *J. Appl. Polym. Sci.* **2017**, *134*, 44988, doi:10.1002/APP.44988.

177. Lin, D.; Jin, S.; Zhang, F.; Wang, C.; Wang, Y.; Zhou, C.; Cheng, G.J. 3D stereolithography printing of graphene oxide reinforced complex architectures. *Nanotechnology* **2015**, *26*, 434003, doi:10.1088/0957-4484/26/43/434003.

178. Chen, S.; Yang, J.; Jia, Y.G.; Lu, B.; Ren, L. A study of 3D-printable reinforced composite resin: PMMA modified with silver nanoparticles loaded cellulose nanocrystal. *Materials (Basel).* **2018**, *11*, 2444, doi:10.3390/ma11122444.

179. Cortés, A.; Aguilar, J.L.; Cosola, A.; Fernández Sanchez-Romate, X.X.; Jiménez-Suárez, A.; Sangermano, M.; Campo, M.; Prolongo, S.G. 4D-Printed Resins and Nanocomposites Thermally Stimulated by Conventional Heating and IR Radiation. *ACS Appl. Polym. Mater.* **2021**, *3*, 5207–5215, doi:10.1021/acsapm.1c00970.

180. Liu, J.; Sun, L.; Xu, W.; Wang, Q.; Yu, S.; Sun, J. Current advances and future perspectives of 3D printing natural-derived biopolymers. *Carbohydr. Polym.* **2019**, *207*, 297–316, doi:10.1016/J.CARBPOL.2018.11.077.

181. Kousaalya, A.B. Sustainable photo-curable polymers in additive manufacturing arena: A review. *ACS Symp. Ser.* **2020**, *1372*, 89–98, doi:10.1021/BK-2020-1372.CH005.

182. Voet, V.S.D.; Guit, J.; Loos, K. Sustainable Photopolymers in 3D Printing: A Review on Biobased, Biodegradable, and Recyclable Alternatives. *Macromol. Rapid Commun.* **2021**, *42*, 2000475, doi:10.1002/MARC.202000475.

183. Guit, J.; Tavares, M.B.L.; Hul, J.; Ye, C.; Loos, K.; Jager, J.; Folkersma, R.; Voet, V.S.D. Photopolymer Resins with Biobased Methacrylates Based on Soybean Oil for Stereolithography. *ACS Appl. Polym. Mater.* **2020**, *2*, 949–957, doi:10.1021/ACSAPM.9B01143.

184. Silbert, S.D.; Simpson, P.; Setien, R.; Holthaus, M.; Scala, J. La; Ulven, C.A.; Webster, D.C. Exploration of Bio-Based Functionalized Sucrose Ester Resins for Additive Manufacturing via Stereolithography. *ACS Appl. Polym. Mater.* **2020**, *2*, 2910–2918, doi:10.1021/ACSAPM.0C00417.

185. Branciforti, D.S.; Lazzaroni, S.; Milanese, C.; Castiglioni, M.; Auricchio, F.; Pasini, D.; Dondi, D. Visible light 3D printing with epoxidized vegetable oils. *Addit. Manuf.* **2019**, *25*, 317–324, doi:10.1016/J.ADDMA.2018.11.020.

186. Sutton, J.T.; Rajan, K.; Harper, D.P.; Chmely, S.C. Lignin-Containing Photoactive Resins for 3D Printing by Stereolithography. *ACS Appl. Mater. Interfaces* **2018**, *10*, 36456–36463, doi:10.1021/ACSAMI.8B13031.

187. Bassett, A.W.; Honnig, A.E.; Breyta, C.M.; Dunn, I.C.; Scala, J.J. La; Joseph F. Stanzione, I. Vanillin-Based Resin for Additive Manufacturing. *ACS Sustain. Chem. Eng.* **2020**, *8*, 5626–5635, doi:10.1021/ACSSUSCHEMENG.0C00159.

188. Ding, R.; Du, Y.; Goncalves, R.B.; Francis, L.F.; Reineke, T.M. Sustainable near UV-curable acrylates based on natural phenolics for stereolithography 3D printing. *Polym. Chem.* **2019**, *10*, 1067–1077, doi:10.1039/C8PY01652F.

189. Miao, J.-T.; Peng, S.; Ge, M.; Li, Y.; Zhong, J.; Weng, Z.; Wu, L.; Zheng, L. Three-Dimensional Printing Fully Biobased Heat-Resistant Photoactive Acrylates from Aliphatic Biomass. *ACS Sustain. Chem. Eng.* **2020**, *8*, 9415–9424, doi:10.1021/ACSSUSCHEMENG.0C02168.

190. Krishnamoorthy, S.; Wadnap, S.; Noorani, B.; Xu, H.; Xu, C. Investigation of gelatin methacrylate working curves in dynamic optical projection

stereolithography of vascular-like constructs. *Eur. Polym. J.* **2020**, *124*, 109487, doi:10.1016/J.EURPOLYMJ.2020.109487.

191. Melilli, G.; Carmagnola, I.; Tonda-Turo, C.; Pirri, F.; Ciardelli, G.; Sangermano, M.; Hakkarainen, M.; Chiappone, A. DLP 3D printing meets lignocellulosic biopolymers: Carboxymethyl cellulose inks for 3D biocompatible hydrogels. *Polymers (Basel).* **2020**, *12*, 1655, doi:10.3390/POLYM12081655.

192. Shen, Y.; Tang, H.; Huang, X.; Hang, R.; Zhang, X.; Wang, Y.; Yao, X. DLP printing photocurable chitosan to build bio-constructs for tissue engineering. *Carbohydr. Polym.* **2020**, *235*, 115970, doi:10.1016/J.CARBPOL.2020.115970.

193. Kim, S.H.; Yeon, Y.K.; Lee, J.M.; Chao, J.R.; Lee, Y.J.; Seo, Y.B.; Sultan, M.T.; Lee, O.J.; Lee, J.S.; Yoon, S. Il; et al. Precisely printable and biocompatible silk fibroin bioink for digital light processing 3D printing. *Nat. Commun.* **2018**, *9*, 1–14, doi:10.1038/s41467-018-03759-y.

194. Weems, A.C.; Chiaie, K.R.D.; Worch, J.C.; Stubbs, C.J.; Dove, A.P. Terpene- and terpenoid-based polymeric resins for stereolithography 3D printing. *Polym. Chem.* **2019**, *10*, 5959–5966, doi:10.1039/C9PY00950G.

195. Zhao, Z.; Kuang, X.; Yuan, C.; Qi, H.J.; Fang, D. Hydrophilic/Hydrophobic Composite Shape-Shifting Structures. *ACS Appl. Mater. Interfaces* **2018**, *10*, 19932–19939, doi:10.1021/ACSAMI.8B02444.

196. Zarek, M.; Mansour, N.; Shapira, S.; Cohn, D. 4D Printing of Shape Memory-Based Personalized Endoluminal Medical Devices. *Macromol. Rapid Commun.* **2017**, *38*, 1600628, doi:10.1002/marc.201600628.

197. Zarek, M.; Layani, M.; Cooperstein, I.; Sachyani, E.; Cohn, D.; Magdassi, S. 3D Printing of Shape Memory Polymers for Flexible Electronic Devices. *Adv. Mater.* **2016**, *28*, 4449–4454, doi:10.1002/adma.201503132.

198. Dutta, S.; Cohn, D. Temperature and pH responsive 3D printed scaffolds. *J. Mater. Chem. B* **2017**, *5*, 9514–9521, doi:10.1039/C7TB02368E.

199. Ge, Q.; Sakhaei, A.H.; Lee, H.; Dunn, C.K.; Fang, N.X.; Dunn, M.L. Multimaterial 4D Printing with Tailorable Shape Memory Polymers. *Sci. Rep.* **2016**, *6*, 1–11, doi:10.1038/srep31110.

200. Liu, G.; Zhao, Y.; Wu, G.; Lu, J. Origami and 4D printing of elastomer-derived ceramic structures. *Sci. Adv.* **2018**, *4*, 641–658, doi:10.1126/SCIADV.AAT0641.

201. Zhao, Z.; Wu, J.; Mu, X.; Chen, H.; Qi, H.J.; Fang, D. Desolvation Induced Origami of Photocurable Polymers by Digit Light Processing. *Macromol. Rapid Commun.* **2017**, *38*, 1600625, doi:10.1002/MARC.201600625.

202. Invernizzi, M.; Turri, S.; Levi, M.; Suriano, R. 4D printed thermally activated self-healing and shape memory polycaprolactone-based polymers. *Eur. Polym. J.* **2018**, *101*, 169–176, doi:10.1016/j.eurpolymj.2018.02.023.

203. Li, X.; Yang, Y.; Zhang, Y.; Wang, T.; Yang, Z.; Wang, Q.; Zhang, X. Dual-method molding of 4D shape memory polyimide ink. *Mater. Des.* **2020**, *191*, 108606, doi:10.1016/j.matdes.2020.108606.

204. Del Valle, E.M.M. Cyclodextrins and their uses: A review. *Process Biochem.* **2004**, *39*, 1033–1046, doi:10.1016/S0032-9592(03)00258-9.

205. Crini, G. Review: A History of Cyclodextrins. *Chem. Rev.* **2014**, *114*, 10940–10975, doi:10.1021/cr500081p.

206. Kurkov, S. V.; Loftsson, T. Cyclodextrins. *Int. J. Pharm.* **2013**, *453*, 167–180, doi:10.1016/j.ijpharm.2012.06.055.

207. Biwer, A.; Antranikian, G.; Heinzle, E. Enzymatic production of cyclodextrins. *Appl. Microbiol. Biotechnol.* **2002**, *59*, 609–617, doi:10.1007/s00253-002-1057-x.

208. Řezanka, M. Synthesis of substituted cyclodextrins. *Environ. Chem. Lett.* **2019**, *17*, 49–63, doi:10.1007/s10311-018-0779-7.

209. Cosola, A.; Conti, R.; Grützmacher, H.; Sangermano, M.; Roppolo, I.; Pirri, C.F.; Chiappone, A. Multiacrylated Cyclodextrin: A Bio-Derived Photocurable Macromer for VAT 3D Printing. *Macromol. Mater. Eng.* **2020**, *305*, 2000350, doi:10.1002/MAME.202000350.

210. Gil, E.S.; Wu, L.; Xu, L.; Lowe, T.L. β-cyclodextrin-poly(β-amino ester) nanoparticles for sustained drug delivery across the blood-brain barrier. *Biomacromolecules* **2012**, *13*, 3533–3541, doi:10.1021/bm3008633.

211. Rölling, P.; Lamers, M.; Staudt, C. Cross-linked membranes based on acrylated cyclodextrins and polyethylene glycol dimethacrylates for aromatic/aliphatic separation. *J. Memb. Sci.* **2010**, *362*, 154–163, doi:10.1016/J.MEMSCI.2010.06.036.

212. Chaudhuri, S.; Fowler, M.J.; Baker, C.; Stopka, S.A.; Regan, M.S.; Sablatura, L.; Broughton, C.W.; Knight, B.E.; Stabenfeldt, S.E.; Agar, N.Y.R.; et al. β-Cyclodextrin-poly (β-Amino Ester) Nanoparticles Are a

Generalizable Strategy for High Loading and Sustained Release of HDAC Inhibitors. *ACS Appl. Mater. Interfaces* **2021**, *13*, 20960–20973, doi:10.1021/ACSAMI.0C22587.

213. Andrzejewska, E.; Rabek Lars-A, J.F. Modelling the Kinetics of Photoinitiated Polymerization of Di(meth)acrylates. *Polym. Int.* **1997**, *42*, 179–187, doi:10.1002/(SICI)1097-0126(199702)42:2.

214. Fox, T.G.; Loshaek, S. Influence of molecular weight and degree of crosslinking on the specific volume and glass temperature of polymers. *J. Polym. Sci.* **1955**, *15*, 371–390, doi:10.1002/pol.1955.120158006.

215. Lovestead, T.M.; O'Brien, A.K.; Bowman, C.N. Models of multivinyl free radical photopolymerization kinetics. *J. Photochem. Photobiol. A Chem.* **2003**, *159*, 135–143, doi:10.1016/S1010-6030(03)00178-3.

216. Charlesworth, J.M. Effect of crosslink density on molecular relaxations in diepoxide-diamine network polymers. Part 2. The rubbery plateau region. *Polym. Eng. Sci.* **1988**, *28*, 230–236, doi:10.1002/pen.760280406.

217. Simon, G.P.; Allen, P.E.M.; Williams, D.R.G. Properties of dimethacrylate copolymers of varying crosslink density. *Polymer (Guildf).* **1991**, *32*, 2577–2587, doi:10.1016/0032-3861(91)90337-I.

218. Edwards, S.S. Relaxation phenomena in polymers. *Polym. Int.* **1993**, *32*, 435–435, doi:10.1002/pi.4990320416.

219. Allen, P.E..; Clayton, A..; Williams, D.R.. Dynamic-mechanical properties and cross-polarized, proton-enhanced, magic-angle spinning 13C-NMR time constants of urethane acrylates—2. Copolymer networks. *Eur. Polym. J.* **1994**, *30*, 427–432, doi:10.1016/0014-3057(94)90039-6.

220. Park, J.; Eslick, J.; Ye, Q.; Misra, A.; Spencer, P. The influence of chemical structure on the properties in methacrylate-based dentin adhesives. *Dent. Mater.* **2011**, *27*, 1086–93, doi:10.1016/j.dental.2011.07.011.

221. Cook, W.D. Thermal aspects of the kinetics of dimethacrylate photopolymerization. *Polymer (Guildf).* **1992**, *33*, 2152–2161, doi:10.1016/0032-3861(92)90882-W.

222. Hill, D.J.T.; Perera, M.C.S.; Pomery, P.J.; Toh, H.K. Dynamic mechanical properties of networks prepared from siloxane modified divinyl benzene pre-polymers. *Polymer (Guildf).* **2000**, *41*, 9131–9137, doi:10.1016/S0032-3861(00)00260-3.

223. Voet, V.S.D.; Strating, T.; Schnelting, G.H.M.; Dijkstra, P.; Tietema, M.; Xu, J.; Woortman, A.J.J.; Loos, K.; Jager, J.; Folkersma, R. Biobased Acrylate Photocurable Resin Formulation for Stereolithography 3D Printing. *ACS Omega* **2018**, *3*, 1403–1408, doi:10.1021/ACSOMEGA.7B01648.

224. Goddard, J.M.; Hotchkiss, J.H. Polymer surface modification for the attachment of bioactive compounds. *Prog. Polym. Sci.* **2007**, *32*, 698–725, doi:10.1016/J.PROGPOLYMSCI.2007.04.002.

225. Arnold, R.M.; Huddleston, N.E.; Locklin, J. Utilizing click chemistry to design functional interfaces through post-polymerization modification. *J. Mater. Chem.* **2012**, *22*, 19357–19365, doi:10.1039/C2JM31708G.

226. Wang, X.; Cai, X.; Guo, Q.; Zhang, T.; Kobe, B.; Yang, J. i3DP, a robust 3D printing approach enabling genetic post-printing surface modification. *Chem. Commun.* **2013**, *49*, 10064–10066, doi:10.1039/C3CC45817B.

227. Roppolo, I.; Frascella, F.; Gastaldi, M.; Castellino, M.; Ciubini, B.; Barolo, C.; Scaltrito, L.; Nicosia, C.; Zanetti, M.; Chiappone, A. Thiol–yne chemistry for 3D printing: exploiting an off-stoichiometric route for selective functionalization of 3D objects. *Polym. Chem.* **2019**, *10*, 5950–5958, doi:10.1039/C9PY00962K.

228. Gonzalez, G.; Chiappone, A.; Dietliker, K.; Pirri, C.F.; Roppolo, I. Fabrication and Functionalization of 3D Printed Polydimethylsiloxane-Based Microfluidic Devices Obtained through Digital Light Processing. *Adv. Mater. Technol.* **2020**, *5*, 2000374, doi:10.1002/ADMT.202000374.

229. Nair, D.P.; Podgórski, M.; Chatani, S.; Gong, T.; Xi, W.; Fenoli, C.R.; Bowman, C.N. The Thiol-Michael Addition Click Reaction: A Powerful and Widely Used Tool in Materials Chemistry. *Chem. Mater.* **2013**, *26*, 724–744, doi:10.1021/CM402180T.

230. Heggli, M.; Tirelli, N.; Zisch, A.; Hubbell, J.A. Michael-Type Addition as a Tool for Surface Functionalization. *Bioconjug. Chem.* **2003**, *14*, 967–973, doi:10.1021/BC0340621.

231. Rulev, A.Y. Aza-Michael reaction: achievements and prospects. *Russ. Chem. Rev.* **2011**, *80*, 197–218, doi:10.1070/RC2011V080N03ABEH004162/XML.

232. Young, J.S.; Bowman, C.N. Effect of Polymerization Temperature and Cross-Linker Concentration on Reaction Diffusion Controlled Termination. *Macromolecules* **1999**, *32*, 6073–6081, doi:10.1021/MA9902955.

233. Anseth, K.S.; Anderson, K.J.; Bowman, C.N. Radical concentrations, environments, and reactivities during crosslinking polymerizations. *Macromol. Chem. Phys.* **1996**, *197*, 833–848, doi:10.1002/MACP.1996.021970306.

234. Kim, M.; Schmitt, S.K.; Choi, J.W.; Krutty, J.D.; Gopalan, P. From Self-Assembled Monolayers to Coatings: Advances in the Synthesis and Nanobio Applications of Polymer Brushes. *Polym. 2015, Vol. 7, Pages 1346-1378* **2015**, *7*, 1346–1378, doi:10.3390/POLYM7071346.

235. Wang, S.; Wang, Z.; Li, J.; Li, L.; Hu, W. Surface-grafting polymers: from chemistry to organic electronics. *Mater. Chem. Front.* **2020**, *4*, 692–714, doi:10.1039/C9QM00450E.

236. Zhou, J.; Allonas, X.; Liu, X.; Wu, S. Facile modification on the oxygen-inhibited layer of photopolymerized acrylates via aza-Michael addition. *Polym. Int.* **2021**, *70*, 845–850, doi:10.1002/PI.6174.

237. Ran, Q.; Li, B.; Sun, D.; Yin, H.; Wan, Y.; Yang, C.; Liu, Y.; Mao, Y. Using self-synthesized aminopropyl-terminated polydimethylsiloxane to toughen epoxy resin: The role of molecular weight of polydimethylsiloxane. *J. Vinyl Addit. Technol.* **2017**, *23*, 305–311, doi:10.1002/VNL.21506.

238. Kuypers, S.; Pramanik, S.K.; D'Olieslaeger, L.; Reekmans, G.; Peters, M.; D'Haen, J.; Vanderzande, D.; Junkers, T.; Adriaensens, P.; Ethirajan, A. Interfacial thiol–isocyanate reactions for functional nanocarriers: a facile route towards tunable morphologies and hydrophilic payload encapsulation. *Chem. Commun.* **2015**, *51*, 15858–15861, doi:10.1039/C5CC05258K.

239. Porcaro, F.; Carlini, L.; Ugolini, A.; Visaggio, D.; Visca, P.; Fratoddi, I.; Venditti, I.; Meneghini, C.; Simonelli, L.; Marini, C.; et al. Synthesis and structural characterization of silver nanoparticles stabilized with 3-mercapto-1-propansulfonate and 1-thioglucose mixed thiols for antibacterial applications. *Materials (Basel).* **2016**, *9*, doi:10.3390/ma9121028.

240. Fontana, L.; Bassetti, M.; Battocchio, C.; Venditti, I.; Fratoddi, I. Synthesis of gold and silver nanoparticles functionalized with organic dithiols. *Colloids Surfaces A Physicochem. Eng. Asp.* **2017**, *532*, 282–289, doi:10.1016/J.COLSURFA.2017.05.005.

241. Sulaiman, K.O.; Sudheeshkumar, V.; Scott, R.W.J. Activation of atomically precise silver clusters on carbon supports for styrene oxidation reactions. *RSC Adv.* **2019**, *9*, 28019–28027, doi:10.1039/C9RA05566E.

242. Jockusch, S.; Landis, M.S.; Freiermuth, B.; Turro, N.J. Photochemistry and Photophysics of α-Hydroxy Ketones. *Macromolecules* **2001**, *34*, 1619–1626, doi:10.1021/MA001836P.

243. Scaiano, J.C.; Aliaga, C.; Maguire, S.; Wang, D. Magnetic field control of photoinduced silver nanoparticle formation. *J. Phys. Chem. B* **2006**, *110*, 12856–12859, doi:10.1021/JP061723T/SUPPL_FILE/JP061723TSI20060320_072929.PDF.

244. Marin, M.L.; McGilvray, K.L.; Scaiano, J.C. Photochemical strategies for the synthesis of gold nanoparticles from Au(III) and Au(I) using photoinduced free radical generation. *J. Am. Chem. Soc.* **2008**, *130*, 16572–16584, doi:10.1021/JA803490N/SUPPL_FILE/JA803490N_SI_001.PDF.

245. Scaiano, J.C.; Stamplecoskie, K.G.; Hallett-Tapley, G.L. Photochemical Norrish type I reaction as a tool for metal nanoparticle synthesis: importance of proton coupled electron transfer. *Chem. Commun.* **2012**, *48*, 4798–4808, doi:10.1039/C2CC30615H.

246. Dietliker, K.; Jung, T.; Benkhoff, J.; Kura, H.; Matsumoto, A.; Oka, H.; Hristova, D.; Gescheidt, G.; Rist, G. New Developments in Photoinitiators. *Macromol. Symp.* **2004**, *217*, 77–98, doi:10.1002/MASY.200451307.

247. Shergill, R.; Haberler, M.; Vink, C.B.; Patten, H. V.; Woodward, J.R. Evidence for a novel bisacylphosphine oxide photoreaction from TRIR, TREPR and DFT studies. *Phys. Chem. Chem. Phys.* **2009**, *11*, 7248–7256, doi:10.1039/B904982G.

248. Makarov, T.; Savitsky, A.; … K.M.-T.J. of; 2005, undefined Multifrequency time-resolved electron paramagnetic resonance investigations after photolysis of phosphine oxide photoinitiators. Dependence of triplet mechanism. *ACS Publ.* **2005**, *109*, 2254–2263, doi:10.1021/jp0454725.

249. Spichty, M.; Turro, N.J.; Rist, G.; Birbaum, J.L.; Dietliker, K.; Wolf, J.P.; Gescheidt, G. Bond cleavage in the excited state of acyl phosphene oxides: Insight on the role of conformation by model calculations: a concept. *J. Photochem. Photobiol. A Chem.* **2001**, *142*, 209–213, doi:10.1016/S1010-6030(01)00515-9.

250. Jockusch, S.; Koptyug, I. V.; McGarry, P.F.; Sluggett, G.W.; Turro, N.J.; Watkins, D.M. A steady-state and picosecond pump-probe investigation of the photophysics of an acyl and a Bis(acyl)phosphine oxide. *J. Am. Chem.*

Soc. **1997**, *119*, 11495–11501, doi:10.1021/JA971630C.

251. Sluggett, G.W.; Turro, C.; Turro, N.J.; George, M.W.; Koptyug, I. V. (2,4,6-Trimethylbenzoyl)diphenylphosphine Oxide Photochemistry. A Direct Time-Resolved Spectroscopic Study of Both Radical Fragments. *J. Am. Chem. Soc.* **1995**, *117*, 5148–5153, doi:10.1021/JA00123A018.

252. Sangermano, M.; Periolatto, M.; Castellino, M.; Wang, J.; Dietliker, K.; Grützmacher, J.L.; Grützmacher, H. A Simple Preparation of Photoactive Glass Surfaces Allowing Coatings via the "grafting-from" Method. *ACS Appl. Mater. Interfaces* **2016**, *8*, 19764–19771, doi:10.1021/ACSAMI.6B05822.

253. Sahin, M.; Krawczyk, K.K.; Roszkowski, P.; Wang, J.; Kaynak, B.; Kern, W.; Schlögl, S.; Grützmacher, H. Photoactive silica nanoparticles: Influence of surface functionalization on migration and kinetics of radical-induced photopolymerization reactions. *Eur. Polym. J.* **2018**, *98*, 430–438, doi:10.1016/J.EURPOLYMJ.2017.11.046.

254. Razza, N.; Rizza, G.; Coulon, P.-E.; Didier, L.; Fadda, G.C.; Voit, B.; Synytska, A.; Grützmacher, H.; Sangermano, M. Enabling the synthesis of homogeneous or Janus hairy nanoparticles through surface photoactivation. *Nanoscale* **2018**, *10*, 14492–14498, doi:10.1039/C8NR04239J.

255. Wang, J.; Siqueira, G.; Müller, G.; Rentsch, D.; Huch, A.; Tingaut, P.; Levalois-Grützmacher, J.; Grützmacher, H. Synthesis of new bis(acyl)phosphane oxide photoinitiators for the surface functionalization of cellulose nanocrystals. *Chem. Commun.* **2016**, *52*, 2823–2826, doi:10.1039/c5cc09760f.

256. Eibel, A.; Fast, D.E.; Sattelkow, J.; Zalibera, M.; Wang, J.; Huber, A.; Müller, G.; Neshchadin, D.; Dietliker, K.; Plank, H.; et al. Star-shaped Polymers through Simple Wavelength-Selective Free-Radical Photopolymerization. *Angew. Chemie Int. Ed.* **2017**, *56*, 14306–14309, doi:10.1002/ANIE.201708274.

257. Benedikt, S.; Wang, J.; Markovic, M.; Moszner, N.; Dietliker, K.; Ovsianikov, A.; Grützmacher, H.; Liska, R. Highly efficient water-soluble visible light photoinitiators. *J. Polym. Sci. Part A Polym. Chem.* **2016**, *54*, 473–479, doi:10.1002/pola.27903.

258. Gong, T.; Adzima, B.J.; Bowman, C.N. A novel copper containing photoinitiator, copper(II) acylphosphinate, and its application in both the

photomediated CuAAC reaction and in atom transfer radical polymerization. *Chem. Commun.* **2013**, *49*, 7950–7952, doi:10.1039/C3CC43637C.

259. Laurino, P.; Hernandez, H.F.; Bräuer, J.; Krüger, K.; Grützmacher, H.; Tauer, K.; Seeberger, P.H. Snowballing Radical Generation Leads to Ultrahigh Molecular Weight Polymers. *Macromol. Rapid Commun.* **2012**, *33*, 1770–1774, doi:10.1002/MARC.201200384.

260. Darvasiová, D.; Barberiková, Z.; Eibel, A.; Schmallegger, M.; Gescheidt, G.; Zalibera, M.; Neshchadin, D. Probing the first steps of photoinduced free radical polymerization at water–oil interfaces. *Polym. Chem.* **2017**, *8*, 6943–6947, doi:10.1039/C7PY01414G.

261. Zhou, J.; Allonas, X.; Ibrahim, A.; Liu, X. Progress in the development of polymeric and multifunctional photoinitiators. *Prog. Polym. Sci.* **2019**, *99*, 101165, doi:10.1016/J.PROGPOLYMSCI.2019.101165.

262. Burrows, R.; Davidson, R.; Illsley, D. Multifunctional photoinitiators (MFPIs): A new concept. *Surf. Coatings Int. Part B Coatings Trans.* **2004**, *87*, 127–135, doi:10.1007/BF02699607.

263. Cosola, A.; Conti, R.; Rana, V.K.; Sangermano, M.; Chiappone, A.; Levalois-Grützmacher, J.; Grützmacher, H. Synthesis of γ-cyclodextrin substituted bis(acyl)phosphane oxide derivative (BAPO-γ-CyD) serving as multiple photoinitiator and crosslinking agent. *Chem. Commun.* **2020**, *56*, 4828–4831, doi:10.1039/d0cc01732a.

264. Gorsche, C.; Koch, T.; Moszner, N.; Liska, R. Exploring the benefits of β-allyl sulfones for more homogeneous dimethacrylate photopolymer networks. *Polym. Chem.* **2015**, *6*, 2038–2047, doi:10.1039/C4PY01582G.

265. Mitterbauer, M.; Knaack, P.; Naumov, S.; Markovic, M.; Ovsianikov, A.; Moszner, N.; Liska, R. Acylstannanes: Cleavable and Highly Reactive Photoinitiators for Radical Photopolymerization at Wavelengths above 500 nm with Excellent Photobleaching Behavior. *Angew. Chemie Int. Ed.* **2018**, *57*, 12146–12150, doi:10.1002/ANIE.201804094.

266. Trofimov, B.A.; Arbuzova, S.N.; Gusarova, N.K. Phosphine in the synthesis of organophosphorus compounds. *Russ. Chem. Rev.* **1999**, *68*, 215–228, doi:10.1070/RC1999V068N03ABEH000464.

267. Müller, G.; Zalibera, M.; Gescheidt, G.; Rosenthal, A.; Santiso-Quinones, G.; Dietliker, K.; Grützmacher, H. Simple One-Pot Syntheses of Water-Soluble Bis(acyl)phosphane Oxide Photoinitiators and Their Application in

Surfactant-Free Emulsion Polymerization. *Macromol. Rapid Commun.* **2015**, *36*, 553–557, doi:10.1002/MARC.201400743.

268. Aparicio, J.L.; Elizalde, M. Migration of Photoinitiators in Food Packaging: A Review. *Packag. Technol. Sci.* **2015**, *28*, 181–203, doi:10.1002/PTS.2099.

269. Lendlein, A.; Langer, R. Biodegradable, elastic shape-memory polymers for potential biomedical applications. *Science (80-.).* **2002**, *296*, 1673–1676, doi:10.1126/science.1066102.

270. Neuss, S.; Blomenkamp, I.; Stainforth, R.; Boltersdorf, D.; Jansen, M.; Butz, N.; Perez-Bouza, A.; Knüchel, R. The use of a shape-memory poly(ε{lunate}-caprolactone)dimethacrylate network as a tissue engineering scaffold. *Biomaterials* **2009**, *30*, 1697–1705, doi:10.1016/j.biomaterials.2008.12.027.

271. Metcalfe, A.; Desfaits, A.C.; Salazkin, I.; Yahia, L.; Sokolowski, W.M.; Raymond, J. Cold hibernated elastic memory foams for endovascular interventions. *Biomaterials* **2003**, *24*, 491–497, doi:10.1016/S0142-9612(02)00362-9.

272. Reed, Jr., J.L.; Hemmelgarn, C.D.; Pelley, B.M.; Havens, E. Adaptive wing structures. In Proceedings of the Smart Structures and Materials 2005: Industrial and Commercial Applications of Smart Structures Technologies; White, E. V., Ed.; SPIE, 2005; Vol. 5762, p. 132.

273. Lan, X.; Liu, Y.; Lv, H.; Wang, X.; Leng, J.; Du, S. Fiber reinforced shape-memory polymer composite and its application in a deployable hinge. *Smart Mater. Struct.* **2009**, *18*, 024002, doi:10.1088/0964-1726/18/2/024002.

274. Browne, A. L.; Johnson N. L. Shape memory polymer seat assemblies. US Patent 7309104, 2007.

275. Gall, K.; Kreiner, P.; Turner, D.; Hulse, M. Shape-memory polymers for microelectromechanical systems. *J. Microelectromechanical Syst.* **2004**, *13*, 472–483, doi:10.1109/JMEMS.2004.828727.

276. Takehara, H.; Jiang, C.; Uto, K.; Ebara, M.; Aoyagi, T.; Ichiki, T. Novel microfluidic valve technology based on shape memory effect of poly(ε-caprolactone). *Appl. Phys. Express* **2013**, *6*, 037201, doi:10.7567/APEX.6.037201.

277. Sekitani, T.; Zschieschang, U.; Klauk, H.; Someya, T. Flexible organic transistors and circuits with extreme bending stability. *Nat. Mater.* **2010**, *9*, 1015–1022, doi:10.1038/nmat2896.

278. Yu, Z.; Zhang, Q.; Li, L.; Chen, Q.; Niu, X.; Liu, J.; Pei, Q. Highly flexible silver nanowire electrodes for shape-memory polymer light-emitting diodes. *Adv. Mater.* **2011**, *23*, 664–668, doi:10.1002/adma.201003398.

279. Xia, Y.; He, Y.; Zhang, F.; Liu, Y.; Leng, J. A Review of Shape Memory Polymers and Composites: Mechanisms, Materials, and Applications. *Adv. Mater.* **2020**, 2000713, doi:10.1002/adma.202000713.

280. Chu, H.; Yang, W.; Sun, L.; Cai, S.; Yang, R.; Liang, W.; Yu, H.; Liu, L. 4D Printing: A Review on Recent Progresses. *Micromachines* **2020**, *11*, 796, doi:10.3390/mi11090796.

281. Sachyani Keneth, E.; Kamyshny, A.; Totaro, M.; Beccai, L.; Magdassi, S. 3D Printing Materials for Soft Robotics. *Adv. Mater.* **2020**, 2003387, doi:10.1002/adma.202003387.

282. Yang, H.; Leow, W.R.; Wang, T.; Wang, J.; Yu, J.; He, K.; Qi, D.; Wan, C.; Chen, X. 3D Printed Photoresponsive Devices Based on Shape Memory Composites. *Adv. Mater.* **2017**, *29*, 1701627, doi:10.1002/ADMA.201701627.

283. Nadgorny, M.; Xiao, Z.; Chen, C.; Connal, L.A. Three-Dimensional Printing of pH-Responsive and Functional Polymers on an Affordable Desktop Printer. *ACS Appl. Mater. Interfaces* **2016**, *8*, 28946–28954, doi:10.1021/ACSAMI.6B07388.

284. Mao, Y.; Yu, K.; Isakov, M.S.; Wu, J.; Dunn, M.L.; Jerry Qi, H. Sequential Self-Folding Structures by 3D Printed Digital Shape Memory Polymers. *Sci. Rep.* **2015**, *5*, 13616, doi:10.1038/srep13616.

285. Zhang, B.; Li, H.; Cheng, J.; Ye, H.; Sakhaei, A.H.; Yuan, C.; Rao, P.; Zhang, Y.-F.; Chen, Z.; Wang, R.; et al. Mechanically Robust and UV-Curable Shape-Memory Polymers for Digital Light Processing Based 4D Printing. *Adv. Mater.* **2021**, *33*, 2101298, doi:10.1002/ADMA.202101298.

286. Ratna, D.; Karger-Kocsis, J. Recent advances in shape memory polymers and composites: A review. *J. Mater. Sci.* **2008**, *43*, 254–269, doi:10.1007/s10853-007-2176-7.

287. Xie, T. Recent advances in polymer shape memory. *Polymer (Guildf).* **2011**, *52*, 4985–5000, doi:10.1016/j.polymer.2011.08.003.

288. Lewis, C.L.; Dell, E.M. A review of shape memory polymers bearing reversible binding groups. *J. Polym. Sci. Part B Polym. Phys.* **2016**, *54*, 1340–1364, doi:10.1002/polb.23994.

289. Rabani, G.; Luftmann, H.; Kraft, A. Synthesis and characterization of two shape-memory polymers containing short aramid hard segments and poly(ε{lunate}-caprolactone) soft segments. *Polymer (Guildf).* **2006**, *47*, 4251–4260, doi:10.1016/j.polymer.2006.03.106.

290. Pandini, S.; Passera, S.; Messori, M.; Paderni, K.; Toselli, M.; Gianoncelli, A.; Bontempi, E.; Ricc, T. Two-way reversible shape memory behaviour of crosslinked poly(ε-caprolactone). *Polymer (Guildf).* **2012**, *53*, 1915–1924, doi:10.1016/j.polymer.2012.02.053.

291. Messori, M.; Degli Esposti, M.; Paderni, K.; Pandini, S.; Passera, S.; Riccò, T.; Toselli, M. Chemical and thermomechanical tailoring of the shape memory effect in poly(ε-caprolactone)-based systems. *J. Mater. Sci.* **2013**, *48*, 424–440, doi:10.1007/s10853-012-6757-8.

292. Pandini, S.; Baldi, F.; Paderni, K.; Messori, M.; Toselli, M.; Pilati, F.; Gianoncelli, A.; Brisotto, M.; Bontempi, E.; Riccò, T. One-way and two-way shape memory behaviour of semi-crystalline networks based on sol-gel cross-linked poly(ε-caprolactone). *Polymer (Guildf).* **2013**, *54*, 4253–4265, doi:10.1016/j.polymer.2013.06.016.

293. Li, J.; Viveros, J.A.; Wrue, M.H.; Anthamatten, M. Shape-memory effects in polymer networks containing reversibly associating side-groups. *Adv. Mater.* **2007**, *19*, 2851–2855, doi:10.1002/adma.200602260.

294. Li, J.; Lewis, C.L.; Chen, D.L.; Anthamatten, M. Dynamic mechanical behavior of photo-cross-linked shape-memory elastomers. *Macromolecules* **2011**, *44*, 5336–5343, doi:10.1021/ma2004019.

295. Liu, G.; Guan, C.; Xia, H.; Guo, F.; Ding, X.; Peng, Y. Novel Shape-Memory Polymer Based on Hydrogen Bonding. *Macromol. Rapid Commun.* **2006**, *27*, 1100–1104, doi:10.1002/marc.200600189.

296. Ware, T.; Hearon, K.; Lonnecker, A.; Wooley, K.L.; Maitland, D.J.; Voit, W. Triple-shape memory polymers based on self-complementary hydrogen bonding. *Macromolecules* **2012**, *45*, 1062–1069, doi:10.1021/ma202098s.

297. Cosola, A.; Sangermano, M.; Terenziani, D.; Conti, R.; Messori, M.; Grützmacher, H.; Pirri, C.F.; Chiappone, A. DLP 3D – printing of shape memory polymers stabilized by thermoreversible hydrogen bonding interactions. *Appl. Mater. Today* **2021**, *23*, 101060, doi:10.1016/J.APMT.2021.101060.

298. Morita, S. Hydrogen-bonds structure in poly(2-hydroxyethyl methacrylate)

studied by temperature-dependent infrared spectroscopy. *Front. Chem.* **2014**, *2*, 10, doi:10.3389/fchem.2014.00010.

299. Lewis, C.L.; Stewart, K.; Anthamatten, M. The influence of hydrogen bonding side-groups on viscoelastic behavior of linear and network polymers. *Macromolecules* **2014**, *47*, 729–740, doi:10.1021/ma402368s.

300. Kuo, S.W.; Tsai, H.T. Complementary multiple hydrogen-bonding interactions increase the glass transition temperatures to PMMA copolymer mixtures. *Macromolecules* **2009**, *42*, 4701–4711, doi:10.1021/ma900640a.

301. Chalmers, J.M.; Griffiths, P.R. *Handbook of Vibrational Spectroscopy*; John Wiley & Son: Chichester, UK, 2002;

302. Morita, S.; Kitagawa, K.; Ozaki, Y. Hydrogen-bond structures in poly(2-hydroxyethyl methacrylate): Infrared spectroscopy and quantum chemical calculations with model compounds. *Vib. Spectrosc.* **2009**, *51*, 28–33, doi:10.1016/j.vibspec.2008.09.008.

303. Morita, S.; Tanaka, M.; Ozaki, Y. Time-resolved in situ ATR-IR observations of the process of sorption of water into a poly(2-methoxyethyl acrylate) film. *Langmuir* **2007**, *23*, 3750–3761, doi:10.1021/la0625998.

304. Lee, B.S.; Chun, B.C.; Chung, Y.C.; Sul, K. Il; Cho, J.W. Structure and thermomechanical properties of polyurethane block copolymers with shape memory effect. *Macromolecules* **2001**, *34*, 6431–6437, doi:10.1021/ma0018421.

305. Liu, G.; Ding, X.; Cao, Y.; Zheng, Z.; Peng, Y. Shape memory of hydrogen-bonded polymer network/poly(ethylene glycol) complexes. *Macromolecules* **2004**, *37*, 2228–2232, doi:10.1021/ma035717w.

306. Liu, Y.; Han, C.; Tan, H.; Du, X. Thermal, mechanical and shape memory properties of shape memory epoxy resin. *Mater. Sci. Eng. A* **2010**, *527*, 2510–2514, doi:10.1016/J.MSEA.2009.12.014.